Lead-free $BiFeO_3$-$BaTiO_3$ high temperature piezoceramics

A thesis submitted to
The University of Manchester
for the degree of Doctor of Philosophy
in the Faculty of Science & Engineering

2018

Ilkan Calisir

School of Materials

Contents

Word Count: 56810

List of Publications

The thesis is partly composed of the following original publications, reproduced with permission from the Royal Society of Chemistry.

1. Calisir, I. & Hall, D. A. *Chemical heterogeneity and approaches to its control in $BiFeO_3$–$BaTiO_3$ lead-free ferroelectrics*. J. Mater. Chem. C **6,** 134–146 (2018).

2. Calisir, I., Amirov, A. A., Kleppe, A. K. & Hall, D. A. *Optimisation of functional properties in lead-free $BiFeO_3$–$BaTiO_3$ ceramics through La^{3+}substitution strategy*. J. Mater. Chem. A 6, (2018).

Abstract

High temperature piezoelectrics are a crucial material group that are used in actuation and sensing applications working in harsh environments. However, due to the limited material selection range providing cost-effective, high temperature reliability and lead-free content, the research in this area has been accelerated to find a potential candidate conforming these properties. For this purpose, the $BiFeO_3$-$BaTiO_3$ solid solution system has been proposed as a potential candidate and this study aims to investigate its (micro)structure-property relationships in detail.

In the present study, the selected compositions are prepared *via* the solid state reaction method. It is found that without modification, the ceramics show high conductivity. Therefore, systematic doping strategies are employed using MnO_2, La_2O_3 and TiO_2. Nonetheless, during these investigations, a serious issue of chemical heterogeneity is identified, which has substantial impact on the functional properties. Such heterogeneity is detected in the form of core and shell regions which are $BiFeO_3$-rich and-depleted, respectively. The formation mechanism for such core-shell-type microstructures is discussed in terms of kinetic factors and thermodynamic immiscibility, which are found to be directly linked to the incorporation of MnO_2 and the influence of donor substitution of La^{3+} and Ti^{4+} ions on the solubility of the perovskite end-members ($BiFeO_3$ and $BaTiO_3$). Their influence on the phase content, microstructure and functional properties are significant and give rise to unique features such as discontinuity in ferroic domains across the grain morphology, prominent pseudocubic phase content, suppressed polarisation, reduced electrostrain, and temperature-dependent dielectric anomalies.

On the other hand, it is shown that the application of thermal quenching treatment induces substantial alterations in the crystal structure of the shell phase, which transforms from pseudocubic symmetry (short-range ferroelectric ordering) to untilted rhombohedral symmetry (long-range ferroelectric ordering). Such a transformation is confirmed using high resolution and *in-situ* high energy X-ray synchrotron diffraction investigations. The *in-situ* studies are carried out on the samples under electric field and reveal a novel actuation mechanism which is induced by quenching. The effect of quenching on polarisation, temperature-dependent dielectric properties and magnetoelectric coupling is also investigated, by comparing with the slow-cooled states of the studied compositions. It is also found that the most dramatic alterations in structure and properties, due to quenching, are evident in the compositions with high $BiFeO_3$ content (≥75%).

Declaration

No portion of the work referred to in the thesis has been submitted in support of an application for another degree or qualification of this or any other university or other institute of learning.

Copyright Statement

i. The author of this thesis (including any appendices and/or schedules to this thesis) owns certain copyright or related rights in it (the "Copyright") and s/he has given The University of Manchester certain rights to use such Copyright, including for administrative purposes.

ii. Copies of this thesis, either in full or in extracts and whether in hard or electronic copy, may be made **only** in accordance with the Copyright, Designs and Patents Act 1988 (as amended) and regulations issued under it or, where appropriate, in accordance with licensing agreements which the University has from time to time. This page must form part of any such copies made.

iii. The ownership of certain Copyright, patents, designs, trademarks and other intellectual property (the "Intellectual Property") and any reproductions of copyright works in the thesis, for example graphs and tables ("Reproductions"), which may be described in this thesis, may not be owned by the author and may be owned by third parties. Such Intellectual Property and Reproductions cannot and must not be made available for use without the prior written permission of the owner(s) of the relevant Intellectual Property and/or Reproductions.

iv. Further information on the conditions under which disclosure, publication and commercialisation of this thesis, the Copyright and any Intellectual Property and/or Reproductions described in it may take place is available in the University IP Policy (see http://documents.manchester.ac.uk/DocuInfo.aspx?DocID=24420), in any relevant Thesis restriction declarations deposited in the University Library, The University Library's regulations (see http://www.library.manchester.ac.uk/about/regulations/) and in The University's policy on Presentation of Theses

Acknowledgement

I would first and foremost like to thank my supervisor Dr. David Hall. He allowed me to work independently and gave me great confidence to overcome challenges that we encountered during my project. He has been more than a supervisor, and his patience and his guidance will always be missed.

I would also like to acknowledge my dear colleagues who are the members of ferroelectric group; Mohammed Naji Al-Aaraji, Abdulkarim Khalf, , Yizhe Li and Jirapa Tangsritarakul, Ge Wang, Ang Gao, Bing Wang, and thermoelectric group; Dursinov the greatest, Diana Talia Alvarez Ruiz, Dongting Jiang, Nuth Kulwongwit and troublemaker Bin Qi.

During this journey, I had enormous help from the staff in School of Materials and would like to acknowledge John Warren, Gary Harrison, Andrew Forest and Kenneth Gyves. I would also like to thank people who I had a chance to collaborate with, including Annette A. Kleppe, Prof. Chiu Tang, Claire Murray (Diamond National Light Source), my dear friend Abdulkarim A. Amirov (Immanuel Kant Baltic Federal University), Dr. Antonio Feteira (Sheffield Hallam University), Ian Maclaren and Shane McCartan (University of Glasgow).

Also, I would like to thank my housemates who has made this journey more fun; Jatinder (Jay), Richard, Suzanne, and Jacop. My lifelong buddy Jay and his kind-hearted partner Clare definitely deserve a special thank here, their sincere and unconditional supports are unforgettable. Jay buddy, maybe this is the year you have been waiting for [insert the image of the Liverpool fan with eye-glasses].

I have also had many great Turkish friends during this period and greatly acknowledge each of them. However, I have decided not to mention their name since I am concerned this may jeopardize their career, they know what I mean. Speaking of which I would like to send my warmest wishes to our tallest and greatest leader and also greatly acknowledge National Higher Education of Ministry, which provides a world-class education/scholarship system, for funding this PhD programme and making this journey even more interesting with their outstanding decision about me./s

Manchester, UK, 26 September 2018

Ilkan Calisir

This work is dedicated to my parents; my mom Ayse, my dad Mahmut, my beloved brothers; Ercan, Erhan, Tanju and Omer Faruk, and my love Yu-Chi Liu.

Without their endless support and love, none of this would have been possible.

Chapter 1

Introduction and Background

1.1 Overview

High temperature piezoceramics are in demand for actuator and sensor applications under extreme environments for example in fuel modulation, space exploration, deep oil drilling, nuclear reactors and wind turbines.[1–3] These applications usually require materials which can withstand temperatures ≈300°C or greater. Therefore, material selection for these extreme conditions is crucial and some commercially available and potential candidates are listed in Figure 1(a). Among non-ferroelectric piezoelectric materials, single crystals are potential candidates for such applications. For example, single crystals of quartz (SiO_2) have been used in the temperature range of 500–600°C, and it is the most commonly used piezoelectric operating at high temperatures.[2] However, cost of single crystals is much higher than polycrystalline oxide equivalents as well as exhibiting relatively low piezoelectric activity.[2,3] Conversely, ferroelectric ceramics could offer higher piezoelectric coefficients and due to the accommodating nature of the perovskite structure, composition and properties can be greatly tailored. Recent research has identified a number of ferroelectric materials having very high T_C which can be considered for high-temperature piezoelectric applications, but finding suitable combinations of high T_C and high piezoelectric properties in a single material is difficult.

This issue has currently been overcome by transducer design strategies such as using an intermediate component coupled with a material having moderate T_C to prevent the direct contact with the high temperature environment, as illustrated in Figure 1(b). However, this brings more complexity for device design along with extra cost. Thus, the search for piezoelectrics working in high temperature applications (>300 °C) has been a continuous effort in the field of electroceramics.[1–3]

Current efforts on the development of high Curie temperature ferroelectric ceramics still primarily focus on modifying $PbTiO_3$-based systems, since $PbTiO_3$ is a stable perovskite with high T_C (≈490°C), but the development of this material is challenging due to its intrinsic high tetragonality (*c*/*a*), which induces cracks during sintering.[2] Therefore, solid solutions of $PbTiO_3$ with alternative end members were found as the most effective approach and thus was extensively studied.[1,2,4] Bi-based perovskite end-members are the ones exhibiting the most

promising properties, including $BiFeO_3$, $BiScO_3$, $BiYbO_3$, $BiInO_3$, $Bi(Mg_{1/2}Ti_{1/2})O_3$, $(Bi_{1/2}K_{1/2})TiO_3$ and $BiGaO_3$ *etc*. However, the majority of these systems have shown either limited solubility or inferior electrical properties. In addition, due to human health and environmental concerns regarding to use of lead(Pb)-based compounds in electronics, new types of of lead-free piezoceramics has been targeted over the recent years.[5–7]

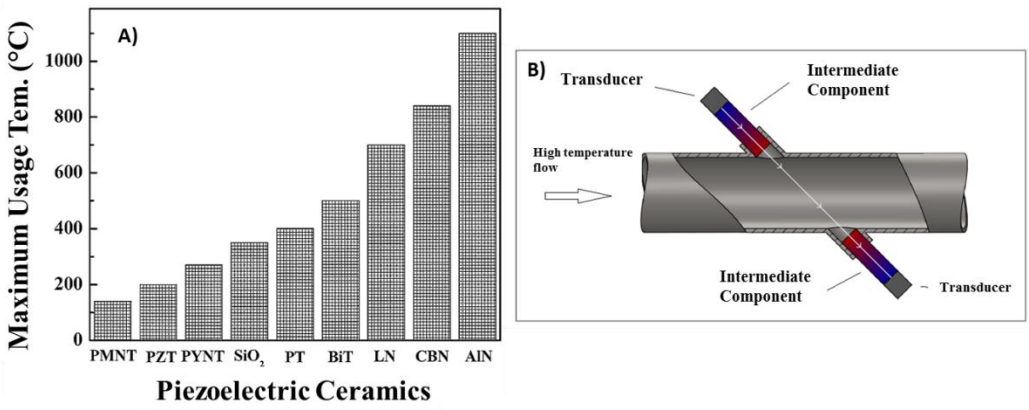

Figure 1 a) High temperature piezoceramics and their approximate maximum usage temperatures. PMNT: $Pb(Mg_{1/3}Nb_{2/3})O_3$-$PbTiO_3$, PZT: $Pb(Zr,Ti)O_3$,PYNT: $Pb(Yb_{1/2}Nb_{1/2})O_3$-$PbTiO_3$, PT: $PbTiO_3$, BiT: Bismuth-based tungsten-bronze structure, LN: $LiNbO_3$, CBN: $CaBi_2Nb_2O_9$ (textured), AlN: Aluminium Nitride.[2] **b)** An illustration of ultrasonic transducer attached to a pipeline to monitor high temperature flow.[a]

In conjunction with these advances, in 2009, the lead-free $BiFeO_3$-$BaTiO_3$ (BF−BT) solid system caught attention due to its reported moderate d_{33} of 116 pC/N and high T_C of ≈620°C (depolarization ≈470°C).[8] In the following years, a large number of studies have focused on this system to further explore not only its high temperature capability but also its intriguing ferroelectric behaviour at the micro-nano scale, electromechanical coupling, temperature-dependent dielectric properties, dielectric energy storage performance and multiferroic properties.

1.2 Motivation and Concept of the Thesis

The major motivation of the work presented here is to identify reported issues for $BiFeO_3$-$BaTiO_3$ lead-free piezoceramics and propose methods to optimise their structural and functional stability for high temperature applications. Throughout this project, various aspects were investigated including processing issues, chemical and structural (in)stabilities, doping effects, the influence of

[a] Web reference: https://ionixadvancedtechnologies.co.uk/

quenching, composition-temperature-dependent dielectric and ferroelectric properties, and electromechanical actuation mechanisms.

The thesis is written in the alternative format with two published articles and a manuscript which is in preparation for publication. The thesis concept is organized as follows:

Chapter 1 introduces the basic theory and literature review of topics addressed in subsequent chapters.

Chapter 2 presents the fundamental aspects of the experimental techniques utilised during this work.

Chapter 3 is the section where research outputs are included and major topics are divided into the relevant sub-sections.

i) Chemical heterogeneity: This section is composed of a published article with a title "Chemical heterogeneity and approaches to its control in $BiFeO_3$-$BaTiO_3$ lead-free ferroelectrics". This article addresses the method of incorporation of MnO_2 in BF-BT ceramics.

ii) Substitution strategies: A published manuscript with the title "Optimisation of functional properties in lead-free $BiFeO_3$-$BaTiO_3$ ceramics through La^{3+} substitution strategy" is included for this section. A strategy was developed using La^{3+} as either a donor or isovalent dopant in BF-BT ceramics. Its effect in regard to polarisation, strain, dielectric energy storage, ferromagnetic/magnetoelectric properties was comprehensively investigated with relation to the influence of thermal quenching treatment.

iii) Actuation mechanisms: This particular research output is composed of two articles in preparation; one contains a thorough microscopic and macroscopic strain analysis for a particular core-shell structured composition, while the second part expands the search for the morphotropic phase boundary (MPB) compositions in a much wider range of the $BiFeO_3$–$BaTiO_3$ binary system with a minor donor substitution of Ti^{4+} for Fe^{3+}. Since these parts are related to each other, they are treated in the same section.

Chapter 4 contains general conclusions and conveys some recommendations for future research for this system.

It should be also noted that each chapter is self-contained, therefore the numerical order for figures, tables, equations, footnotes and references is given within the relevant chapter.

1.3 Basic Theory

This section aims to cover the basic theory governing the behaviour of electroceramics, primarily dealing with relationships between structure and properties. The chapter starts with the description of crystal structure, and then highlights the importance of perovskite-type oxides in electroceramics. Dielectric

phenomena, which are the core characteristic of electroceramics is introduced. Subsequently, the fundamentals of ferroelectricity and piezoelectricity, known as special properties of polar dielectrics, are thoroughly covered.

1.3.1 Crystal Structure

An understanding of the concept of solid materials begins with the internal structure of the material. Therefore, the starting point should be the basis of a single crystallite and its components. The crystallite is composed of atoms that are constrained to occupy specific positions in a repeating manner to each other, thus the crystal structure or lattice of the crystal is constructed. The smallest repeating unit of the lattice is called a *unit cell*, and it is a vital component in the crystallography as well as in material world, since the specific symmetry possessed by the unit cell determines whether it is scientifically and/or technologically viable for the desired properties to exist in a crystal.[9–11]

The unit cell can be categorised by one of seven lattice systems in crystallography which is based on their different shapes and sizes, as illustrated in Figure 2. It is basically determined by the cell edge lengths, or lattice vectors *a*, *b*, *c*, and the angles between them alpha, beta, gamma, as well as the presence of a body- or face-centred atom.[9]

The possible combinations of these lattice parameters can then produce cubic, hexagonal, tetragonal, rhombohedral, orthorhombic, monoclinic and triclinic crystal symmetries. Further combination of these symmetries with the various possible lattice centres *i.e.* primitive, body-centred, face-centred, centred or base-centred and rhombohedral primitive, means that crystal structure can be defined with one of fourteen *Bravais lattices*.[9]

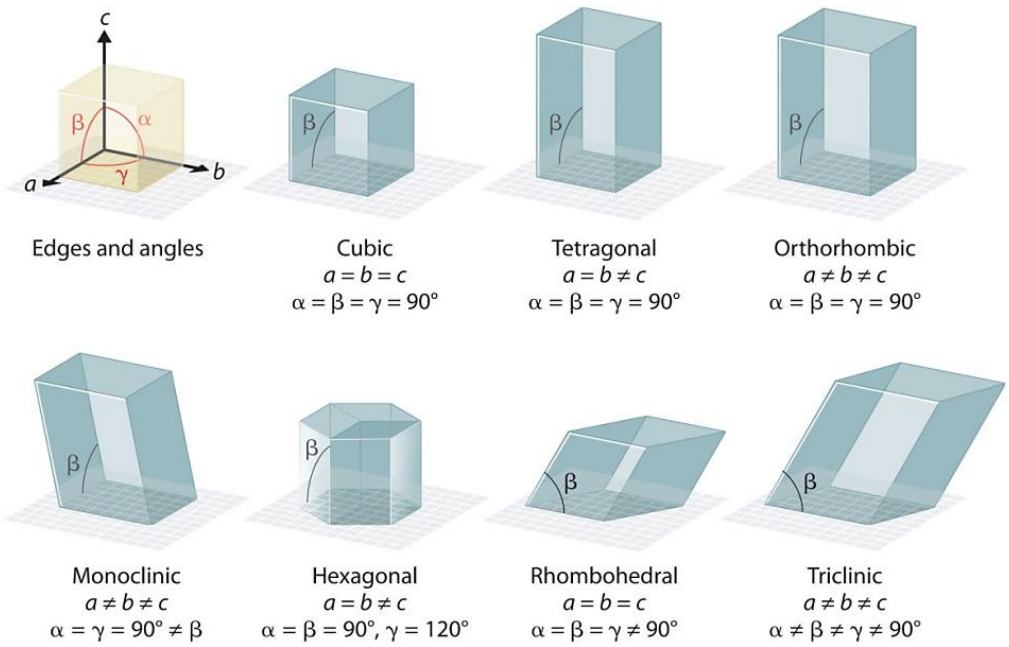

Figure 2 The illustration of unit cell edge lengths and angles (β implies the angle between *a* and *c* in the associated symmetries) in respect to seven types of crystal symmetry.[b]

The elements of symmetry that are utilized by crystallographers to define point symmetry in space are a centre of symmetry, axes of rotation, mirror planes, and combinations of these.[11] Once these are also combined with translational elements such as glide planes and screw axes, then a detailed description of the structure is obtained and it allows us to determine the *space group* of the crystal structure, which resulted in 230 different symmetry types that define the only ways in which identical objects can be arranged in an infinite lattice.[9–11]

A special notation system to describe a space group was developed by Hermann-Mauguin,[c] which is mostly composed of three or four symbols. It starts with one of the letters referring to Bravais lattice types as P (primitive), I (body-centred), F (face-centred), C (side-centred), and R (primitive rhombohedral). Then it continues with additional important crystallographic information such as mirror planes, fold rotations or glide planes. As an example, a well-known ferroelectric tetragonal phase is commonly denoted as *P4mm* space group indicating that it has a primitive unit cell (P) with four-fold rotation (4) and two mirror planes (mm). It should be also noted that three crystal classes contain most of the ferroelectric compounds, which have proved important in the field of

[b] Web reference: https://saylordotorg.github.io/text_general-chemistry-principles-patterns-and-applications-v1.0/s16-solids.html

[c] Hermann-Mauguin notation system is also known as *international notation* due to standardization made by the International Tables For Crystallography. The evolution of notation system for symbolizing space groups can be found in detail: https://it.iucr.org/Ab/ch12o1v0001

piezoelectric ceramics, which are 4mm (tetragonal), 3m (rhombohedral) and mm2 (orthorhombic).[9,11]

All crystals can be also divided into 32 different classes or point groups utilizing these symmetry elements. These 32 point groups are subdivisions of seven basic crystal systems. Of the 32 point groups, 21 classes are noncentrosymmetric (a necessary condition for piezoelectricity to exist) and 20 of these are piezoelectric. One class, although lacking a centre of symmetry, is not piezoelectric because of other combined symmetry elements.[9,11]

Crystal structure, functionality and performance are highly correlated factors for crystalline materials. Based on the fundamental crystal unit cell structure, crystalline ceramics can be categorized into four basic types:[11] *i)* the tungsten-bronze group, *ii)* the perovskite group, *iii)* the pyrochlore octahedral group, and *iv)* the layer structure group.

Among these, the perovskite type ones are the most studied family of ferroelectrics are the most important because of its simplicity and wide use in applications, with compositions such as $BaTiO_3$ in dielectric-related, $Pb(Zr_xTi_{1-x})O_3$ (PZT) in piezoelectric-related, $BiFeO_3$ in multiferroic-related, and $(K_xNa_{1-x})NbO_3$ (KNN) in electro-optic-related applications.[9,11]

1.3.1.1 Perovskite Structure

Perovskite compounds are represented by the formula of ABO_3, where A and B each represent a cation element or mixture of two or more such elements or vacancies. The physical properties of the entire family are extremely diverse; depending on the composition and cationic ordering, they can be metallic or insulating and exhibit many different types of structural and magnetic order.[9]

The ABO_3-type structure is exemplified by the cubic phase of $CaTiO_3$, as shown in Figure 3. In this structure, the Ti^{4+} ion is located at the centre of the unit cell, the O^{2-} ions sit at the centre of each face of the unit cell, and the Ca^{2+} ions occupy at each corner. In each unit cell, the single Ti^{4+} ion contributes +4 charge; the six O^{2-} ions contribute -6 charge, with each O^{2-} ion shared at the face of two unit cells and the eight Ca^{2+} ions contribute +2 charge with each calcium ion shared at the corner of eight unit cells. In total, the charges sum to zero; in the cubic phase, the unit cell exhibits overall neutral charge with the positive and negative charge centres overlaid spatially.[9]

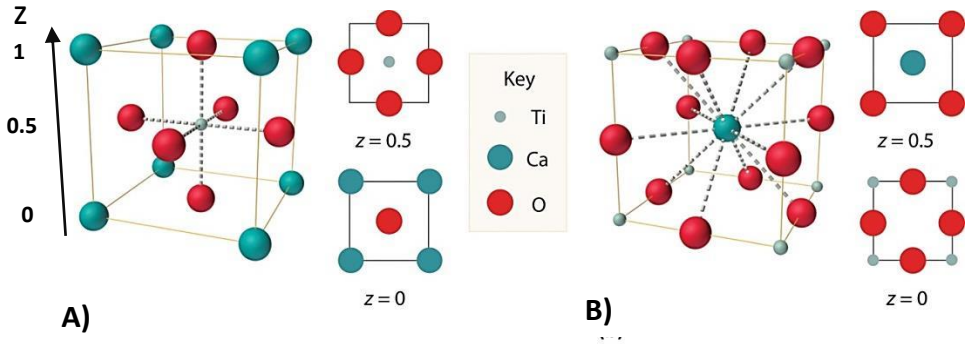

Figure 3 ABO_3 type crystal structure is represented for $CaTiO_3$ with two equivalent views: **(a)** a view with the Ti atom at the center and **(b)** an alternative view with the Ca atom at the center.[d]

The perovskite family is extremely accommodating of ions having differing valence, with the A-site permitting monovalent, divalent or trivalent ions and the B-site permitting trivalent, tetravalent and pentavalent ions provided that the total valence is 6+. A fractional combination of cations is also allowed such as in $(Bi^{3+}_{1/2}Na^{1+}_{1/2})Ti^{4+}O^{2-}_3$. It would be reasonable to presume that a large amount of disorder would be expected in binary, ternary and quaternary systems with varying A- and B-site cations.[9] This is particularly useful when searching for new morphotropic phase boundary (MPB) piezoelectric ceramics as many symmetry variant end members can be incorporated, for example with the $PbTiO_3$ end-member.[9–11]

The origin of ferroelectric behaviour and phase stability in perovskites, in general, can be simplified as shifts of the B-site and O ions in relation to the large A-site cation,[9,12] as depicted in Figure 4 with the example of ferroelectric $BaTiO_3$. Nonetheless, the polarizability of the A-site ion can also influence the local fields acting upon the B-site ion, thus causing a displacement in similar types of perovskites.[12,13]

[d] Web reference: https://saylordotorg.github.io/text_general-chemistry-principles-patterns-and-applications-v1.0/s16-solids.html

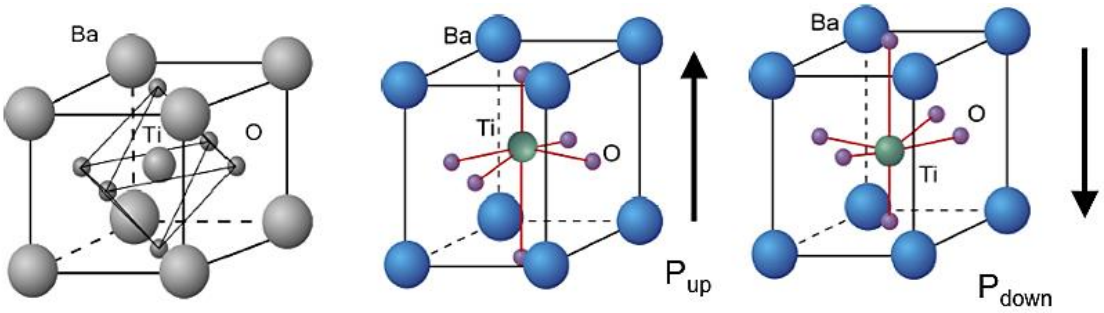

Figure 4 Crystal structure of the perovskite ferroelectric $BaTiO_3$. High-temperature paraelectric cubic phase with no polarisation is represented in gray scale. A room temperature ferroelectric tetragonal phase is shown in color, showing up and down polarization variants.[e]

Since a large number of substitutions in perovskites are possible, Goldschmidt developed a model for the stability limit of the perovskite structure and proposed the following equation:

$$t = \frac{r_A + r_O}{\sqrt{2}(r_B + r_O)} \quad (1)$$

The constant (t) is known as tolerance factor, and other constituents r_A, r_B, and r_O are the radii of the A , B cations and O ions, respectively. The tolerance factor simply determines the degree of structural distortion compared to the ideal cubic perovskite. Generally, this value should be within the range of $0.8 < t < 1.05$ for the stability range of the perovskite structure. If the tolerance factor is equal to 1, then the perovskite structure is an ideal cubic. In addition, empirical evidence shows that when the tolerance factor is greater than 1, the symmetry would be assumed to be stabilised in tetragonal or hexagonal configuration. The structures yielding tolerance factor smaller than 1 would result in low symmetries such as rhombohedral, monoclinic, and orthorhombic.[9]

It must be stated that the existence of ferroelectricity cannot be elucidated from this calculation. This method has its limitations as the ionic radius is not disclosed for Bi^{3+} and many other ions. However, estimations have been made based upon extrapolated data from Shannon.[14] An assumption is made that all bonds are totally ionic whereas it has been shown that this is often not the case, an example being $PbTiO_3$ which has been shown to demonstrate considerable covalence.[12] The tolerance factor approach also does not apply to perovskites with extensive A-site ionic vacancies.[9]

The stability of the perovskite structure in a material is governed not only by the tolerance factor, but also by the electronegativity difference between substituent cations and anions. The electronegativity difference (ΔEN) is given in the following equation:

$$\Delta EN = \frac{(X_{A-O} + X_{B-O})}{2} \quad (2)$$

[e] Web reference: http://mini.physics.sunysb.edu/~mdawber/research.htm

where X_{A-O} is the difference between the electronegativity of the A ion and the oxygen ion, X_{B-O} is the difference between the electronegativity of the B ion and the oxygen ion. This factor describes the ionic character of bonding in the compound. Greater differences in electronegativity result in a more stable perovskite structure because of the higher degree of ionic bonding.[9]

1.3.2 Dielectrics

A dielectric is an electrical insulator that can be defined as a material with a high electrical resistivity that can store electrical energy through the polarization of dipoles. When a dielectric is placed between parallel conductor plates and an electric field (E) is applied, the electric charges do not flow through the dielectric but instead displace from their equilibrium positions. The positive charges shift toward the applied electric field while the negative charges move in the opposite direction, resulting in a dipole moment or a polarization (P) within the dielectric. The polarizability of a material can be determined by the dielectric constant (K) or relative permittivity (ε_r). The following equations reveals the relationships between polarisation (P), dielectric displacement (D) and electric field (E) and:[9,10,15]

$$P = (\varepsilon_r - 1)\varepsilon_0 E \tag{3}$$

$$D = P + \varepsilon_r \varepsilon_0 E \tag{4}$$

Based on this relationship, a linear dielectric can then be expressed by

$$D = \varepsilon_r \varepsilon_0 E \tag{5}$$

where ε_0 is the permittivity of free space or vacuum (8.854 x 10^{-12} F/m). ε_r is a parameter to determine the efficiency at which the material can store charges between the parallel electrodes through comparing the material to those with identical electrodes separated by vacuum. This is generally the ratio between the material permittivity ε in farads per meter and that of free space ε_0. Therefore, the relative dielectric permittivity itself is dimensionless. With alternating voltages, the relative permittivity, $\varepsilon^*$is also a complex number that consists of real (ε', in phase) and imaginary (ε'', out of phase) parts as follows:

$$\varepsilon^* = \varepsilon' + i\varepsilon'' \tag{6}$$

ε' represents the energy storage in dielectric materials, while ε'' indicates the energy loss caused by either resistive leakage or dielectric absorption. Nonetheless, dielectric loss is generally expressed by the following equation:

$$tan\delta = \frac{\varepsilon''}{\varepsilon'} \tag{7}$$

Dielectric loss or $tan\delta$ is used to determine to how lossy the material is and if the $tan\delta$ value is very small (close to 0), the material would be considered as an ideal dielectric.[9,10,15]

For measuring the dielectric properties of ferroelectrics, capacitance measurement is used to obtain dielectric permittivity under an AC electric field as a function of frequency, by taking into account the sample thickness, d and the area of the electrodes, A. This relationship is expressed by the following equation:

$$C = \frac{\varepsilon_r \varepsilon_0 A}{d} \quad (8)$$

1.3.2.1 Polarisation Mechanisms

As an electric field is subjected to an ideal dielectric material, long range transport of charge cannot occur but only a limited rearrangement such that the dielectric acquires a dipole moment and can be polarized. Atomic polarization, which occurs in all materials, is a small displacement of the electrons in an atom relative to the nucleus; in ionic materials there is, in addition, ionic polarization involving the relative displacement of cation and anion sublattices. Dipolar materials, such as water, can be polarized since the applied electric field can orient the molecules. Finally, space charge polarization involves a limited transport of charge carriers until they are stopped at a potential barrier, possibly a grain boundary or phase boundary.[9,15] Such various polarisation mechanisms are primarily categorised into four types as shown in Figure 5, and their corresponding frequency ranges, or response rates are depicted in Figure 6.

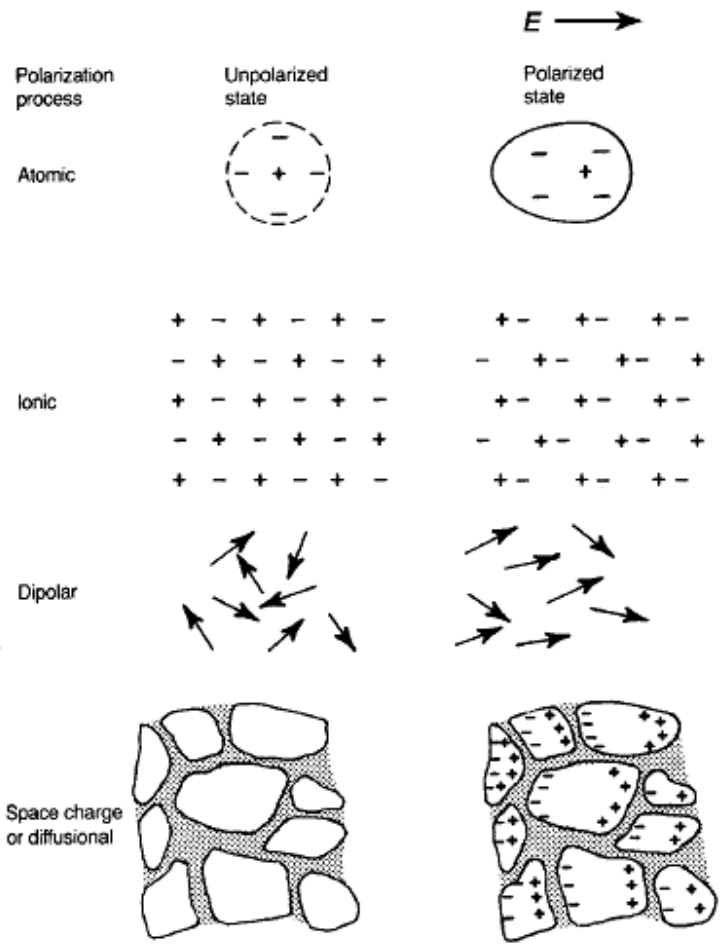

Figure 5 Illustration of various polarization mechanisms.[9]

These mechanisms can be summarised in order of increasing response time (Figure 6) as follows:

i. Electronic(atomic) polarisation: The distortion of the electron cloud surrounding an atom causes this polarization, as shown in Figure 5. This mechanism occurs in all materials, at all temperatures, and at frequencies up to about 10^{15}-10^{17} Hz.

ii. Ionic polarisation: Negatively and positively charged ions displace from their equilibrium positions when the electric field is applied. The positively charged ions move toward the electric field and the negatively charged ions move in the opposite direction, resulting in dipole moments. This polarization usually appears at the frequencies up to 10^{12}-10^{14} Hz.

iii. Dipolar polarisation: This polarization occurs due to permanent molecular size dipoles. In contrast to electronic and ionic polarization, this mechanism shows relaxation at the frequencies of 10^{7}-10^{10} Hz instead of resonance due to their size and the interaction between dipoles. This relaxation process is also dependent on a number of factors such as temperature, pressure and chemical surroundings.

iv. Space-charge polarisation: This polarization occurs at low frequencies which is mainly due to the trapping of charge carriers in the interfaces of inhomogeneous

microstructure. When an electric field is applied to a material, charge carriers are trapped at the grain boundaries, resulting in a charge separation across the grains.

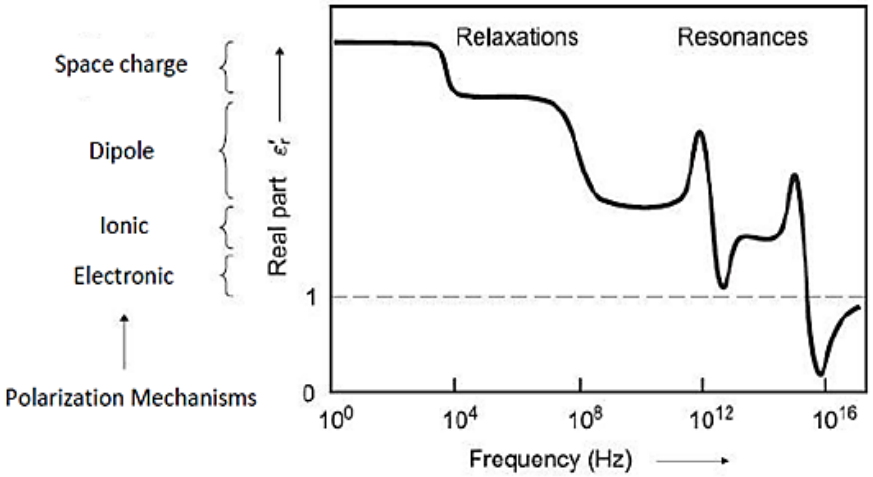

Figure 6 Polarisation mechanisms in dielectric materials.[15]

A group of dielectrics possesses a unique polar axis even with no external stimulus. This class of dielectrics can be classified as polar. Subgroups of polar dielectrics are piezoelectrics, pyroelectrics, and ferroelectrics. In the following section the principle of coupling phenomena in these subgroups is reviewed.

1.3.3 Piezoelectricity

Piezoelectricity is the ability of certain crystalline materials to develop an electrical displacement, D that is proportional to an applied mechanical stress, σ. This is called the *direct piezoelectric effect*. Piezoelectric materials also show a *converse effect*, where a mechanical strain, S is generated by the application of an electric field, E.[15,16] Both effects are illustrated in Figure 7(a) and (b).

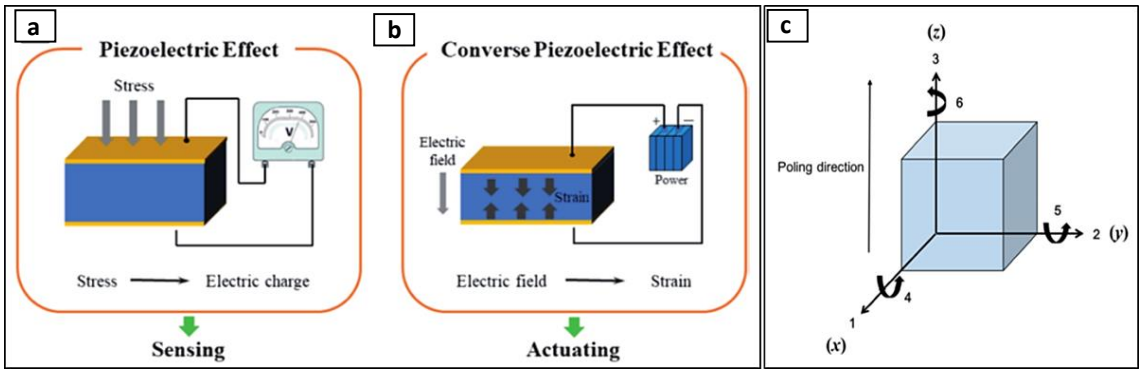

Figure 7 (a) The direct and **(b)** the converse piezoelectric effects. The direct piezoelectric effect generates an electric charge under the application of a mechanical stress, while the converse piezoelectric effect describes the situation where strain develops under an applied electric field.[5] **(c)** Direction indices of electromechanical constants in poled piezoceramics.[17]

The piezoelectric coupling is described by a linear relationship between the first-rank tensor or vector (D or E) and the second-rank tensor (σ or S), the

corresponding coupling coefficients d_{kij} form a third-rank tensor.[16] Thus, the direct and converse piezoelectric effects can be mathematically written in the following form using tensor notation (i, j, k = 1, 2, 3) as follows:[15,16]

$$D_i = d_{ijk}\,\sigma_{jk} \tag{9}$$

$$S_{ij} = d_{kij}\,E_k \tag{10}$$

where D_i is the electric displacement generated along the i-axis in response to the applied stress σ_{jk} , and d_{ijk} (=d_{kij}) is the piezoelectric charge coefficient. For the converse effect, S_{ij} is the strain generated in a particular orientation of the crystal on the application of electric field E_k along the k-axis.

Piezoelectric ceramics are anisotropic in nature, meaning that the electromechanical coupling exhibits a maximum value along a specific crystallographic direction. The properties are commonly described using two subscripts which represent the direction of the electrical and mechanical parameters. Figure 7(c) shows the direction indices of the coefficients, as exemplified in an orthogonal reference system.[9,15–17] The principal properties along the X, Y and Z axes are denoted by 1, 2 and 3 indices, respectively. The shear constants are also represented by 4, 5 and 6 respectively. For example, the most commonly used indicator for piezoelectric materials is the piezoelectric charge coefficient d_{33}, implying that electrodes are placed perpendicular to axis 3 and that the applied electric field or generated voltage is along direction 3, corresponding to the first and second index of subscript.[17]

As discussed earlier, the non-centrosymmetric crystal symmetries play a vital role in piezoelectricity. According to the definition of the piezoelectric effect, all components of the piezoelectric tensor should vanish in crystals possessing a centre of symmetry. Among the 20 piezoelectric crystal classes, there are ten *pyroelectric* point groups that possess a unique polar axis. Pyroelectric crystals contain a built-in polarization, which manifests itself in temperature-induced changes of the total dipole moment within the unit cell when there is no external stimuli.[15] It is basically an effect that arises from the temperature dependence of the spontaneous polarisation of polar dielectrics. If such *spontaneous polarization* can be reversed by a sufficiently high electric field, then a different subgroup of polar dielectrics emerges in this case, which is known as *ferroelectrics*, as will be discussed below in more detail.

1.3.4 Ferroelectricity

Ferroelectrics are polar materials having at least two equilibrium orientations of the spontaneous polarization vector in the absence of an electric field, and in which the spontaneous polarization vector may be switched between those orientations by an electric field. The polarization comes from the separation of positive and negative charges in the crystals which is a result of crystal distortions from a crystallographic phase transition.[9,10,15,18]

It is apparent that ferroelectricity is prohibited if there is a centre of symmetry. If the structure is non-centrosymmetric, the remaining crystal classes have one or more polar axes. Those that have a unique polar axis are ferroelectric and have a spontaneous electrical polarisation, as illustrated in Figure 8. Nonetheless, the others would exhibit the piezoelectric effect, wherein an electrical polarisation is induced by application of an elastic stress (tensile or compressive), which induces electrical polarisation of opposite signs.

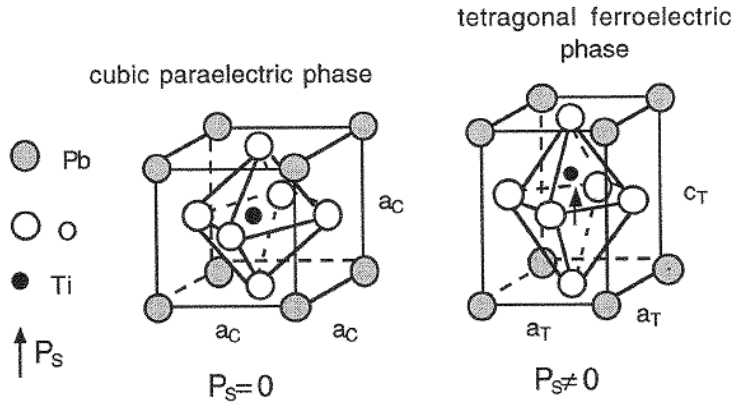

Figure 8 Illustration of paraelectric and ferroelectric phases in the perovskite $PbTiO_3$.[15]

Ferroelectrics exhibit various types of characteristic behaviour, which will be discussed in the following sub-sections.

1.3.4.1 Phase transitions

Most ferroelectric materials undergo a structural phase transition from a high-temperature paraelectric phase into a low-temperature ferroelectric phase, as illustrated in Figure 9.. The symmetry of the ferroelectric phase must be lower than that of the paraelectric phase. The temperature of the phase transition is called *the Curie point*, T_C. Above the Curie point the dielectric permittivity, ε drops significantly with temperature according to the Curie–Weiss law:[10,15]

$$\varepsilon = \varepsilon_0 + \frac{C}{T-T_0} \approx \frac{C}{T-T_0} \tag{11}$$

where C is the Curie constant, T_0 ($T_0 \leq T_C$) is the Curie–Weiss temperature. Temperature changes induce phase transitions such as in ferroelectric $BaTiO_3$; as the ceramic is cooled down from the temperature above T_C, the phase transition sequence is cubic → tetragonal → orthorhombic → rhombohedral, and they take place at around 120°C, 5°C, –90°C, respectively. However, only the transition temperature into the first ferroelectric phase is called the Curie point.

The transition into a ferroelectric phase usually induces strong anomalies in the dielectric, elastic, thermal and other properties of the material[15] and leads to dimensional changes in the associated unit cell. This is called the *spontaneous strain*, x_s. It represents the relative difference in the dimensions of the ferroelectric and paraelectric unit cells.[15] This strain is associated with the spontaneous polarization through electrostrictive coefficients. The variations in properties

with temperature that can occur in a ferroelectric material as it transforms from a paraelectric cubic into a ferroelectric tetragonal phase are depicted in Figure 9.

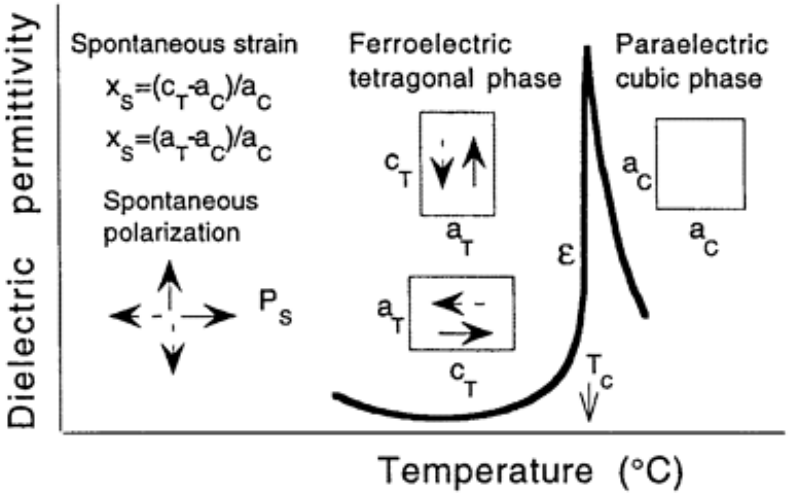

Figure 9 Illustration of the changes in a ferroelectric material which transforms from a paraelectric cubic into ferroelectric tetragonal phase with temperature. The arrows show possible directions of the spontaneous polarization (in two dimensions). The unit cell is represented by a square and rectangle for the cubic and the tetragonal phases, respectively.[15]

Generally, such polymorphic phase transformations (PPT) can occur both above and below room temperature; therefore, the aim is to modify the materials by the addition of dopants in order to shift these transformations towards room temperature. It is found that at the PPTs, the increased polarizability associated with the transition leads to improved dielectric and piezoelectric properties, although a low T_C can also destabilise the piezoelectric behaviour.[10,15]

Another factor that induces phase transitions in ferroelectrics is compositional variation. For this case, PZT is an excellent example due to its well-studied phase diagram. The binary $PbZrO_3$–$PbTiO_3$ phase diagram is shown in Figure 10. In this phase diagram, there is an almost vertical line between the ferroelectric rhombohedral and tetragonal phases, this boundary is called *the morphotropic phase boundary* (MPB) and plays a key role in the development of high performance piezoceramics. Since the electromechanical properties of a ferroelectric material exhibit outstanding behaviour thanks to the contribution of both rhombohedral and tetragonal phases. However, the renaissance of issue began with the finding of Noheda *et al.*,[19] who proposed a monoclinic phase (F_M, shaded region in Figure 10) which acts as a bridge between the rhombohedral and tetragonal phases in the PZT system. Subsequently, a large number of studies have been conducted in different ferroelectric ceramic systems in order to identify similar phenomena.

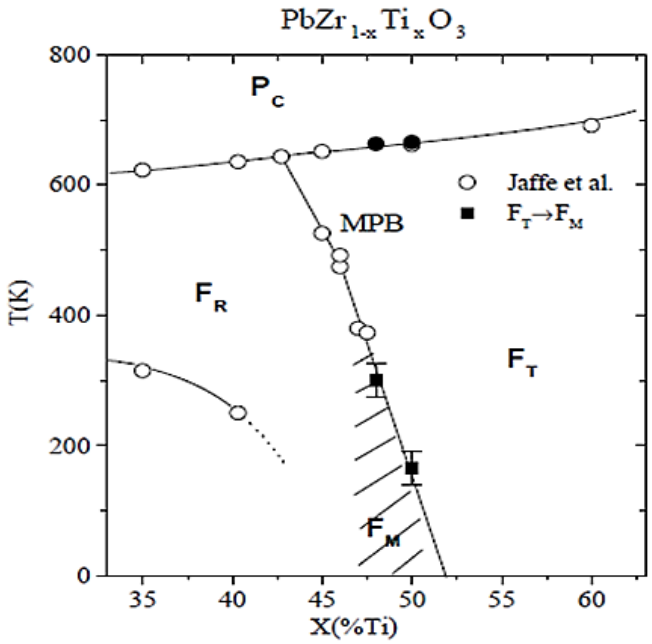

Figure 10 Phase diagram of PZT ceramics modified by Noheda *et al.*,[19] P_C: Paraelectric cubic phase, F_T: Ferroelectric tetragonal phase, F_R: Ferroelectric rhombohedral phase F_M: Ferroelectric monoclinic phase.

1.3.4.2 Domains and Domain Walls

Ferroelectric domains are known as sub regions in a crystalline grain. Each domain has one vector showing the direction of polarisation. These domains form during cooling, triggered by the phase transitions, due to the fact that the crystal always tends to minimize the electrostatic and elastic energies in the system. When a ferroelectric ceramic is not subjected to an electric field and under stress-free conditions, all the domain states have the same energy; however when it is under the electric field, the free energy of the system is lowered by aligning the polarization along the applied field. Thus, large applied electric fields can permanently reorient the polarization between the allowed domain states, which are restricted by crystallography. Domain structures are also strongly dependent on the symmetry of the ferroelectric phase. As changes occur in symmetry, different domain configurations are observed as shown in Figure 11.[9,10,15]

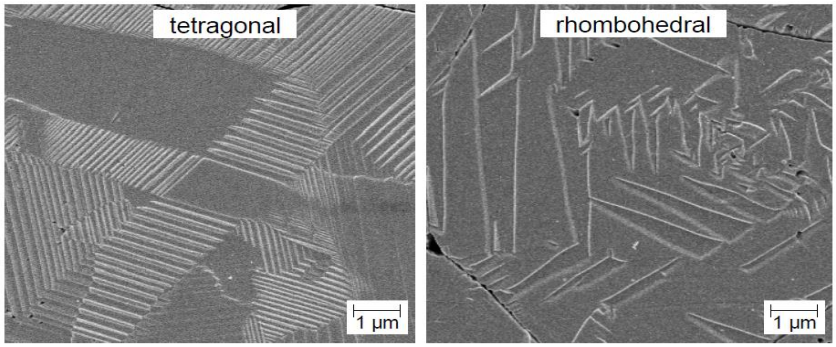

Figure 11 Comparison of soft (rhombohedral) and hard (tetragonal) PZT ceramics based on domain wall density.[20]

The region between the two domains is termed a *domain wall*. A wall between two oppositely oriented polarizations is a 180° wall, while those that separate regions with mutually perpendicular polarization are 90° walls, as depicted in Figure 12.

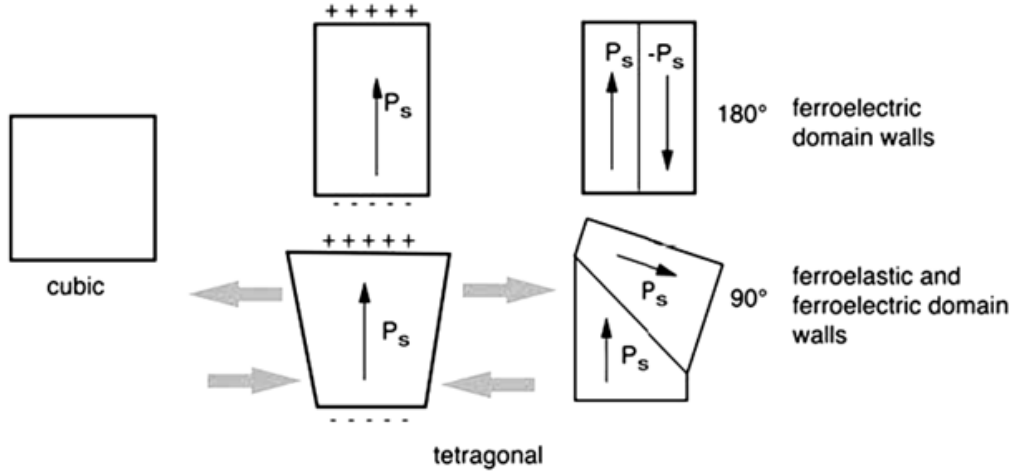

Figure 12 Illustration of the formation of 180° and 90° ferroelectric domain walls in a tetragonal ferroelectric material.[21]

In a single crystal, this multi domain state can usually be transformed into a single domain by applying a field parallel to one of the polar directions. The domains with their spontaneous polarisation, P_s along the field direction grow at the expense of those directed oppositely until only a single domain remains. The presence of mechanical stress in a crystal results in the development of 90° domains configured in order to minimize the strain. For example, when polycrystalline $BaTiO_3$ is cooled through T_C individual crystallites are subjected to large mechanical stresses leading to the development of 90° domains (Figure 12). The types of domain walls that can occur in a ferroelectric crystal depend on the symmetry of both the non-ferroelectric and ferroelectric phases of the crystal (Figure 11). In the rhombohedral phase of lead zirconate titanate, PZT, the direction of the polarization develops along the (111) direction of the paraelectric cubic unit cell. This gives eight possible directions of the spontaneous polarization with 180°, 71° and 109° domain walls.[9,10,15]

The configurations can be modified by the application of either an electric field (ferroelectric) or a mechanical stress (ferroelastic). A polycrystalline ceramic that has not been subjected to a static field acts like a non-polar material even though the crystals comprising it are polar. This brings about another one of the most valuable features of ferroelectric behaviour is that ferroelectric ceramics can be transformed into polar materials by applying a static field. This process is called *poling*, as shown in Figure 13. This process can also be reversed by the application of appropriate electric fields or mechanical stresses, termed as *depoling*.[9,10,15]

The poling process gives a new preferred polarisation direction which is along the applied electric field to the grains so as to produce net piezoelectric coefficients, as shown in Figure 13. Consequently, the reoriented grains show greater piezoelectricity, although they contain a number of domain walls mentioned above. The movement of these walls leading to ferroelectric domain switching can provide vital information about the intrinsic and extrinsic properties of ferroelectric materials.[9,10,15]

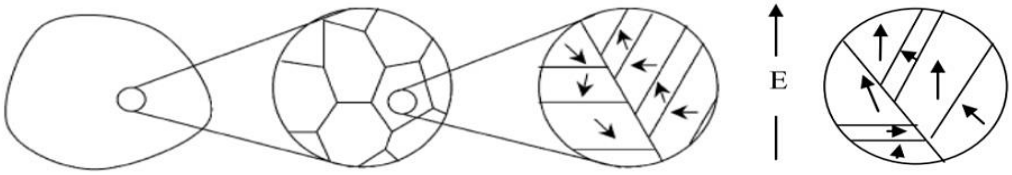

Figure 13 The illustration of the poling process in a polycrystalline ferroelectric ceramic.[15]

With the rapid advances in microscopy techniques, ferroic domain observations in materials has become viable using several methods.[9,22] including optical microscopy, scanning electron microscopy (SEM) with electron backscatter diffraction (EBSD), Transmission electron microscopy (TEM), X-ray diffraction, and various scanning probe microscopy (SPM) techniques, for example piezoresponse force microscopy (PFM), confocal Raman microscopy (CRM), and electric force microscopy (EFM). Although there are a number of different techniques to observe domain structures, the usefulness of each technique differs from one material to another, with the shape, size, transparency of the crystal, and the expected outcome of the observations. These methods can be also combined for the maximum efficiency. The most commonly used methods for domain visualization in ferroelectric ceramics with high spatial resolution are SEM after selective chemical etching, TEM, PFM, and CRM.

1.3.4.3 Hysteresis Loops

A distinctive feature of ferroelectricity is the reorientation of the polarization by an electric field. Therefore, the observation of some evidence of switching is fundamental to determine ferroelectricity and this evidence can be given by the ferroelectric hysteresis loop, as illustrated in Figure 14.

In theory, all ferroelectric materials exhibits a unique hysteresis loop as a fingerprint. Ferroelectric behaviour of a material can be directly identified *via* the hysteresis loops. The characteristic parameters are labelled as such saturated polarization (P_{Sa}) in polycrystalline materials or spontaneous polarization (P_S) in single crystals, remnant polarization (P_r), and coercive field (E_C) and those values can be straightforwardly determined.[15,21,23]

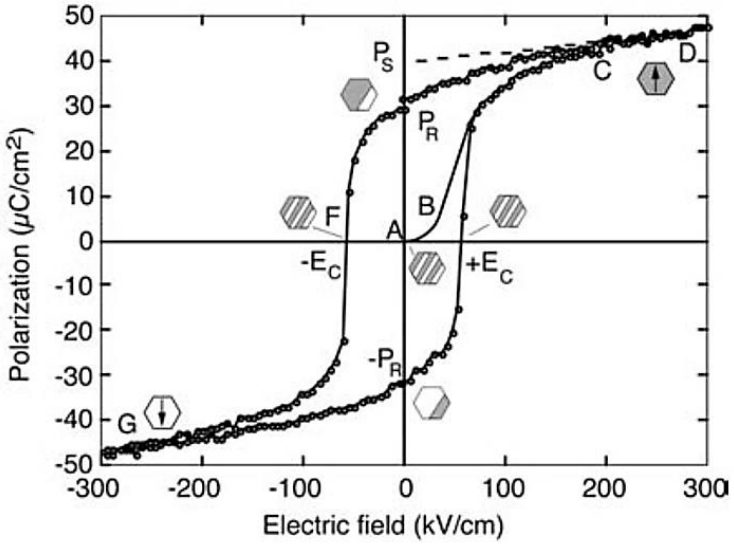

Figure 14 A typical hysteresis loop measured in ferroelectric materials.[21]

The grains in polycrystalline ceramics are always split into multi domains due to the energy minimization, as mentioned in the previous section. Furthermore, those domains are randomly oriented and result in zero net polarization within the ceramic. As the external field exceeds E_C, the polycrystalline ferroelectric ceramic may gain a polar state. As illustrated in Figure 14, a macroscopic polarization is gradually induced by increasing the electric field strength. A significant change in the polarization in the vicinity of E_C is mainly due to the polarization reversal, namely domain switching. Conversely, at the high electric field the polarization reaches a saturation point and the ceramic behaves as a linear dielectric. When the electric field is gradually removed, some domains switch back to their original position, yet the net polarization is not zero even when the electric field is zero. This polarisation is called the remnant polarization, P_r. A zero polarization can be obtained by the application of electric field of sufficient magnitude in the opposite direction. Such an electric field is known as the coercive field. A similar rearrangement of the polarization occurs in the negative electric field part.[15,21,23]

In addition to the P-E loops, spontaneous strain can also be induced by an external electric field and if this strain is monitored like polarisation, a butterfly shaped curve can be obtained, referred as the strain-electric field loops (S-E).

Regarding the classification of the hysteresis loops, the P–E loops and S-E curves can be categorized into four groups,[23] as depicted in Figure 15. Predominant mechanisms associated with these loops are summarized below:

Classical Loop: Ferroelectrics yield typical classic hysteresis loops and bipolar S–E curves show symmetric butterfly curves. Such non-linear response under electric field in P-E and S–E curves is mainly attributed to the ferroelectric domain switching.

Double Hysteresis Loop: This shape is well-known for antiferroelectric materials. Its mechanism is essentially based on the existence of two opposite electric dipoles adjacent to each other in a crystalline lattice. Due to such an arrangement, the net polarization of antiferroelectrics is zero in their unpoled state. Upon applying a high enough electric field, at which macroscopic polarization can be induced, an antiferroelectric-to-ferroelectric phase transition occurs. The induced polarizations switch back to zero through another ferroelectric-to-antiferroelectric phase transition after the removal of the external electric field. These features of antiferroelectrics results in such unique hysteresis loops.

Asymmetric Hysteresis Loops: This type of loop is usually observed in poled hard ferroelectrics. It can be seen that both the negative E_C^- and positive E_C^+ shift to right or left with respect to the horizontal axis to a certain degree. Normally this shift is attributed to the existence of an internal bias field, which is determined as $E_{int} = (E_C^+ - E_C^-)/2$. However, for hard ferroelectrics (lower valence doped systems), due to the pinning effect by defect dipoles or defect clusters on domain walls, the poling/depoling process is much harder than those of ferroelectrics without such pinning effects, *i.e.* therefore soft and hard terms are used. A macroscopic polarization is built up during the poling process, which is stabilized through the internal bias field during aging. On the contrary, even if a net polarization is induced by poling in a soft ferroelectric, the measured hysteresis loop will transform from asymmetric to symmetric shape with electric field strength exceeding E_C, due to the lack of pinning defect dipoles.

Slim Hysteresis Loops: It is generally observed in a material possessing a pseudocubic phase structure of a relaxor ferroelectric; microdomains or polar nanoregions (PNRs) instead of the macroscopic domains do exist in a wide temperature range in the vicinity of the phase transition. Due to their much smaller characteristic size, the response of micro domains to the external field is much faster than macroscopic domains and often result in a slim loop. This type of loop is a great interest in applications requiring precise actuation and high dielectric energy storage owing to its rapid response with a small field and reduced hysteresis (energy) loss, respectively.

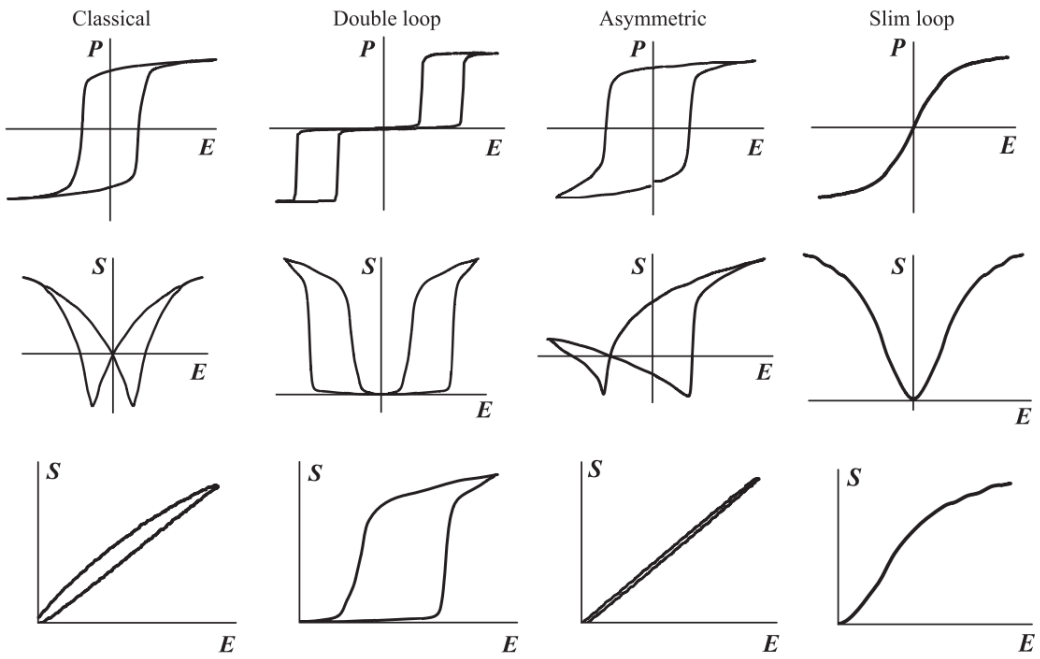

Figure 15 Classification of P–E hysteresis loops and their corresponding S–E curves in relation to ferroelectric (classical and asymmetric), antiferroelectric (double loop), and relaxor ferroelectric (slim loop) behaviour.[23]

As stated above, classical ferroelectric P-E loops must show saturation and have hysteresis in the P *vs.* E relationship for being suitable for piezo/pyroelectric applications. In reality, many factors affect the shape of hysteresis loops. These could be sample thickness, composition, heat treatment, charged defects, mechanical stresses and measurement conditions.[23] It is crucial to be aware of those potential factors for the accurate interpretation.[24] For example in $BiFeO_3$ ceramics, charged defects lead to cigar-shaped P-E loops, which may lead to misinterpretation concerning its ferroelectric behaviour under the electric field.[24]

1.3.4.4 Relaxor ferroelectrics

Relaxor ferroelectrics were first discovered by Smolenskii in the 1950s. Relaxor behaviour, that has been observed and studied most extensively in disordered ABO_3 perovskites, has been one of the hot recent topics in ferroelectricity. They are a distinct class of ferroelectric materials that can maintain multiple ionic species on the same crystallographic site. In order to understand relaxor behaviour, the main differences between normal ferroelectrics and relaxor ferroelectrics are illustrated in Figure 16.[15,25,26]

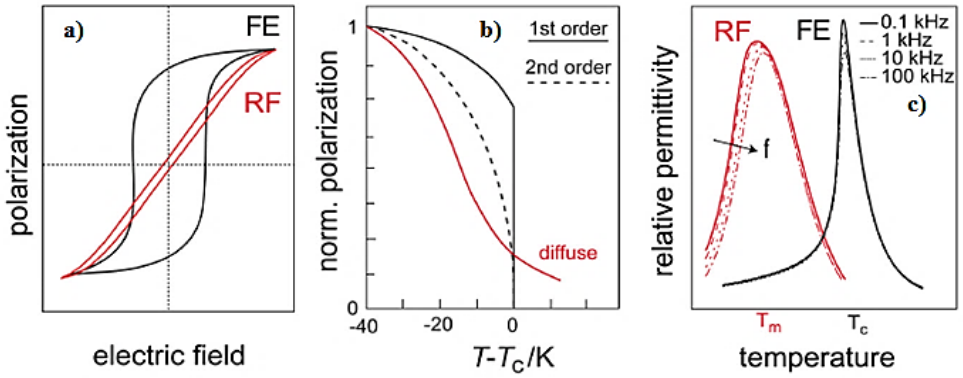

Figure 16 Comparison of normal ferroelectrics (FE) and relaxor ferroelectrics (RF) in terms of **(a)** P-E loops, **(b)** temperature-dependent polarization and **(c)** relative permittivity.[25]

A universal signature of the relaxor behaviour is a broad frequency-dependent peak in the real part of the temperature-dependent dielectric susceptibility, as shown in Figure 16(c). The peak, which shifts to higher temperatures with increasing frequency, defines a dynamic freezing or glass-like transition temperature, T_m. The strong frequency dispersion in the real part of the dielectric constant, ε' on the low temperature side of T_m is associated with decelerating of dipolar fluctuations within the polar nano domains. At a sufficient low temperature all dipolar motion freezes, and the dispersion disappears. In addition to thatrelaxor behaviour is also manifested by a frequency-dependent peak in the imaginary part of the dielectric constant, ε'' or in dielectric loss, $\tan\delta$.[25]

Another distinctive feature of relaxor ferroelectrics is that they exhibit a slim hysteresis loop, as illustrated in Figure 16(a). It is explained on the basis that the nanodomains of the relaxor can be oriented with a high field leading to large polarization; however, on removal of the field most of these domains gain their random orientations resulting in a small remnant polarization, P_r. The low P_r is evidence for the presence of some degree of frozen polar nanodomains.

On the other hand, a number of models have been proposed to describe relaxor behaviour. One is the compositional fluctuation model which is based on the compositional variations of the disordered B-site species (B′ and B′′ ions) in a perovskite and those ions lead to fluctuations in the local ferroelectric Curie temperature, thus resulting in a diffuse rather than sharp loss of spontaneous polarization (Figure 16(b)), and thus T_m can be represented as a mean Curie temperature. It should be noted that, there is no structural phase transition across T_m in relaxor ferroelectrics, while there is a macroscopic structural change at T_C in normal ferroelectrics.

Another model, named as the polar region size effect, has been proposed by Cross.[27] This suggests that broad transition is due to the nucleation of polar nanoregions (PNRs) when the material cools through the Burns Temperature, T_B. These polar nanoregions are believed to form due to multiple species on the same site which frustrates long range ferroelectric order. These nanodomains can exist with relatively smaller sizes compared to the macro-sized ferroelectric domains

and they are associated with a characteristic relaxation frequency. Their occurrence is now considered to be crucial to the understanding of the properties of relaxor ferroelectrics.

1.4 Lead-free piezoceramics

Lead (Pb) has been excluded from many commercial applications and materials such as from solder, glass and pottery glaze due to concerns regarding its toxicity[6,28,29]. In relation to this, the European Union has proposed legislation on the restriction of the use of lead in piezoelectric devices unless exempted under specific conditions.[6] However, lead zirconate titanate (PZT) ceramics are high-performance piezoelectric materials, which are widely used in sensors, actuators and other electronic devices; they contain more than 60 $wt\%$ lead.[7,28] Thus, there has been a tremendous effort to develop lead-free piezoelectric compounds.[5,7,28,29] Despite the legislation[6] on use of PZT-based materials in electronic devices, PZT will be preferred until an alternate lead-free material is available with equivalent or better piezoelectric properties. Currently, lead-free piezoceramics are in the development stage and the technology for device fabrication using lead free piezoceramics has been in progress.[5] The related research outputs also show an increasing trend in each year (Figure 17(a)).

On the other hand, according to recent studies,[7,30] the use of lead-free devices in practical applications has been already considered with the increasing trend in the number of patents on this field (Figure 17(b)). In spite of the promising properties of the newly developed lead-free compounds, industry is still hesitant about implementation of these materials. This is partly due to the low motivation to replace the well-established PZT with lead-free materials. Nevertheless, changes may occur in the near future due to the increasing amount of available lead-free products, emergence of new players on the market, increased environmental and health awareness of consumers, and expected changes in governmental regulations.[5–7,30]

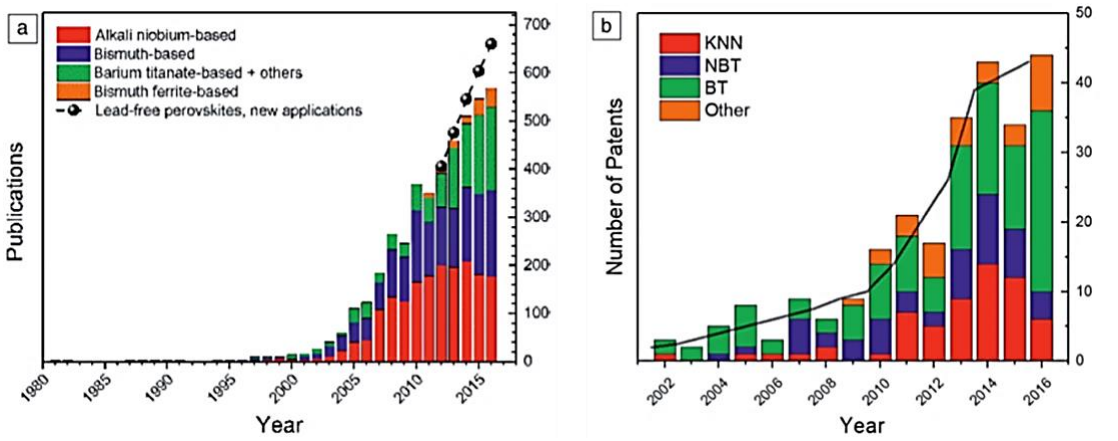

Figure 17 Evolution of lead-free piezoceramics research output in terms of **(a)** number of publications and **(b)** patents. The color bars in (a) represent the piezoelectric applications, while the black circles with the dashed line (lead-free perovskites, new applications) outline spin-off applications stemming from research into lead-free piezoceramics. Abbreviations used in (b) are KNN, potassium sodium niobate; NBT, sodium bismuth titanate; BT, barium titanate.[5]

In general, lead-free piezoceramics can be classified into two broad groups:[7]

i) One group is that of the perovskite-structured $(K_{0.5}Na_{0.5})NbO_3$, $(Bi_{0.5}Na_{0.5})TiO_3$-$BaTiO_3$, and (Ba,Ca)(Zr,Ti)O_3-based materials whose properties can compete with PZT for targeting the same applications. This group has currently been dominating the research on the development of lead-free compounds. (Figure 17(a)).

ii) There is a second group that PZT cannot compete with, which includes single crystals of SiO_2, AlN, and $LiNbO_3$, tungsten-bronze structured ceramics, Bi-based layered structures, and other high temperature piezoelectrics including $BiFeO_3$-based piezoceramics.

One of the advantages of lead-free piezoceramics is their lower densities which are typically two-thirds the density of PZT (7.8 g/cm^3). This would be a major advantage for lead-free ceramics in applications, where the use of PZT is limited due to its high density.[31,32] Although $BiFeO_3$-based lead-free ceramics have similar density to PZT, the major advantages of these ceramics include higher T_C and the presence of multiferroic ordering.

In previous progress reports on lead-free piezoceramics research, $BiFeO_3$-based materials have been rarely mentioned.[29,31,32] However recent advances by a number of researchers show the promise for use of $BiFeO_3$-based materials at high temperatures, not only replacing PZT, but also considerably improving on its high-temperature capabilities. Therefore, $BiFeO_3$-based ceramics have now taken an important place in future development plans, as shown in Figure 17(a).

Detailed reviews on the developed lead-free compounds and their applicability in devices, that currently use lead-based components, can be found in the associated references.[7,28,31,32]

1.5 $BiFeO_3$-based piezoceramics

Among the various types of multiferroic oxides, bismuth ferrite ($BiFeO_3$, BF) is a particularly important compound since it is the only single phase multiferroic material exhibiting simultaneously (anti)ferromagnetic and strong ferroelectric behaviour at room temperature. This unique property promises a wide range of applications in multifunctional devices. $BiFeO_3$ exhibits extremely versatile crystal structures and a broad palette of physical properties, as revealed by a vast number of studies since its first discovery in 1957.[33] Therefore, the research area in $BiFeO_3$ is significantly broad and translational. For example, Figure 18 shows the statistical data[33] of refereed publications on various properties of $BiFeO_3$ from 2000 to 2015. It is apparent that most attention has been on the ferroelectric, magnetic, dielectric, magnetoelectric, piezoelectric, and more recently photovoltaic properties of BF-based materials, though ferroelectric and magnetic studies have taken up about 65% of the total share, as expected due to promising implications for current and future electronic devices.

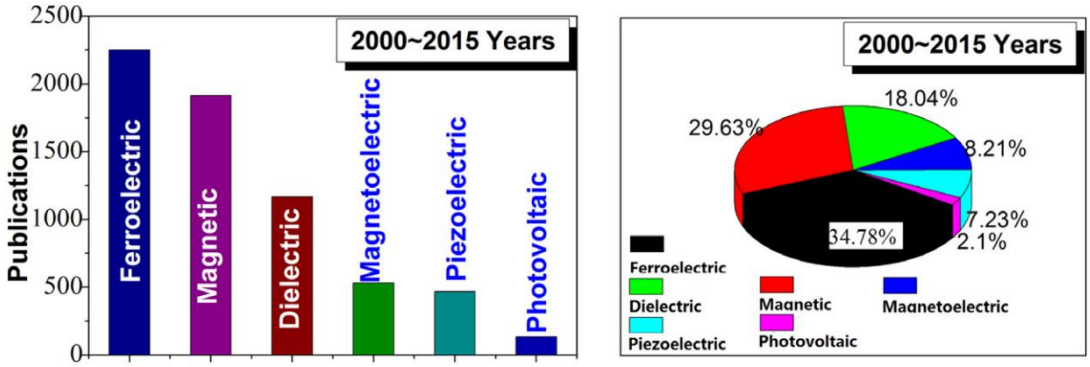

Figure 18 Statistical data of refereed publications on the various functional properties of $BiFeO_3$ over the period of 2000–2015.[33]

$BiFeO_3$, in its various forms such as ceramic bulk, thin films, and nanostructures have been extensively studied.[33–37] A number of intriguing findings related to this oxide have been reported. For example, the remanent polarisation, P_r can exceed 150 $\mu C/cm^2$ in BF-based thin films, as a result of the substrate or lattice strain, composition tuning, and influence of buffer layers.[33,34] In particular, the crystal structures and physical properties of these thin films are very sensitive to substrate strain due to the strong interplay between different degrees of freedom, for example in lattice strain, charge, spin and orbital.[33,34]

In the bulk form of BF-based ceramics, researchers have investigated methods of suppressing high leakage current and improving synthesis methods to obtain highly insulating and high quality single phase $BiFeO_3$. They have managed to provide a promising range of functional properties, for example high d_{33} value (>50 pC/N) and high T_C of >700°C,[33,38,39] which are superior to those of bismuth layer-structured ceramics for high temperature piezoceramic applications. More recently, a remarkably high d_{33} of 402 pC/N was reported for the pseudo-ternary $BiFeO_3$-$BaTiO_3$-$BiGaO_3$ ceramic system[40] by forming a rhombohedral-tetragonal (R-T) phase boundary similar to the morphotropic phase boundary (MPB) in lead

zirconium titanate (PZT). These exciting results have motivated the further research on BF-based piezoceramics in conjunction with magnetoelectricity.

The following sections are composed of three parts: *i)* the introduction of $BiFeO_3$ comprising its crystal symmetry, phase diagram and issues regarding to processing and reported functional properties, *ii)* a review on the $BiFeO_3$-$BaTiO_3$ solid solution system which is one of the most investigated BF-based ceramics, *iii)* a recent progress report on the research of BF-based ceramics.

1.5.1 $BiFeO_3$

1.5.1.1 Crystal Structure

$BiFeO_3$ crystallizes with a rhombohedrally distorted perovskite structure defined by a space group of *R*3*c*, as illustrated in Figure 19. The associated lattice parameters can be illustrated in various ways, depending on what type of lattice system is taken as a reference. For example, the lattice parameter for primitive rhombohedral is found to be approximately $a_{rh} \approx 5.64$ Å corresponding to a rhombohedral inter-axial angle of ≈59°,[41] while in pseudocubic unit cell at room temperature, it is represented as $a_{pc} \approx 3.965$ Å, yielding an angle, α_{pc} of 89.3–89.48°.[34] Nonetheless, it is more common to represent $BiFeO_3$ in a hexagonal setting of *R*3*c* space group with lattice parameters of approximately $a_h \approx 5.58$ Å and $c_h \approx 13.90$ Å.[34,41]

The highly distorted *R3c* symmetry of $BiFeO_3$ was experimentally confirmed using X-ray and neutron diffraction.[34,42] At room temperature, *R*3*c* symmetry can be described with the Bi^{3+} ions occupying cubo-octahedral positions within the perovskite with the Fe^{3+} ions in octahedral coordination. The cations displace off their centre of symmetry along the $[111]_c$ direction in the pseudocubic unit cell, corresponding to the $[001]_h$ direction in hexagonal configuration, with the FeO_6 octahedra rotated antiphase around the rhombohedral axis[34,41]. In detail, two kinds of distortions are observed within the unit cell of $BiFeO_3$ arising from the cubic perovskite structure, both of which can be observed in Figure 19. One is the polar displacements of associated anion and cation sub-lattices relative to each other, resulting in spontaneous polarization. Antiferrodistortive rotation of the FeO_6 octahedra is the second type of distortion along the [111] direction with alternating sense of rotation along the [111] axis. These polar displacements alone would lower the centrosymmetric of cubic *Pm*-3*m* to rhombohedral *R*3*m*, whereas the rotation of the FeO_6 octahedra alone would lead to the paraelectric phase with the space group *R*-3*c*. The combination of both types of distortions yields the actual well-known ferroelectric phase of $BiFeO_3$ with the space group of *R*3*c*.[42]

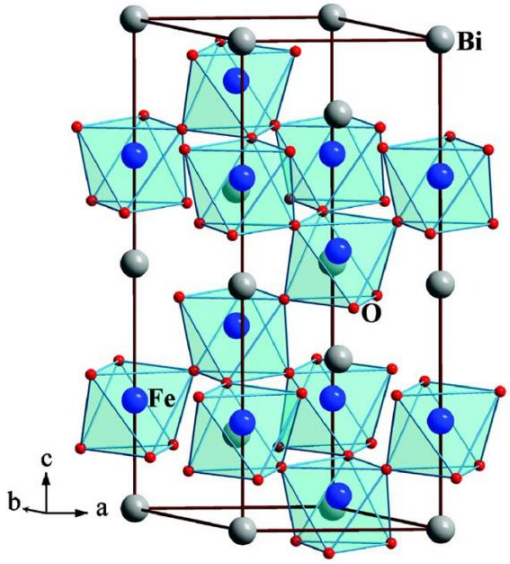

Figure 19 Crystal structure of $BiFeO_3$ in the ferroelectric *R*3*c* structures. Highly distorted FeO_6 octahedra are corner shared through oxygen. Bi atoms are not present exactly in the middle between the FeO_6 octahedra owing to the off-centre displacement of Bi due to the presence of 6*s* lone pair electrons.[42]

However, defining the exact centrosymmetric phase (non-polar) at high temperature prior to polar rhombohedral is extensively under debate,[34,41] the uncertainty being whether it belongs to cubic *Pm-3m* or orthorhombic *Pbnm*. Recent neutron diffraction studies, however, suggest the coexistence of intermediate centrosymmetric orthorhombic *Pbnm* between non-polar *Pm-3m* and polar *R3c* phases. These rhombohedral, orthorhombic, and cubic symmetries will be later referred to as alpha(α), beta(β), and gamma(γ) phases on the phase diagram, respectively, in the following section. More detail of structural discussions and findings on this specific issue including the influence of various dopants on phase transitions of $BiFeO_3$ can be found in the associated references.[34,41,43–45]

The rhombohedral structure of $BiFeO_3$ corresponds to a Glazer tilt system of $a^-a^-a^-$ which induces a superlattice peak at (½ ½ ½) reciprocal lattice positions.[46] The intensity of the superlattice peak can have the role of an order parameter to indicate the extent of band width and bond angle tilt.[35,41]

In relation to this, the rotation angle of the oxygen octahedra, ω is a crucial structural parameter in $BiFeO_3$. This angle would be 0° for a cubic perovskite with perfectly matched ionic sizes. A measure of how well the ions fit into a perovskite unit cell is the ratio $(r_{Bi} + r_O)/l$, where r is the ionic radius of the respective ion and l is the length of the octahedral edge. This ratio is analogous to the Goldschmidt tolerance factor, t described in the section 1.3.1.1. The tolerance factor of $BiFeO_3$ is found to be 0.88 when considering Bi^{3+} in eight-fold

coordination[f] and Fe^{3+} in high spin state with six-fold coordination.[34] When this ratio is smaller than one, the oxygen octahedra must buckle in order to fit into a cell that is too small. This is attributed to the fact that the smaller A-site cations cannot fill the empty space fully and instead the BO_6 octahedra cage is tilted, and thus shrinking the space.[35] The tilting angle for $BiFeO_3$, ω is reported to be in the range 11–14° around the polar [111] axis, with the directly related Fe–O–Fe angle, 154–156°.[34] Experimental estimation of the bond angle can be simply found *via* detection of a superlattice peak, indicating a consequence of cooperative tilt of antiferrodistortive octahedra. The Fe–O–Fe angle in $BiFeO_3$ is an important parameter since it is found to control both the magnetic exchange and orbital overlap between Fe and O, and as such it determines the magnetic ordering temperature and the conductivity.[34,35,41]

1.5.1.2 Phase Diagram and Processing issues

1.5.1.2.1 Phase Diagram

The Bi_2O_3–Fe_2O_3 phase diagram[43] is shown in Figure 20(a). Three equilibrium phases are noticed:

i) Orthorhombic $Bi_2Fe_4O_9$,

ii) Rhombohedral perovskite $BiFeO_3$ which decomposes peritectically to $Bi_2Fe_4O_9$ and a liquid phase at ≈935°C,

iii) Cubic $Bi_{25}FeO_{39}$ the latter exhibiting peritectic decomposition to Bi_2O_3 and a liquid phase at ≈790°C.[36,43]

At approximately 825°C there is a first-order transition to a high-temperature β phase that is accompanied by a sudden volume change.[34,43] The transition is also accompanied by a peak in the dielectric constant;[34] this has been considered as an indication of a ferroelectric–paraelectric transition. It should be noted that dielectric peaks can also occur in ferroelectric–ferroelectric transitions, known as polymorphic phase transition (PPT), the orthorhombic–rhombohedral transition in the archetypal perovskite ferroelectric $BaTiO_3$, being one example. Although there is disagreement about the exact symmetry of the β phase above 825°C, as previously discussed in the crystal structure section, most reports[34,41,43,44] agree that it is centrosymmetric, thus it is now widely accepted that the alpha(α)–beta(β) phase transition at $T_C \approx 825$°C is indeed indicating the ferroelectric–paraelectric transition for the single phase of $BiFeO_3$.[34,41]

[f] A rough estimation for Bi^{3+} corresponding to a twelve-fold coordination can be made *via* extrapolation based on the Shannon's tables of radii.[14]

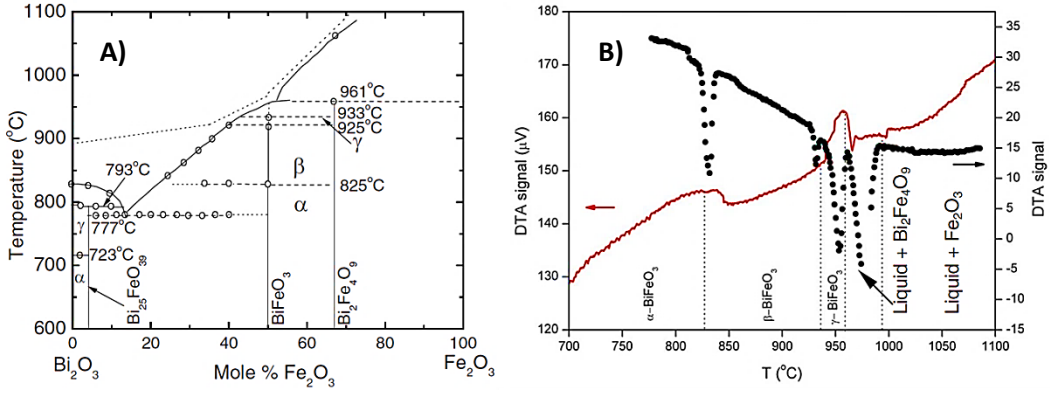

Figure 20 (a) Phase diagram of the Bi_2O_3-Fe_2O_3 system.[43] Open circles show the data points obtained by DTA. The dotted line above the liquidus represents the approximate temperature limit not to be surpassed for avoiding decomposition. The alpha, beta, and gama phases are rhombohedral, orthorhombic, and cubic, respectively. **(b)** DTA studies on crushed dendritic single crystal (dotted points) and thin film (solid red line) of $BiFeO_3$. For clarity signal has been inverted and offset.[43]

On the other hand, high-temperature instability of $BiFeO_3$ was experimentally reported by several authors.[34,36,43,47] Due to the difficulty in the synthesis of single phase perovskite by a heat treatment of a Bi_2O_3–Fe_2O_3 with 1:1 ratio, the researchers generally refer to the *metastability* of $BiFeO_3$.[36] It is then found that a phase pure $BiFeO_3$ can be indeed prepared by reacting a Bi_2O_3–Fe_2O_3 mixture at 850°C for a short time of 5–10 min. However, upon further thermal treatment at the same temperature for 2h, the obtained single phase of $BiFeO_3$ started to decompose into $Bi_{25}FeO_{39}$ and $Bi_2Fe_4O_9$, revealing more direct evidence of the thermodynamic instability of $BiFeO_3$.[36] This decomposition was later verified by different processing methods, for example, sol–gel synthesized $BiFeO_3$ at 600°C for 65 h.[36] A final confirmation of the instability of $BiFeO_3$ was performed on its single crystal and thin film forms using Differential Thermal Analysis (DTA) in conjunction with high-temperature reflected polarized light microscopy (Figure 20(b)). The combined data then revealed the phase transformation sequence and thus inherent nature of the thermodynamic instability.[43]

1.5.1.2.2 Processing issues

The conventional solid-state reaction route to fabricate $BiFeO_3$ ceramics involves mixing/milling of the appropriate metal oxides and then calcination at high temperature to allow interdiffusion of the cations. The chemical reaction occurs by solid-state diffusion of the ions, which is characterized by a slow kinetic rate. Powder particle sizes after milling are of particular importance. The reaction starts at the points of contact between the components Bi_2O_3 and Fe_2O_3 and continues successively by ionic interdiffusion through the final product of $BiFeO_3$. The initial reaction is rapid due to short diffusion paths, but further reaction proceeds more slowly. In many cases, a number of unwanted phases such as $Bi_2Fe_4O_9$, $Bi_{25}FeO_{40}$, Bi_2O_3 are inevitably formed, which is reported to be due to the fact that even small amounts of impurities introduced from starting powders,

milling media, crucibles *etc.* may lead to the system falling into a narrow 'three-phase field' *i.e* Bi_2O_3-Fe_2O_3-AO_x (AO_x is impurity oxides such as SiO_2 or Al_2O_3) where partial decompositions occur, leading to the formation of large amounts of secondary phases (Figure 21).[36,48–50] Therefore, extreme care is needed when processing $BiFeO_3$ ceramics.

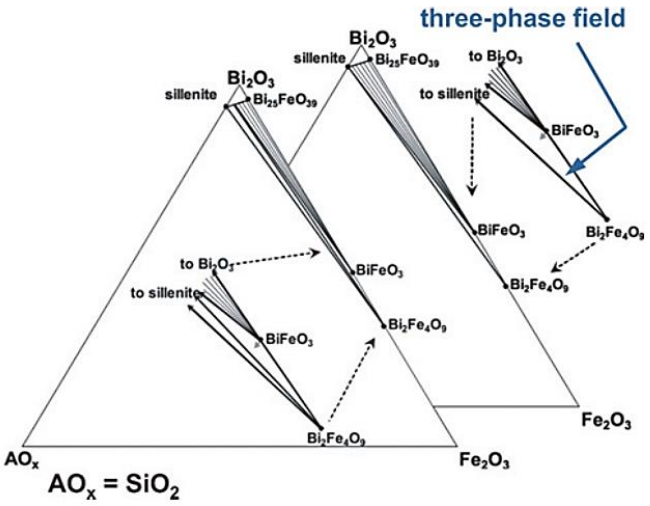

Figure 21 Phase relations in the ternary system of Bi_2O_3–Fe_2O_3–AO_x system. Based on the proposed phase diagram, a minor amount of SiO_2 added to the Bi_2O_3–Fe_2O_3 mixture should result in a large amount of secondary phases at equilibrium.[36,50]

As stated above, it is often difficult to synthesise a secondary phase-free $BiFeO_3$ ceramics *via* conventional solid-state reaction method.[36] Due to the possible influence of these secondary phases on the conductivity, its electrical properties cannot be properly assessed.[33] Several processing techniques, as an alternative to the solid-state reaction method, have been developed to produce high quality $BiFeO_3$ ceramic in bulk form. Leaching the impurity phases with dilute nitric acid was reported as one method applied to conventionally prepared ceramics; however the ceramics suffered from low density leading to poor ferroelectric properties.[51] On the other hand, liquid phase sintering, mechanical activation and spark-plasma sintering have been widely used to obtain single phase $BiFeO_3$ ceramics, as briefly described below.

Liquid Phase Sintering is suggested to achieve high dense, high resistive and phase pure $BiFeO_3$ ceramics.[50,52,53] The initial steps of these processes are similar to the conventional solid state reaction method, where the pressed powder samples are sintered at a given temperature for a short period of time. The method developed by Wang *et al.*[53] was used to prepare $BiFeO_3$ ceramics with single phase structure and high resistivity. The ceramics were sintered at 880°C using a heating of rate 100°C/s with holding time of 450 s. It is proposed that the Bi_2O_3-based liquid phase accelerates the reaction due to its low melting point (817°C), which facilitates sintering and prevents the formation of impurities. As a result, a single-phase $BiFeO_3$ ceramic could be attained. It is also reported that defect concentrations/sources (*e.g.* oxygen vacancies and reduction of Fe^{3+} to Fe^{2+})

could be greatly suppressed, resulting in a highly resistive ceramic. Spontaneous polarisation and relative density values were 8.9 μC/cm^2 and 92%, respectively, proving that this method is viable to produce single phase $BiFeO_3$ ceramics. Later, this method was widely adopted to prepare high-quality $BiFeO_3$-based ceramics with further modifications such as controlling the particle size in the starting materials and application of thermal quenching.[33]

Mechanical Activation is a method that uses high energy planetary ball milling on the starting powders for a long time (up to 100 h, for example) to start the required reactions for phase formation and aiming to attain single phase at relatively low temperatures. High energy milling leads to atomic-scale mixing of the reagents, thus forming a homogenous amorphous mixture. In a conventional solid state reaction, $BiFeO_3$ is formed at temperatures above 825°C, whereas with this method the sintering temperature was lowered to 700°C.[36,54]

Spark-plasma sintering (SPS) is another method to fabricate single phase $BiFeO_3$ ceramics. It was employed in order to bypass the regions where $BiFeO_3$ decomposes into $Bi_2Fe_4O_9$. In this technique, the ceramic is quickly densified at a relatively low temperature over a few minutes, and thus both the Bi volatilization and the reduction of Fe^{3+} are suppressed. $BiFeO_3$-based ceramics fabricated by SPS exhibit a high bulk density of up to 96% theoretical density.[33]

In addition, a recent work by Gil-Gonzalez *et al.*[55] showed that highly insulating nanostructured single-phase $BiFeO_3$ ceramics can be obtained by applying a small DC voltage to a mixture of Bi_2O_3 and Fe_2O_3 at a furnace temperature of 625°C in air for a few seconds, referring to this method as *reaction flash sintering*.

In general, it is evident that synthesis issues in regards to obtaining high-quality $BiFeO_3$-based ceramics have been overcome by the application of the methods described above. These methods are also highly effective to prevent volatilisation of Bi and the valence fluctuation of Fe^{4+}-Fe^{3+}-Fe^{2+}. There are also several other processing techniques that can be employed to improve the synthesis and electrical properties of $BiFeO_3$-based ceramics, for example by the reactive templated grain growth, Pechini method and wet chemical methods,[56] use of sintering aids and control of sintering atmosphere. A detailed review of the various processing techniques was provided by Silva *et al.*[54]

1.5.1.3 Functional Properties

$BiFeO_3$ ceramics offer a wide range of functional properties due to their multifunctional nature. This section aims to give a brief insight into their viable functional properties, with particularly regard to electromechanical and dielectric-ferroelectric-related properties.

As we start with the DC resistivity of $BiFeO_3$, it can exceed 10^{10} Ω cm and as temperature increases, the resistivity gradually drops due to its wide-bandgap semiconducting nature.[34] While measuring resistivity upon heating, some anomalies are noticed; such anomalies coincide with the antiferromagnetic phase

transition temperature, called the Neel Temperature, T_N, (≈370°C for $BiFeO_3$).[34,57] This confirms that magnetic ordering variations can interact with the associated conductivity in $BiFeO_3$ and such correlation suggests that $BiFeO_3$ has the potential of being magnetoresistive.[34] Dielectric anomalies at T_N in $BiFeO_3$ are also indirectly verified by temperature-dependent dielectric measurements, suggesting the possibility of magneto-electric coupling, and magnetodielectric coupling.[34,57,58]

Regarding to dielectric permittivity, ε_r at room temperature, it has reported as $\varepsilon_r \approx 30$ in the GHz range. This value is considerably smaller compared with those of typical ferroelectrics such as $BaTiO_3$, and $Pb(Zr,Ti)O_3$ (PZT)[34]. On the other hand, impedance measurements in parallel-plate capacitors at lower frequencies often yield relatively higher values in between 50 and 300 depending upon factors such as sample morphology, orientation, and selected frequency range.[34] These measured higher values can be attributed to the influence of domain-wall motion and space-charge contributions on the permittivity at the relatively lower frequencies (100 Hz to 1 MHz, for example). The small value of ε_r measured in the GHz range may seem small for a ferroelectric, however it is reasonable due to the very high T_C (≈825C°) of $BiFeO_3$, indicating that at room temperature the ferroelectric polarization is already saturated, and therefore small electric fields during the measurement of dielectric permittivity would have minimal effect.[34]

It is found that there are fundamental differences between the macroscopic piezoelectric response of $BiFeO_3$ and other conventional types of piezoceramics,[38] as shown in Figure 22. It is surprising that the underlying mechanisms of domain-wall motion in the case of $BiFeO_3$ are elusive compared to those of conventional ferroelectrics, exemplified by Nb-doped soft PZT. The macroscopic piezoelectric response is presented in Figure 22 in terms of the longitudinal piezoelectric coefficient, d_{33} , and the tangent of the piezoelectric phase angle, $tan\delta$, as a function of frequency, f.

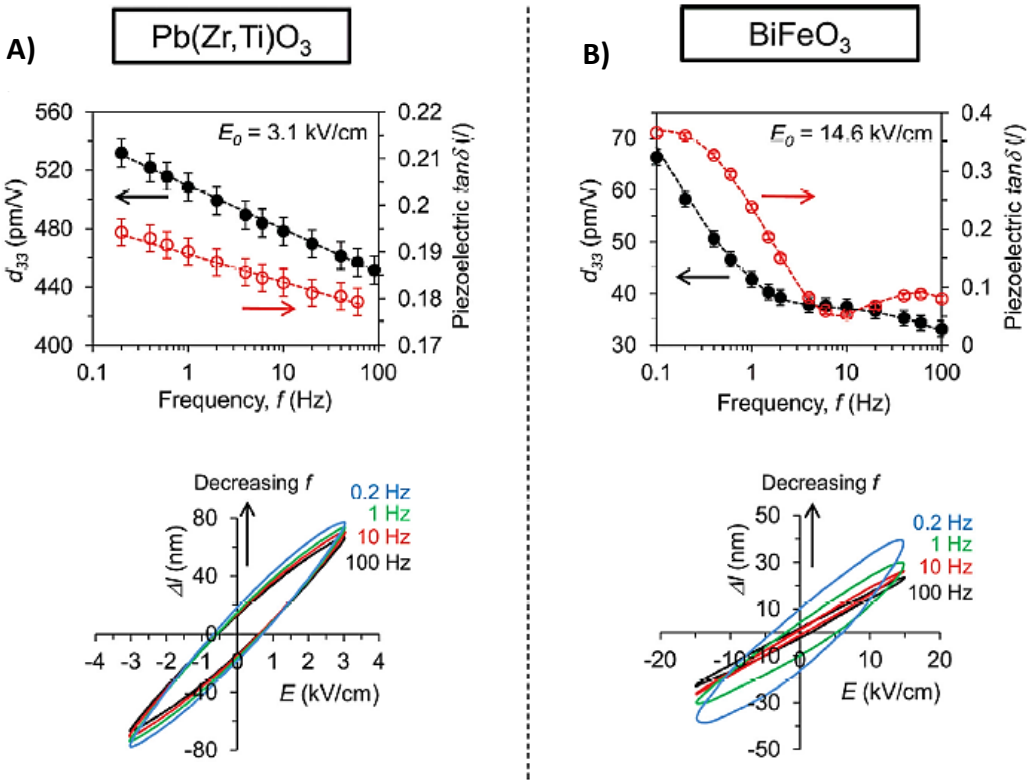

Figure 22 Comparison of converse piezoelectric response of PZT and $BiFeO_3$ ceramics. Piezoelectric d_{33} coefficient and tanδ as a function of frequency of the driving electric field for **a)** Nb-doped morphotropic PZT and **b)** $BiFeO_3$ ceramics. The electric field amplitudes, E_0 are noted on the graphs.[38]

In general, ferroelectric ceramics, also known as disordered systems, show linear-logarithmic behaviour, as illustrated in Figure 22(a). This feature is interpreted as the field-induced domain wall motions with presence of random pinning centres. On the contrary, $BiFeO_3$ exhibits a frequency dispersion that is characterized by an abrupt increase in d_{33} and *tanδ* at low frequencies (Figure 22(b)). Evidently, such behaviour cannot be understood by considering the well-accepted mechanisms for conventional type ferroelectrics. The origin of such frequency dispersion in $BiFeO_3$ is mainly associated with non-linear, irreversible domain-wall displacements at low driving frequencies.[38] This mechanism was later combined with the observation of conductive domain walls in the study of Rojac *et al.*[37,38]

The influence of the irreversible non-180° domain switching on the electric field-induced strain in $BiFeO_3$ was to be found significant, thus leading to strongly hysteretic strain curves with increasing electric field,[36,59] as shown in Figure 23(a). The extent of non-180° domain switching in a rhombohedral ceramic can be determined by measuring the relative intensities of the $\{111\}_{PC}$ diffraction peaks along particular angles relative to the applied electric field direction. The possible contribution of non-180° domain walls on the polarisation switching in a poled rhombohedral $BiFeO_3$ is verified by the *ex-situ* x-ray diffraction profile for $\{111\}_{PC}$

as a function of grain orientation relative to the electric field direction (Figure 23(b)).

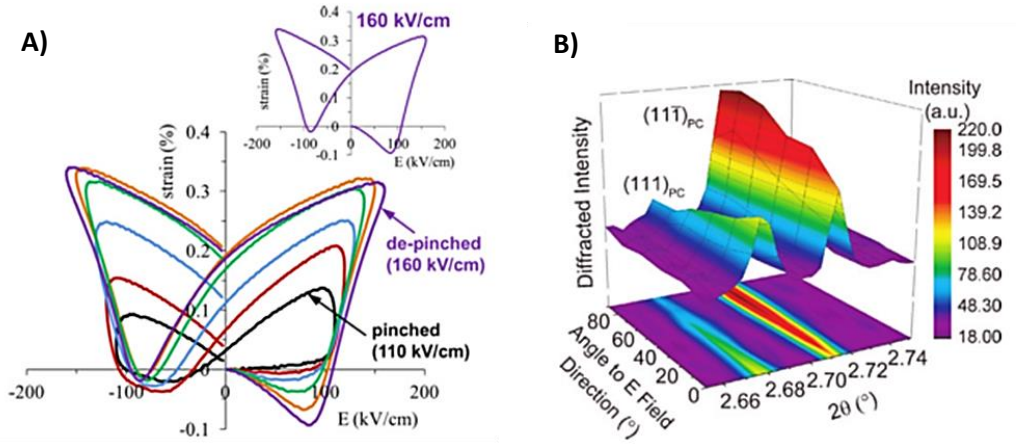

Figure 23 a) Strain–Electric field hysteresis loops of $BiFeO_3$ ceramics measured at 0.1 Hz with increasing electric field magnitudes. The inset shows the loop measured at 160 kV/cm. **b)** X-ray diffraction profile for $(111)_{pc}/(11\text{-}1)_{pc}$ doublet in a poled state of $BiFeO_3$.[36]

Reports on the ferroelectric switching behavior for $BiFeO_3$ ceramics have faced considerable challenges owing to the combination of high electrical conductivity and high coercive field of this material, which is often observed for Bi-based ferroelectrics. Due to the high leakage current and low breakdown field, sub-coercive (unsaturated) polarization-electric field (P–E) loops are reported for $BiFeO_3$, which are frequently confused with the actual switched (saturated) P–E loops. This issue was highlighted by J. F. Scott[24] in 2008 in a humorous way and it was a warning to the research community working on multiferroic $BiFeO_3$ to take care when measuring its ferroelectric property.

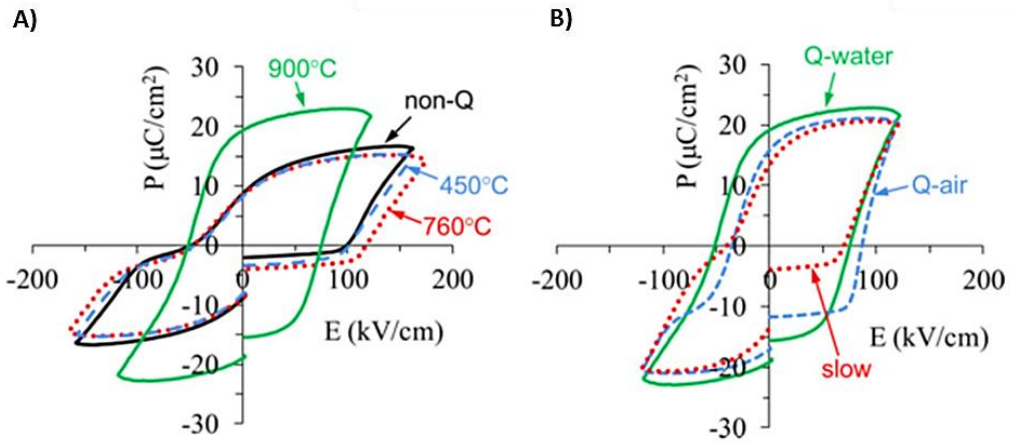

Figure 24 (a) Polarization–electric field (P–E) hysteresis loops of as-sintered $BiFeO_3$ ceramics (non-Q) and after water-quenching from temperatures of 450°C, 760°C, and 900°C with a dwelling time of 5 min at each temperature. **(b)** P–E loops of ceramics annealed at 900°C for 5 min, followed by quenching in water (Q-water) and air (Q-air), and by slow cooling within the furnace with 1°C/min cooling rate (slow).[36]

On the other hand, the actual non-linear and hysteretic P-E loop characteristic of polycrystalline $BiFeO_3$ was measured with the advances in doping/processing methods[36] and a strong asymmetric shape (pinched) was noticed in most cases, as illustrated in Figure 24. The origin of pinched or constricted ferroelectric hysteresis loops in $BiFeO_3$ is proposed to be due to the presence of domain-wall pinning centers created by charged defect complexes.[36] To support this hypothesis, electric field cycling and thermal quenching studies were employed on the as-sintered ceramics.[36,60] Field cycling on the sample was not as effective as the quenching treatment, revealing the presence of strong domain wall pinning in $BiFeO_3$.[36,60] Figure 24(a) shows open P–E loops after quenching from $T>T_C$ suggesting that the material has to be brought into the paraelectric phase, where the defects may be disordered due to the absence of the spontaneous polarization.[36,60] The strong influence of the defects on the switching behavior of $BiFeO_3$ is further confirmed by experiments conducted with different cooling rates (Figure 24(b)). Reducing the cooling rate, from quenching in air to slow cooling within a furnace, while keeping the same target temperature (900°C, above T_C), resulted in a progressive reappearance of the constriction and the associated reduction in remanent polarisation, P_r The results are thus consistent with the gradual reordering of the defects as the cooling rate is decreased.

Observations regarding the macroscopic ferroelectric character of $BiFeO_3$ lead to the conclusion that the domain-wall mobility in $BiFeO_3$ is strongly inhibited by charged defects, most probably acceptor-oxygen-vacancy defect pairs. The restrained domain switching can be substantially increased by preventing the defects from migrating into their stable configuration; this can be effectively achieved by thermal quenching from above T_C ≈825°C, which freezes the disordered defect state.[36,60]

It is also noteworthy that doping with certain rare-earth elements (Gd, Sm and Dy) in $BiFeO_3$ induces large structural variations from rhombohedral to orthorhombic symmetry. This structural sequence has a significant impact on the P-E loops, inducing a gradual transition from wide open loops to 'double' antiferroelectric-like hysteresis loops with increasing dopant content.[61–65] This double hysteresis loop is attributed to coexistence of antiferroelectric orthorhombic phase in rare-earth modified $BiFeO_3$ and should not be confused with the defect-induced loops, as discussed above for pristine $BiFeO_3$. Based on this phase transition sequence, an MPB region through *incommensurate phases* between ferroelectric rhombohedral and antiferroelectric orthorhombic was proposed by the investigations on rare-earth-doped $BiFeO_3$.[63–65]

1.5.2 $BiFeO_3$-$BaTiO_3$

As mentioned above, one of the major problems in BF-based materials is high leakage current which affects the measurement of dielectric/ferroelectric properties. The high conductivity in $BiFeO_3$ materials is mainly attributed to the oxidation reduction of multivalent Fe ions, Bi_2O_3 loss during sintering creating oxygen vacancies for charge compensation, and the combination of both mechanisms.[8,34,66] To suppress this apparent high conductivity as well as intrinsic thermodynamic instability of BF materials, it is found that the processing of solid solutions with the substitutions of ABO_3 perovskite compounds is an effective approach, thereby $BiFeO_3$–$BaTiO_3$ system has been extensively investigated.

$BaTiO_3$ (BT) is a well-known ferroelectric material with a low Curie temperature, Tc ≈120°C. Although its low T_C was initially questionable when aiming for high temperature applications, its promising features such as superior dielectric/ferroelectric properties, tetragonal symmetry at room temperature and lead-free nature make it a suitable candidate in order to enhance the poor dielectric and low ferro-piezoelectric activities of BF.

Structural variations as a function of temperature in BF–xBT were reported by Wang *et al.*,[67] performing high-resolution XRD measurements, as illustrated in Figure 25. For pure BF, a rhombohedral phase (R) is observed until 825°C, where the symmetry changes to an orthorhombic (O) symmetry and continues up to 850°C, and then paraelectric cubic (C). For x=0.1, a transition from rhombohedral to cubic phase is observed within the temperature range of 700–760°C. A similar feature was also noticed for BF–xBT with x=0.2, which shows a rhombohedral-to-cubic phase transition near 740°C. For the composition with x=0.3, a coexistence of cubic and rhombohedral with major phase of cubic was observed and this multiphase completely transforms into cubic near 680°C. The appearance of cubic phase with increasing BT content is attributed to increased random distribution of Bi^{3+} and Ba^{2+} ions on the A-site, and Fe^{3+} and Ti^{4+} ions on the B-site[67] as well as chemical pressure due to ionic radii mismatch between the associated site elements.[66]

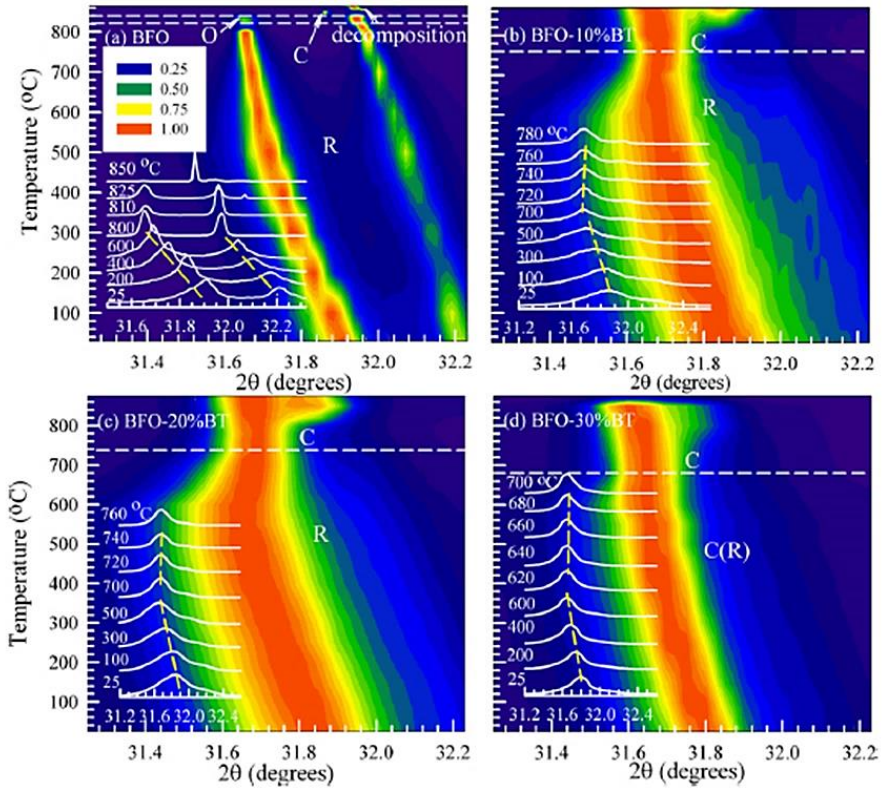

Figure 25 Synchrotron XRD spectra of (110) peak for **(a)** BF, **(b)** BF-10%BT, **(c)** BF-20%BT, and **(d)** BF-30%BT upon heating. The insets show the diffraction peak profile of rhombohedral(R)–cubic(C) phase transitions. The dashed line indicates the Curie temperature, T_C.[67]

To reveal the functional phase diagram of the BF–BT systems, the proposed structural data should be combined with thermal measurements and temperature-dependent dielectric data. Leontsev *et al.*[8] suggested a revised phase diagram for BF–BT solid solutions *via* thermal and dielectric measurements. It was reported that exceeding 25% BT content in BF–BT may lead to appearance of pseudocubic phase, as also illustrated in Figure 26(a). A recent study of Kim *et al.*[68] also confirmed this trend by a combination of high resolution structural data and temperature-dependent dielectric measurements (Figure 26(b)). However, it is noticed that extracting precise information about the phase transformation for compositions above 30%BT content in BF–BT is challenging, since increasing pseudocubic phase content affects the structural data and dielectric data upon heating/cooling, leading to broad peaks in both cases. Tetragonal symmetry is reported for this system in the region close to the BT side ($x < 0.075$).[66]

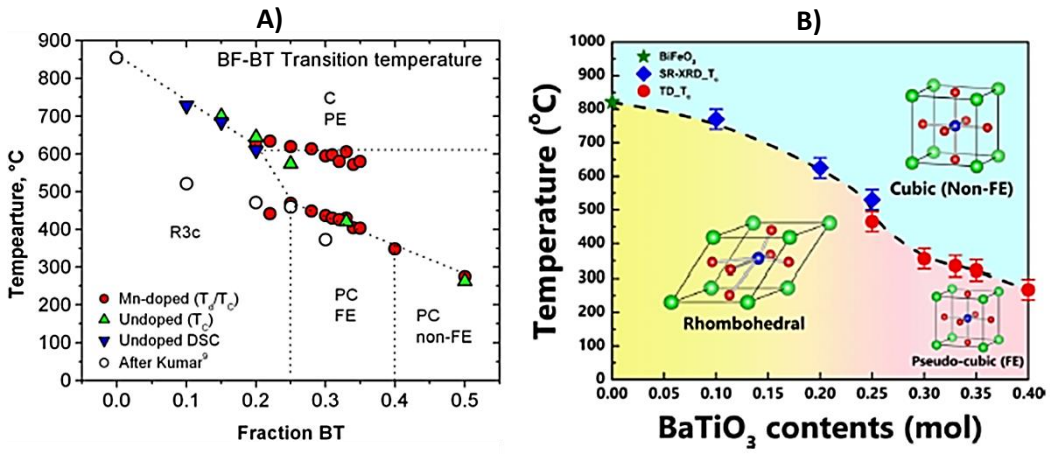

Figure 26 Reported phase diagrams for the BF–*x*BT system: **(a)** Dielectric and thermal measurements were combined to reveal the phase diagram by Leontsev *et al.*[8] Phases are denoted as C PE (cubic paraelectric), PC FE (pseudo-cubic ferroelectric). **(b)** Kim *et al.*[68] carried out synchrotron radiation X-ray diffraction (SR-XRD_T_C), and temperature-dependence of dielectric constant (T_D_T_C) data to construct the phase diagram.

Hence, observations from these phase diagrams suggest that a specific region/point/boundary that is composed of coexisting rhombohedral-tetragonal symmetries, similar to the MPB in PZT ceramics, does not occur the BF-BT solid solution system. However, the most attention for this solid solution system is focussed on the region of $0.67 \leq x \leq 0.75$ since this region reportedly exhibits MPB-like features due to the presence of rhombohedral and pseudocubic phases, resulting in high ferro-piezo performance as well as high T_C.

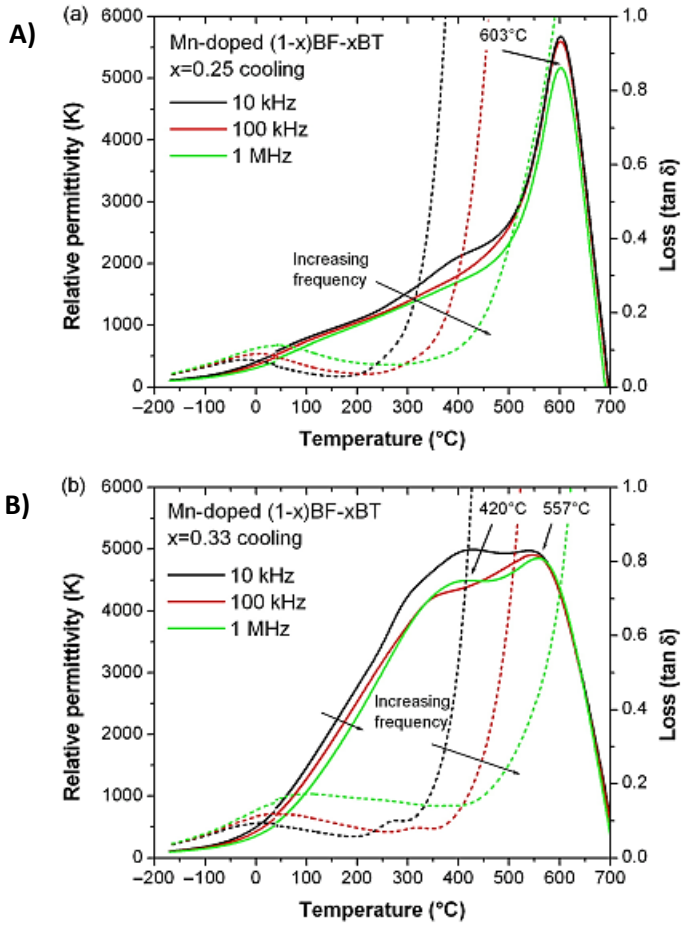

Figure 27 Temperature-dependence of the relative permittivity and dielectric loss for Mn-doped BF–0.25BT **(a)** and BF–0.33BT **(b)** ceramics, measured upon cooling by Leontsev *et al.*[8]

On the other hand, significant enhancements in dielectric properties occur when an increasing amount BT is incorporated into BF. For example, the low dielectric permittivity of pristine BF[34] is increased from 30 to 500 with the incorporation of 30%BT.[67] In addition, it is found that high T_C with moderate piezoelectric coefficient, d_{33} can be achieved *via* a minor MnO_2 addition into the composition BF–0.25BT (T_C=603° and d_{33}=116 pC/N), as shown in Figure 27(a). Nevertheless, for BF–0.33BT, dielectric data upon cooling reveals two dielectric anomalies as 420°C and 557° (Figure 27(b)), it is suggested that the one at lower temperature is associated with a depolarisation temperature while the second one is the Curie temperature.[8] However, the origin of such dielectric anomalies is extensively under debate,[8,66,67] while the predominant conduction mechanism and coexistence of phases in the high temperature regime in BF–BT ceramics warrant further investigations.

Regarding the ferroelectric properties of the BF–BT system, a typical saturated ferroelectric P-E hysteresis loop is rarely reported in the unmodified BF-BT system,[69] particularly in the BF-rich side of the solid solution. It is due to the high leakage current, as previously discussed. However, Leontsev *et al.*[8] reported that the addition of 0.1 *wt*% of MnO_2 into the BF-BT ceramics greatly suppressed the

high conductivity and yielded well-saturated P-E hysteresis loops. This work accelerated the ferroelectric/dielectric research on this system and further systematic studies[8,70,71] show that MnO_2 additions in the range 0.1 to 0.6 *wt*% are beneficial to suppress high conductivity.

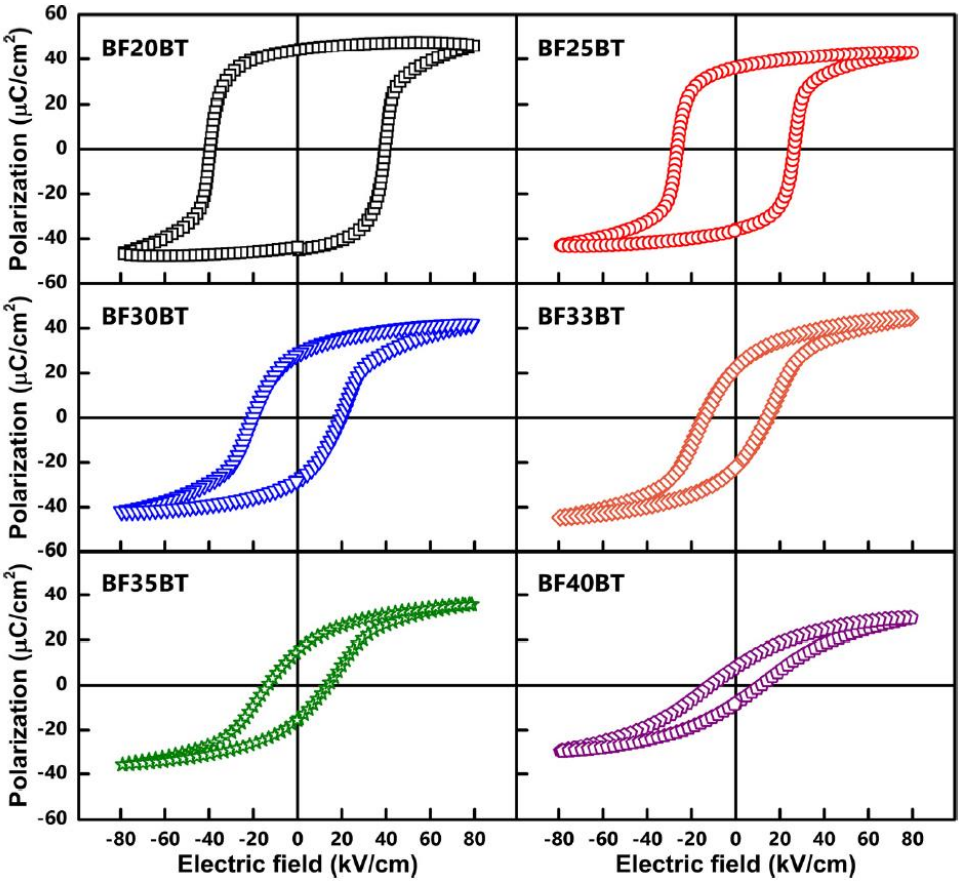

Figure 28 Polarisation-Electric field (P-E) hysteresis loops measured at room temperature with a frequency of 0.1 Hz for $BiFeO_3$-$BaTiO_3$ ceramics as a function of $BaTiO_3$ concentration by Kim *et. al.*[68]

Another beneficial method proposed for this system is the use of thermal quenching treatment. This method has been widely used in BF–BT ceramics in order to enhance functional properties. Figure 28 shows P-E hysteresis loops of quenched BF–BT ceramics with various BT contents. It is apparent that the shape of loops is highly dependent upon BT content for this system, indicating that the ferroelectric domain switching mechanism is impaired with increasing BT content, presumably due to reductions in the intrinsic spontaneous polarisation. This was also confirmed by the strain-electric field loops reported by Kim *et al.*[68] Figure 29 shows that the maximum strain value continuously increases with increasing BT content and attained the highest value for the BF30BT composition and followed a decreasing trend until the BF40BT composition. Thus, it is suggested that a crossover from strong ferroelectric to relaxor ferroelectric character can be achieved by the incorporation of BT into BF ceramics.

The role of the quenching treatment in BF–BT ceramics is often attributed to the influence of charged defects;[68,72,73] however, it is found that a thorough

evaluation microstructure and crystal structure, in combination with measurements of functional properties, is required in order to reveal the actual role of such treatment.[71,74]

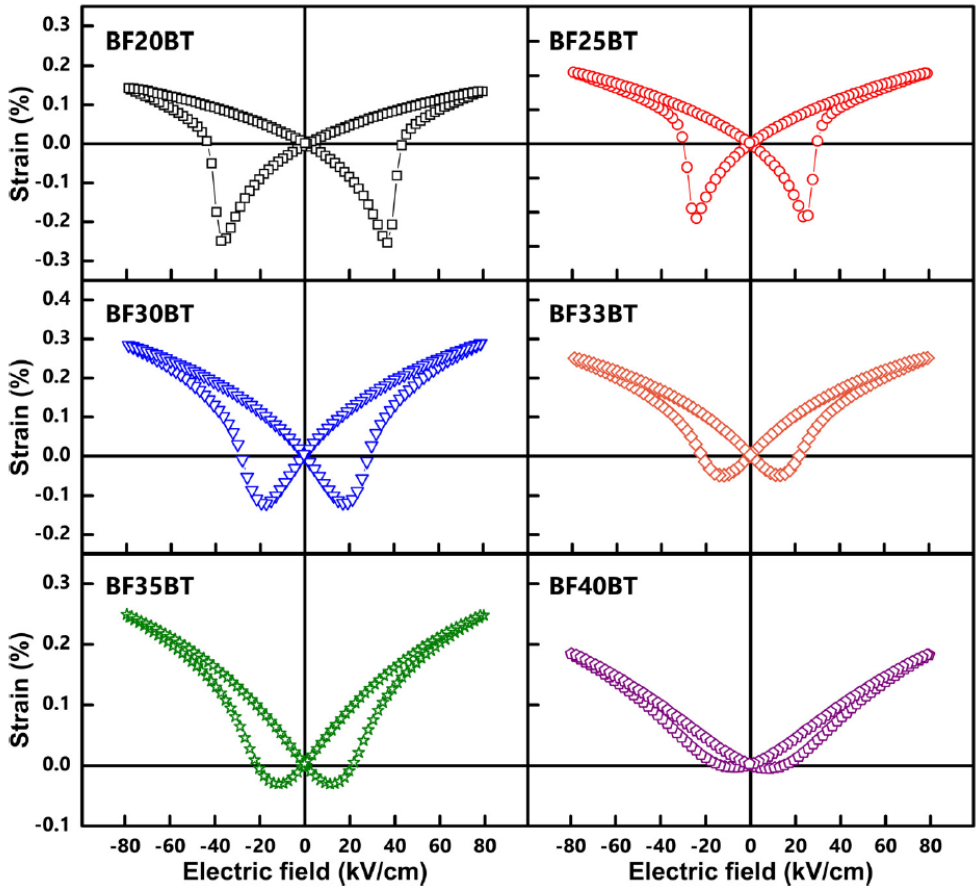

Figure 29 Strain-Electric field (S-E) curves of $BiFeO_3$-$BaTiO_3$ ceramics as a function of $BaTiO_3$ concentration.[68]

Figure 30 shows the piezoelectric coefficient, d_{33} ,as a function of $BaTiO_3$ concentration, as reported in the studies of Leontsev *et al.*[8] and Kim *et al.*[68] It is evident that d_{33} values decreases with increasing BT content in BF-BT compositions, which is attributed to increasing coexistence of pseudocubic phases in BT-rich BF-BT compositions. Since the polarisation is expected to be reduced due to the transformation from polar non-centrosymmetric (distorted rhombohedral) to non-polar centrosymmetric phase (pseudocubic). In contrast, the piezoelectric actuator constant, d^*_{33} for the compositions with high BT content shows relatively higher values since the pseudocubic phase is predominant in those compositions, meaning that highly reversible domain switching, which is crucial for d^*_{33}, can be readily obtained from polar nano regions embedded within the pseudocubic matrix. It should be also noted that the d_{33} and d^*_{33} values reported in the literature for BF-BT ceramics are dependent upon various factors such as doping type, poling field, annealing and quenching temperature, annealing atmosphere type *etc.*[8,40,68–71,73,75–77]

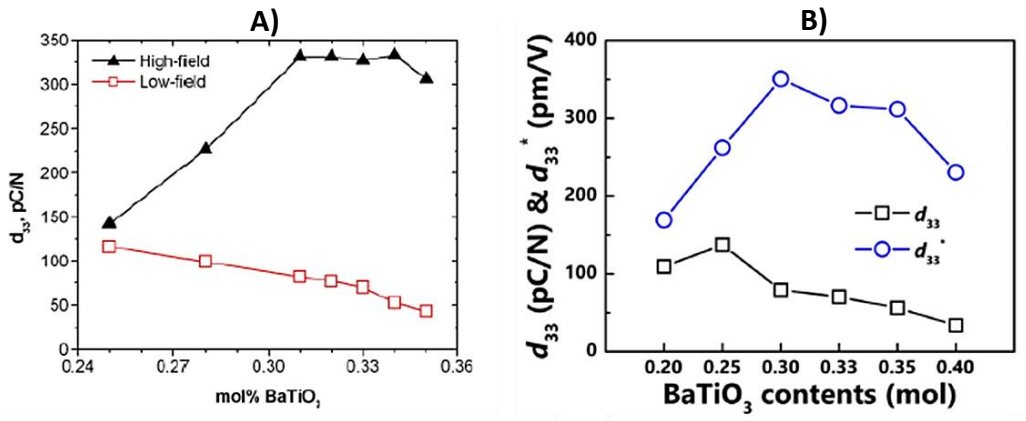

Figure 30 Compositional dependence piezoelectric d_{33} coefficients by **(a)** Leontsev *et al.*[8] for Mn-doped BF–*x*BT ceramics, and **(b)** Kim *et al.*[68] for quenched BF-*x*BT compositions, comparing d_{33} and d^*_{33} (effective piezoelectric actuator constant).

1.5.3 Recent advances

After the discovery of domain wall conduction in ferroelectric thin films by Seidel *et al.*,[78] an exciting finding in relation to that was reported for polycrystalline $BiFeO_3$ by Rojac *et al.*[37,38] It was shown that the local domain-wall conductivity in $BiFeO_3$ interferes with the dynamics of the domain walls within the grains, leading to an unexpectedly large effect on the macroscopic piezoelectric response. The results thus bridge the local conductivity and the macroscopic piezoelectricity *via* domain-wall dynamics. Hence it is suggested that the domain-wall conductivity must be taken account when interpreting and controlling macroscopic electromechanical properties.[38]

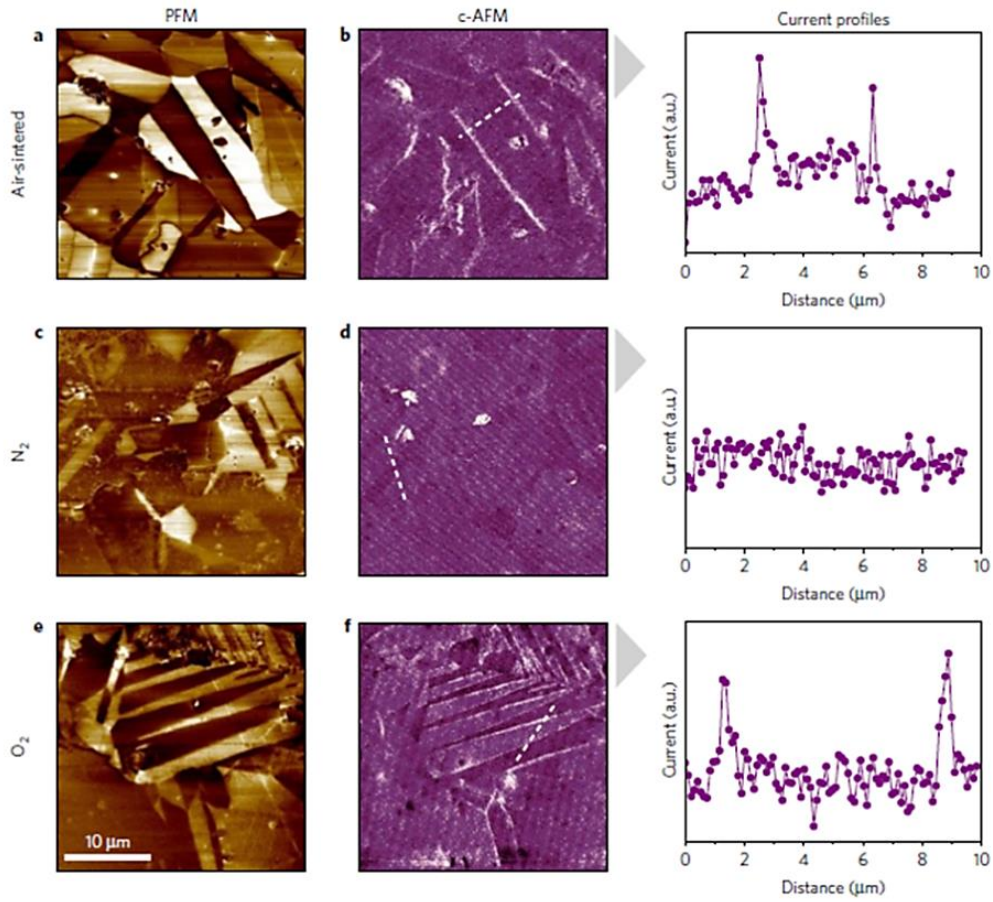

Figure 31 Control of local conductivity at domain walls in polycrystalline $BiFeO_3$ in air-sintered **(a-b),** followed by post-annealing in nitrogen **(c-d)**, and oxygen atmosphere **(e-f)**, represented by piezoresponse force microscopy (PFM) and conductive atomic force microscopy (c-AFM). The electric-current profiles across selected domain walls in each of the three samples as indicated by dashed lines on respective c-AFM images.[37]

Very recent work by the same group[37] also has given an insight into atomic-scale chemical and structural relations revealing evidence for the accumulation of charged defects at domain walls in $BiFeO_3$. The defects were identified as Fe^{4+} cations and bismuth vacancies, leading to *p-type* hopping conduction at domain walls induced by the presence of electron holes associated with Fe^{4+}. In agreement with the *p-type* behaviour of $BiFeO_3$ ceramics,[79,80] it was further shown that controlling the atmosphere during heat treatment prominently affected the local domain-wall conductivity (Figure 31), giving the opportunity for engineering local conductivity in ferroelectrics and associated devices.

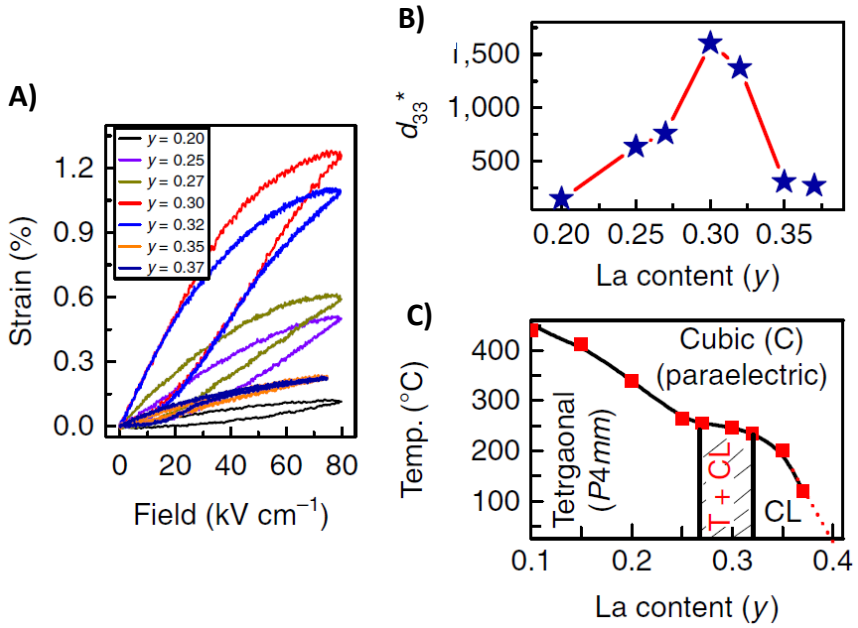

Figure 32 Structure–property correlations in $0.55Bi_{1-y}La_yFeO_3$–$0.45PbTiO_3$ as a function of La concentration: **(a)** Electric-field dependent unipolar strain, **(b)** d^*_{33} (the large-signal piezoelectric coefficient), **(c)** Compositional phase diagram by Narayan *et al.*[81]

A report by Narayan *et al.*[81] in 2018 proposed a material design strategy to achieve an extraordinary electrostrain value of 1.3% in a polycrystalline BF-based pseudo-ternary system (>50% $BiFeO_3$), $BiFeO_3$–$PbTiO_3$–$LaFeO_3$ synthesised by the solid-state reaction method (Figure 32(a)). It is found that this high electrostrain is associated with a combination of several factors: a large spontaneous lattice strain of the piezoelectric phase, domain miniaturization, a low-symmetry ferroelectric phase and a very large reversible switching of the non-180° domains. Based on the findings, it is argued that design criterion for the development of large-strain actuator materials (Figure 32 (b)) should start with the selection of a ferroelectric host (tetragonal) exhibiting a large spontaneous polarization/strain, and then finding an appropriate chemical substituent that introduces a heterogeneous domain structure and is capable of lowering the symmetry of the ferroelectric phase, which is referred to cubic-like (CL) structure in Figure 32(c). It is believed that this insight into the design of a new class of electroactive ceramics with high electrostrain may be a cost-effective approach to develop alternatives to single crystal actuators, together with a consideration of further reduction in lead (Pb) content.

A new type of BF-based lead-free perovskite ceramic, $Bi(Zn_{0.5}Ti_{0.5})O_3$-$x$$BiFeO_3$, has been synthesized *via* a high-pressure and high-temperature method by Pan *et al.*[82] in 2016. Intriguing properties including giant polarization, morphotropic phase boundary (MPB), and monoclinic phase are reported for this system (Figure 33). For example, large tetragonality (c/a =1.228) and spontaneous polarization of 110 μC/cm² has been obtained for x=0.4, which is much higher than that of most available lead-free ceramics and conventional $Pb(Zr,Ti)O_3$. An

MPB is also proposed to be constituted of tetragonal and monoclinic phases at x=0.5. Markedly, a single monoclinic phase has been also observed at x=0.6, which exhibits promising high temperature properties. It is concluded that chemical substitution of $BiFeO_3$ remarkably enhanced the tetragonality of the parent compound of $Bi(Zn_{0.5}Ti_{0.5})O_3$ and this system will stimulate further investigations on the enhancement of physical and functional properties *via* various chemical doping or substitution strategies.

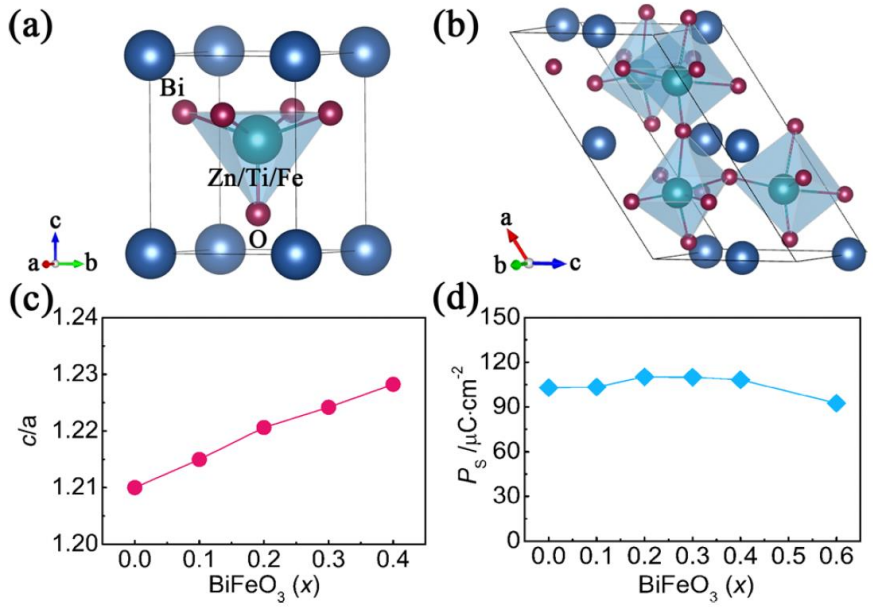

Figure 33 Crystal structures of $Bi(Zn_{0.5}Ti_{0.5})O_3$–$x$$BiFeO_3$ **(a)** tetragonal (x = 0.1−0.4) and **(b)** monoclinic (x = 0.6) phases. **(c)** c/a ratio. **(d)** Calculated spontaneous polarization as a function of $BiFeO_3$ content.[82]

The best piezoelectric performance in the bulk form of lead-free BF-based ceramics was reported by Lee *et al.*[40] in 2015, exhibiting d_{33} value of 402 pC/N with T_C of 454°C for a water-quenched 3 mol% $BiGaO_3$ (BG)-doped 0.67$BiFeO_3$-$BaTiO_3$ composition (BF33BT-3BG). The 3 mol%$Bi(Zn_{0.5}Ti_{0.5})O_3$ (BZT)-doped composition also yielded a high d_{33} value (324 pC/N) and high T_C (466°C), as compared with other known lead-free and lead-based compounds in Figure 34. It was reported that such high piezoelectric values are mainly attributed to the addition of *super tetragonal* compounds of BZT and BG into the selected composition and influence of water quenching treatment, with the combination of both factors creating an MPB for the BF-xBT system at x=0.33. Although this study shows the significance of doping strategies and quenching operation in lead-free BF-based ceramics, it remains only report showing such high piezoelectric performance. Most reports on d_{33} values for this system, however, approximately fall into the range of 100-200 pC/N.[8,68,69,73,75,76]

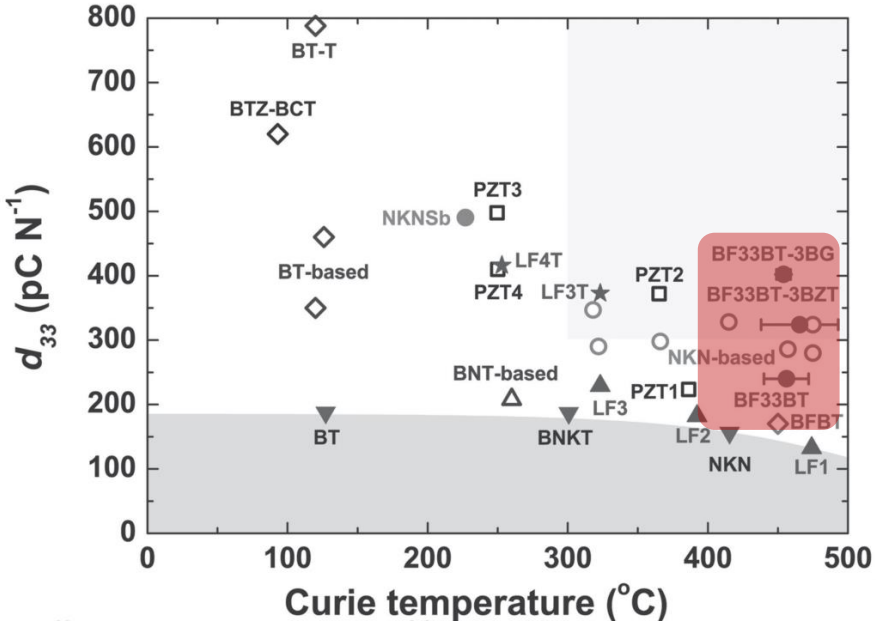

Figure 34 Room temperature piezoelectric constant, d_{33} *vs.* Curie temperature, T_C of various lead-free and lead-based piezoceramics. The filled circles (highlighted region) represent water-quenched 0.67BiFeO3-0.33BaTiO3 abbreviated as BF33BT and modified ones BF33BT-3BZT, and BF33BT-3BG ceramics. More detail for BT-, BNT-, KNN- and PZT-based compounds represented on the figure can be found in Ref.[40]

There have also been advances on the microstructural design approach in BF-based ceramics. Recent studies featured a unique core-shel type microstructure, as illustrated in Figure 35. Such heterogeneous microstructure was previously observed in $Bi(Mg_{0.5}Ti_{0.5})O_3$-doped $BiFeO_3$-$BaTiO_3$ by Yabuta *et al.*[83] in 2012. Nonetheless, comprehensive microstructure-property relations were investigated by the reports in 2018 conducted on the lead-free ceramics of Mn- and La-doped BF-BT,[71,74] $Bi(Zn_{2/3}Nb_{1/3})O_3$-modified BF-BT ceramics,[84] and lead-contained pseudo-ternary system of $0.24BiFeO_3$-$0.56K_{1/2}Bi_{1/2}TiO_3$-$0.20PbTiO_3$.[85] These studies shed light on the origin of degradation/enhancement in polarisation and in respect to strain hysteresis response, which is useful to design various functional properties accordingly. It is concluded that this type of composite-like microstructure in BF-based ceramics could be further exploited within the context of dielectric energy storage, electromechanical actuation and magnetoelectric coupling, for example.

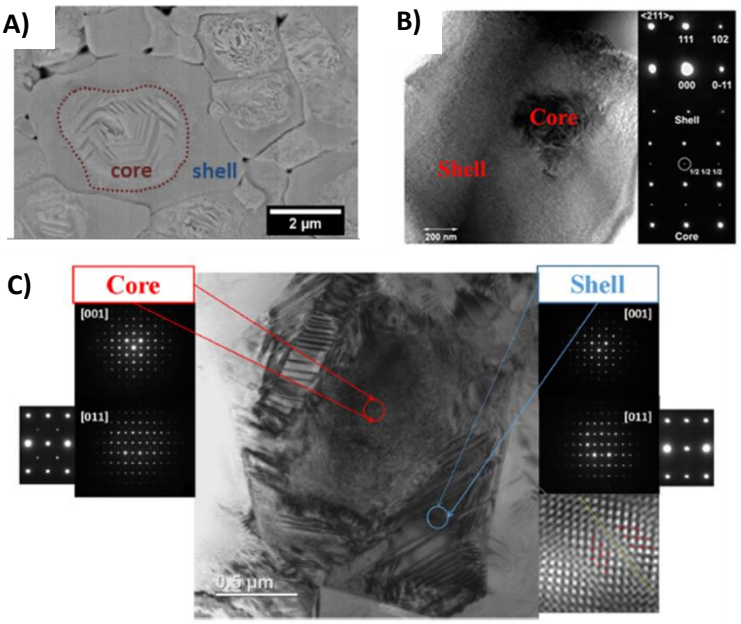

Figure 35 Observation of core-shell type microstructures in BF-based ceramics: **a)** SEM micrograph of Mn-modified $0.75BiFeO_3$-$0.25BaTiO_3$ by Calisir *et al.*[71], **b)** TEM image of $Bi(Zn_{2/3}Nb_{1/3})O_3$-modified $0.70BiFeO_3$-$0.30BaTiO_3$ by Wang *et al.*[84] and **c)** TEM image of in $0.24BiFeO_3$-$0.56K_{1/2}Bi_{1/2}TiO_3$-$0.20PbTiO_3$ exhibiting inverted type core-shell microstructure by Li *et al.*[85]

REFERENCES

1. Stevenson, T. *et al.* Piezoelectric materials for high temperature transducers and actuators. *J. Mater. Sci. Mater. Electron.* **26,** 9256–9267 (2015).

2. Shinekumar, K. & Dutta, S. High-Temperature Piezoelectrics with Large Piezoelectric Coefficients. *J. Electron. Mater.* **44,** 613–622 (2014).

3. Yan, H. *et al.* A Lead-Free High-Curie-Point Ferroelectric Ceramic, $CaBi_2Nb_2O_9$. *Adv. Mater.* **17,** 1261–1265 (2005).

4. Cumming, D. J., Sebastian, T., Sterianou, I., Rödel, J. & Reaney, I. M. $Bi(Me)O_3$ –$PbTiO_3$ high T_C piezoelectric multilayers. *Mater. Technol.* **28,** 247–253 (2013).

5. Rödel, J. & Li, J. F. Lead-free piezoceramics: Status and perspectives. *MRS Bull.* **43,** 576–580 (2018).

6. Bell, A. J. & Deubzer, O. Lead-free piezoelectrics—The environmental and regulatory issues. *MRS Bull.* **43,** 581–587 (2018).

7. Rödel, J. *et al.* Transferring lead-free piezoelectric ceramics into application. *J. Eur. Ceram. Soc.* **35,** 1659–1681 (2015).

8. Leontsev, S. O. & Eitel, R. E. Dielectric and Piezoelectric Properties in Mn-Modified (1-x)$BiFeO_3$ - x$BaTiO_3$ Ceramics. *J. Am. Ceram. Soc.* **92,** 2957–2961 (2009).

9. Moulson, A. J. & Herbert, J. M. *Electroceramics*. **2nd Ed.,** (2003).

10. Rabe, K. M., Ahn, C. H., Triscone, J. M.-M., Dawber, M. & Lichtensteiger, C. *Physics of Ferroelectrics*. *Springer* **105,** (2007).

11. Haertling, G. Ferroelectric ceramics: History and Technology. *J. Am. Ceram. Soc.* **82,** 718–818 (1999).

12. Cohen, R. E. Origin of ferroelectricity in perovskite oxides. *Nature* **358,** 136–138 (1992).

13. Kinase, W., Nakamura, K. & Harada, K. Origin of ferroelectricity in the perovskite ABO_3 crystals. *Ferroelectrics* **259,** 175–180 (2001).

14. Shannon, R. D. Revised effective ionic radii and systematic studies of interatomic distances in halides and chaleogenides. *Acta Cryst.* **A 32,** 751–767 (1976).

15. Damjanovic, D. Ferroelectric, dielectric and piezoelectric properties of ferroelectric thin films and ceramics. *Reports Prog. Phys.* **61,** 1267 (1998).

16. Kholkin, a. L., Pertsev, N. a. & Goltsev, a. V. in *Piezoelectric and Acoustic Materials for Transducer Applications* 17–38 (2008).

17. Priya, S. *et al.* A Review on Piezoelectric Energy Harvesting: Materials, Methods, and Circuits. *Energy Harvest. Syst.* **4,** 3–39 (2017).

18. Riedel, R., Ionescu, E. & Chen, I.-W. in *Ceramics Science and Technology* 3–34 (2008).

19. Noheda, B. *et al.* A monoclinic ferroelectric phase in the $Pb(Zr_{1-x}Ti_x)O_3$ solid solution. *Appl. Phys. Lett.* **74,** 2059–2061 (1999).

20. Hoffmann, M. J., Hammer, M., Endriss, a. & Lupascu, D. C. Correlation between microstructure, strain behavior, and acoustic emission of soft PZT ceramics. *Acta Mater.* **49,** 1301–1310 (2001).

21. Damjanovic, D. in *The Science of Hysteresis* **3,** 337–465 (2005).

22. Alikin, D., Turygin, A., Kholkin, A. & Shur, V. Ferroelectric Domain Structure and Local Piezoelectric Properties of Lead-Free $(Ka_{0.5}Na_{0.5})NbO_3$ and $BiFeO_3$-Based Piezoelectric Ceramics. *Materials (Basel).* **10,** 47 (2017).

23. Jin, L., Li, F. & Zhang, S. Decoding the Fingerprint of Ferroelectric Loops: Comprehension of the Material Properties and Structures. *J. Am. Ceram. Soc.* **97,** 1–27 (2014).

24. Scott, J. F. Ferroelectrics go bananas. *J. Phys. Condens. Matter* **20,** 021001 (2008).

25. Samara, G. A. The relaxational properties of compositionally disordered ABO_3 perovskites. *J. Phys. Condens. Matter* **15,** 367–411 (2003).

26. Goodenough, J. B. Electronic and ionic transport properties and other physical aspects of perovskites. *Reports Prog. Phys.* **67,** 1915–1993 (2004).

27. Cross, L. E. Relaxor ferroelectrics: An overview. *Ferroelectrics* **151,** 305–320 (1994).

28. Saito, Y. *et al.* Lead-free piezoceramics. *Nature* **432,** 84–87 (2004).

29. Shrout, T. R. & Zhang, S. J. Lead-free piezoelectric ceramics: Alternatives for PZT? *J. Electroceramics* **19,** 111–124 (2007).

30. Shibata, K., Wang, R., Tou, T. & Koruza, J. Applications of lead-free piezoelectric materials. *MRS Bull.* **43,** 612–616 (2018).

31. Rödel, J. *et al.* Perspective on the Development of Lead-free Piezoceramics. *J. Am. Ceram. Soc.* **92,** 1153–1177 (2009).

32. Panda, P. K. Review: environmental friendly lead-free piezoelectric materials. *J. Mater. Sci.* **44,** 5049–5062 (2009).

33. Wu, J., Fan, Z., Xiao, D., Zhu, J. & Wang, J. Multiferroic bismuth ferrite-based materials for multifunctional applications: Ceramic bulks, thin films and nanostructures. *Prog. Mater. Sci.* **84,** 335–402 (2016).

34. Catalan, G. & Scott, J. F. Physics and applications of bismuth ferrite. *Adv. Mater.* **21,** 2463–2485 (2009).

35. Yang, C., Kan, D., Takeuchi, I., Nagarajan, V. & Seidel, J. Doping $BiFeO_3$: approaches and enhanced functionality. *Phys. Chem. Chem. Phys.* **14,** 15953–15962 (2012).

36. Rojac, T. *et al.* $BiFeO_3$ Ceramics: Processing, Electrical, and Electromechanical Properties. *J. Am. Ceram. Soc.* **97,** 1993–2011 (2014).

37. Rojac, T. *et al.* Domain-wall conduction in ferroelectric $BiFeO_3$ controlled by accumulation of charged defects. *Nat. Mater.* **16,** 322–327 (2017).

38. Rojac, T., Ursic, H., Bencan, A., Malic, B. & Damjanovic, D. Mobile domain walls as a bridge between nanoscale conductivity and macroscopic electromechanical response. *Adv. Funct. Mater.* **25,** 2099–2108 (2015).

39. Walker, J. *et al.* Temperature dependent piezoelectric response and strain–electric-field hysteresis of rare-earth modified bismuth ferrite ceramics. *J. Mater. Chem. C* **4,** 7859–7868 (2016).

40. Lee, M. H. *et al.* High-performance lead-free piezoceramics with high curie temperatures. *Adv. Mater.* **27,** 6976–6982 (2015).

41. Arnold, D. C. Composition-driven structural phase transitions in rare-earth-doped $BiFeO_3$ ceramics : A review. *IEEE Trans. Ultrason. Ferroelectr. Freq. Control* **62,** 62–82 (2015).

42. Ravindran, P., Vidya, R., Kjekshus, A., Fjellvåg, H. & Eriksson, O. Theoretical investigation of magnetoelectric behavior in $BiFeO_3$. *Phys. Rev. B* **74,** 224412 (2006).

43. Palai, R. *et al.* β phase and γ-β metal-insulator transition in multiferroic $BiFeO_3$. *Phys. Rev. B - Condens. Matter Mater. Phys.* **77,** 1–11 (2008).

44. Selbach, S. M., Tybell, T., Einarsrud, M. A. & Grande, T. The ferroic phase transitions of $BiFeO_3$. *Adv. Mater.* **20,** 3692–3696 (2008).

45. Lennox, R. C. *et al.* Strain driven structural phase transformations in dysprosium doped $BiFeO_3$ ceramics. *J. Mater. Chem. C* **2,** 3345–3360 (2014).

46. Glazer, a. M. The classification of tilted octahedra in perovskites. *Acta Crystallogr. Sect. B Struct. Crystallogr. Cryst. Chem.* **28,** 3384–3392 (1972).

47. Selbach, S. M., Einarsrud, M. & Grande, T. On the thermodynamic stability of $BiFeO_3$. *Chem. Mater.* **21,** 169–173 (2009).

48. Bernardo, M. S. *et al.* Intrinsic compositional inhomogeneities in bulk Ti-doped $BiFeO_3$: Microstructure development and multiferroic properties. *Chem. Mater.* **25,** 1533–1541 (2013).

49. Bernardo, M. S., Jardiel, T., Peiteado, M., Caballero, a. C. & Villegas, M. Sintering and microstuctural characterization of W^{6+}, Nb^{5+} and Ti^{4+} iron-substituted $BiFeO_3$. *J. Alloys Compd.* **509,** 7290–7296 (2011).

50. Valant, M., Axelsson, A., Alford, N. & Bifeo, P. Peculiarities of a Solid-State Synthesis of Multiferroic Polycrystalline $BiFeO_3$. *Chem. Mater.* **19,** 5431–5436 (2007).

51. Kumar, M. M., Palkar, V. R., Srinivas, K. & Suryanarayana, S. V. Ferroelectricity in a pure $BiFeO_3$ ceramic. *Appl. Phys. Lett.* **76,** 2764–2766 (2000).

52. Kumar, M. & Yadav, K. L. Rapid liquid phase sintered Mn doped $BiFeO_3$ ceramics with enhanced polarization and weak magnetization. *Appl. Phys. Lett.* **91,** 242901 (2007).

53. Wang, Y. P. *et al.* Room-temperature saturated ferroelectric polarization in $BiFeO_3$ ceramics synthesized by rapid liquid phase sintering. *Appl. Phys. Lett.* **84,** 1731–1733 (2004).

54. Silva, J., Reyes, A., Esparza, H., Camacho, H. & Fuentes, L. $BiFeO_3$: A Review on Synthesis, Doping and Crystal Structure. *Integr. Ferroelectr.* **126,** 47–59 (2011).

55. Gil-González, E. *et al.* Phase-pure $BiFeO_3$ produced by reaction flash- sintering of Bi_2O_3 and Fe_2O_3. *J. Mater. Chem. A* **6,** 5356–5366 (2018).

56. Selbach, S. M., Einarsrud, M. A., Tybell, T. & Grande, T. Synthesis of $BiFeO_3$ by wet chemical methods. *J. Am. Ceram. Soc.* **90,** 3430–3434 (2007).

57. Kumari, S. *et al.* Dielectric anomalies due to grain boundary conduction in chemically substituted $BiFeO_3$. *J. Appl. Phys.* **117,** 114102 (2015).

58. Kavanagh, C. M., Goff, R. J., Daoud-Aladine, A., Lightfoot, P. & Morrison, F. D. Magnetically Driven Dielectric and Structural Behavior in $Bi_{0.5}La_{0.5}FeO_3$. *Chem. Mater.* **24,** 4563–4571 (2012).

59. Rojac, T., Kosec, M. & Damjanovic, D. Large electric-field induced strain in $BiFeO_3$ ceramics. *J. Am. Ceram. Soc.* **94,** 4108–4111 (2011).

60. Rojac, T., Kosec, M., Budic, B., Setter, N. & Damjanovic, D. Strong ferroelectric domain-wall pinning in $BiFeO_3$ ceramics. *J. Appl. Phys.* **108,** 074107 (2010).

61. Yang, C. H., Kan, D., Takeuchi, I., Nagarajan, V. & Seidel, J. Doping $BiFeO_3$: Approaches and enhanced functionality. *Phys. Chem. Chem. Phys.* **14,** 15953–15962 (2012).

62. Walker, J. *et al.* Dual strain mechanisms in a lead-free morphotropic phase boundary ferroelectric. *Sci. Rep.* **6,** 1–8 (2016).

63. Cheng, C.-J., Kan, D., Anbusathaiah, V., Takeuchi, I. & Nagarajan, V. Microstructure-electromechanical property correlations in rare-earth-substituted $BiFeO_3$ epitaxial thin films at morphotropic phase boundaries. *Appl. Phys. Lett.* **97,** 212905 (2010).

64. Kan, D. *et al.* Universal behavior and electric-field-induced structural transition in rare-earth-substituted $BiFeO_3$. *Adv. Funct. Mater.* **20,** 1108–1115 (2010).

65. Cheng, C.-J. *et al.* Structural transitions and complex domain structures across a ferroelectric-to-antiferroelectric phase boundary in epitaxial Sm-doped $BiFeO_3$ thin films. *Phys. Rev. B* **80,** 014109 (2009).

66. Kumar, M. M., Srinivas, A. & Suryanarayana, S. V. Structure property relations in $BiFeO_3$/$BaTiO_3$ solid solutions. *J. Appl. Phys.* **87,** 855–862 (2000).

67. Wang, T.-H. *et al.* Phase transition and ferroelectric properties of $xBiFeO_3$–$(1-x)BaTiO_3$ ceramics. *Curr. Appl. Phys.* **11,** S240–S243 (2011).

68. Kim, S. *et al.* Structural and electrical characteristics of potential candidate lead-free $BiFeO_3$ -$BaTiO_3$ piezoelectric ceramics. *J. Appl. Phys.* **122,** 164105 (2017).

69. Wei, Y. *et al.* Polar order evolutions near the rhombohedral to pseudocubic and tetragonal to pseudocubic phase boundaries of the $BiFeO_3$-$BaTiO_3$ system. *Materials (Basel).* **8,** 8355–8365 (2015).

70. Guo, Y. *et al.* Critical roles of Mn-ions in enhancing the insulation, piezoelectricity and multiferroicity of $BiFeO_3$-based lead-free high temperature ceramics. *J. Mater. Chem. C* **3,** 5811–5824 (2015).

71. Calisir, I. & Hall, D. A. Chemical heterogeneity and approaches to its control in $BiFeO_3$–$BaTiO_3$ lead-free ferroelectrics. *J. Mater. Chem. C* **6,** 134–146 (2018).

72. Kim, S. *et al.* Revealing the role of heat treatment in enhancement of electrical properties of lead-free piezoelectric ceramics. *J. Appl. Phys.* **122,** 014103 (2017).

73. Kim, D. S., Cheon, C. Il, Lee, S. S. & Kim, J. S. Effect of cooling rate on phase transitions and ferroelectric properties in $0.75BiFeO_3$-$0.25BaTiO_3$ ceramics. *Appl. Phys. Lett.* **109,** 202902 (2016).

74. Calisir, I., Amirov, A. A., Kleppe, A. K. & Hall, D. A. Optimisation of functional properties in lead-free $BiFeO_3$-$BaTiO_3$ceramics through La^{3+}substitution strategy. *J. Mater. Chem. A* **6,** (2018).

75. Li, Q., Wei, J., Tu, T., Cheng, J. & Chen, J. Remarkable piezoelectricity and stable high-temperature dielectric properties of quenched $BiFeO_3$-$BaTiO_3$ ceramics. *J. Am. Ceram. Soc.* **100,** 5573–5583 (2017).

76. Murakami, S. *et al.* Optimising dopants and properties in $BiMeO_3$(Me = Al, Ga, Sc, Y, $Mg_{2/3}Nb_{1/3}$, $Zn_{2/3}Nb_{1/3}$, $Zn_{1/2}Ti_{1/2}$) lead-free $BaTiO_3$-$BiFeO_3$ based ceramics for actuator appl. *J. Eur. Ceram. Soc.* **38,** 4220–4231 (2018).

77. Wang, D. *et al.* Temperature dependent, large electromechanical strain in Nd-doped $BiFeO_3$-$BaTiO_3$ lead-free ceramics. *J. Eur. Ceram. Soc.* **37,** 1857–1860 (2017).

78. Seidel, J. *et al.* Conduction at domain walls in oxide multiferroics. *Nat. Mater.* **8,** 229–234 (2009).

79. Masó, N. & West, A. R. Electrical properties of Ca-doped $BiFeO_3$ ceramics: From p-type semiconduction to oxide-ion conduction. *Chem. Mater.* **24,** 2127–2132 (2012).

80. Schrade, M., Masó, N., Perejón, A., Pérez-Maqueda, L. A. & West, A. R. Defect chemistry and electrical properties of $BiFeO_3$. *J. Mater. Chem. C* **5,** 10077–10086 (2017).

81. Narayan, B. *et al.* Electrostrain in excess of 1% in polycrystalline piezoelectrics. *Nat. Mater.* **17,** 427–431 (2018).

82. Pan, Z. *et al.* Giant Polarization and High Temperature Monoclinic Phase in a Lead-Free Perovskite of $Bi(Zn_{0.5}Ti_{0.5})O_3$-$BiFeO_3$. *Inorg. Chem.* **55,** 9513–9516 (2016).

83. Yabuta, H. *et al.* Microstructure of $BaTiO_3$–$Bi(Mg_{1/2}Ti_{1/2})O_3$–$BiFeO_3$ piezoelectric ceramics. *Jpn. J. Appl. Phys.* **51,** 09LD04 (2012).

84. Wang, D. *et al.* High Energy Storage Density and Large Strain in $Bi(Zn_{2/3}Nb_{1/3})O_3$ -Doped $BiFeO_3$– $BaTiO_3$ Ceramics. *ACS Appl. Energy Mater.* **1,** 4403–4412 (2018).

85. Li, Y., Zhang, Z., Chen, Y. & Hall, D. a. Electric field-induced strain in core-shell structured $BiFeO_3K_{0.5}Bi_{0.5}TiO_3PbTiO_3$ ceramics. *Acta Mater.* **160,** 199–210 (2018).

Chapter 2

Experimental Techniques

This section aims to cover fundamental aspects of the experimental methods utilised throughout this project. It starts with an overview of ceramic processing *via* the solid-state reaction method and continues with the description and application of physical characterization methods on the synthesised ceramics, covering the specific aspects of X-Ray diffraction and microstructure imaging, and follows with the basics of the electrical measurements. Specific details regarding the experimental methods used in this work are given within the relevant subsections of research outputs in Chapter 3.

2.1 Ceramic Processing

Functional ceramics are generally prepared by a standard processing method known as solid-state reaction from stoichiometric amounts of the required elements in their oxide and carbonate forms. The high purity reagent powders are first mixed and then milled until a homogeneous mixture is obtained. A calcination process is normally done after milling in order to improve homogeneity and enable the decomposition of carbonates to oxides. The mixture is pressed into pellets for improving particle-particle contacts. The pellets are sintered on an alumina plate within a high temperature furnace. The sintering temperature can be up to 1400°C depending on the melting point of ceramics. After a certain time holding at the sintering temperature, the ceramics are cooled down to room temperature with a certain cooling rate. The progress of reactions is monitored by X-ray powder diffractometer after both calcination and sintering processes so as to check the formation of required phases and homogeneity of the

material. This monitoring process can be repeated until a single phase is obtained.[1,2]

2.2 X-Ray Diffraction

X-ray diffraction is an essential non-destructive analytical technique for revealing information about the crystallographic structure and phase identification in crystalline materials. Since the wavelength of X-rays is comparable to atomic spacing, this method is suitable in order to probe the structural arrangements of atoms and molecules in a wide range of materials. A monochromatic X-ray beam with a specific wavelength λ, incident on a crystalline sample at an angle θ, leads to diffraction, as the distance travelled by the rays reflected from successive planes d, varies by a complete number of wavelengths, $n\lambda$.[3,4]

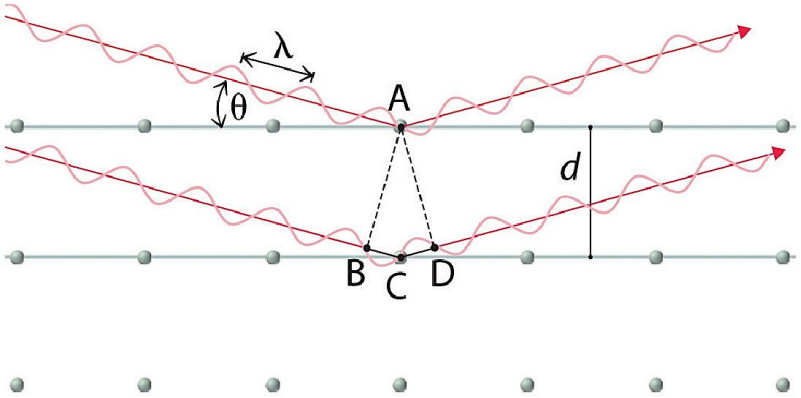

Figure 1 Illustration of the geometry used for the derivation of Bragg's law.[g]

These relations between d-spacing, the wavelength λ, and the angle θ, are illustrated in Figure 1 and expressed by Bragg's Law as

$$n\lambda = 2d\ sin\theta \tag{1}$$

Nonetheless, in a solid, many different sets of planes of atoms can diffract x-rays. Each has a different inter-planar distance d_{hkl}, and therefore diffracts the x-rays at a different angle θ_{hkl}, which generates a characteristic pattern of spots with a

[g] Web Reference: https://saylordotorg.github.io/text_general-chemistry-principles-patterns-and-applications-v1.0/s16-solids.html

defined intensity. The data obtained from a diffractometer, contains a series of diffraction peaks illustrated by the recorded intensity as a function of the scattering angle $2\theta_{hkl}$. By applying Bragg's law it is possible to determine the distances d_{hkl} and then to assign the correct crystal structure of the sample, by following the steps discussed below.[3,4]

2.2.1 Structure Refinement

As stated above, diffraction profiles are recorded by the intensity Y_i, at each small step i, corresponding to an angle of $2\theta_{hkl}$, between the incident beam and detector. It is presumed that all crystallographic orientations are present within a polycrystal, and thus only a 1D pattern of intensity as a function of $2\theta_{hkl}$ is recorded. The information about the type of crystal symmetry is correlated to the positions of the peaks and the atomic positions to the relative intensities of those peaks. It should be noted that for polycrystalline materials, crystal structure determination from the obtained diffraction profile can sometimes be challenging due to the overlap of reflections in a single peak.[5–8]

Next, the obtained experimental data should be fitted with a model in order to determine the crystal structure of the studied material. Rietveld refinement is therefore utilized as a method that can model the crystal structure in powder diffraction. This method is a full-pattern analysis technique. A crystal structure, together with instrumental and microstructural information, is used to generate a calculated diffraction profile that can be compared to the observed profile. A least squares procedure is then used to minimize the difference between the calculated pattern and each point of the observed pattern by refining model parameters. This relation can be expressed as

$$S_Y = \sum_i w_i \left(Y_{i(observed)} - Y_{i(calculated)}\right)^2 \quad (2)$$

The observed and the calculated intensity at the i^{th} step are defined as $Y_{i(observed)}$ and $Y_{i(calculated)}$. S_Y is the minimized residual between the observed and calculated intensity, and w_i is $(Y_{i(observed)})^{-1}$.

This process requires a number of iterations to obtain chemically and physically plausible results. It is also necessary to input approximate information about the phase(s)[h] and the diffractometer parameters used to record the data. It should also be noted that, this is a structural refinement technique, not a method for structure solution.

Although a residual profile plot (or graphical fit) is suggested to be the best way to follow and use as guidance during the refinement,[7] the fit of the calculated pattern relative to the observed data can also be given numerically.[6] This can be quantified in the form of residual or reliability factors, also denoted as R-factors, which are R-weighted (R_{wp}) and R-expected (R_{exp}) profiles. R_{wp} gives the most useful quantity as the numerator is S_Y, the residual is minimised and hence provides the best indication of the progress of the refinement. A measure of the expected value from statistical analysis is given by R_{exp}. These R-factors are expressed by the equations[6] as follows:

$$R_{wp} = \left[\frac{\sum_i w_i(Y_{i(observed)} - Y_{i(calculated)})^2}{\sum_i w_i(Y_{i(observed)})^2}\right]^{1/2} \quad (3)$$

$$R_{exp} = \left[\frac{N-P}{\sum_i^N w_i(Y_{i(observed)})^2}\right]^{1/2} \quad (4)$$

where N is the number of data points and P is the total number of refined parameters. Ideally, the final R_{wp} should approach the statistically expected R value, R_{exp}. The ratio between these two R-factors is used as a figure of merit for the structure refinement and is mostly known as Goodness of Fit (GoF),

$$GoF = \frac{R_{wp}}{R_{exp}} \quad (5)$$

Goodness of fit can also be represented as chi-squared, χ^2. This value usually aims to obtain a value close to 1, indicating a good fit.[6,7] The R-factors obtained from a Rietveld fit may seem satisfactory, while extreme care should be taken in their

[h] Crystal structure database services are provided by Cambridge Crystallographic Data Centre (CCDC) in https://www.ccdc.cam.ac.uk and National Chemical Database Service in http://cds.rsc.org

interpretation, since there are a number of challenges which can be encountered during refinement and those must be interpreted within physical sense.[6–8]

The full description of the Rietveld analysis including the detailed guidelines, mathematical and physical background, and all associated challenges are not within the scope of this work. However, these can be found in detail in the works of McCusker *et al.*[6], Toby,[7] and Cheary and Coelho.[8]

2.2.2 Synchrotron Radiation

Synchrotrons can be used to generate X-rays with intensities much greater than the use of lab-based sources and are highly useful for problems that cannot be solved using in-house equipment. Synchrotron radiation also has high collimation and can be tuned to specific wavelengths.[9,10]

The advantages of synchrotron light over laboratory sources are that the brilliance and high intensity of the X-rays often allows transmission through bulk, relatively large samples, rather than surface diffraction from the laboratory counterpart, or further penetration through heavily X-ray absorbing elements like lead. Synchrotrons emit a continuum of photon energies allowing the various beamlines to select energies or wavelengths in accordance with experimental requirements.[9,10]

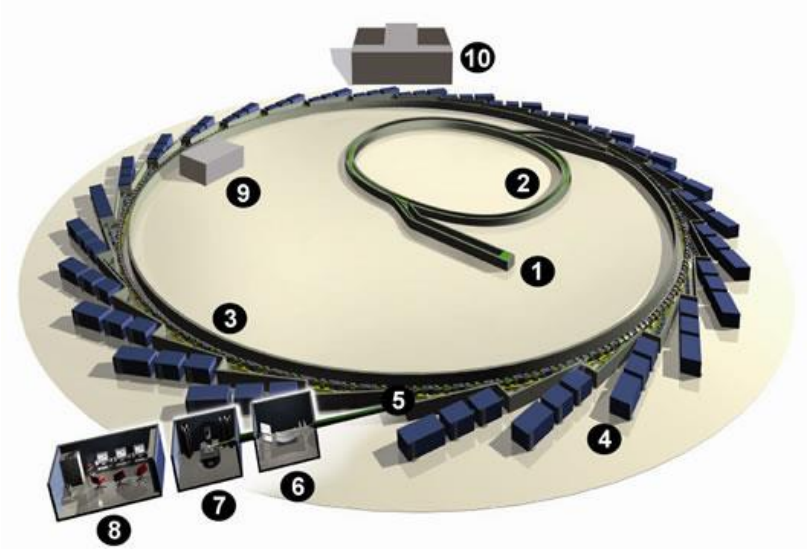

Figure 2 Schematic of Diamond synchrotron facility composed of the sections: The injection system (1), the booster synchrotron (2), the storage ring (3), the beamline (4), the front end (5), the optics hutch (6), the experimental hutch (7), the control hutch (8), the Radiofrequency (RF) cavity and the Diamond house (10).[i]

When electrons moving at approximately the speed of light are caused to move along a bent trajectory, they emit synchrotron radiation at GeV energies. At synchrotron radiation sources electrons are injected first into a linear accelerator and then into a booster ring where the beam of electrons are accelerated to approximately the speed of light (using an electric field) and kept within the ring using bending magnets. The beam is transferred to a storage ring where bending magnets are used to keep it in a circular orbit. The ring must be kept under very high vacuum to prevent beam and energy loss. Also within the ring there are insertion devices which generate stronger radiation within the straight sections of the "ring", increasing the intensity of the beam; these devices are called wigglers or undulators as they cause the electrons to move sinusoidally within the ring. At points where the beam is bent, *i.e.* at positions in the ring where the insertion devices or the bending magnets are present, beam energy is lost in the

[i] Web reference: https://www.diamond.ac.uk/Science/Machine/Components.html

form of synchrotron radiation tangentially to the direction of the beam. It is the front end where openings in the ring are made onto the beamlines, which contain mirrors, slits and monochromators (optic hutch) to deliver radiation of a required wavelength and collimation to an experimental hutch, which is designed for a specific type of study on materials by beamline users. Due to degradation of the orbit or gas molecule collisions the electron density decreases over time and it requires a routine re-fill of the storage ring.[9,10]

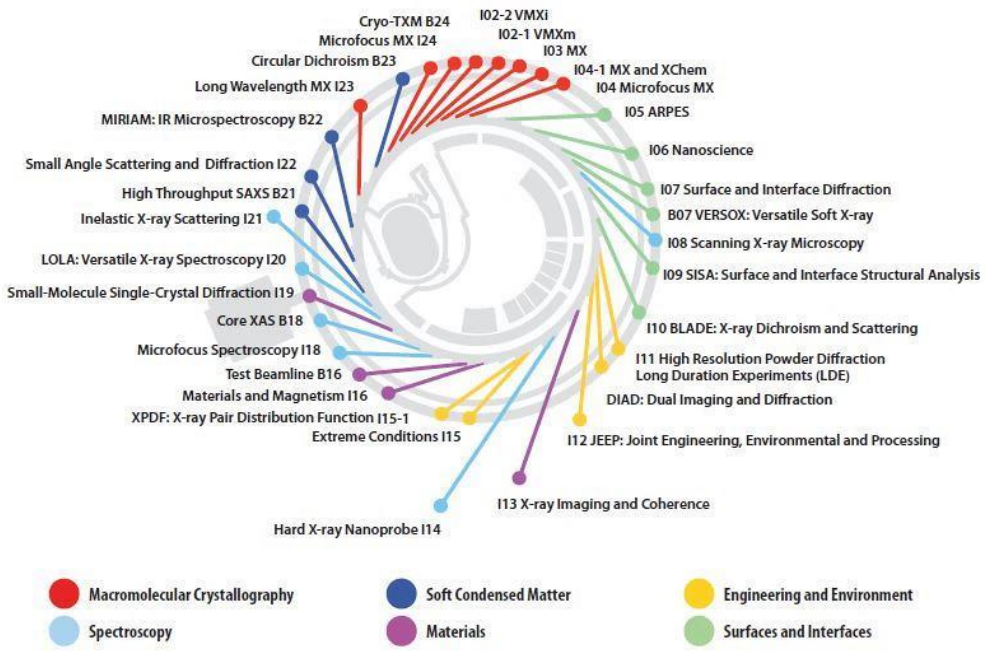

Figure 3 Layout of available beamlines at the Diamond National Light Source.[9]

A schematic diagram of the Diamond synchrotron source is shown in Figure 2. This facility was opened at Harwell Science and Innovation Campus in 2007 and consists of several elements as illustrated in the figure and various beamlines (currently 28) available in Diamond. Each beam line is associated with specific groups of researchers investigating the properties of a wide range of materials/substances, as shown in Figure 3.[9,10]

2.2.3 Diffraction studies under electric field in piezoceramics

Most crystals contain imperfections producing local distortions of the lattice, resulting in a non-homogeneous strain field (Figure 4). The influence on position,

shape and extension of reciprocal space points, and as a result on diffraction peak profiles, is generally more complicated than that of the domain size.[11–15] The effect of a macroscopically homogeneous strain, is expressed as

$$\varepsilon = \frac{\Delta d}{d} \tag{6}$$

When a crystal is strained, the *d*-spacings vary. A macroscopic strain changes the inter-planar spacing by Δd, giving rise to a shift in the average position of the diffraction peak of $\Delta 2\theta$. This is the well-known basis for the residual stress (or residual strain) analysis by diffraction techniques. As illustrated in Figure 4(b), macrostrain produces a shift in the position of peak. The effect can be measured for different sample orientations and different peaks, thus providing rather detailed information on the strain tensor and, with subsequent proper modelling, on the stress tensor.[15]

If the strain field is not homogeneous on the length scale of the crystallite size or smaller, then different parts of the material diffract at slightly different angles, thus producing a peak broadening. Profile width and shape will evidently depend on the strain distribution across the sample.[15]

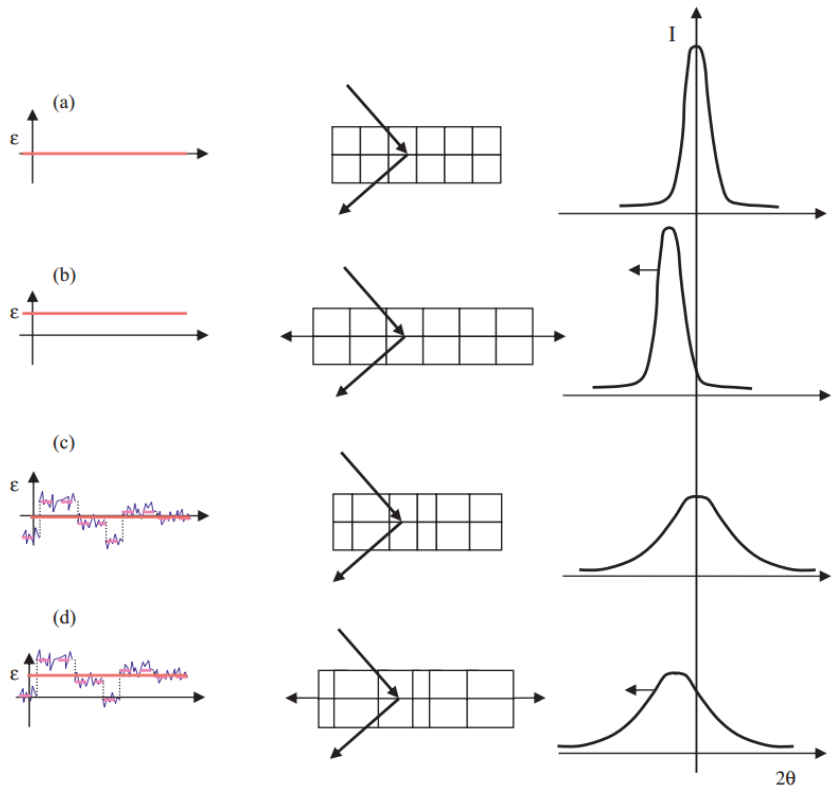

Figure 4 X-ray diffraction peak profiles under various strain conditions: **a)** for zero strain (no macrostrain and no microstrain), **b)** macrostrain (tensile), **c)** microstrain and **d)** combined effect of microstrain and macrostrain. Strain (ε) is plotted on the left as a function of the position within a material microstructure indicated in the middle sketch.[15]

Such X-ray diffraction studies are a particularly powerful experimental technique used in piezoceramics to extract information about intrinsic and extrinsic contributions to the electric-field induced strain. Wide varieties of diffraction instruments and characterisation approaches are now available but selection of the most appropriate source and instrument are very important. The ability of x-ray diffraction to probe matter on multiple length scales can give unpresented insight to understand the internal dynamics of functional materials. These studies can be performed on an electroactive material, which shows prominent crystallographic variations under external stimuli (electric field, pressure, temperature *etc.*) with a set-up of *ex-situ* (recording data before and after exposure) or *in-situ* (real-time measurement). However, in some cases, the *ex-situ*

studies may not provide adequate information. For example, as for the case of recording electric field-induced strain effect on the obtained diffraction profile in a piezoceramic, *ex-situ* measurements are unable to elucidate intermediate stages such as the critical field for structural alteration or the evolution of crystallographic texturing *via* progressive domain switching/domain wall motion. In addition to that, transient states which only exist under field would not be observed. Conversely, *in-situ* high-energy xray diffraction can comprehensively provide information for which is used to analyse field-induced structural variations for the studied ceramics.[11–15]

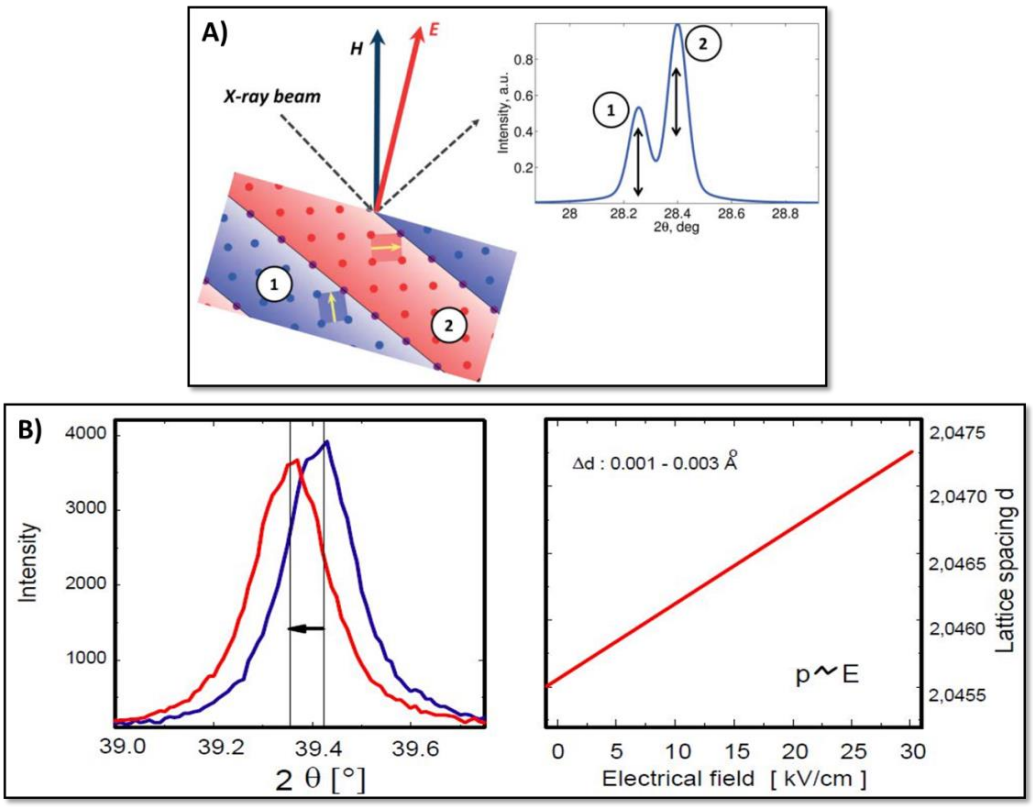

Figure 5 a) Extrinsic effect: A schematic for the diffraction of probing dynamics of ferroelectric/ferroelastic domains in a single grain of ferroelectric, which consists of domain microstructure (red and blue regions). External electric field (E) promotes domain growth in which spontaneous polarization within the grain aligns at a smaller angle to the electric field. For this grain, Type 1 domains should grow and Type 2 domains should shrink, resulting in intensity variations as increase and decrease of the corresponding peaks in response to an applied electric field, as shown in the inset.[16] **b)** Intrinsic effect: The applied electric field causes a shift of the ions in a unit cell, which results in a change of the *d*-spacing and the corresponding diffraction angle in a ferroelectric ceramic.[17]

Two approaches are commonly used in the diffraction studies of ferroelectrics under a field to analyse the deformation in terms of atomic structure and crystal lattice, *i.e.* as an intrinsic piezoelectric effect, and the deformation induced by domain wall motion, *i.e.* as electromechanical strains of extrinsic origin.[11,16] To verify a prominent electromechanical response, one has to analyse diffraction profiles under electric field. The extrinsic effect of domain wall motion leads to a

strong texturing in characteristic peaks of the associated structure (Figure 5(a)). For example, variation in the relative intensities for (*002*)/(*200*) and (*111*)/(*11-1*) can highlight field-induced domain texture variations in tetragonal and rhombohedral systems, respectively. The intrinsic effect results in a measurable change in *d*-spacing, accordingly lattice constants (Figure 5(b)) which cause peak shifts for *(111)* and *(200)* for tetragonal and rhombohedral, respectively. These two phenomena simultaneously occur within the ceramic under the application of electric field, therefore time-resolved *in-situ* diffraction studies are extremely useful techniques for providing both qualitative and quantitative information regarding the actuation mechanisms (Figure 6). It should also be noted that electric field-induced phase transformations can also be analysed and seen as an extrinsic factor by observing the change/evolution in diffraction patterns using this technique.[11,12,18]

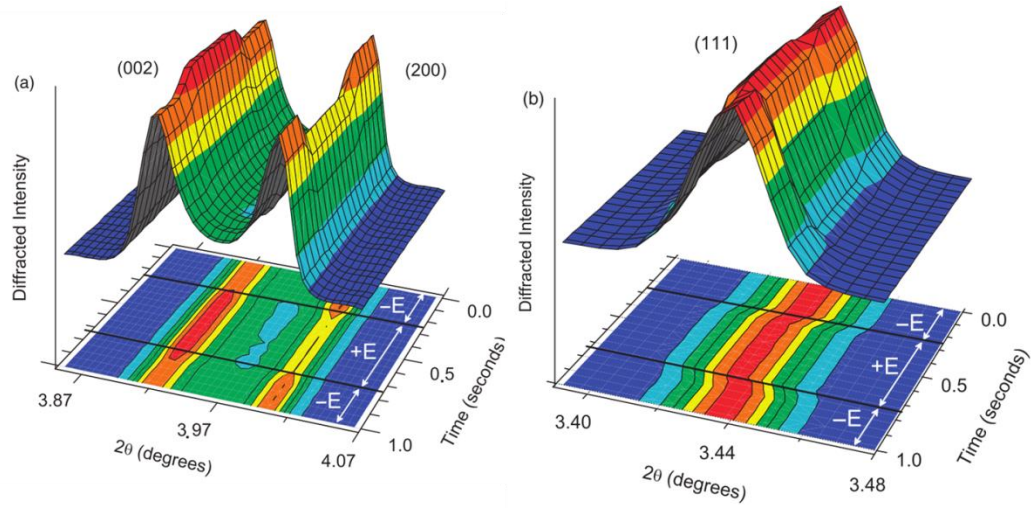

Figure 6 Time-resolved diffraction patterns during the application of electric field in a bipolar square wave form: **(a)** Intensity variation in 002 and 200 diffraction peaks indicate a result of change in volume fraction of ferroelectric domains with (002) and (200) orientations**, (b)** a shift in the 2Θ position of the (111) diffraction peak is noticed with time, as a result of (111) electric-field-induced lattice strain.[11]

As for the strain determination in ferroelectrics, domain walls and intergranular stresses are the sources of microstrains and those can cause asymmetric

broadening of diffraction peaks in these materials. When we analyse the peak shifts and broadening, lattice strain during application of electric field can simply be quantified using the equation given above ($\varepsilon = \Delta d/d$) , while the determination of volume fraction of the associated domains varies with the structure. For example, in a tetragonal crystal structure, the volume fraction of the material with (002) domains parallel with particular specimen direction is given by[11]

$$v_{002} = \frac{\frac{I_{002}}{I'_{002}}}{\frac{I_{002}}{I'_{002}} + 2\left(\frac{I_{200}}{I'_{200}}\right)} \tag{7}$$

where I_{hkl} is the integrated area of the hkl diffraction peak for a given sample with a preferred orientation of 90° domains and I'_{hkl} is the integrated area of the same peak for a sample with no preferred orientation of 90° domains.

On the other hand, the volume fraction of the (111) domains along a particular specimen direction for a rhombohedral perovskite ferroelectric is obtained by the following modification of above equation:

$$v_{111} = \frac{\frac{I_{111}}{I'_{111}}}{\frac{I_{111}}{I'_{111}} + 3\left(\frac{I_{11-1}}{I'_{11-1}}\right)} \tag{8}$$

where lattice spacings for (111) planes are larger than that of (11-1) planes.

For a random distribution of non-180° domains, η_{002} is equal to $1/3$ and η_{111} is equal to $1/4$, corresponding to equal distribution of possible ferroelastic domain variants. Therefore, the volume fraction of the material, which has been reoriented through application of a given loading condition, is given below[11]

$$\text{for tetragonal structure;} \quad \eta_{002} = v_{002} - \frac{1}{3} \tag{9}$$

$$\text{for rhombohedral structure;} \quad \eta_{111} = v_{111} - \frac{1}{4} \tag{10}$$

The lattice strain quantification and determination of volume fraction for the involved domains during loading are the main components of the microscopic and macroscopic strain analysis in ferroelectrics.

Although *in-situ* measurements can be done using laboratory-based x-ray diffraction instruments, information is limited due to the experimental geometry. This geometrical constraint arises as a conventional x-ray source does not possess sufficient x-ray energy to penetrate most of the bulk materials of interest here, and is hence limited to reflection geometry. For instance, the penetration depth of a conventional x-ray source (Cu *Ka*) in most ceramics is usually in the range of a few microns. Another drawback is that they do not provide full access to all scattering vector orientations relative to an applied field vector. This indicates that the method used reflection geometry can only provide limited information. On the other hand, a large penetration depth in ceramics (typically several millimetres) can be obtained using high-energy x-rays source, and thus the quantification of the microscopic origin of electromechanical strain in piezoceramics is available to be studied.[11–15]

As discussed in the section of synchrotron radiation, x-ray energies can be adjusted dependent on the type of studies and materials. For this purpose, the x-ray attenuation length, τ_0 comes to one of the most important parameters to be considered during the investigation of bulk samples. This can be calculated from the mass absorption coefficient, μ and density of the materials, ρ as $\tau_0 = 1/\mu\,\rho$. This parameter for the studied elements, compounds *etc.* can be conveniently found in the NIST database[j].

[j] National Institute of Standards and Technology (NIST): https://physics.nist.gov/PhysRefData/FFast/html/form.html

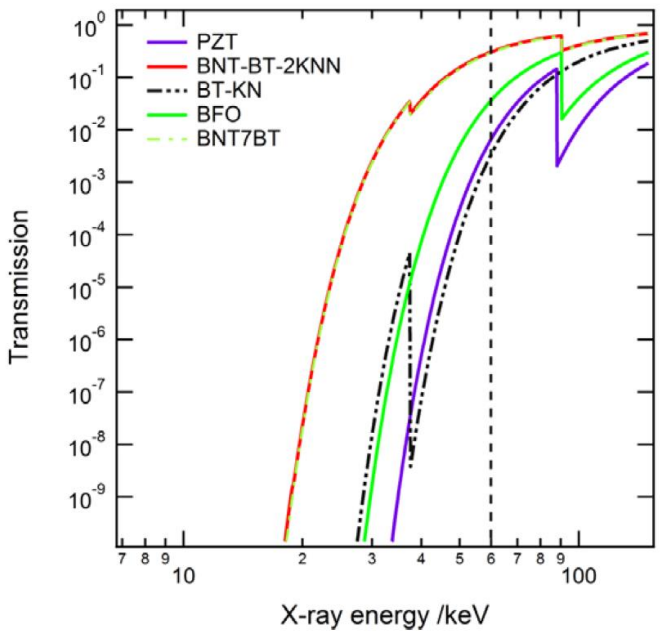

Figure 7 Transmission in various ferroelectric ceramics of 1 mm thickness as a function of x-ray energy. Dashed line indicates where x-ray energies greater than 60 keV can allow large fractions of bulk materials to be probed. Abbreviations, PZT: lead zirconate titanate, BNT: bismuth sodium titanate, BT: barium titanate, KNN: Potassium sodium niobate, BFO: bismuth ferrite.[19]

Figure 7 shows an example of calculated transmission of x-ray energies in various ferroelectric materials of 1 mm thickness. As can be seen in Figure 7, below the dashed line the transmission through a 1 mm section of the materials of interest is relatively low. As the x-ray photon energy is increased above 60 keV, sufficient beam transmission is achieved to perform x-ray diffraction experiments in transmission geometry *i.e.* Debye-Scherrer.

Using a large area 2D detector in the synchrotron radiation beamline is also ideal to monitor field-induced structural changes in bulk ceramic materials. The area detector placed behind a sample in transmission mode with high energy can ease the experimental setups with fast data collection. The combination of high energy x-rays and a large area detector also facilitates recording a large number of entire Debye-Scherrer rings in a rather small 2θ range.[18–20]

2.3 Microstructure Imaging

For microstructure imaging in solids, Scanning Electron Microscopy (SEM) is a powerful micro-analytical technique which is capable of reaching higher resolution as compared with optical microscopy. It is a type of electron microscope which takes images from the sample surface by scanning with a highly energetic electron beam. SEM consists of an electron optical column, a vacuum system, and connected electronics with two modes detecting, secondary and backscattered electrons The electron beam generated by the electron gun at the top of the column is focussed into a very fine spot on the sample surface. This beam scans over the sample and secondary electrons are generated on the surface and detected by a special detector. Topography of the sample surface determines the amplitude of the secondary electron signal. Thus, those signals are amplified and used to monitor the corresponding specimen morphology. This is the most common imaging mode used in SEM and collects low energy secondary electrons, which originate within a few nanometres from the specimen surface.[21]

Another imaging mode in SEM uses the backscattered electrons which consist of high energy electrons in the electron beam reflected out of the specimen interaction volume. This mode is used to determine chemical information about the scanned specimen. The principle is that heavy elements having high atomic number backscatter electrons more severely as compared to light elements and resulting in a brighter region during the imaging process and this provides the contrast between different regions or phases in the image with respect to chemical compositions. Backscattered electrons are also performed to determine crystallographic structure of the materials and this method is known as electron backscatter diffraction, EBSD.[21]

An analytical technique known as Energy Dispersive X-Ray Spectroscopy (EDS) is also linked with SEM. This method makes elemental analysis of the specimen possible while imaging in SEM by selecting scan types such as line scan, point scan and elemental mapping of the whole image with respect to what information is needed. EDS is one the variants of X-ray fluorescence spectroscopy

analysing X-rays emitted by the matter in response to being hit by electrons. Its basic principle is that each element has a unique atomic structure, which allows X-rays that are characteristic of an element's atomic structure to be identified individually from the atoms present in the scanned area.[21]

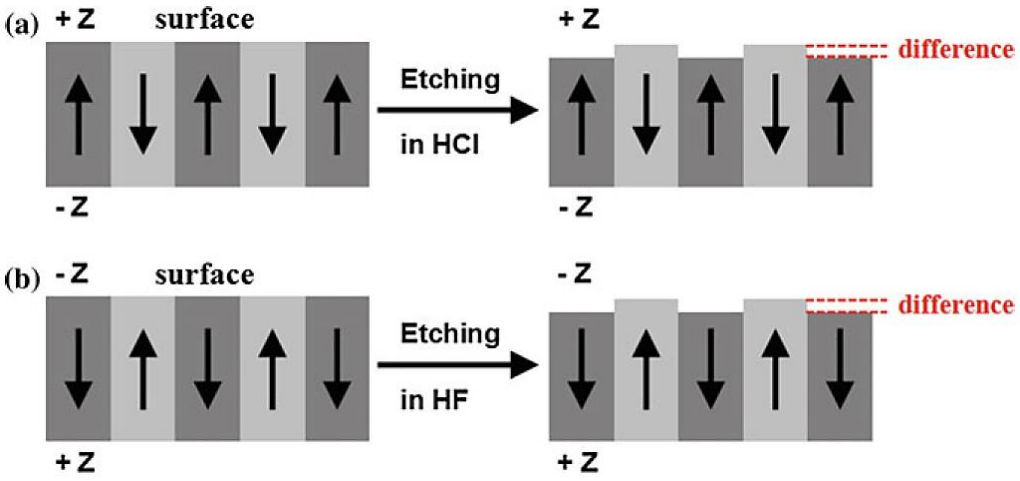

Figure 8 Schematic of etching process in **a)** $BaTiO_3$ and **b)** $LiNbO_3$ single crystal. −Z and +Z showing negative and positive end of electric dipoles, respectively.[22,23]

For microstructural imaging, the thermochemical etching technique is a common method to reveal ferroelectric type domains in electroceramics,[22–24] which is based on the different etching rates between the positive and negative ends of ferroelectric dipoles. After the etching process, the ferroelectric domains can be further observed by other techniques, including optical microscopy, scanning electron microscopy (SEM) and atomic force microscopy (AFM). As etching reagents, HF, HCl, $HNbO_3$ or the mixed solutions of two of them are commonly used. The etching technique was first used in $BaTiO_3$ single crystals to reveal the antiparallel 180° ferroelectric *c*-domains, and it was found that the positive end of the electric polarization etched much faster than the negative one, giving a noticeable difference on the surface, as illustrated in Figure 8. Although it is destructive and carried out *ex-situ*, this method is still widely applied on various ferroelectric ceramics possessing different types of domain structures due to variety of characteristic polarisation directions in tetragonal, rhombohedral, and orthorhombic crystal structures.[22,23]

2.4 Electrical property measurements

To characterize ferroelectric properties of ceramics, a special electrical circuit was developed by Sawyer and Tower and they first characterized Rochelle salt. After the success of this circuit, it was named as the Sawyer-Tower circuit and outline of the circuit is illustrated in Figure 9. An AC voltage is applied across an electroded ferroelectric sample, placed on the horizontal plates of an oscilloscope. Therefore, the quantity plotted on the horizontal axis is proportional to the field across the crystal. A linear capacitor C_0 is connected in series with the ferroelectric sample. The voltage across C_0 is proportional to the polarization (P) of the ferroelectric sample. In fact, the relations between dielectric displacement (D) and polarization are expressed by the following equation:[1,25,26]

$$D = \varepsilon_0 E + P \tag{11}$$

where D is the charge density collected by C_0. For the larger value of P, the contribution by $\varepsilon_0 E$ can be neglected. Thus, the obtained D can be considered as P in practice. This equipment yields polarisation (P) through charge or current integration techniques following with compensation by a variable resistor R shown in the outline (Figure 9).With the advent of well-developed electronic techniques, this circuit is no longer used as its original form. Most testing systems for measuring P-E behaviour of ferroelectric materials have been made using commercial equipment.[1,25,26]

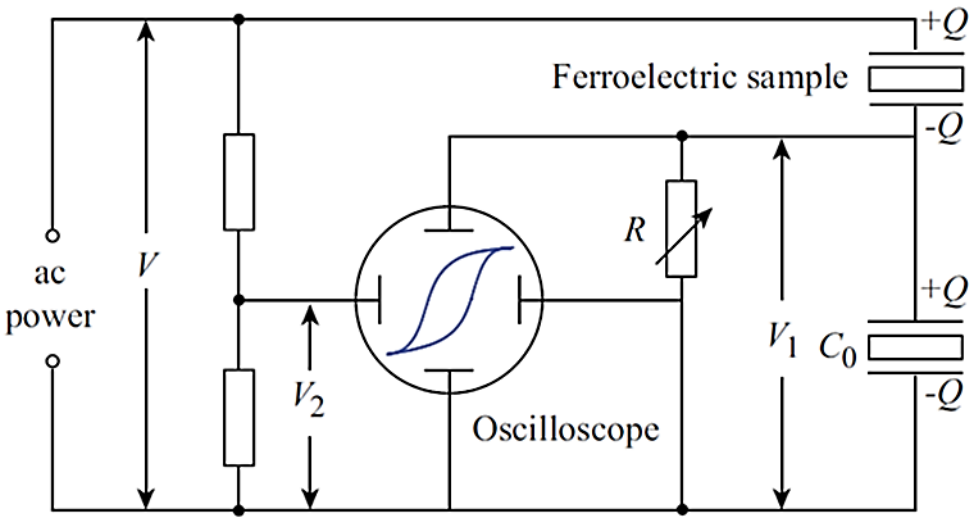

Figure 9 The outline of Sawyer-Tower circuit for measuring the P-E hysteresis loops of ferroelectric materials.[25]

As mentioned above, P-E measurements are conveniently performed thanks to well-developed measuring techniques. However, the most challenging part of this characterization is to interpret the obtained P-E loops. Conductivity strongly affects the P-E behaviour and may cause misinterpretation.

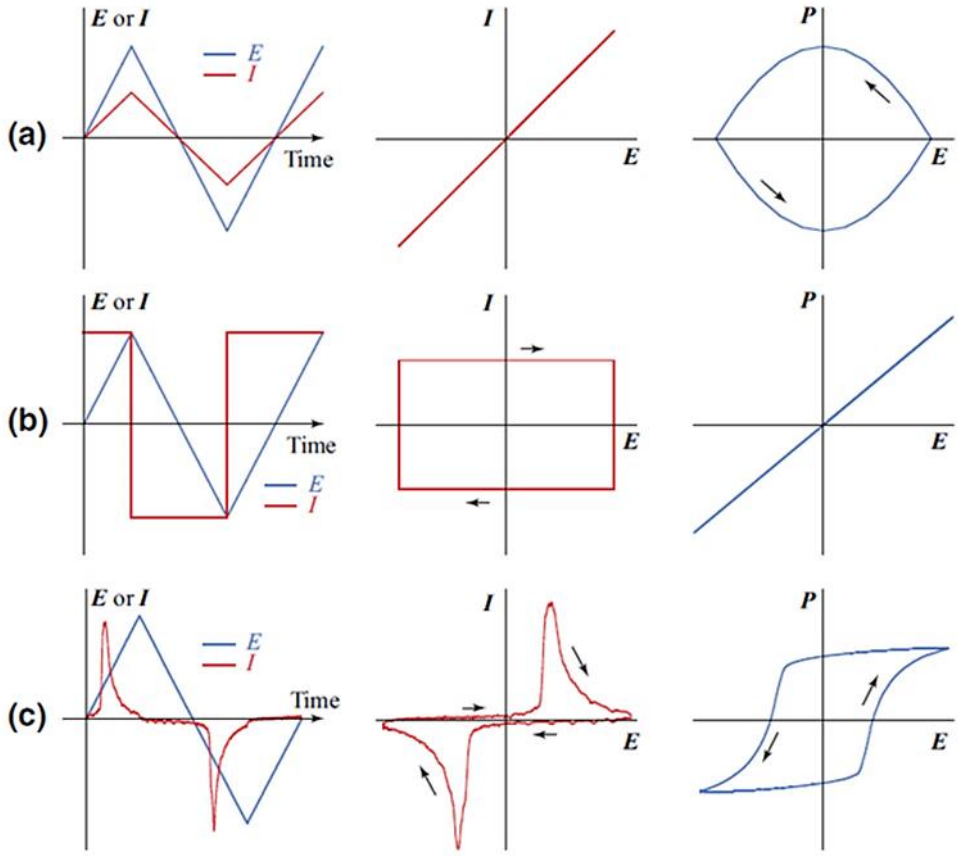

Figure 10 The relationships between electric field (E), current (I), and polarization (P) with respect to ac electric field for (a) a linear resistor, (b) a linear capacitor, and (c) a ferroelectric crystal, respectively.[25]

Figure 10 concisely shows the relationship between three materials having different electric nature in order to understand the behaviour of P-E loops. The term 'linear' used for defining resistors and capacitors in the figure refers to whether the resistance or capacitance alters with respect to the applied electric field. For the linear resistor case, current (I) follows the same phase with electric field (E), resulting in a linear relationship between them and a symmetric rounded P-E loop indicating high conductivity within the sample, as illustrated in Figure 10(a). As for linear capacitor behaviour in Figure 10(b), the current of the capacitor is the differential of E with time; a constant current is obtained with respect to the constantly changing electric field, but alters the sign for the reversal of electric field direction. As can be seen in the I–E curve, a square loop is shown with a clockwise flowing direction and results in a linear P–E loop. Conversely,

ferroelectric materials exhibit completely different behaviour compared to the linear resistor and capacitor, as illustrated in Figure 10(c). As the electric field increases, there are obvious current peaks. These maximum current peaks correspond to a specific electric field observed in ferroelectrics called coercive electric field (E_C) and this E_C is determined by P-E loops where the polarisation (P) rapidly increases. It should be noted that the current peaks do not occur at the maxima of electric field, due to the fact that the current is related to the domain reversal, rather than the conductivity. Only the current maxima resulting from the domain reversal or switching is the sign of ferroelectricity. It can be clearly seen that real hysteresis loops are constructed in this case and always possess an anticlockwise hysteresis between P and E.[25]

For measuring the dielectric properties of a ferroelectric ceramic, the parallel-plate capacitor method is a common one which basically requires a pellet of material between two electrodes to form a capacitor. Capacitance measurement is then carried out to obtain dielectric permittivity under an AC electric field as a function of frequency by taking into account the sample thickness, d and the area of the electrodes, A. This relationship is expressed by the following equation:

$$C = \frac{\varepsilon_r \varepsilon_0 A}{d} \tag{12}$$

A typical dielectric measurement system using the parallel-plate method consists of an LCR meter or impedance analyser.

REFERENCES

1. Moulson, A. J. & Herbert, J. M. *Electroceramics*. **2nd Ed.,** (2003).
2. Riedel, R., Ionescu, E. & Chen, I.-W. in *Ceramics Science and Technology* 3–34 (2008).
3. Dinnebier, R. E. & Billinge, S. J. L. in *Powder Diffraction: Theory and Practice* 1–19 (2008).
4. Jenkins, R. & Snyder, R. L. in *Introduction to X-ray Powder Diffractometry* 47–95 (1996).
5. Dreele, R. B. Von. in *Powder Diffraction: Theory and Practice* 266–281 (2008).
6. Mccusker, L. B., Dreele, R. B. Von, Cox, D. E., Loue È R D, D. & Scardi, P. Rietveld refnement guidelines. *Int. Union Crystallogr. J. Appl. Crystallogr. J. Appl. Cryst* **32,** 36–50 (1999).
7. Toby, B. H. R factors in Rietveld analysis: How good is good enough? *Powder Diffr.* **21,** 67–70 (2006).
8. Cheary, R. W. & Coelho, A. Fundamental parameters approach to x-ray line-profile fitting. *J. Appl. Crystallogr.* **25,** 109–121 (1992).
9. Materlik, G., Rayment, T. & Stuart, D. I. Diamond Light Source: Status and perspectives. *Philos. Trans. R. Soc. A Math. Phys. Eng. Sci.* **373,** (2015).
10. Ladd, M. & Palmer, R. *Structure determination by X-ray Crystallography*. *Springer New York* **5th Ed.,** (2013).
11. Pramanick, A., Damjanovic, D., Daniels, J. E., Nino, J. C. & Jones, J. L. Origins of Electro-Mechanical Coupling in Polycrystalline Ferroelectrics During Subcoercive Electrical Loading. *J. Am. Ceram. Soc.* **94,** 293–309 (2011).
12. Hall, D. A., Steuwer, A., Cherdhirunkorn, B., Mori, T. & Withers, P. J. A high energy synchrotron x-ray study of crystallographic texture and lattice strain in soft lead zirconate titanate ceramics. *J. Appl. Phys.* **96,** 4245–4252 (2004).
13. Hall, D. A. *et al.* Domain switching in rhombohedral PZT ceramics under electrical and mechanical loading. *Mater. Sci. Technol.* **24,** 927–933 (2008).
14. Esteves, G., Fancher, C. M. & Jones, J. L. In situ characterization of polycrystalline ferroelectrics using x-ray and neutron diffraction. *J. Mater. Res.* **30,** 340–356 (2015).
15. Scardi, P. in *Powder Diffraction: Theory and Practice* 376–413 (2008).
16. Gorfman, S. Sub-microsecond X-ray crystallography: Techniques, challenges, and applications for materials science. *Crystallogr. Rev.* **20,** 210–232 (2014).

17. Hoffmann, M. J., Hammer, M., Endriss, a. & Lupascu, D. C. Correlation between microstructure, strain behavior, and acoustic emission of soft PZT ceramics. *Acta Mater.* **49,** 1301–1310 (2001).

18. Daniels, J. E., Finlayson, T. R., Studer, A. J., Hoffman, M. & Jones, J. L. Time-resolved diffraction measurements of electric-field-induced strain in tetragonal lead zirconate titanate. *J. Appl. Phys.* **101,** 094104 (2007).

19. Khansur, N. H. Contrasting strain mechanisms in lead-free piezoelectric ceramics. *PhD Thesis* (2015).

20. Daniels, J. E. & Drakopoulos, M. High-energy x-ray diffraction using the Pixium 4700 flat-panel detector. *J. Synchrotron Radiat.* **16,** 463–468 (2009).

21. Goldstein, J. *et al. Scanning Electron Microscopy and X-Ray Microanalysis*. *Springer New York* (2003).

22. Wu, J. *Advances in Lead-free Piezoelectric Materials*. (Springer, 2018).

23. Soergel, E. Visualization of ferroelectric domains in bulk single crystals. *Appl. Phys. B Lasers Opt.* **81,** 729–752 (2005).

24. Owate, I. O. & Freer, R. Thermochemical Etching Method for Ceramics. *J. Am. Ceram. Soc.* **75,** 1266–1268 (1992).

25. Jin, L., Li, F. & Zhang, S. Decoding the Fingerprint of Ferroelectric Loops: Comprehension of the Material Properties and Structures. *J. Am. Ceram. Soc.* **97,** 1–27 (2014).

26. Stewart, M., Cain, M. G. & Hall, D. Ferroelectric hysteresis measurement & analysis. *NPL Rep. C. 152* 1–57 (1999).

Chapter 3

Research Outputs

Chemical heterogeneity and approaches to its control in $BiFeO_3$-$BaTiO_3$ lead-free ferroelectrics

Ilkan Calisir and David A. Hall

School of Materials, University of Manchester, M13 9PL, Manchester, UK

ABSTRACT

1 mol% MnO_2 was used to improve electrical resistivity of lead-free $0.75BiFeO_3$-$0.25BaTiO_3$ (75BFBT) ferroelectric ceramics; the materials were perovskite structured with major rhombohedral (*R3c*) phase. The method of incorporation of MnO_2 was found to exert a significant influence on the structure, microstructure and electrical properties. Chemical heterogeneity in the form of core-shell grain microstructures was observed when MnO_2 was added into the undoped calcined powder, in contrast to the relatively homogeneous materials that resulted from adding MnO_2 into the precursor oxide mixture prior to calcination. Compositionally graded regions were detected across the grains consisting of a BF–rich core and BF–depleted shell.

The occurrence of core-shell type microstructures led to various characteristic features including a high cubic phase fraction, contrast between ordered ferroelectric domain configurations in the rhombohedral core and the relatively featureless pseudo-cubic shell, constrained ferroelectric domain switching, and two distinct anomalies in dielectric permittivity at temperatures of 485 and 635˚C. The latter features are attributed to separate phase transitions in the relaxor ferroelectric shell and normal ferroelectric core regions respectively. The

application of a thermal quenching procedure caused the formation of ferroelectric domain structures throughout the microstructure and resulted in dramatically enhanced ferroelectric switching behaviour. For example, the remanent polarisation of the as-sintered 75BFBT ceramic increased from 0.06 to 0.31 C m^{-2} after air-quenching. These effects are tentatively attributed to nanoscale phase segregation in the shell region of the as-sintered ceramics, resulting from thermodynamic immiscibility between the BF and BT solid solutions.

1. INTRODUCTION

Bismuth ferrite (BF) and its solid solution systems have been the subject of intensive research, due to its attractive combination of high ferroelectric Curie temperature (~825 °C),[1] high remanent polarisation (~100 μC cm^{-2} in single crystal along the pseudo-cubic $[111]_{pc}$ direction[1] and ~20 μC cm^{-2} in bulk form[2]) and multiferroic behaviour.[1,3] Due to its promising multifunctional properties, considerable research has focused recently on the recognised issues of high leakage current and the synthesis of single-phase $BiFeO_3$ without impurities.[1,3,4]

The origin of high conductivity in $BiFeO_3$ has been a controversial issue, but recent findings have theoretically[5] and experimentally[6–8] confirmed that the conduction mechanism for $BiFeO_3$ synthesised in air (oxygen-rich) is p-type. Based on this observation, the conductivity is attributed to the incorporation of excess oxygen (filling some oxygen vacancies) and the associated formation of electron holes. This can then lead to the conversion of Fe^{2+} ions to Fe^{3+} and Fe^{3+} ions to Fe^{4+}.[8] It was also found that decreasing partial oxygen pressure during synthesis led to a shift from p-type to n-type in $(Bi_{0.5}K_{0.5})TiO_3$–modified $BiFeO_3$.[8] Conversely, for Ca^{2+} (acceptor)-doped $BiFeO_3$ it was found that sintering in a N_2 atmosphere induced a transition from a p-type semiconductor to oxide ion conductor.[7]

According to the binary phase diagram of the Bi_2O_3-Fe_2O_3 system, it has been noted that a stable single pure $BiFeO_3$ phase can be obtained only within a narrow temperature range, which can lead to the formation of secondary phases such as $Bi_2Fe_4O_9$, $Bi_{25}FeO_{39}$, and $Bi_{36}Fe_2O_{57}$.[2,9,10] These reported obstacles have been overcome using various processing methods including mechanochemical synthesis,[2] rapid liquid phase sintering,[11] sol-gel method,[12] microwave synthesis,[13] chemical leaching,[14] annealing under magnetic field[15] *etc.* Furthermore, *site engineering* has been applied to $BiFeO_3$ by partial substitutions of A- and B-site ions in the $BiFeO_3$ perovskite structure,[16] including rare earth ions substituted for Bi^{3+},[17–23] and transition metal ions for Fe^{3+}.[24–28] In addition,

solid solution formation with other ABO_3-type perovskite ceramics leads to binary,[29–34] ternary[35–37] or even quaternary[38] compounds.

Although $BiFeO_3$-$PbTiO_3$ in particular has been reported to show superior properties, rising environmental concerns on the usage of lead-based ceramics[39–41] have led to extensive research on lead-free solid solution combinations. Among them, $BiFeO_3$-$BaTiO_3$ (BF-BT) ceramics have been intensively studied as promising candidates for lead-free, high temperature ceramics. Nonetheless, the main focus of such research was primarily concerned with the magnetic properties due to the observation of weak ferromagnetism at room temperature. Subsequently, the dielectric, ferroelectric and piezoelectric properties have been explored and received considerable attention, particularly for high temperature applications.[37,42]

Despite improvements in the synthesis of single perovskite phase BF-BT ceramics, well-saturated P-E loops and low dielectric loss are rarely reported without any further modification,[30] due to the presence of a relatively high leakage current. Therefore, many researchers have employed additional aliovalent dopants in order to increase its insulation behaviour. Among these, it has been found that a small amount of Mn has a beneficial effect on the electrical properties of $BiFeO_3$-based ceramics.[30,43–47] However, Mn is a transition metal that can exhibit various valence states (Mn^{2+}, Mn^{3+} and Mn^{4+}) depending on the oxygen partial pressure during heat treatment.[48,49]

The influence of Mn on the properties of $BiFeO_3$-based compounds has been systematically studied and it has been concluded that determination of the optimum amount of Mn is crucial, since excessive amounts are found to cause deterioration of the electrical resistivity due to increasing valence fluctuations generating extrinsic oxygen vacancies.[43] Generally it was found that 0.1-0.6 *wt*% MnO_2 addition has a positive effect on increasing the resistivity. However, Mn was incorporated into the compositions in various different ways, including addition to the pre-calcined compositions as a sintering aid,[30,43,50–52] as a substitution on to the Fe-site[11,46] or as an excess addition into other starting precursor powders.[44,53–56] This raises some uncertainty about the origins of the observed variations in the reported ferroelectric (remanent polarisation, coercive field), dielectric properties (relative permittivity, tanδ and T_C), and structural as well as microstructural features.

Although extensive research has been carried out on Mn-doped $BiFeO_3$-$BaTiO_3$, no single study has addressed the issue of which addition route could be the most beneficial in terms of sintering, resistivity, ferroelectric and dielectric properties. Therefore, we aimed to clarify this point by evaluating different Mn-addition strategies. For this study, the $0.75BiFeO_3$-$0.25BaTiO_3$ composition was selected to

be doped with 1 mol% Mn (equivalent to ≈0.3 *wt*%) due to its reported promising properties[30] and major rhombohedral phase existence,[57] which can help to provide a clear indication of the influence of the Mn incorporation route on structural distortions. The doped ceramics exhibited highly insulating behaviour with interesting features, which were found to depend on the doping strategy employed; these included highly saturated or pinched P-E loops, multiple or single peaks in the dielectric permittivity-temperature relationship and homogeneous or heterogeneous microstructure leading to core-shell type grain formation. It is shown that the cooling rate plays a key role in determining the level of chemical heterogeneity and subsequently the functional properties.

2. EXPERIMENTAL PROCEDURES

Undoped and Mn-doped $0.75BiFeO_3$-$0.25BaTiO_3$ (75BFBT) ceramics were synthesized by the conventional solid state reaction method. Bi_2O_3 (99%, Alfa Aesar), Fe_2O_3 (99%, Sigma Aldrich), $BaCO_3$ (99%, Alfa Aesar) and TiO_2 (99%, Fisher Scientific) were used as starting powders for undoped 75BFBT ceramics and MnO_2 (99%, Fluka Chemica) was added as a modifier. 2 mol% Bi_2O_3 excess was added into all compositions to compensate for the loss of this volatile oxide during high temperature heat treatment. This level of bismuth excess was determined as the minimum required to avoid the formation of Fe-rich secondary phases. Two different Mn-incorporation routes were utilised, denoted as *Mn-BC* (1 mol% MnO_2 added as excess in the mixed oxide precursor powders before calcination), *Mn-AC* (1 mol% MnO_2 added as excess in the pre-reacted and milled 75BFBT powder). In the case of Mn-BC, we suppose that the added Mn could be incorporated in solid solution, while for Mn-AC there may be a tendency for segregation in the grain boundary region.

The precursor oxides were weighed according to the required stoichiometric ratios followed by mixing/milling for 24 h using propan-2-ol and yttria-stabilized zirconia media. The milled powders were dried at 85°C overnight followed by calcination at 850°C for 2 h. The calcined powders were milled again for 24 h to reduce the particle size down to the sub-micron region. Polyethylene glycol (PEG) solution as a lubricant was added at a concentration of 2 *wt*% of the dry weight of the powder into the calcined powders to improve compaction behaviour. The calcined powders were uniaxially cold-pressed at around 150 MPa into 8 mm diameter pellets. The pellets were placed on a layer of calcined powder having the same composition to reduce the volatilisation of Bi_2O_3 and to avoid reaction with the supporting alumina plate. Burn-out of the organic additive was achieved by holding at a temperature of 600°C for 1 h, following which the ceramics were sintered at temperatures between 990 and 1050°C for 2-

4 h in air, using a heating and cooling rate of 5°C/min. The *as-sintered* ceramics were annealed at 750°C for 15 min, then directly quenched to room temperature, referred to below as *air-quenched*.

High resolution synchrotron x-ray powder diffraction (SXPD) patterns were recorded on the I11 powder diffraction beamline at the Diamond light source. The crushed powders of samples were placed in a glass capillary tube, and the data were collected at ambient temperature in the 2Θ range of 5−100° using the position sensitive detector (PSD). The x-ray photon wavelength was 0.494951 Å. Rietveld analysis of the data was undertaken using TOPAS *v*5 software. For the refinement, ICSD#15299 and ICSD#67518 were used for *R3c* rhombohedral and *Pm-3m* cubic phase, respectively.

The sintered pellets were ground using 800, 1200, 2500 and 4000 grade SiC paper and then polished with 3, 1 and 0.25 μm diamond paste followed by diluted OP-S silica colloidal suspension. Well-polished samples were chemically etched by immersing into the etchant solution (95% distilled water + 4% HCl + 1% HF) for 5 seconds. Microstructures of as-sintered and air-quenched surfaces were examined using a Philips XL30 FEGSEM equipped with EDS. The average grain size was determined by the linear intercept method over an area of approximately 4400 μm^2 using a multiplication factor of 1.56.[58]

Prior to electrical measurements, the samples were polished to obtain smooth and parallel surfaces. In order to achieve a sufficiently high electric field for the ferroelectric hysteresis measurements, the thickness of the samples was polished down to 0.5 mm. For dielectric and polarisation-electric field (P-E) hysteresis measurements, silver electrode paste (C2000107P3, Gwent Group) was applied on the top and bottom surfaces and then fired at 600°C for 20 minute. For the *air-quenched* ceramics, an air-dried silver paint (AGG3691, Agar Scientific, UK) was applied onto both surfaces of the pellets at room temperature in order to avoid changes in the effects induced by quenching.

Ferroelectric P-E hysteresis measurements were carried out using a function generator (HP 33120A) connected to a Chevin Research HV amplifier to generate the desired high voltage. The samples were subjected to 4 cycles of a sinusoidal electric field with a frequency of 2 Hz. The measured current waveform was integrated numerically over time to yield charge and hence the polarisation was calculated as the surface charge density.[59] Dielectric measurements were carried out at fixed frequencies from 1 to 100 kHz over the temperature range from 25 to 670 °C using a HP 4284A Impedance analyser and a desktop computer which was operated by LabView-based program. The measurements were conducted in air using a heating rate of 2 °C/min.

3. RESULTS and DISCUSSION

3.1 Structural characterisation

Full-pattern Rietveld refinement was performed to determine the crystal structures of undoped and Mn-doped ceramic powders. Figure 1 shows the XRD refinements of the undoped 75BFBT, Mn-BC, Mn-AC and air-quenched Mn-AC, while the crystallographic parameters derived from the refinements are summarized in Table 1. Undoped 75BFBT and Mn-BC ceramics predominantly consist of *R3c* rhombohedral phase with phase fractions of 96.5% and 90.3% respectively, the remainder being cubic *Pm-3m*. For the case of as-sintered and air-quenched Mn-AC, the phase fraction of *Pm-3m* was significantly higher in Mn-AC, indicated by the increase in intensity of the reflection at approximately 12.3 °2θ in Figure 1(c), whilst the *R3c* phase fraction increased from 53.6% to 70% as a result of air-quenching , as shown in Figure 1(d). It is apparent that as a small amount of MnO_2 is added into the calcined composition (Mn-AC), it causes significant structural transformations and the formed phases are also highly sensitive to further thermal treatment procedures such as air-quenching.

By examining the involved cations in order to find the origin of such structural changes induced by Mn, it is considered that Bi^{3+} and Ba^{2+} occupy the A-site, while Fe^{3+}, Ti^{4+} and a small amount of multivalent Mn occupy the B-site of the perovskite structure. These cations have different Pauling's electronegativities and ionic radii. The ionic radii of the B-site ions are reported as Ti^{4+}(0.605 Å), Fe^{3+}(0.645 Å), Mn^{4+}(0.53 Å), Mn^{3+}(0.645 Å) and Mn^{2+}(0.83 Å).[60] The ionic radii of Mn in both 4+ and 3+ valence states are within the range of sizes of Fe^{3+} and Ti^{4+}, which could enter the lattice without distorting the structure. However, the ionic size of Mn^{2+} is relatively large compared to that of Fe^{3+} and Ti^{4+}. Thus, Mn^{2+} could enter into either the A- or B-sites. On the other hand, it has been reported that Mn^{4+} is unstable at high temperatures, therefore the valence state of Mn regardless of starting compound can be considered as a mixture of 3+ and 2+ depending on the oxygen environment.[48]

It is also reported that the incorporation of 25 mol% of $BaTiO_3$ into $BiFeO_3$ causes a slight reduction of the rhombohedral distortion and the presence of a small amount of pseudo-cubic phase.[57] Further additions induce a transformation from rhombohedral to pseudo-cubic relaxor ferroelectric phase over a wide range of composition in the solid solution system due to the large ionic size mismatch and charge difference between Bi^{3+}(1.03 Å) and Ba^{2+}(1.35 Å) at the A-site.[57] Our results also confirm that undoped 75BFBT exhibits a predominantly rhombohedral phase, as depicted in Figure 1(a) and Table 1. The effect of adding Mn ions on the

crystal structure of BF-BT, specifically the transformation from predominantly *R3c* to a mixture of coexisting *R3c* and *Pm-3m* phases, cannot be explained purely on the basis of the ionic substitution. Instead, we interpret this effect as being due to the development of core-shell (rhombohedral-cubic) type microstructures in the Mn-doped ceramics, as discussed further below.

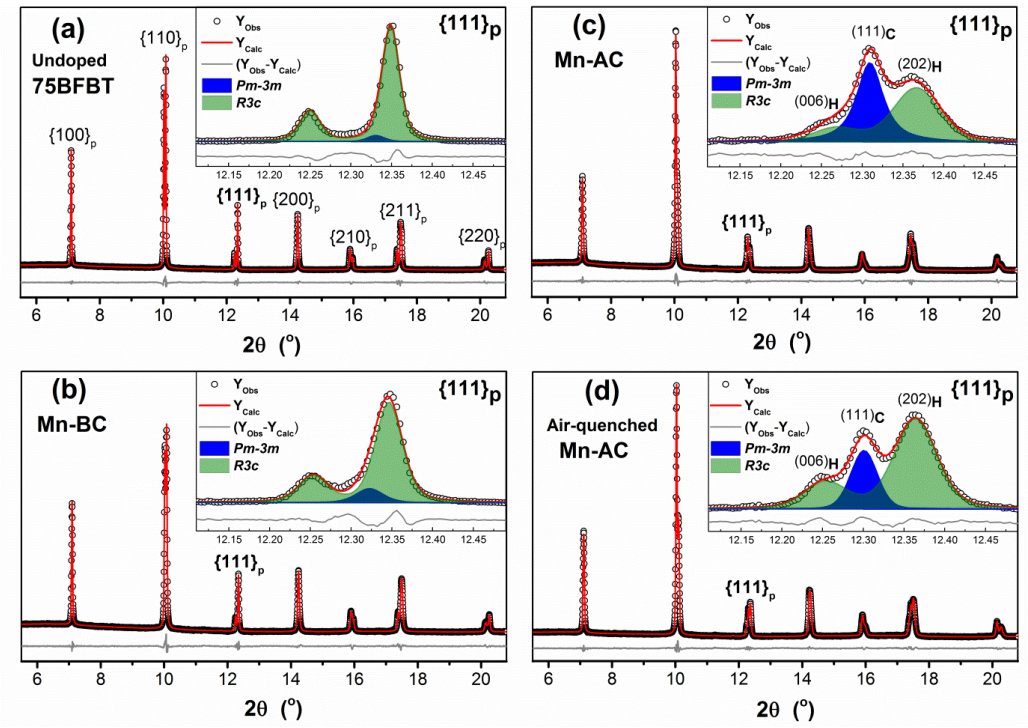

Figure 1 High resolution SXPD patterns of undoped and Mn-doped 75BFBT ceramics. The fitting results of refined structures for **a)** undoped 75BFBT, **b)** Mn-BC, **b)** Mn-AC and **d)** air-quenched Mn-AC ceramics. The insets show the $\{111\}_P$ peak profiles in relation to rhombohedral, *R3c* (the reflection of $(006)_H$ and $(202)_H$ in hexagonal setting), and single (111) reflection of cubic, *Pm-3m*, phases.

For the refinement of the Mn-AC powder, several binary phase models were considered in order to fit the broad asymmetric peaks; the best fitting was achieved by a combination of *R3c* rhombohedral + *Pm-3m* cubic, as noted above. In spite of the improvement relative to the single phase models, broad asymmetry was still present in the peak profiles for certain reflections, which was tentatively attributed to anisotropic strain. To verify this assumption, Stephenson's model[61] was applied to these data during Rietveld refinement and an improved fit was obtained, as can be seen in the insets of Figure 1(c)-(d) for the $\{111\}_P$ peak. Microstructural observations, described in section 3.2 below, indicate the presence of core-shell type grains in the ceramics, which may be the source of the anisotropic strain and the associated peak broadening. It has been suggested that chemical heterogeneity in the form of core-shell structures can introduce internal stresses and lead to broad asymmetric peaks.[62,63]

Table 1: Structural parameters of undoped 75BFBT and Mn-doped ceramics obtained from Rietveld refinement. *Goodness of Fit (*GoF*) is the value of R_{wp}/R_{exp}.

Parameters	**Undoped 75BFBT**		**Mn-BC**		**Mn-AC**		**Air-quenched Mn-AC**	
Phases	*R3c*	*Pm-3m*	*R3c*	*Pm-3m*	*R3c*	*Pm-3m*	*R3c*	*Pm-3m*
Fraction, %	96.5(1)	3.5(1)	90.3(6)	9.7(6)	53.6(5)	46.4(5)	70.(4)	30.0(4)
Unit cell parameters, Å								
a	5.6241(1)	3.9866(2)	5.6245(3)	3.9867(2)	5.6158(6)	3.9932(4)	5.6158(4)	3.9957(3)
c	13.9009(5)	= a	13.8939(8)	= a	13.8784(15)	= a	13.8939(10)	= a
Cell volume, Å^3	380.78(3)	63.363(8)	380.65(5)	63.445(12)	379.05(8)	63.670(2)	379.47(6)	63.792(14)
R-factors								
R_{wp}	3.23		3.26		3.2		3.33	
R_{exp}	1.56		1.59		1.71		1.53	
GoF*	2.07		2.04		1.87		2.18	

Similar observations were made previously by Lennox *et al.*[64] on the basis of neutron diffraction studies on $BiFeO_3$-$KNbO_3$ solid solutions. It was suggested that regions consisting of different A-site and B-site ion ratios, as a consequence of chemical inhomogeneity, can lead to peak broadening. Dolgos *et al.*[65] also reported large thermal parameters in $0.75Bi(Fe_{2/8}Ti_{3/8}Mg_{3/8})O_3$-$0.25BaTiO_3$ for the oxygen and A-site cations which is associated with considerable local strain as confirmed by diffuse scattering in the electron diffraction patterns. Our results are supportive of the argument that Bi:Ba and Fe:Ti:Mn ratios may vary in the core and shell regions resulting in local strain within the grains.

3.2 Microstructure

Figure 2 shows the microstructures of polished surfaces for undoped and Mn-doped 75BFBT ceramics sintered at 990°C for 4 h. The results clearly show that the grain size of 75BFBT can be considerably affected by a small amount of Mn addition. Comparing Figures 2(a) and (b), it is evident that a slight decrease in grain size (from 11.9 to 8.8 μm), with a relatively uniform grain size distribution, was observed for Mn-BC ceramics. This could be attributed to enhanced distribution of Mn when it is added as a precursor powder. On the other hand, systematic studies[44,53,55] show that increasing Mn content above this level

generally causes significant grain growth in $BiFeO_3$-$BaTiO_3$ ceramics and degradation of electrical resistivity.

The incorporation of excess MnO_2, introduced as an additive prior to calcination, in solid solution can be understood in terms of the defect chemistry of the $BiFeO_3$-based system, as follows. Firstly, we should recognise that some loss of bismuth oxide is expected during the high temperature calcination and sintering stages, leading to the formation of bismuth and oxygen vacancies.[8]

$$2Bi_{Bi}^{x} + 3O_O^x \rightarrow 2V_{Bi}^{///} + 3V_O^{\bullet\bullet} + Bi_2O_3(g) \quad (1)$$

This provides a mechanism for the incorporation of excess oxygen, leading to p-type electronic conductivity.

$$2V_O^{\bullet\bullet} + O_2(g) \rightarrow 2O_O^x + 4h^{\bullet} \quad (2)$$

The volatilisation of bismuth oxide during processing is commonly compensated by providing an excess in the starting composition, which was 2 mol% in the present case. For Mn-BC, the reaction of part of the excess bismuth oxide with manganese oxide facilitates the formation of the solid solution during the calcination stage. We assume that the manganese is incorporated in the form of Mn^{3+} or Mn^{2+} due to the instability of Mn^{4+} ions at high temperatures.[49] The former case involves isovalent substitution, while in the latter acceptor-type defects with charge-compensating oxygen vacancies are formed. The overall reactions for isovalent and aliovalent (acceptor-type) incorporation, which include the reduction of Mn^{4+} to either Mn^{3+} or Mn^{2+}, are represented in equations (3) and (4) respectively.

$$2Bi_2O_3 + 4MnO_2 \rightarrow 4Bi_{Bi}^{x} + 4Mn_{Fe}^{x} + 12O_O^x + O_2(g) \quad (3)$$

$$Bi_2O_3 + 2MnO_2 \rightarrow 2Bi_{Bi}^{x} + 2Mn_{Fe}^{/} + 5O_O^x + V_O^{\bullet\bullet} + O_2(g) \quad (4)$$

Subsequently, Mn^{2+} ions can be converted to Mn^{3+} by trapping electron holes,[49] leading to a reduction in p-type electronic conductivity and therefore improved insulation resistance, as observed in many studies.[30,43,53]

$$Mn_{Fe}^{/} + h^{\bullet} \rightarrow Mn_{Fe}^{x} \quad (5)$$

According to the above argument, the incorporation of the added MnO_2 in solid solution requires the presence of excess bismuth oxide (Equations 3 and 4). For Mn-AC, the reaction between the bismuth and manganese oxides could be hindered by the volatilisation of bismuth oxide during sintering, since there was no available opportunity for reaction during a separate calcination stage. In such a case, the incorporation mechanism for additional MnO_2 must involve the formation of additional bismuth and oxygen vacancies, which would reduce the

solubility dramatically. The corresponding isovalent and aliovalent (acceptor-type) incorporation mechanisms are represented in equations (6) and (7) respectively.

$$4MnO_2 \rightarrow 4V_{Bi}^{///} + 4Mn_{Fe}^{x} + 6O_O^x + 6V_O^{\bullet\bullet} + O_2(g) \quad (6)$$

$$4MnO_2 \rightarrow 4V_{Bi}^{///} + 4Mn_{Fe}^{/} + 4O_O^x + 8V_O^{\bullet\bullet} + 2O_2(g) \quad (7)$$

In contrast to the case of Mn-BC, grain growth was greatly suppressed in the Mn-AC ceramic, as illustrated in Figure 2(c); the average grain size was determined as 3.6 μm. This could be associated with segregation of Mn near grain boundaries, creating pinning centres that restrict grain growth during sintering. Therefore, the inhibited grain growth and associated formation of core-shell structures for Mn-AC can be understood on the basis of the reduced solubility of manganese oxide and its effect on grain growth. It was also previously reported that the grain growth can be hindered by the excess Mn accumulated at the grain boundaries, when MnO_2 is added into pre-calcined compositions followed by sintering.[43,47] In the present study, it was found that increasing the milling time for the Mn-AC powder had little effect on the microstructure of the sintered ceramic, indicating that the production of finer particles could not induce a significant improvement in chemical homogeneity when the MnO_2 was added after the initial calcination reaction.

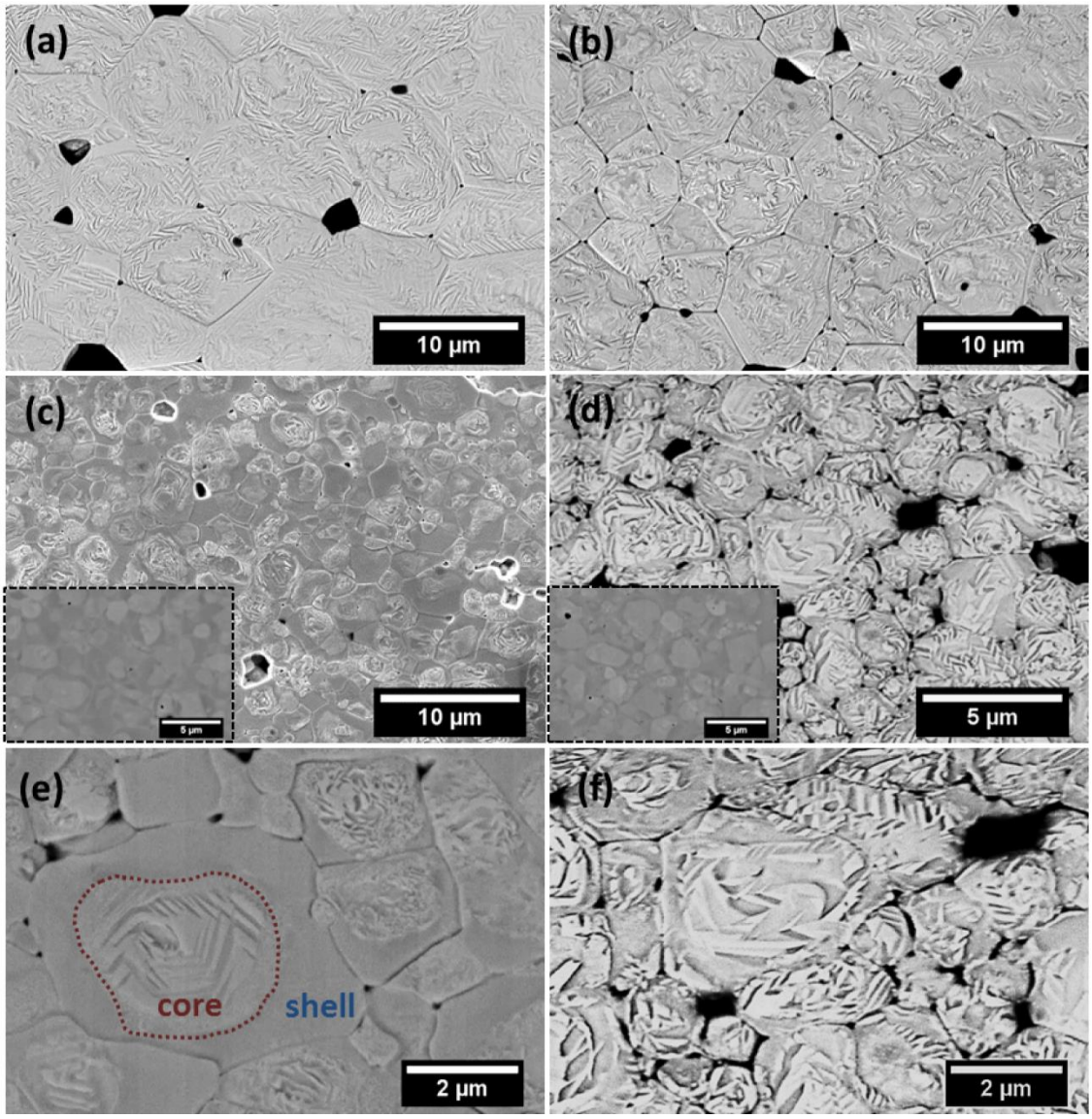

Figure 2 SEM images of chemically etched surfaces of **a)** undoped 75BFBT, **b)** Mn-BC, **c)** Mn-AC ceramics and **d)** air-quenched Mn-AC. Inset images in **(c)** and **(d)** show non-etched sections of the as-sintered and air-quenched ceramics under backscattered imaging mode in SEM (scale bar of inset image is 5 µm). Images **e)** and **f)** illustrate expanded views of core-shell structure in Mn-AC and widespread domain structures in air-quenched Mn-AC.

It is evident that chemically etched undoped 75BFBT and Mn-BC ceramics display clear and homogeneous domain distributions across the grains as seen in Figure 2(a) and (b), whilst the grains of Mn-AC seem partially etched, as shown in Figure 2(c) and (e). A heterogeneous domain distribution was also observed, with domains occurring only at the core of grains. This was not observed in Mn-BC or undoped ceramic. It was first thought that this effect could be due to the artefacts of chemical etching; therefore, in order to eliminate the etchant effect, the surface was examined without any etching as shown in the inset of Figure 2(c). In Mn-AC ceramics the greyscale contrast of the SEM micrographs, being

related to the average atomic numbers, indicated the occurrence of microscale chemical segregation in the form of a core shell structure.

Prior to discussion of elemental analysis relating to the observed elemental micro-segregation, it is worth comparing the as-sintered (Figures 2(c-e)) and air-quenched (Figure 2(d-f)) microstructures for Mn-AC. It is evident that the domain distributions across the grains in the quenched Mn-AC are relatively more homogeneous in comparison with the as-sintered case. It should be noted that both samples were mounted on the same resin mould and etched simultaneously in order to prevent any etching-related microstructural variations. Therefore, it is confirmed that the chemical heterogeneity, which leads to the formation of core-shell type grain structures in the ceramics, is modified by air-quenching. The development of more homogeneous ferroelectric domain structures, achieved by quenching in Mn-AC, may also be responsible for improved ferroelectric properties, as discussed in section 3.4 below.

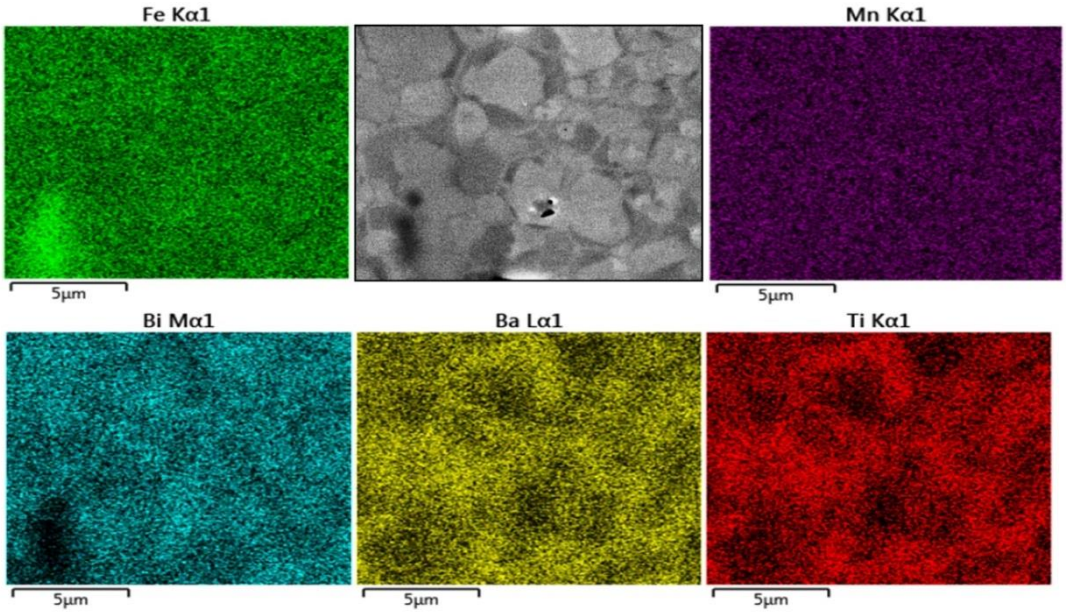

Figure 3 The SEM-EDS elemental mapping results of Mn-AC ceramics sintered at 1050°C for 2h exhibiting core-shell grains.

The SEM-Energy Dispersive Spectroscopy (SEM-EDS) elemental mapping results of non-etched, as-sintered Mn-AC ceramics are illustrated in Figure 3. It can be clearly seen that Ba and Ti signals are weaker in the brighter regions of the SEM image, associated with the grain cores, under secondary electron mode (also confirmed for backscattered electron imaging mode, Figure S1 in the supporting information, Appendix I). Conversely, Bi and Fe elements exhibited a slightly increased intensity in the same brighter areas. The results obtained for the Mn distribution were relatively noisy and uninformative due to the low concentrations. These results indicate that the observed core-shell like structures

in Mn-AC are associated with the micro-segregation of Ba and Ti elements into the shell regions, while Bi and Fe are more concentrated in the core regions. A small amount of Fe-rich secondary phase was also identified, which has been reported in other $BiFeO_3$–based ceramics,[2,25] as highlighted by the Fe elemental map. It should be noted that the SEM-EDS studies were performed on the sample with a relatively short measurement time (1 min.) in order to avoid the volatilisation of Bi due to irradiation.

It was suggested above that when MnO_2 is added into the calcined powder, for Mn-AC, it accumulates in the grain boundary region and can inhibit grain-growth. Therefore, the formation of the core-shell structure may be indirectly linked to Mn addition since the ratio of shell thickness to grain size will be larger when the grain size is smaller. In previous work, the formation of core-shell microstructures was attributed to either kinetic or thermodynamic factors.[66] For the former case, it can be argued that the $BiFeO_3$-rich grain cores are formed first due to the higher reactivity of the constituent oxides, with the $BaTiO_3$-rich shell being incorporated at a later stage of sintering. Such a situation is supported by the observation that the core-shell structure is favoured when grain growth is suppressed. The presence of MnO_2 has the effect of retarding grain growth and interferes with chemical homogenisation during sintering. Hence, we suppose that the formation of the core-shell structure is driven by kinetic factors related to differences in reactivity[66,67] and/or diffusivity of the oxide components.[68]

Thermodynamic immiscibility in the $BiFeO_3$-$BaTiO_3$ system could also play a role in modifying the structure and resulting properties of the pseudo-cubic shell phase. During slow cooling, the presence of a region of immiscibility would provide a driving force for chemical segregation that becomes more pronounced as the temperature is reduced.[38,69] This could lead to nanoscale chemical heterogeneity in the shell regions after slow cooling. The effect of air quenching can be understood on the basis that such nanoscale phase separation is avoided or reduced, providing that the quenching temperature lies near to or above the region of immiscibility.

3.3 Dielectric Properties

The temperature dependence of dielectric permittivity, ε_r and loss, tanδ, as a function of frequency for Mn-doped 75BFBT ceramics is illustrated by the results presented in Figure 4. It is evident that the Mn-BC ceramic exhibits a relatively sharp peak in ε_r at 570 ^oC, which is characteristic of a conventional ferroelectric and indicates the Curie temperature, T_C, corresponding to the transition from the

ferroelectric to paraelectric state on heating. Both the permittivity and loss appeared to increase at temperatures above 600 °C, particularly when measured at low frequencies; these effects are attributed to increasing electrical conductivity and the associated space-charge polarisation.[70] For Mn-AC ceramics, the ε_r–T results measured at 100 kHz indicate an increase in T_C to approximately 635 °C. Furthermore, an additional frequency-dependent dielectric peak became apparent at lower temperatures (350 to 500 °C), which is characteristic of a relaxor ferroelectric contribution.

We propose that the unusual dielectric behaviour of the Mn-AC ceramic is a direct consequence of the core-shell microstructure, since it is anticipated that the core and shell regions will exhibit different types of thermally-induced ferroelectric phase transformations, both of which contribute to the overall measured dielectric response. It was shown in section 3.2 above that the core and shell regions in the Mn-AC ceramic are either $BiFeO_3$-rich or $BiFeO_3$-depleted, respectively. In a previous study, it was found that BF-BT ceramics with relatively high BT contents tend to exhibit more diffuse phase transitions.[71,72] Therefore, the low-temperature peak in dielectric permittivity can be tentatively attributed to the contribution from the shell region. The frequency-dependent behaviour of this contribution is consistent with the presence of polar nano-regions and a relaxor ferroelectric character. The presence of a pseudo-cubic phase (Figure 1(c)) and a relatively featureless shell microstructure (Figure 2(e)) provide further evidence to support this argument, since both of these points to the presence of polar nanoregions having pseudocubic symmetry in the shell region. The slight increase in T_C, from 570 to 635 °C, for the higher temperature dielectric peak is consistent with a contribution from the ferroelectric core region, within which the BF-content for Mn-AC is enhanced relative to Mn-BC.

In previous studies, Kiyanagi *et al.*[32] suggested that the observed broad relaxation in dielectric permittivity for BF-BT solid solutions is related to influence of a cubic phase coexisting with the rhombohedral phase. This proposition was supported by Rietveld analysis of XRD data and verified by Ozaki's TEM investigation.[73] In other reports, the occurrence of multiple anomalies in the ε_r –T relationships for $BiFeO_3$-based solid solutions have been attributed to the influence of polymorphic phase transitions,[35] magnetic-electric dipole interactions,[1,74] depolarisation processes,[30] Maxwell-Wagner relaxation[75] and thermodynamic immiscibility of two ferroelectric phases during sintering.[38,69] The development of chemical heterogeneity, in the form of core-shell microstructures, introduces further complexity in the processing-structure-property relationships of such materials but also provides further opportunities for controlling their functional properties.

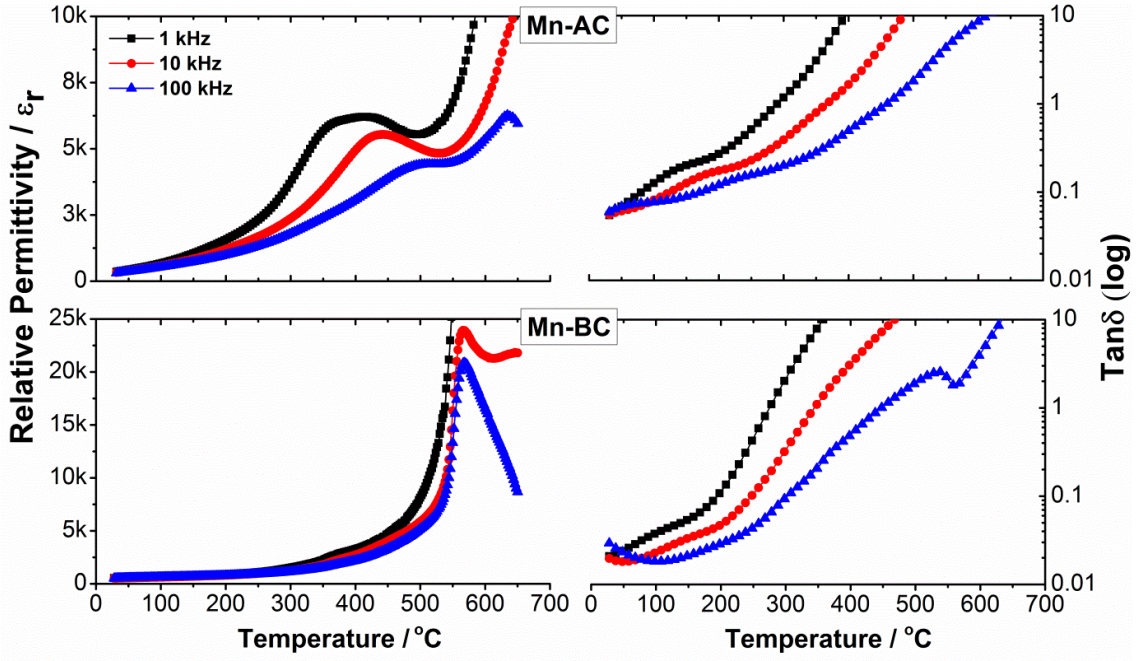

Figure 4 ε_r –T and tan δ–T relationships for Mn-AC and Mn-BC ceramics as a function of frequency.

The influence of air-quenching on the dielectric properties of the Mn-AC ceramics is illustrated in Figure 5(a), which compares the ε_r–T relationships of the as-sintered and air-quenched ceramics. For the Mn-AC ceramic, the main effect of air-quenching was an enhancement of the low-temperature shoulder on the dielectric peak, which developed into a clearly defined second peak. The frequency dispersion of the lower-temperature dielectric peak (represented by ΔT_{Max}) was also reduced after quenching, as shown in Figure 5(b) and Table 2. These results demonstrate that air-quenching had a profound impact on the structure of the shell and is consistent with the transformation from nanopolar to conventional long-range ordered ferroelectric state. The influence of quenching on the ferroelectric ordering within the shell region could be explained by the presence of a region of thermodynamic immiscibility, as noted above in section 3.2. Further studies using high resolution TEM are necessary to establish whether evidence can be found to identify changes in nanoscale chemical segregation associated with variations in cooling rate.

Table 2. Transition temperatures for the corresponding regions of T_{High} and T_{Low} in the as-sintered and air-quenched (15 min and 21 h) Mn-AC ceramics**.** The degree of frequency dispersion was given based on the formula of $\Delta T_{Max} = (T_{Max}^{100\ kHz} - T_{Max}^{1\ kHz})$.

	As-sintered	**Air-Quenched**	
	Sintering condition	*Holding time at 750°C*	
	990°C-4 h	15 min	21 h
T_{Low} at 100 kHz	482°C	484°C	510°C
T_{High} at 100 kHz	635°C	639°C	-
ΔT_{Max} for T_{Low}	102°C	33°C	25°C

The occurrence of two strong dielectric anomalies in the ε_r–T plot for the air-quenched Mn-AC ceramic indicates that the underlying chemical heterogeneity, in the form of the core-shell microstructure, is still present after quenching. To verify the stability of the chemical heterogeneity associated with the core-shell structure, the annealing time at 750°C was increased to 21 h, followed by air-quenching. The results, presented in Figure 5(c), show that the two dielectric anomalies largely merged into one broad peak although the inflection in the ε_r–T curve around 630 °C suggests that the underlying contribution from the core is still present. Furthermore, microstructural examination suggested that the core-shell features still persisted after annealing for 21 h, as illustrated in Figures S2 and S3 (Appendix I).

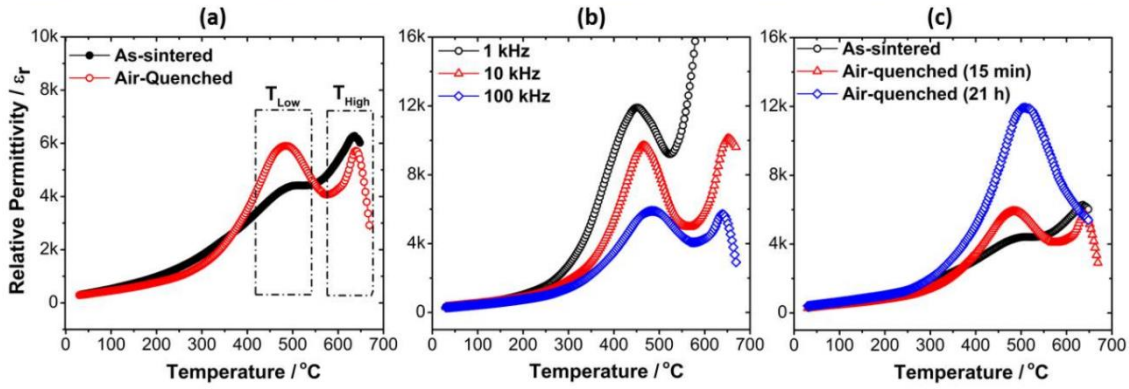

Figure 5 ε_r –T relationships for **a)** as-sintered and air-quenched Mn-AC at 100 kHz **b)** air-quenched Mn-AC at various frequencies **c)** as-sintered Mn-AC samples quenched after annealing at 750°C for 15 min. and 21 h, measured at 100 kHz.

The significant alteration in the ε_r–T characteristics indicates that some inter-diffusion of core and shell phases might have occurred during the extended

annealing procedure. On the other hand the pronounced frequency-dependence of ε_r and tanδ in the high temperature region, which are attributed to the effects of increasing electrical conductivity and associated interfacial (space-charge) polarisation mechanisms, could offer an alternative explanation. In this case it may be suggested that the apparent increase in permittivity is actually a result of further volatilisation of bismuth oxide during annealing (Equation 1), which could increase the p-type electronic conductivity according to equation 2. Calculations of the equivalent AC conductivity, σ_{AC}, in the high temperature region indicate that the conductivity was reduced after quenching but increased slightly for the 21 h-annealed sample, as illustrated in Figure S4 (Appendix I). Therefore, we suppose that the increase in the dielectric peak height is primarily due to partial inter-diffusion of the core and shell phases during annealing, although the influence of bismuth volatilisation during annealing cannot be completely discounted. Further studies, for example involving electrical impedance measurements at high temperatures, would help to clarify this point.

3.4 Ferroelectric Properties

It is commonly reported that $BiFeO_3$-$BaTiO_3$ ceramics prepared in the absence of additional dopants tend to display rounded ferroelectric hysteresis loops, indicating poor insulation behaviour and high dielectric loss.[30,76] On the other hand, well-saturated hysteresis loops of Mn-doped 75BFBT have been reported in several studies.[30,44,55] In the present work, we observed near-rectangular, tilted and/or constricted P-E hysteresis loops for Mn-doped 75BFBT ceramics, depending on the processing methods and sintering conditions. Representative P-E hysteresis loops are illustrated in Figure 6(a), while the loop parameters are summarised in Table 3. The rounded P-E loops obtained for undoped 75BFBT and excessive MnO_2 (3 mol% MnO_2 added before calcination) doped compositions are also presented in Figure S5 (see the Appendix I) for comparison.

It is evident that the shape of the P-E loop for Mn-AC was unsaturated when sintered at relatively low temperatures, while a well-saturated P-E loop with a remanent polarisation value, P_r, of 0.27 C m^{-2} was obtained for Mn-BC ceramics under the same conditions. On increasing the sintering temperature, a constriction became apparent in the P-E loops of Mn-AC, suggesting the occurrence of an inhibited domain switching behaviour; similar effects were reported previously in $BiFeO_3$ ceramics.[77] The J-E loops for Mn-AC also exhibited multiple broad switching peaks, in contrast to the single sharp peaks of Mn-BC (Figure S6, Appendix I). On the other hand, a gradual decrease in the remanent polarisation of Mn-BC with increasing sintering temperature is attributed to the volatilisation of bismuth oxide, leading to the formation of Fe-rich secondary

phases and a reduction in density (from 97 to 92%). It should be noted that sintering above 1050°C caused a reaction with the alumina support plate, which precluded the use of sintering procedures at temperatures above this level.

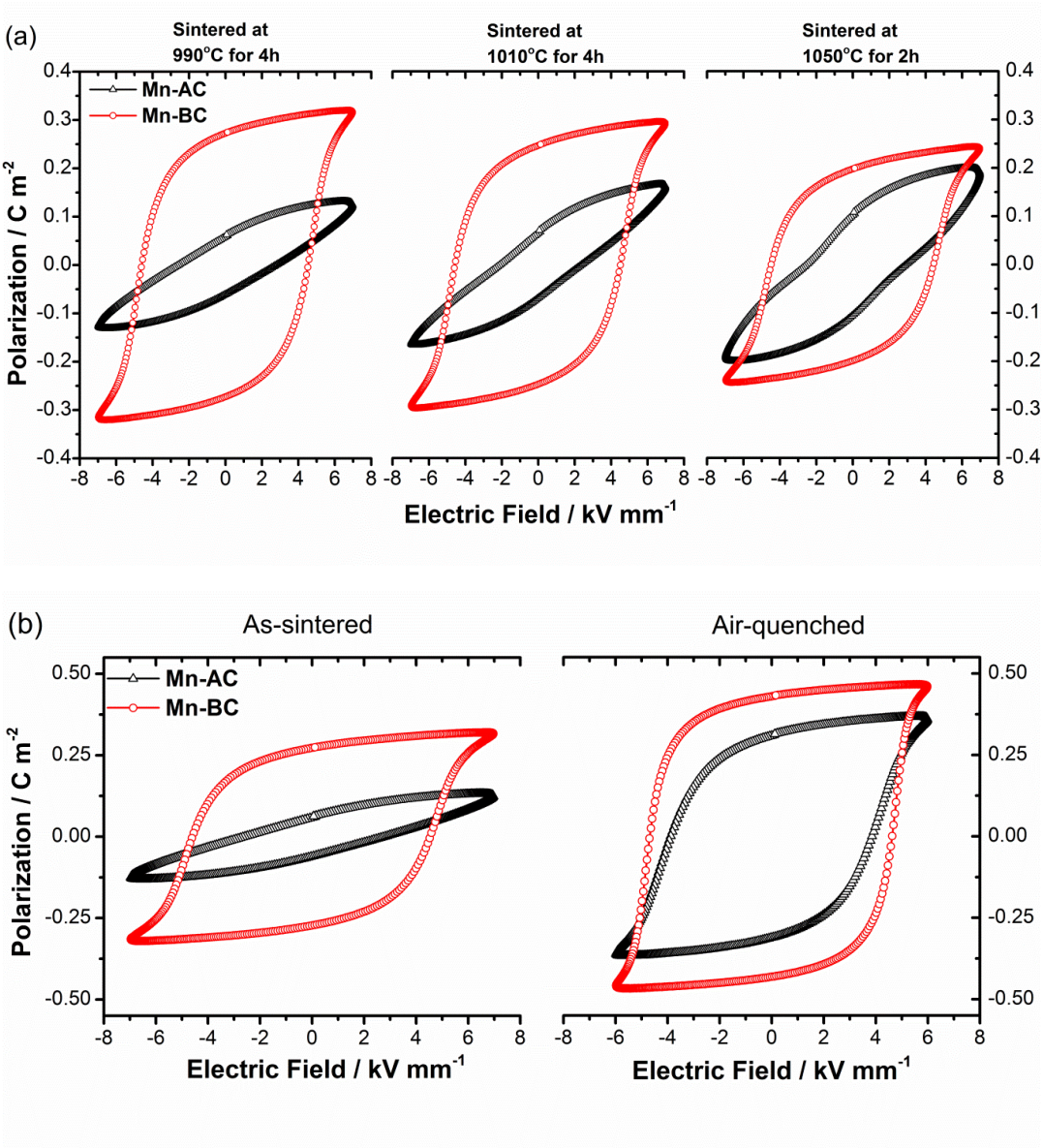

Figure 6 a) Ferroelectric P-E hysteresis loops Mn-AC and Mn-BC ceramics with increasing sintering temperature, **b)** P-E loops of as-sintered (sintered at 990°C for 4h) and air-quenched (annealed at 750°C for 15 min then air-quenched) Mn-doped ceramics.

The occurrence of tilted and/or constricted P-E loops in ferroelectric ceramics can be attributed to several factors[78,79] including domain wall pinning due to oxygen vacancy-cation defect dipoles with related ageing effects,[80,81] the presence of antiferroelectric phases[82,83] or, as reported recently, reversible electric field-induced relaxor ferroelectric to ferroelectric transformations.[84] For undoped

$BiFeO_3$ ceramics, it is commonly reported that the constriction phenomenon is associated with 'domain wall pinning' by defect dipoles.[77,85]

Several methods have been reported in the literature to identify the mechanisms responsible for such distorted hysteresis loops, including studies of functional property variations after poling or thermal annealing ('ageing' effects),[86,87] application of a continuous cyclic electric field (field-forced 'deaging'),[77,87] poling at high temperature and thermal quenching. In the present work, it was found that continuous cycling under a high AC electric field (8kV/mm), either at room temperature or at an elevated temperature of 130°C, did not cause any significant changes in the constricted P-E loops. Therefore, it seems unlikely that a domain wall pinning effect caused by dipolar defect associates could be responsible for such restricted and reversible ferroelectric switching behaviour.

Table 3. Summary of measured ferroelectric P-E loops parameters in the as-sintered and air-quenched Mn-BC and Mn-AC ceramics including remanent polarisation P_r, spontaneous polarisation P_s, and coercive field E_c.

	Sintering conditions			**Air-quenching**
Mn-AC	990°C-4h	1010°C-4h	1050°C-2h	*(from annealing at 750°C-15 min)*
P_r ($C\ m^{-2}$)	0.06	0.07	0.11	0.31
P_s ($C\ m^{-2}$)	0.13	0.17	0.20	0.37
E_c ($kVmm^{-1}$)	2.81	2.46	2.98	3.85
Mn-BC				
P_r ($C\ m^{-2}$)	0.27	0.25	0.22	0.43
P_s ($C\ m^{-2}$)	0.32	0.3	0.26	0.47
E_c ($kVmm^{-1}$)	4.59	4.58	4.53	4.63

On the basis of the microstructural observations in section 3.2 above, we can propose an additional mechanism to restrict ferroelectric domain switching, which has its origin in the core-shell type phase microsegregation, particularly

for $BiFeO_3$-rich solid solutions. Due to the compositional variations over the grain, taking the form of core and shell regions, two different solid solutions exist, which have different dielectric and ferroelectric properties. The core region is $BiFeO_3$-rich and exhibits a ferroelectric rhombohedral *R3c* structure while the shell region is $BaTiO_3$-rich and exhibits a pseudo-cubic structure, presumably with relaxor ferroelectric characteristics.[32,72]

One possible explanation is that the reorientation of macroscopic ferroelectric domains in the core is constrained elastically by the nanodomain-structured shell, giving rise to a largely reversible domain switching behaviour. As the high electric field is applied to the core-shell type grains, the macrodomains in the core, which are assumed to be a predominantly rhombohedral structure due to the $BiFeO_3$-rich phase, tend to switch along the electric field direction, resulting in a partial polarisation switching within the grain. However, due to elastic constraint of the core by the shell, the domain switching is partially suppressed giving rise to gradual changes in polarisation over a wide range of electric field strength rather than at a distinct coercive field level. The partially poled core is subject to residual stress upon removal of the electric field, which leads to reversal of the domain switching.

On the other hand, it should be recognised that the shell is likely to contain nano-sized domains, or polar nanoregions (PNRs), which is a signature of relaxor ferroelectric-type materials.[88–90] In view of recent studies on electric field-induced phase transformations in lead-free relaxor ferroelectrics,[84] an alternative explanation for the reversible polarisation switching behaviour can be proposed in which changes in polarisation occur predominantly in the shell region due to electric field-induced relaxor ferroelectric to ferroelectric phase transformations. In this case, the active shell region would be subject to elastic constraint by a relatively inactive $BiFeO_3$-rich ferroelectric core having a high coercive field.

Therefore, the underlying mechanism is most likely based on heterogeneous ferroelectric switching behaviour within the shell and core regions, but at present it is not yet possible to identify which of these is the most active. Elastic interactions between the shell and the core give rise to predominantly reversible ferroelectric switching behaviour. It was reported by Liu *et al.*[91] that the strain and polarisation mismatch can also induce lateral domain nucleation at the interface of the core and shell in $0.75Bi_{0.5}Na_{0.5}TiO_3$-$0.25SrTiO_3$ ceramics. The occurrence of both inter-granular and intra-granular stresses could play an important role in the electro-mechanical fatigue behaviours of these core-shell structured materials, in addition to their influence on the polarisation- and strain-electric field relationships.

The core-shell type microstructure described here for $BiFeO_3$-$BaTiO_3$ ceramics has particular interest due to its influence on the reversibility of the polarisation switching behaviour and the electric field-induced strain. Recently, this type of microstructure has been reported in other Bi-based ferroelectrics.[66,91,67,92] In the case of $0.75Bi_{0.5}Na_{0.5}TiO_3$-$0.25SrTiO_3$, a large unipolar strain output of 0.3% at 4 kV mm^{-1} was attributed to the effects of reversible electric field-driven phase transformations in the shell region. On the other hand, to our knowledge core-shell microstructures have not been reported previously in $BiFeO_3$-$BaTiO_3$ ceramics.

In view of the previous studies on the influence of cooling rate on BF-based ceramics, we performed thermal quenching of the ceramics in air. The influence of such a procedure on the ferroelectric domain switching behaviour is illustrated by the P-E hysteresis loops shown in Figure 6(b). It is evident that quenching greatly improved the polarisation switching behaviour of the ceramics; P_r values of 0.06 and 0.31 C m^{-2} were obtained for the as-sintered and quenched Mn-AC ceramics respectively. The observation of macro-sized ferroelectric domains throughout the grains in the air-quenched Mn-AC specimen, illustrated in Figure 2(f), is directly associated with the enhancement in polarisation switching behaviour. At first sight, thermal quenching appears to eliminate the formation of core-shell structures based on the domain structures that are evident in the micrograph of the chemically-etched Mn-AC ceramic. However, microstructural examination of the air-quenched Mn-AC sample before etching revealed that the chemical inhomogeneity is still present, as shown in Figure S1 (see the Appendix I)). The appearance of domains in the shell region for the air-quenched ceramic, in contrast to the lack of macro-domains in the case of the as-sintered material, indicates differences in ferroelectric ordering within the shell. With slow cooling (as-sintered), the shell tends to be pseudocubic with relaxor ferroelectric nature, while air-quenching transforms the shell into a long range-ordered ferroelectric state which is coherent with the core. Further evidence to support this argument was presented in the section 3.3 above.

It is also worth noting that fast cooling has been reported widely in processing of $BiFeO_3$-based solid solutions as a means to enhance their ferroelectric and piezoelectric properties; the underlying mechanisms are often unclear but usually attributed to ordering of charged defects.[77,93–95] In a recent study by Kim *et al.*[93] on the influence of cooling rate on the properties of undoped $0.75BiFeO_3$-$0.25BaTiO_3$, the beneficial effects of fast cooling procedures were attributed to the influence of oxygen vacancies on the rhombohedral distortion and the transformation to an intermediate orthorhombic phase at high temperatures. In the present case, it is argued that the changes in ferroelectric behaviour are most

likely to be associated with nanoscale phase separation, although further evidence (e.g. from TEM studies) is required to support this proposal.

4. CONCLUSIONS

Lead-free $0.75BiFeO_3$-$0.25BaTiO_3$ ferroelectric ceramics were modified by the addition of 1 mol% MnO_2 into either precursor mixed oxide powders (Mn-BC) or undoped calcined powder (Mn-AC). The former incorporation method (Mn-BC) yielded chemically homogeneous materials with saturated P-E ferroelectric hysteresis loops, having a P_r/P_s ratio of 0.84, and a single peak in the dielectric permittivity-temperature relationship indicating a Curie point of approximately 570°C. In contrast, the latter method (Mn-AC) led to the formation of chemically heterogeneous core-shell type microstructures, with constricted P-E hysteresis loops, showing dramatically reduced P_r values and two dielectric anomalies associated with separate phase transitions in the core and shell regions. The temperatures of the peaks in dielectric permittivity were approximately 635 and 480 °C, which are attributed to phase transitions in the core and shell regions respectively. The observation of constricted P-E loops for the Mn-AC BF-BT ceramics is attributed to heterogeneous polarisation switching behaviour in the rhombohedral core and pseudo-cubic shell regions, combined with the effects of elastic constraint. Further work is required to determine which of these regions exhibits the more active polarisation switching characteristics.

The formation of the core-shell structure is attributed to kinetic factors and differences in reactivity during sintering, with the $BiFeO_3$-rich core forming initially and the $BaTiO_3$-rich shell forming at a later stage. Thermodynamic immiscibility between the $BiFeO_3$ and $BaTiO_3$ solid solutions could also play an important role, leading to further nanoscale segregation in the shell region during cooling. Quenching of the BF-BT ceramics in air from a temperature of 750 °C led to significant improvements in ferroelectric switching behaviour. The effects of such a procedure were particularly pronounced for the Mn-AC materials, leading to more clearly-defined peaks in the dielectric permittivity-temperature relationship and the appearance of ferroelectric domain structures within the shell region.

The results of the present study suggest that control of chemical heterogeneity in BF-BT ceramics by manipulation of processing methods and heat treatment procedures could lead to intriguing changes in the electro-mechanical properties associated with different types of ferroelectric switching behaviour. Further investigations of multiferroic/magnetoelectric properties are also warranted as a

result of the formation of the multiferroic $BiFeO_3$ phase grain core surrounded by the ferroelectric $BaTiO_3$ solid solution.

Acknowledgements

We thank Diamond Light Source for access to beamline I11 (proposal number EE14061) that contributed to the results presented here. The assistance of Dr Sarah Day and Prof Chiu Tang is gratefully acknowledged. I. Calisir thanks the National Education of Turkish Republic for financial support throughout his PhD.

5. REFERENCES

1. Catalan, G. & Scott, J. F. Physics and Applications of Bismuth Ferrite. *Adv. Mater.* **21,** 2463–2485 (2009).
2. Rojac, T. *et al.* $BiFeO_3$ Ceramics Processing, Electrical, and Electromechanical Properties. *J. Am. Ceram. Soc.* **97,** 1993–2011 (2014).
3. Wang, L., Yang, C.-H. & Wen, J. Physical Principles and Current Status of Emerging Non-Volatile Solid State Memories. *Electron. Mater. Lett.* **11,** 505–543 (2015).
4. Ortega, N., Kumar, A., Scott, J. F. & Katiyar, R. S. Multifunctional magnetoelectric materials for device applications. *J. Phys. Condens. Matter* **27,** 23pp (2015).
5. Zhang, Z., Wu, P., Chen, L. & Wang, J. Density functional theory plus U study of vacancy formations in bismuth ferrite. *Appl. Phys. Lett.* **96,** (2010).
6. Schrade, M., Masó, N., Perejón, A., Pérez-Maqueda, L. A. & West, A. R. Defect chemistry and electrical properties of $BiFeO_3$. *J. Mater. Chem. C* **5,** 10077–10086 (2017).
7. Masó, N. & West, A. R. Electrical properties of Ca-doped $BiFeO_3$ ceramics: From p-type semiconduction to oxide-ion conduction. *Chem. Mater.* **24,** 2127–2132 (2012).
8. Wefring, E. T., Einarsrud, M. & Grande, T. Electrical conductivity and thermopower of (1 - x) $BiFeO_3$ - $xBi_{0.5}K_{0.5}TiO_3$ (x = 0.1, 0.2) ceramics near the ferroelectric to paraelectric phase transition. *Phys. Chem. Chem. Phys.* **17,** 9420–8 (2015).
9. Selbach, S. M., Einarsrud, M. & Grande, T. On the Thermodynamic Stability of $BiFeO_3$. *Chem. Mater.* **21,** 169–173 (2009).

10. Valant, M., Axelsson, A. & Alford, N. Peculiarities of a Solid-State Synthesis of Multiferroic Polycrystalline $BiFeO_3$. *Chem. Mater.* **19,** 5431–5436 (2007).

11. Kumar, M. & Yadav, K. L. Rapid liquid phase sintered Mn doped $BiFeO_3$ ceramics with enhanced polarization and weak magnetization. *Appl Phys Lett* **91,** (2007).

12. Suresh, P. & Srinath, S. Effect of synthesis route on the multiferroic properties of $BiFeO_3$: A comparative study between solid state and sol-gel methods. *J. Alloys Compd.* **649,** 843–850 (2015).

13. Reddy, V. R. *et al.* Reduced leakage current of multiferroic $BiFeO_3$ ceramics with microwave synthesis. *Ceram. Int.* **40,** 4247–4250 (2014).

14. Kumar, M. M., Palkar, V. R., Srinivas, K. & Suryanarayana, S. V. Ferroelectricity in a pure $BiFeO_3$ ceramic. *Appl. Phys. Lett.* **76,** 2764–2766 (2000).

15. Zhang, S., Ma, Y., Awaji, S. & Watanabe, K. Effects of high magnetic field annealing on microstructure and multiferroic properties of $Bi_{1-x}La_xFeO_3$ ceramics. *Ceram. Int.* **42,** 18785–18790 (2016).

16. Yang, C., Kan, D., Takeuchi, I., Nagarajan, V. & Seidel, J. Doping $BiFeO_3$: approaches and enhanced functionality. *Phys. Chem. Chem. Phys.* **14,** 15953–15962 (2012).

17. Walker, J. *et al.* Temperature dependent piezoelectric response and strain–electric-field hysteresis of rare-earth modified bismuth ferrite ceramics. *J. Mater. Chem. C* **4,** 7859–7868 (2016).

18. Yuan, G. L., Or, S. W. & Chan, H. L. W. Structural transformation and ferroelectric – paraelectric phase transition in Bi_{1-x} La_x FeO_3 (x = 0–0.25) multiferroic ceramics. *J. Phys. D. Appl. Phys.* **40,** 1196–1200 (2007).

19. Zhang, L. & Yu, J. Residual tensile stress in robust insulating rhombohedral $Bi_{1-x}La_xFe_{1-y}Ti_yO_3$ multiferroic ceramics and its ability to pin ferroelectric polarization switching. *Appl. Phys. Lett.* **106,** 112907 (2015).

20. Sati, P. C., Arora, M., Chauhan, S., Kumar, M. & Chhoker, S. Effect of Dy substitution on structural , magnetic and optical properties of $BiFeO_3$ ceramics. *J. Phys. Chem. Solids* **75,** 105–108 (2014).

21. Uniyal, P. & Yadav, K. L. Pr doped bismuth ferrite ceramics with enhanced multiferroic properties. *J. Phys.Condens. Matter* **21,** 405901 (2009).

22. Mao, W. *et al.* Effect of Ln (Ln = La , Pr) and Co co-doped on the magnetic and ferroelectric properties of $BiFeO_3$ nanoparticles. *J. Alloys Compd.* **584,** 520–523 (2014).

23. Trivedi, P. *et al.* Modifications in the electronic structure of Rare-Earth doped $BiFeO_3$ multiferroic. *Solid State Commun.* **222,** 5–8 (2015).

24. Bernardo, M. S. *et al.* Intrinsic Compositional Inhomogeneities in Bulk Ti-Doped $BiFeO_3$: Microstructure Development and Multiferroic Properties. *Chem. Mater.* **25,** 1533–1541 (2013).

25. Azough, F. *et al.* Microstructure and properties of Co- , Ni- , Zn- , Nb- and W-modified multiferroic $BiFeO_3$ ceramics. *J. Eur. Ceram. Soc.* **30,** 727–736 (2010).

26. Jun, Y.-K. *et al.* Effects of Nb-doping on electric and magnetic properties in multi-ferroic $BiFeO_3$ ceramics. *Solid State Commun.* **135,** 133–137 (2005).

27. Anjum, G. *et al.* NEXAFS studies of $La_{0.8}Bi_{0.2}Fe_{1-x}Mn_xO_3$ ($0.0 \leq x \leq 0.4$) multiferroic system using x-ray absorption spectroscopy. *J. Phys. D. Appl. Phys.* **44,** 075403 (2011).

28. Kawae, T., Terauchi, Y., Tsuda, H., Kumeda, M. & Morimoto, A. Improved leakage and ferroelectric properties of Mn and Ti codoped $BiFeO_3$ thin films. *Appl Phys Lett* **92,** 112904 (2009).

29. Comyn, T. P., McBride, S. P. & Bell, A. J. Processing and electrical properties of $BiFeO_3$–$PbTiO_3$ ceramics. *Mater. Lett.* **58,** 3844–3846 (2004).

30. Leontsev, S. O. & Eitel, R. E. Dielectric and Piezoelectric Properties in Mn-Modified (1-x)$BiFeO_3$ – x$BaTiO_3$ Ceramics. *J. Am. Ceram. Soc.* **92,** 2957–2961 (2009).

31. Dorcet, V., Marchet, P. & Trolliard, G. Structural and dielectric studies of the $Na_{0.5}Bi_{0.5}TiO_3$ – $BiFeO_3$ system. *J. Eur. Ceram. Soc.* **27,** 4371–4374 (2007).

32. Kiyanagi, R. *et al.* Structural and Magnetic Phase Determination of (1-x)$BiFeO_3$ – x$BaTiO_3$ Solid Solution. *J. Phys. Soc. Japan* **81,** 024603 (2012).

33. Wang, Q. Q., Wang, Z., Liu, X. Q. & Chen, X. M. Improved Structure Stability and Multiferroic Characteristics in $CaTiO_3$-Modified $BiFeO_3$ Ceramics. *J. Am. Ceram. Soc.* **95,** 670–675 (2012).

34. Saad, Y., Alvarez-Serrano, I., Lopez, M. L. & Hidouri, M. Structural and dielectric characterization of new lead-free perovskites in the ($SrTiO_3$)-($BiFeO_3$) system. *Ceram. Int.* **42,** 8962–8973 (2016).

35. Lin, D. *et al.* Microstructure , ferroelectric and piezoelectric properties of $Bi_{0.5}K_{0.5}TiO_3$-modified $BiFeO_3$–$BaTiO_3$ lead-free ceramics with high Curie temperature. *J. Eur. Ceram. Soc.* **33,** 3023–3036 (2013).

36. Yabuta, H. *et al.* Microstructure of $BaTiO_3$ – $Bi(Mg_{1/2}Ti_{1/2})O_3$ – $BiFeO_3$ Piezoelectric Ceramics. *Jpn. J. Appl. Phys.* **51,** 09LD04 (2012).

37. Lee, M. H. *et al.* High-Performance Lead-Free Piezoceramics with High Curie Temperatures. *Adv. Mater.* **27,** 6976–6982 (2015).

38. Sebastian, T. *et al.* High temperature piezoelectric ceramics in the $Bi(Mg_{1/2}Ti_{1/2})O_3$-$BiFeO_3$-$BiScO_3$-$PbTiO_3$ system. *J. Electroceramics* **25,** 130–134 (2010).

39. Rödel, J. *et al.* Transferring lead-free piezoelectric ceramics into application. *J. Eur. Ceram. Soc.* **35,** 1659–1681 (2015).

40. Panda, P. K. Review: environmental friendly lead-free piezoelectric materials. *J. Mater. Sci.* **44,** 5049–5062 (2009).

41. Shrout, T. R. & Zhang, S. J. Lead-free piezoelectric ceramics: Alternatives for PZT? *J. Electroceramics* **19,** 111–124 (2007).

42. Leontsev, S. O. & Eitel, R. E. Progress in engineering high strain lead-free piezoelectric ceramics. *Sci. Technol. Adv. Mater.* **11,** 044302 (2010).

43. Guo, Y. *et al.* Critical roles of Mn-ions in enhancing the insulation, piezoelectricity and multiferroicity of $BiFeO_3$-based lead-free high temperature ceramics. *J. Mater. Chem. C* **3,** 5811–5824 (2015).

44. Liu, X., Xu, Z., Qu, S., Wei, X. & Chen, J. Ferroelectric and ferromagnetic properties of Mn-doped $0.7BiFeO_3$-$0.3BaTiO_3$ solid solution. *Ceram. Int.* **34,** 797–801 (2008).

45. Ye, W., Tan, G., Yan, X., Ren, H. & Xia, A. Influence of Mn dopants on the structure and multiferroic properties of a $Bi_{0.90}Ho_{0.10}FeO_3$ thin film. *RSC Adv.* **5,** 43594–43600 (2015).

46. Kim, D. J. *et al.* Ferroelectric and piezoelectric properties of Mn-modified $BiFeO_3$-$BaTiO_3$ ceramics. *J. Electroceramics* **33,** 37–41 (2014).

47. Joo, H. W., Kim, D. S., Kim, J. S. & Cheon, C. I. Piezoelectric properties of Mn-doped $0.75BiFeO_3$−$0.25BaTiO_3$ ceramics. *Ceram. Int.* **42,** 10399–10404 (2016).

48. Ng, Y. S. & Alexander, S. M. Structural studies of manganese stabilised lead-zirconate-titanate. *Ferroelectrics* **51,** 81–86 (1983).

49. Yoneda, Y., Kitanaka, Y., Noguchi, Y. & Miyayama, M. Electronic and local structures of Mn-doped $BiFeO_3$ crystals. *Phys. Rev. B* **86,** 184112 (2012).

50. Chen, J. & Cheng, J. Enhanced thermal stability of lead-free high temperature $0.75BiFeO_3$–$0.25BaTiO_3$ ceramics with excess Bi content. *J. Alloys Compd.* **589,** 115–119 (2014).

51. Yao, Z. *et al.* Manganese-Doped $BiFeO_3$–$BaTiO_3$ High-Temperature Piezoelectric Ceramics: Phase Structures and Defect Mechanism. *Int. J. Appl. Ceram. Technol.* **13,** 549–553 (2016).

52. Wan, Y. *et al.* Microstructure, Ferroelectric, Piezoelectric, and Ferromagnetic Properties of Sc-Modified $BiFeO_3$ – $BaTiO_3$ Multiferroic Ceramics with MnO_2 Addition. *J. Am. Ceram. Soc.* **97,** 1809–1818 (2014).

53. Li, Q., Cheng, J. & Chen, J. Reduced dielectric loss and enhanced piezoelectric properties of Mn modified $0.71BiFeO_3$–$0.29BaTiO_3$ ceramics sintered under oxygen atmosphere. *J. Mater. Sci. Mater. Electron.* **28,** 1370–1377 (2017).

54. Yang, H. *et al.* Structural , microstructural and electrical properties of $BiFeO_3$ – $BaTiO_3$ ceramics with high thermal stability. *Mater. Res. Bull.* **47,** 4233–4239 (2012).

55. Cen, Z. *et al.* Structural , ferroelectric and piezoelectric properties of Mn-modified $BiFeO_3$-$BaTiO_3$ high-temperature ceramics. *J. Mater Sci Mater Electron* **24,** 3952–3957 (2013).

56. Hang, Q. *et al.* Structural , spectroscopic , and dielectric characterizations of Mn-doped 0.67$BiFeO_3$-0.33$BaTiO_3$ multiferroic ceramics. *J. Adv. Ceram.* **2,** 252–259 (2013).

57. Kumar, M. M., Srinivas, A. & Suryanarayana, S. V. Structure property relations in $BiFeO_3$/$BaTiO_3$ solid solutions. *J. Appl. Phys.* **87,** 855–862 (2000).

58. Mendelson, M. I. Average Grain Size in Polycrystalline Ceramics. *J. Am. Ceram. Soc.* **52,** 443–446 (1969).

59. Stewart, M., Cain, M. G. & Hall, D. Ferroelectric Hysteresis Measurement & Analysis. *NPL Rep. C. 152* 1–57 (1999).

60. Shannon, R. D. Revised Effective Ionic Radii and Systematic Studies of Interatomie Distances in Halides and Chaleogenides. *Acta Cryst.* **A 32,** (1976).

61. Stephens, P. W. Phenomenological model of anisotropic peak broadening in powder diffraction. *J. Appl. Cryst.* **32,** 281–289 (1999).

62. Yasukawa, K. & Nishimura, M. Core–Shell Structure Analysis of $BaTiO_3$ Ceramics by Synchrotron X-Ray Diffraction. *J. Am. Ceram. Soc.* **90,** 1107–1111 (2007).

63. Armstrong, T. R. & Buchanan, R. C. Influence of Core-Shell Grains on the Internal Stress State and Permittivity Response of Zirconia-Modified Barium Titanate. *J. Am. Ceram. Soc.* **73,** 1268–1273 (1990).

64. Lennox, R. C. *et al.* PZT-like structural phase transitions in the $BiFeO_3$–$KNbO_3$ solid solution. *Dalt. Trans.* **44,** 10608–10613 (2015).

65. Dolgos, M. *et al.* Chemical control of octahedral tilting and off-axis A cation displacement allows ferroelectric switching in a bismuth-based perovskite. *Chem. Sci.* **3,** 1426–1435 (2012).

66. Acosta, M. *et al.* Core–Shell Lead–Free Piezoelectric Ceramics: Current Status and Advanced Characterization of the $Bi_{1/2}Na_{1/2}TiO_3$–$SrTiO_3$ System. *J. Am. Ceram. Soc.* **98,** 3405–3422 (2015).

67. Koruza, J. *et al.* Formation of the core – shell microstructure in lead-free $Bi_{1/2}Na_{1/2}TiO_3$-$SrTiO_3$ piezoceramics and its influence on the electromechanical properties. *J. Eur. Ceram. Soc.* **36,** 1009–1016 (2016).

68. Chazono, H. & Kishi, H. Sintering Characteristics in the $BaTiO_3$–Nb_2O_5–Co_3O_4 Ternary System: II, Stability of So-called 'Core–Shell' Structure. *J. Am. Ceram. Soc.* **83,** 101–106 (2000).

69. Sterianou, I., Sinclair, D. C., Reaney, I. M., Comyn, T. P. & Bell, A. J. Investigation of high Curie temperature (1−x) $BiSc_{1-y}Fe_yO_3$ – $xPbTiO_3$ piezoelectric ceramics. *J. Appl. Phys.* **106,** 084107 (2009).

70. Morozov, M. I., Einarsrud, M. A. & Grande, T. Atmosphere controlled conductivity and Maxwell-Wagner relaxation in $Bi_{0.5}K_{0.5}TiO_3$ - $BiFeO_3$ ceramics. *J. Appl. Phys.* **115,** 0–6 (2014).

71. Cao, L. *et al.* Effect of poling on polarization alignment, dielectric behavior, and piezoelectricity development in polycrystalline $BiFeO_3$–$BaTiO_3$ ceramics. *Phys. Status Solidi* **213,** 52–59 (2016).

72. Soda, M., Matsuura, M., Wakabayashi, Y. & Hirota, K. Superparamagnetism Induced by Polar Nanoregions in Relaxor Ferroelectric (1-x)$BiFeO_3$–x$BaTiO_3$. *J. Phys. Soc. Japan* **80,** (2011).

73. Ozaki, T. *et al.* Ferroelectric Properties and Nano-Scaled Domain Structures in (1-x) $BiFeO_3$-x$BaTiO_3$ ($0.33<x<0.5$). *Ferroelectrics* **385,** 6155–161 (2009).

74. Kumari, S. *et al.* Dielectric anomalies due to grain boundary conduction in chemically substituted $BiFeO_3$. *J. Appl. Phys.* **117,** 114102 (2015).

75. Jha, P. K. *et al.* Diffuse phase ferroelectric vs . Polomska transition in (1-x)$BiFeO_3$ - (x)$BaZr_{0.025}Ti_{0.975}O_3$ ($0.1 \leq x \leq 0.3$) solid solutions. *J. Appl. Phys.* **117,** 024102 (2015).

76. Yao, Z. *et al.* Greatly reduced leakage current and defect mechanism in atmosphere sintered $BiFeO_3$ – $BaTiO_3$ high temperature piezoceramics. *J. Mater Sci Mater Electron* **25,** 4975–4982 (2014).

77. Rojac, T., Kosec, M., Budic, B., Setter, N. & Damjanovic, D. Strong ferroelectric domain-wall pinning in $BiFeO_3$ ceramics. *J. Appl. Phys.* **108,** 074107 (2010).

78. Jin, L., Li, F. & Zhang, S. Decoding the Fingerprint of Ferroelectric Loops: Comprehension of the Material Properties and Structures. *J. Am. Ceram. Soc.* **97,** 1–27 (2014).

79. Schenk, T. *et al.* About the deformation of ferroelectric hystereses. *Appl. Phys. Rev.* **1,** 041103 (2014).

80. Yuan, G. L., Yang, Y. & Or, S. W. Aging-induced double ferroelectric hysteresis loops in $BiFeO_3$ multiferroic ceramic. *Appl. Phys. Lett.* **91,** 122907 (2007).

81. Lo, V., Chung, W. W., Cao, H. & Dai, X. Investigating the effect of oxygen vacancy on the dielectric and electromechanical properties in ferroelectric ceramics. *J. Appl. Phys.* **104,** 064105 (2008).

82. Kan, D. *et al.* Universal behavior and electric-field-lnduced structural transition in rare-earth-substituted $BiFeO_3$. *Adv. Funct. Mater.* **20,** 1108–1115 (2010).

83. Tan, X., Ma, C., Frederick, J., Beckman, S. & Webber, K. G. The Antiferroelectric ↔ Ferroelectric Phase Transition in Lead-Containing and Lead-Free Perovskite Ceramics. *J. Am. Ceram. Soc.* **94,** 4091–4107 (2011).

84. Jo, W. *et al.* Giant electric-field-induced strains in lead-free ceramics for actuator applications - Status and perspective. *J. Electroceramics* **29,** 71–93 (2012).

85. Ke, S. *et al.* Tuning of dielectric and ferroelectric properties in single phase $BiFeO_3$ ceramics with controlled Fe^{2+}/ Fe^{3+} ratio. *Ceram. Int.* **40,** 5263–5268 (2014).

86. Carl, K. & Hardtl, K. H. Electrical after-effects in $Pb(Ti,Zr)O_3$ ceramics. *Ferroelectrics* **17,** 473–486 (1977).

87. Genenko, Y. a., Glaum, J., Hoffmann, M. J. & Albe, K. Mechanisms of aging and fatigue in ferroelectrics. *Mater. Sci. Eng. B* **192,** 52–82 (2015).

88. Cross, L. E. Relaxor ferroelectrics: An overview. *Ferroelectrics* **151,** 305–320 (1994).

89. Macutkevic, J., Banys, J., Bussmann-Holder, A. & Bishop, A. R. Origin of polar nanoregions in relaxor ferroelectrics : Nonlinearity , discrete breather formation , and charge transfer. *Phys. Rev. B* **83,** 184301 (2011).

90. Ge, W. *et al.* Direct evidence of correlations between relaxor behavior and polar nano-regions in relaxor ferroelectrics : A case study of lead-free $Na_{0.5}Bi_{0.5}TiO_3$ - x%$BaTiO_3$. *Appl. Phys. Lett.* **103,** 241914 (2013).

91. Liu, N. *et al.* Revealing the core-shell interactions of a giant strain relaxor ferroelectric $0.75Bi_{1/2}Na_{1/2}TiO_3$-$0.25SrTiO_3$. *Sci. Rep.* **6,** 36910 (2016).

92. Ogihara, H., Randall, C. A. & Trolier-McKinstry, S. Weakly Coupled Relaxor Behavior of $BaTiO_3$–$BiScO_3$ Ceramics. *J. Am. Ceram. Soc.* **92,** 110–118 (2009).

93. Kim, D. S., Cheon, C. Il, Lee, S. S. & Kim, J. S. Effect of cooling rate on phase transitions and ferroelectric properties in $0.75BiFeO_3$-$0.25BaTiO_3$ ceramics. *Appl. Phys. Lett.* **109,** 202902 (2016).

94. Lv, J. & Wu, J. Defect dipole-induced poling characteristics and ferroelectricity of quenched bismuth ferrite-. *J. Mater. Chem. C* **4,** 6140–6151 (2016).

95. Kim, S. *et al.* Revealing the role of heat treatment in enhancement of electrical properties of lead-free piezoelectric ceramics. *J. Appl. Phys.* **122,** 014103 (2017).

Optimisation of functional properties in lead-free $BiFeO_3$-$BaTiO_3$ ceramics through La^{3+} substitution strategy

Ilkan Calisir,[1] Abdulkarim. A. Amirov,[2,3] Annette K. Kleppe[4] and David A. Hall[1]

[1]School of Materials, University of Manchester, M13 9PL, Manchester, UK

[2]Center for Functionalized Magnetic Materials (FunMagMa) & Institute of Physics Mathematics and Informational Technologies Immanuel Kant Baltic Federal University, Kaliningrad, Russia

[3]Amirkhanov Institute of Physics Daghestan Scientific Center, Russian Academy of Sciences Makhachkala, Russia

[4]Diamond Light Source Ltd., Harwell Science and Innovation Campus, OX11 0DE, Didcot, UK

ABSTRACT

The paper is concerned with the structure and functional properties of bismuth ferrite-barium titanate, $0.75BiFeO_3$-$0.25BaTiO_3$, solid solutions. Such materials are attracting attention due to their potential applications in high temperature piezoelectric transducers for use in demanding environments in process monitoring, for example. The article focuses on the mechanism of incorporation of the minor dopant lanthanum oxide, either in the form of isovalent or donor-type substitution. It is shown that the development of chemical heterogeneity in the form of core-shell grain microstructures, linked to donor-type substitution, plays a key role in controlling the functional behaviour. The use of an air-quenching procedure results in dramatic improvements in the ferroelectric properties, accompanied by a transformation of the shell regions from a pseudo-cubic, *Pm-3m*, to rhombohedral, *R3c*, structure. These observations are interpreted in terms of a novel mechanism involving nanoscale phase separation in the 'shell' regions during slow cooling, which impedes the development of ferroelectric ordering and leads to the formation of a nano-polar relaxor ferroelectric state. The work highlights the importance of immiscibility in bismuth-based ferroelectric perovskite solid solutions and illustrates how their

ferroelectric, piezoelectric, dielectric energy storage, ferromagnetic and magneto-electric properties can be tuned by consideration of the substitution mechanism and control of thermal processing parameters.

1. INTRODUCTION

In recent decades, there has been intensive research on lead-free electroceramics, with the aim of identifying suitable replacement materials for lead-based ferroelectrics such as lead zirconate titanate (PZT), for example.[1–3] In parallel, multiferroic $BiFeO_3$ has been investigated to provide multifunctionality in current and/or future device applications.[4–6] Increased environmental concerns regarding the usage of 'toxic' lead (Pb) in electronic components have led to EU and worldwide legislation to reduce the use of hazardous substances such as Pb-based oxides in all sectors.[3] Thus, a number of lead-free ferroelectric ceramics to replace PZT have been proposed and developed, including mostly perovskite-structured compounds such as $BaTiO_3$ (BT), $K_{0.5}Na_{0.5}NbO_3$ (KNN), $Bi_{0.5}Na_{0.5}TiO_3$ (BNT) and their modified solid solution systems, including combinations with other perovskites.[3]

KNN-based solid solutions are generally regarded as the leading candidate to replace PZT for piezoelectric applications. However, a revelatory report[7] in 2016 demonstrated that the life cycle stages of KNN, in comparison with PZT, raised serious concerns due to environmental destruction and energy consumption during the mining of Nb_2O_5 which is one of the main constituent oxides in KNN. Thus, the generic term 'lead-free' referring to environmental concerns in the literature (in most cases) may be supplemented by terms such as 'niobium-free' or 'niobium-reduced', in spite of its nontoxicity. In the light of these findings, if the current situation in the mining of niobium oxide does not show any further reformation, it is possible that the focus on finding replacements for lead-based materials may shift to Bi-based titanate solid solutions in perovskites including $(Bi_{0.5}A_{0.5})TiO_3$, A=Na, K and $Bi(B)O_3$, $(Zn_{0.5}Ti_{0.5})$, $(Mg_{0.5}Ti_{0.5})$ or ferrites such as $BiFeO_3$-based ceramics.[8–10]

Among the Bi-based ferroelectric ceramics, $BiFeO_3$ (BF) is renowned as a special compound due to its multiferroic nature at room temperature.[4] Perovskite-structured rhombohedral, *R3c*, $BiFeO_3$ undergoes an antiferromagnetic-paramagnetic phase transition, at T_{Neel}≈370°C and subsequently its ferroelectric nature transforms into paraelectric at T_{Curie} ≈825°C,[4] which is one of the highest amongst perovskite oxides. The intrinsic nature of the large spontaneous polarization, P_s, in single crystal $BiFeO_3$ was reported as ≈100 μC/cm^2 along the

pseudocubic $[111]_{pc}$ direction, which is in agreement in ab-inito calculations.[4] On the other hand, a remanent polarisation, P_r, in the region of 20 $\mu C/cm^2$ was reported for polycrystalline ceramics prepared using a mechanochemical synthesis method.[6]

Nevertheless, pure $BiFeO_3$ ceramics are not generally considered as promising 'lead-free' ferroelectric/piezoelectric candidates due to several factors including high leakage current, difficulties in poling due to the high coercive field and low piezoelectric coefficients. Processing issues such as the volatility of bismuth oxide at high temperatures, frequent secondary phase formation, structural and thermodynamic instability are also important factors that limit its potential usage in various advanced devices.[4–6,11,12]

On the other hand, in order to reveal its potential multifunctional properties, research studies addressing these issues have recently peaked and the obstacles have been overcome using various processing methods[6,13–16] and/or 'site engineering' by means of partial substitutions of A– and B– site ions in the perovskite structure of $BiFeO_3$.[17–25] In addition, solid solution formation with other ABO_3-type perovskite ceramics[8,26] has revealed intriguing functional properties in the form of binary,[9,27,28] ternary,[9,29,30] or even quaternary compounds.[31]

Particular attention can be drawn to the formation of $BiFeO_3$–$BaTiO_3$ (BF–BT) solid solutions, which have been intensively studied as promising candidates for high temperature applications,[9,27,32] surpassing the temperature capability of typical lead-based ferroelectrics that possess lower T_C values. Systematic structural studies in the binary xBF–BT system[8,32,33] showed that the major rhombohedral phase, *R3c*, in $BiFeO_3$ gradually transforms into a pseudocubic phase, starting from $x \leq 0.70$ and the occurrence of a *Pm-3m* cubic phase over a wide compositional range gradually disappears above $x \approx 0.10$, resulting in the appearance of tetragonal structure, *P4mm*, which is the characteristic crystal structure of $BaTiO_3$ at room temperature. Regarding the morphotropic phase boundary (MPB), which is often considered as a crucial feature for enhancement of piezoelectric activity, the most active region has been reported[34] to lie in the range $0.67 \leq x \leq 0.70$, where a mixture of pseudocubic and rhombohedral phases is present. This contrasts with the more traditional MPB between rhombohedral and tetragonal phases in PZT and $BiFeO_3$–$PbTiO_3$, for example.[35]

Developments in the processing of BF–BT ceramics have led to enhanced chemical and structural stability in the synthesis of single phase materials and have successfully inhibited the formation of common secondary phases such as $Bi_2Fe_4O_9$, $Bi_{25}FeO_{39}$, and $Bi_{36}Fe_2O_{57}$.[12,36] Furthermore, weak ferromagnetism was

reported due to suppression of the spin cycloid structure of $BiFeO_3$ through partial Ba^{2+} and Ti^{4+} substitutions.[33] However, the intrinsic ferroelectric character of $BiFeO_3$ in bulk BF–BT ceramics, in the form of saturated polarisation-electric field (P-E) hysteresis loops, has rarely been reported without any further modification,[27] due to the presence of a relatively high leakage current. Therefore, many researchers have employed additional modifiers, such as MnO_2, in order to increase its insulation behaviour,[27,37,38] although the incorporation route could play a key role in chemical homogeneity as discussed in our previous investigation.[39]

There are few studies focused on the influence of rare-earth ions in BF–BT.[40,41] However, a number of publications have attempted to reveal the effects of substituting rare-earth ions for Bi^{3+} in single-phase $BiFeO_3$, and for Ba^{2+} in single-phase $BaTiO_3$. In the former case, trivalent La^{3+} is considered particularly interesting amongst the rare-earth ions since its ionic radius is similar to that of Bi^{3+}. It was reported that partial substitution of La^{3+} for Bi^{3+} in $BiFeO_3$ can be beneficial to stabilise the crystal structure due to increasing ionic bond strength,[42] to suppress oxygen vacancies and secondary phases mainly caused by volatilisation of bismuth oxide, as well as increasing the magnetocrystalline anisotropy making the spin cycloid energetically unfavourable.[22] Structural studies[22,23] are in general agreement that La^{3+} contents up to ≈12.5 mol% do not change the *R3c* rhombohedral symmetry of $BiFeO_3$, while further additions cause significant structural phase transformations. Reports sometimes diverge at that point, but most observed a transition from rhombohedral, *R3c*, to orthorhombic, *Pnma*, symmetry. Defining the exact phase transition points and crystal symmetries is still open to debate.[22,23]

For the case of La^{3+} doping in $BaTiO_3$, studies[43] have shown that La^{3+} ions preferentially substitute for Ba^{2+} on the A-site, despite the smaller ionic radius. Therefore, this type of incorporation requires charge compensation through creation of negatively charged defects such as cation vacancies, anion interstitials, electrons, or acceptor impurities.[44] It is well known that at low La^{3+} dopant concentrations (≈0.5 mol%), donor-doped $BaTiO_3$ exhibits semiconductive behaviour due to electronic compensation, while further La^{3+} additions result in insulating behaviour due to ionic compensation by cation vacancies. It has been suggested that the increase in resistivity could be due to reoxidation of ceramics during cooling[45] rather than switching between electronic and ionic charge compensation.[44,46] It is also reported that with increasing La^{3+} content, the formation of Ti vacancies becomes more favourable, according to the formula $Ba_{1-x}La_xTi_{1-x/4}(V_{Ti}''''')_{x/4}O_3$.[43,44,46] The solid solubility

limit has been found to occur at $x \geq 0.25$ in $BaTiO_3$ ceramics, with further additions leading to the formation of secondary phases formed by expelled oxides.[44,46]

In recent years, it has been found that significant enhancements in the functional properties of BF-BT ceramics can be achieved either by compositional trials using certain dopants[27,37,47] or by thermal quenching treatments.[48–50] However, no single report has addressed the underlying mechanisms responsible for these improvements or, sometimes, apparent degradation. Therefore, we aim to investigate the origins of the reported improvements in functional properties and identify how the properties can be optimised. We also questioned why some previous studies reported that donor doped BF-BT ceramics display significant reductions in remanent polarisation, which makes them promising candidates for energy storage dielectrics,[51] and/or high precision actuators due to reduced hysteresis.[52]

The rationale of the present study was to employ both isovalent and aliovalent substitutions of La^{3+} for Bi^{3+} and Ba^{2+} respectively, in the solid solution $0.75BiFeO_3$-$0.25BaTiO_3$ (75BFBT). This solid solution system was selected due to its proximity to the MPB and the existence of a major rhombohedral phase, which enables any possible structural distortions induced by La^{3+} substitution to be identified. It was found that the major determining factor for high performance in BF-BT ceramics is the state of chemical homogeneity; isovalent doping promotes the solubility and leads to a relatively homogeneous microstructure while donor doping reduces the solubility and causes chemical heterogeneity. The formation of core-shell microstructures in the donor-doped BF-BT ceramics hinders ferroelectric polarisation switching. However, it is shown that thermal quenching has a profound impact on the structure of the shell regions, leading to significant changes in functional properties.

2. EXPERIMENTAL PROCEDURES

2.1 Ceramic processing

La-substituted ceramics were synthesised based on the chemical formula of $0.75(Bi_{0.99}La_{0.01})FeO_3$-$0.25BaTiO_3$ and $0.75BiFeO_3$-$0.25(Ba_{0.99}La_{0.01})TiO_3$ using conventional solid state reaction method. The ceramics are hereafter named as *LaBi* and *LaBa* corresponding to which substitution mechanism is involved, the former being isovalent and the latter aliovalent (donor) type. The undoped composition, abbreviated as 75BFBT, was also prepared to provide a reference for comparing the effects of the La substitutions. Bi_2O_3 (99%, Alfa Aesar), Fe_2O_3 (99%, Sigma Aldrich), $BaCO_3$ (99%, Alfa Aesar), TiO_2 (99%, Fisher Scientific) and

La_2O_3 (99.9% Alfa Aesar) were used as precursor powders. 2 mol% Bi_2O_3 excess was added into all compositions in order to compensate for the loss of this volatile oxide during sintering. Additional compositions were also prepared, containing 3 and 5 mol% La substituted for both Bi and Ba, in order to assess the influence of increasing La concentrations on the structure and functional properties.

The precursor oxides were weighed according to the required stoichiometric ratios, then mixed and milled for 24 h using propan-2-ol and yttria-stabilized zirconia media. The milled powders were dried at 85°C overnight followed by calcination at 850°C for 2 h with heating and cooling rates of 5°C/min. Additional milling was performed again on the calcined powders for 24 h to reduce the particle size down to the sub-micron region. Polyethylene glycol (PEG1500 with an average molar mass of 1500 g mol^{-1}) solution as a lubricant was added into the calcined powders at a concentration of 2 *wt%* in order to improve compaction behaviour. The calcined powders were uniaxially cold-pressed at ≈150 MPa into 8 mm diameter pellets. The pellets were placed on a layer of calcined powder having the same composition and covered with an inverted alumina crucible, in order to create a bismuth-rich atmosphere and also to avoid possible reaction with the supporting alumina plate.[6] The organic additive was burnt-out at a temperature of 600°C for 1 h, following which the ceramics were sintered at a temperature of 1050°C for 2 h in air, using heating and cooling rates of 5°C/min. Additionally, the produced as-sintered *LaBa* composition was annealed at 800°C for 20 min in air, then directly quenched to room temperature, referred to below as *quenched-LaBa*.

The bulk densities of the sintered ceramics were measured by immersion in distilled water using the Archimedes method. Theoretical densities were obtained on the basis of the structural analysis described below, using the unit cell volume determined from full-pattern refinement of the x-ray diffraction patterns and the nominal chemical composition. The relative densities of the sintered ceramics were calculated as the ratio of bulk to theoretical density and found to be in the region of 95 ± 3% for all of the samples prepared during the present study.

2.2 High Resolution Structural Characterisation

High resolution synchrotron x-ray powder diffraction (SXPD) patterns were collected on the I11 powder diffraction beamline at the Diamond Light Source. The crushed powders obtained from sintered samples were placed in a glass

capillary tube. Due to high absorption effects associated with bismuth at the synchrotron radiation energy, the beam energy was adjusted to 25 keV and the glass capillaries with 0.3 mm diameter were used. The diffraction profiles were collected at room temperature using the position sensitive detector (PSD). The x-ray photon wavelength, λ, was determined as 0.494216 Å after calibration using a silicon standard powder. The collected data was later refined based on Rietveld analysis using TOPAS *v*5 software.

The ceramic pellets for in-situ high energy x-ray diffraction experiments were prepared by cutting them into dimensions of approximately 0.5 mm (thickness) x 1 mm (width) x 4 mm (length). The experiment was performed on beamline I15 of the Diamond Light Source using high-energy, monochromatic X-rays with a photon energy of 76 keV. The X-ray beam size was 70 μm in diameter. A custom-designed sample holder was used to support the specimen in the beam and provide electrical contacts, the sample being were immersed in silicone oil to avoid arcing during electric field application. The electric field was applied perpendicular to the beam direction using a high voltage amplifier (Matsusada ECA-10). The specimens were subjected to 2 bipolar cycles of an electric field with amplitude 5 kV mm^{-1}, using a step size of 0.5 kV mm^{-1}. 2D diffraction images were recorded using a Perkin-Elmer XRD 1621 flat-panel detector positioned ≈1.1 m from the sample, with a collection time of 10 s. These 2D images were integrated into 24 sectors using *DAWN* software,[53] yielding orientation-dependent 1D XRD patterns. In the present study, attention is focused on grain orientations with scattering vectors either parallel or perpendicular to the electric field direction, denoted as $\Psi=0^{\circ}$ and $\Psi=90^{\circ}$ respectively. The procedures used for application of the electric field and data analysis were similar to those described by Daniel.[54]

2.3 Microstructure and Electrical Characterisation

The sintered ceramic specimens were ground using 800, 1200, 2500 and 4000 grade SiC paper and then fine polishing was carried out with 3, 1 and 0.25 μm diamond paste followed by diluted OP-S silica colloidal suspension. Well-polished samples were chemically etched by immersing into the etchant solution (95% distilled water + 4% HCl + 1% HF) for 5 seconds. Microstructures of etched and non-etched surfaces were examined using a Philips XL30 FEGSEM equipped with EDS.

For electrical measurements, the samples were polished to obtain smooth and parallel surfaces. In order to achieve a sufficiently high electric field for the

ferroelectric hysteresis measurements, the thickness of the samples was polished down to ≈0.5 mm. Silver electrode paste (C2000107P3, Gwent Group) was applied on the top and bottom surfaces of LaBi and LaBa ceramics and then fired at 600˚C for 20 min. For the quenched-LaBa, an air-dried silver paint (AGG3691, Agar Scientific, UK) was applied onto both surfaces of the pellets at room temperature in order to avoid changes in the effects induced by quenching.

Ferroelectric P-E hysteresis measurements were carried out using a function generator (HP 33120A) connected to a Chevin Research HV amplifier to generate the desired high voltage. The samples were subjected to 4 cycles of a sinusoidal electric field with a frequency of 2 Hz. The measured current waveform was integrated numerically over time to yield charge and hence the polarisation was calculated as the surface charge density[55]. Low-field dielectric measurements were carried out at fixed frequencies from 1 to 100 kHz over the temperature range from 25 to 670˚C using a HP 4284A Impedance Analyser, Carbolite CWF 12/5 furnace and a desktop computer which was operated by LabView-based program. The measurements were conducted in air using a heating rate of 2˚C/min.

2.4 Ferromagnetic and Magnetoelectric Measurements

The bulk ceramics for the magnetic measurements were prepared in form of sintered pellets (t ≈0.5 mm). Ferromagnetic M-H hysteresis measurements were carried out using a vibrating sample magnetometer (Lake Shore 7400). The magnetoelectric measurements were carried out using the methodic described by Amirov.[56] Magnetoelectric (ME) signals were measured by a lock-in amplifier (Stanford research system, Model SR830). Prior to ME measurement, the ceramics were poled for 1 hour under electric fields of 0.15 and 3.5 kV mm^{-1}. The Samples were mounted in longitudinal geometry, i.e. ME voltage is parallel to the direction of AC and DC magnetic fields. The ME coefficient, α_{ME} was calculated using the relation:

$$\alpha_{ME} = \frac{dE}{dH} = \frac{1}{b}\frac{dV}{dH} = \frac{1}{b}\frac{V_{AC}}{H_{AC}}$$

where V_{AC} is the magnetically induced AC electric voltage across the sample, H_{AC} is the amplitude of the AC magnetic field, b is the thickness of the sample. The thermal measurements of ME coefficient in the temperature region (100-500 ˚C) were performed in a special thermo-insulated chamber, designed for high temperature experiments with a quartz sample holder. A cryogen-free

superconducting magnet system with a maximum field of 7 Tesla was used as a source of the magnetic field.

3. RESULTS and DISCUSSION

3.1 Microstructure

For the microstructural examination, chemically etched surfaces of sintered LaBi, LaBa and quenched-LaBa ceramics are presented in Figure 1. Inhomogeneous grain size distributions were observed in both LaBi and LaBa ceramics. However, the range of grain size varied between approximately 4 and 9 μm in LaBi, while that in LaBa compositions was in the range 1 to 5 μm, as can be observed in Fig. 1(a) and (b), respectively. It is evident that large grain size formation could be associated with the isovalent substitution of La^{3+} for Bi^{3+}, which has been reported to enhance the chemical stability of the perovskite structure.[22] However, there was a slight decrease in the average grain size compared with the undoped composition, as given in Figure S1a, which is most likely due to the lower diffusivity of the rare-earth ions. Features associated with ordered ferroelectric domain patterns are also clearly observed throughout the grains in the LaBi ceramics. In contrast, for the case of donor substitution of La^{3+} for Ba^{2+}, the kinetics of grain growth were likely interrupted by factors associated with the creation of charged defects (most likely cation vacancies), which could lead to limited solubility and the possibility of a solute-drag type grain growth retardation mechanism.[24,57–59] It was also observed that retarded grain growth resulted in the formation of chemical heterogeneity in the form of a core-shell type microstructure. In the etched surfaces, the core regions were found to contain distinct ferroelectric domain features, while the shell regions were featureless (Figure 1(b)). Nevertheless, if the LaBa ceramics were quenched after annealing, relatively high domain concentrations were noticed in both core and shell regions, as seen in Figure 1(c).

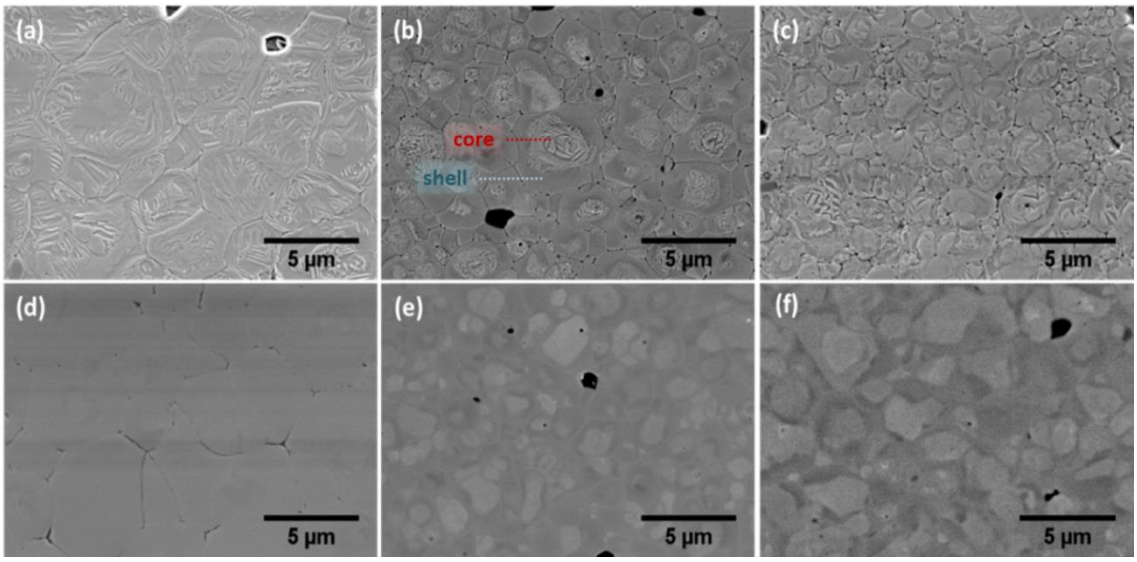

Figure 1 Microstructures of chemically etched sintered surfaces of **a)** LaBi, **b)** LaBa and **c)** quenched-LaBa ceramics. Non-etched polished microstructures of **d)** LaBi, **e)** LaBa and **f)** quenched-LaBa ceramics, which were taken under SEM-backscattered electron (BSE) mode.

Chemically etched sintered surfaces provided invaluable information on the variations in the grain size and domain types, which could be used as strong evidence to correlate the results of structural and electrical characterizations in these ceramics. However, to verify the state of chemical homogeneity, non-etched surfaces of the ceramics were also prepared and examined under the SEM using the backscattered electron (BSE) mode. It was found that there was no clear contrast between core and shell regions in the LaBi ceramics, indicating the chemically homogeneous grain structures (Figure 1(d)). On the other hand, the as-sintered LaBa ceramics showed strong contrast between the core and shell, which correlates well with the features observed in the etched grains, as shown in Figure 1(e). The core regions appear lighter in the BSE images, indicating a concentration of the heavier elements (presumably Bi) in these regions. This type of contrast within the grains was also observed in the non-etched section of the quenched-LaBa ceramic (Figure 1(f)), in contrast to the relatively homogeneous ferroelectric domain distributions in this material (Figure 1(c)). This observation suggests that the quenching process does not significantly affect the micro-scale (core-shell type) chemical heterogeneity in the LaBa ceramic.

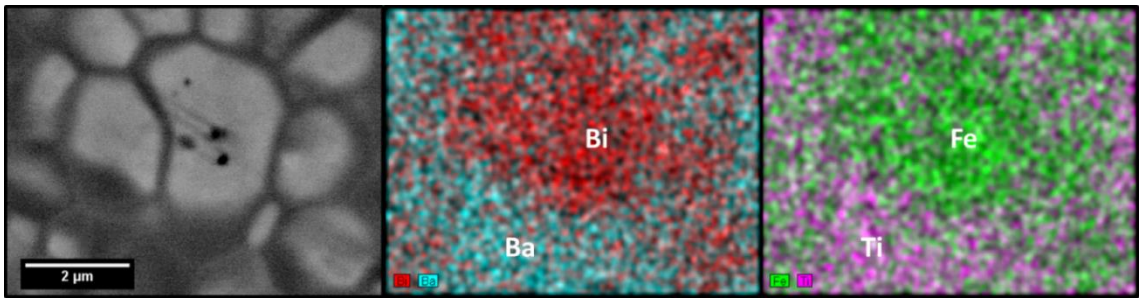

Figure 2 SEM-EDS elemental mapping results of sintered LaBa ceramic exhibiting core-shell grains. Detected elements were also labelled on the regions where were predominantly found.

The occurrence of chemical heterogeneity in the LaBa ceramics was investigated further by means of Energy Dispersive Spectroscopy (EDS). Elemental maps of several grains in the LaBa ceramics are shown in Figure 2. The microsegregation of Bi and Fe elements was clearly detected in the core of grains, corresponding to the lighter regions in the BSE images. In contrast, the signals corresponding to Ba and Ti were mostly evident in the darker shell regions. Due to the small amount of La substitution (1 mol%) in the LaBa ceramics, identification of the La signals from elemental mapping was not feasible. Therefore, we carried out additional EDS investigations on ceramics containing a higher amount of La substitution (3 mol% La^{3+} substituted for Ba^{2+}), yielding the results shown in Figure S2 (Appendix II). It was found that the core regions were relatively deficient in La, leading to the conclusion that the shell may show characteristics of La-doped $BaTiO_3$ ceramics.

On increasing the La content to 5 mol%, needle-like secondary phases were formed at the grain boundaries, while the core-shell type micro-segregation became less evident (Figure S3, Appendix II). Due to the small size of these secondary phases, it was challenging to define their chemical compositions using SEM-EDS. Nonetheless, Makovec[44] observed similar types of secondary phases for heavily La-doped $BaTiO_3$ ceramics(≥25 mol% La), which were said to be associated with the formation of various type of pyrochlore phases due to exceeding the solid solubility limit.

These results demonstrate that 1 mol% donor substitution of La^{3+} for Ba^{2+} in 75BFBT ceramics (LaBa) induced the formation of core-shell type microstructures comprising $BiFeO_3$–rich core and $BaTiO_3$–rich shell regions, with the La^{3+} ions being concentrated in the latter. Increasing levels of substitution led to the disappearance of such features but was also accompanied by the formation of secondary phases, which is indirectly linked to exceeding the solid solubility limit of La^{3+} in in the $BaTiO_3$-enriched shell.

Core-shell type microstructures are a common feature in $BaTiO_3$–based materials[58–60] and can be desirable in order to obtain temperature stable dielectrics.[59,61,62] The core is usually dopant-free, while dopants are mainly segregated in the shell. In the case of the binary solid solution system between $BiFeO_3$ and $BaTiO_3$, differences in reactivity of the constituent oxides are the most likely reason for the occurrence of such features, since it is well established that processing of $BaTiO_3$–based ceramics by solid state reaction methods must be carried out at much higher temperatures than those used for $BiFeO_3$. It was reported that this issue could potentially be overcome by the addition of certain sintering additives/dopants,[27,39,63] increasing the sintering temperature/time[64] or solid solution with other end-members[31] to promote solubility. However, it has been shown that the substitution of 1 mol% La^{3+} for in Ba^{2+} in 75BFBT ceramics leads to the formation of robust chemically heterogeneous microstructures, which are associated with reductions in grain sizes. This could be related to the partial solubility of lanthanum oxide when incorporated in the form of a donor dopant, leading to a solute drag effect on the grain boundaries, as similarly observed in donor Ti^{4+}-substituted $BiFeO_3$.[24]

Relatively homogeneous ferroelectric domain features were noticed throughout the grains regardless of the core and shell regions in the quenched-LaBa ceramics, while the most visible domains were accumulated in the core regions in the as-sintered LaBa ceramics. However the chemical heterogeneity was present in both materials, which could be an indication of possible structural differences in the shell caused by the different cooling procedures. This point is addressed further in the following section.

3.2 Structural Analysis

It has been widely reported that the major phase of the undoped composition (75BFBT) is rhombohedral, with *R3c* space group, which was also verified by our results as shown in Figure S1b. High resolution SXPD measurements were performed to reveal the influence of 1 mol% La substitution for Bi or Ba on the crystal structure of 75BFBT, as well as the effects of air-quenching. The diffraction profiles of LaBi, LaBa and quenched-LaBa ceramics are shown in Figure 3. The diffraction peaks were indexed based on a pseudo-cubic perovskite structure, denoted 'p', and the XRD patterns for all compositions confirmed the formation of perovskite solid solutions without any indication of secondary phases. The essential refined crystallographic parameters, together with reliability factors (R-factors), are given in Table 1. It was found that the small amount of La^{3+} substitution for all specimens caused significant structural distortions and the

appearance of various fractions of a cubic phase, with space group *Pm-3m*. Inspection of the $\{111\}_P$ peak profiles reveals the typical peak splitting of the rhombohedral *R3c* phase, indicated by the $(006)_H$ and $(202)_H$ reflections in the hexagonal setting. These peaks are accompanied by the $(111)_C$ cubic *Pm-3m* reflections for all compositions. However, it is evident that the *Pm-3m* phase fractions varied depending on the substitution type and the application of thermal quenching. These effects are a consequence of the changes in chemical homogeneity associated with isovalent (LaBi) and donor (LaBa) substitutions in 75BFBT.

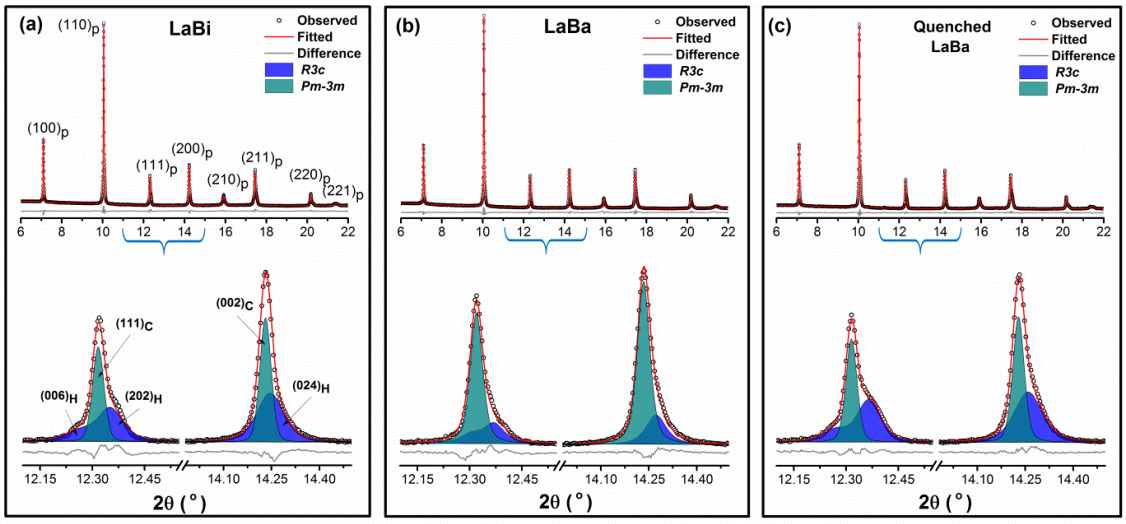

Figure 3 High resolution SXPD patterns and refinements for **a)** LaBi, **b)** LaBa and **c)** quenched-LaBa. The fitted peaks for $\{111\}_P$ and $\{200\}_P$ are highlighted in relation to rhombohedral, *R3c* (doublet of $(006)_H/(202)_H$, and single $(024)_H$ in hexagonal setting), and cubic, *Pm-3m* (single $(111)_C$ and $(002)_C$) phases.

A relatively high *R3c* fraction in LaBi compared to LaBa ceramics could be due to La^{3+} and Bi^{3+} ions sharing similar ionic radii[65] (La^{3+}=1.032 Å and Bi^{3+}=1.03 Å) and the same valence state. Therefore, high structural distortion was not observed or expected in this case. However, structural distortions linked to ferroelectricity are not simply dependent on ionic radii or valence states.[4] The ferroelectric distortion is predominantly contributed by the lone-pair orbital of $Bi^{3+}(6s^2)$ in $BiFeO_3$,[66] but La^{3+} substitution for Bi^{3+} is likely to weaken this lone-pair activity.[4] Therefore, increasing La^{3+} concentration should eventually cause significant structural transformations, as widely reported.[22,23] It should also be noted that the poor perovskite phase stability of $BiFeO_3$ can be improved by La^{3+} substitution since the ionic bond strength can be qualitatively calculated using Pauling's equation given below[67]

$$I_{AB} = 1 - exp[-(\chi_A - \chi_B)^2/4]$$

where I_{AB} is the ionic bond strength with the average electronegativity of anions χ_A and cations χ_B. Based on this equation, the ionic bond strengths of Bi–O and La–O are found to be 0.395 and 0.745, respectively. Therefore, the higher ionic bond strength in La-doped $BiFeO_3$ would make the perovskite phase more stable compared to undoped $BiFeO_3$. A small amount of La was also used effectively in a number of reports to suppress the Bi volatilisation causing serious high leakage current and formation of unwanted phases in pure $BiFeO_3$ ceramics.[13,68] On the other hand, the observation of a pseudo-cubic phase is commonly reported in rare earth-doped $BiFeO_3$-based solid solution systems[40] where its origin is usually attributed to disruption of ferroelectricity and relaxor ferroelectric character.

In the case of the LaBa ceramics, the highest fraction of *Pm-3m* cubic phase was found for the as-sintered (slow-cooled) material, as illustrated in Figure 3(b). There may be several reasons for this, such as the mismatch of ionic radii[65] (La^{3+}=1.032 Å and Ba^{2+}=1.35 Å) and the aliovalent substitution of La^{3+} for Ba^{2+}, which may have a profound impact on the defect chemistry as well as playing a key role in the diffusion kinetics during heat treatment. Previous reports on the crystal structure of the binary solid solution of BF–BT showed that the cubic phase generally becomes increasingly evident as the $BiFeO_3$ content reduces.[33,69,70] Therefore, any significant deviations in stoichiometry, due to the occurrence of chemical heterogeneity, will favour the formation of the cubic phase in $BiFeO_3$–deficient regions. Microstructural observations of the LaBa ceramics clearly confirmed the formation of chemically heterogeneous grain structures consisting of $BiFeO_3$–rich and –depleted regions in the core and shell, respectively (Figure 2). Hence, this is the most likely reason for the high content of cubic phase, which dominates the SXPD peak profile for this composition.

Table 1 Structural parameters of LaBi, LaBa and quenched-LaBa ceramics obtained from Rietveld refinement. *Goodness of fit (*GoF*) is the value of R_{wp}/R_{exp}.

	LaBi		**LaBa**		**Quenched-LaBa**	
	R3c	*Pm-3m*	*R3c*	*Pm-3m*	*R3c*	*Pm-3m*
Phase fractions (%)	40.1(7)	59.9(7)	20.0(4)	80.0(4)	41.3(5)	58.7(5)
Lattice Parameters (Å)						
a	5.6224(4)	3.9902(2)	5.6169(5)	3.9905(3)	5.6170(4)	3.9916(3)
c	13.8829(11)	=*a*	13.8412(18)	=*a*	13.8789(11)	=*a*
Cell Volume ($Å^3$)	380.07(6)	63.533(11)	378.18(9)	63.545(14)	379.22(7)	63.600(12)
R-Factors						
R_{wp} (%)	3.24		3.96		3.22	
R_{exp} (%)	2.02		2.13		1.88	
*GoF**	1.60		1.86		1.71	

Another observation is the presence of significant anisotropic peak broadening for the LaBa ceramics, which could also be a result of the chemical heterogeneity.[71] To overcome this issue during the refinement procedure, the correction proposed by Stephens[72] for materials exhibiting the peak broadening due to 'microstrain' was applied and the fitting was considerably improved. This also implies that compositional fluctuations, taking the form of a core-shell structure in this case, would induce microstrains which may be a key parameter required to correctly refine the structure. The crystal size effect should be also considered as a possible cause of peak broadening. These issues have been recognised in many publications, including those concerned with other $BiFeO_3$-based solid solutions.[28,39,49,73]

In contrast, the diffraction profiles of the thermally quenched-LaBa ceramics were similar to those of the LaBi ceramics. The reappearance of the diffraction peaks associated with the *R3c* phase, as shown in Figure 3(c), is attributed to structural transformations in the shell regions, induced by the quenching procedure. Evidence for an increased incidence of ferroelectric domain structures, as shown in Figure 1(c), supports this assertion since it is anticipated that the visible domain features should be associated with the ferroelectric *R3c* phase. It should also be mentioned that the apparent cubic phase in BF–BT

compositions could actually be rhombohedral or monoclinic on a local scale, as suggested by Singh *et al.*[74]

It is concluded that the process of quenching can transform the featureless pseudo-cubic shell in the LaBa ceramics into rhombohedral ferroelectric domains, as indicated by the increased intensity of the *R3c* reflections in the SXPD profile for the quenched-LaBa ceramics. The underlying cause of this transformation is presently unclear, but it could be associated with nanoscale heterogeneity in the shell regions of the as-sintered (slow-cooled) materials. In turn, this could be a result of immiscibility in the BF–BT system, which would act as a driving force for chemical segregation during cooling and hence would be absent or less effective in the quenched-LaBa ceramics. However, the larger-scale chemical heterogeneity associated with the core-shell microstructure was still maintained regardless of the cooling rate. The occurrence of a significant proportion of cubic phase in the (slow-cooled) LaBi ceramics could also be a result of immiscibility and nanoscale chemical heterogeneity. Further studies involving high resolution TEM would help to test this proposition.

3.3 Dielectric Properties

The variations in the relative dielectric permittivity, ε_r, are employed to evaluate the effects of composition and processing procedures on the ferroelectric phase transformations in these materials. Figure 4 shows the temperature-dependence of the dielectric properties as a function of frequency for LaBi, LaBa and quenched-LaBa ceramics. A single, frequency-independent peak in the ε_r–T plot is usually attributed to the typical ferroelectric to paraelectric transformation, as observed in the case of the LaBi ceramic shown in Figure 4(a). The Curie temperature for this material, which is presumed to be associated with the rhombohedral *R3c* to cubic *Pm-3m* transformation, was found to be approximately 490 °C from these results. Furthermore, the presence of a frequency-dependent shoulder in the temperature range from 300 to 400 °C points to the possible coexistence of relaxor ferroelectric regions as well. This observation is consistent with the identification of a pseudo-cubic phase in LaBi since relaxor ferroelectrics generally exhibit long-range pseudocubic symmetry. The general increase in ε_r at high temperatures/low frequencies is not related to the structural ferroelectric transformations but is instead attributed to an interfacial polarisation mechanism, which is associated with increasing electrical conductivity.[75]

In contrast, two distinct dielectric anomalies were observed in LaBa ceramics; the lower temperature anomaly occurred at a temperature T_1 in the range from 250

to 500 ˚C, while the Curie point occurred at a higher temperature, T_2, which was approximately 630 ˚C, as illustrated in Figure 4(b). The separation of chemically heterogeneous core and shell regions within the grains is the most obvious cause of such behaviour, with the distinct low- and high-temperature dielectric anomalies being a clear indicator of the dielectric responses in the shell and core regions respectively.[62,76] In this case, the lower-temperature peak at T_1 is related to the structural transformation of the shell consisting of a $BaTiO_3$-rich relaxor ferroelectric phase. On the other hand, the higher-temperature anomaly at T_2 can be attributed to the Curie point of the $BiFeO_3$-enriched normal ferroelectric core. This proposal is generally consistent with the higher Curie temperature of $BiFeO_3$ (≈825 °C) in comparison with that of $BaTiO_3$ (≈130 °C). The frequency-dependence of the peak positions, together with the microstructural observations of $BiFeO_3$–rich core and $BaTiO_3$–rich shell regions, also points to this explanation of the dielectric behaviour. The diffuse phase transition and relaxor ferroelectric character is usually attributed to compositional heterogeneity on the nano-scale due to the existence of multiply charged ions in the ABO_3 structure, represented here by Bi^{3+}, Ba^{2+}, and La^{3+} on the A-site. This relaxor-like diffuse behaviour is also in good agreement with previous reports of diffuse phase transitions in xBiFeO$_3$–(1-x)BaTiO$_3$ ceramics with low $BiFeO_3$ contents (x<0.70).[33,69,77,78]

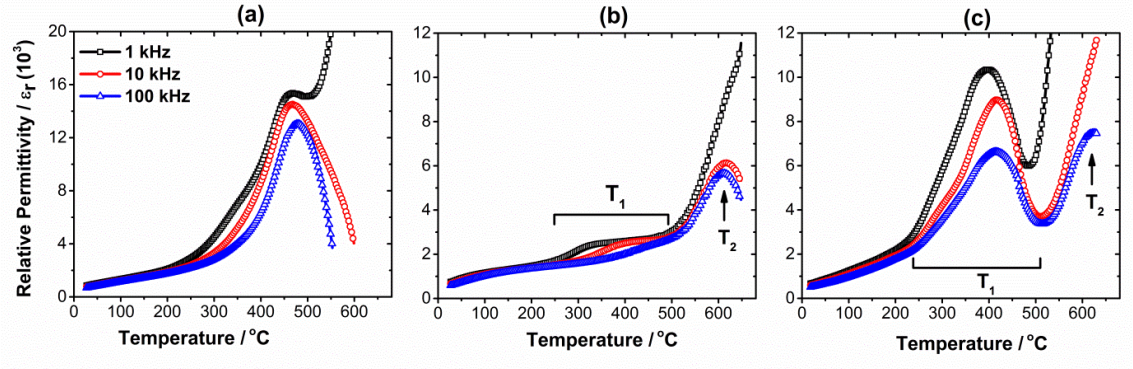

Figure 4 ε_r–T relationships for **a)** LaBi, **b)** LaBa and **c)** quenched-LaBa, measured at various frequencies.

In the case of the quenched-LaBa, it is apparent that the thermal quenching had a profound effect on the ε_r–T relationship, particularly in the region around the lower-temperature anomaly at T_1. The intensity of this peak increased remarkably, while simultaneously the frequency-dependence was reduced. The peak in permittivity at T_2 was affected less, although it became indistinct at lower frequencies due to increasing conductivity. The essential difference, in comparison with the as-sintered LaBa ceramic, is that the shift in peak position with frequency in the region around T_1 was relatively small, indicating that the characteristic relaxor-like behaviour in the shell was diminished. Thus, it is

evident that the transformation from short-range polar nanoregions to long-range ordered ferroelectric domains was achieved by thermal quenching. This is also in agreement with the observation of increased rhombohedral phase fraction by structural analysis (Figure 3(c) and Table 1) and the relatively higher domain concentrations on the etched sections, as illustrated in Figure 1(c).

Similar observations concerning the influence of cooling rate on the temperature-dependent dielectric properties of 75BFBT were reported recently by Kim[48] It was suggested that a sequence of structural transformations occurred during heating, from rhombohedral (*R3c*) to ferroelectric orthorhombic (*Amm2*) near T_1 and then to cubic (*Pm-3m*) above T_2. The influence of oxygen vacancies on rhombohedral distortion was speculated to explain such transformations, although the occurrence of chemical heterogeneity and/or nano-scale phase segregation, as proposed in the present study, was not considered.

3.4 Ferroelectric Properties

Most reports on unmodified $BiFeO_3$-$BaTiO_3$ ceramics show that ferroelectric (P-E) hysteresis loops tend to display rounded features, indicating poor insulation behaviour and high dielectric loss.[27,79] Highly saturated hysteresis loops in modified 75BFBT compositions have been reported in several studies.[27,80,81] In the present work, rounded P-E loops were also recorded for the undoped composition (see the Figure S1c, Appendix II), but these were successfully transformed into well-saturated loops with a high remanent polarisation, $P_r \approx 0.27$ C m^{-2}, via the isovalent substitution of La^{3+} for Bi^{3+}, as illustrated in Figure 5(a). Current density (J-E) switching curves also clearly show that the reversal of polarisation occurred on exceeding the coercive field, E_c, of 4.1 kV mm^{-1}.

In contrast, the P-E loops of the LaBa ceramics exhibit a pinched, or constricted, shape (Figure 5(b)). Previous studies have attributed this type of constrained ferroelectric switching to the presence of antiferroelectric phases,[82,83] domain wall pinning by oxygen vacancy-cation dipolar defects,[84,85] or reversible electric field-induced relaxor to normal ferroelectric transformations.[86] The constricted loops observed in unmodified $BiFeO_3$ ceramics were attributed to domain wall pinning by defect dipoles.[87,88] In the present case, it was found that the P-E loop characteristics did not change significantly over time under the application of a continuous AC electric field with an amplitude of 8 kV mm^{-1} i.e. there was no evidence of field-forced 'de-ageing' effects that might indicate the occurrence of a dipolar defect-related domain stabilisation mechanism.

As an alternative mechanism, we propose that ferroelectric domain switching in the ferroelectric core regions within the LaBa ceramics is constrained by the *ergodic* relaxor ferroelectric nature of the shell regions, within which the polar nanoregions are unable to form long range-ordered ferroelectric domains under the influence of the electric field. The saturation polarisation, $P_S \approx 0.15$ C m^{-2}, is relatively high while the remanent polarisation, $P_r \approx 0.02$ C m^{-2}, is extremely low, indicating that the electric field-induced polarisation is unstable. The J-E curves do not show distinct current switching peaks, suggesting the continuous suppression of ferroelectric domain switching over a wide range of electric field. Thus, the constricted P-E loops in LaBa ceramics are attributed to the heterogeneous switching characteristics in the core and shell regions and the elastic coupling between them.

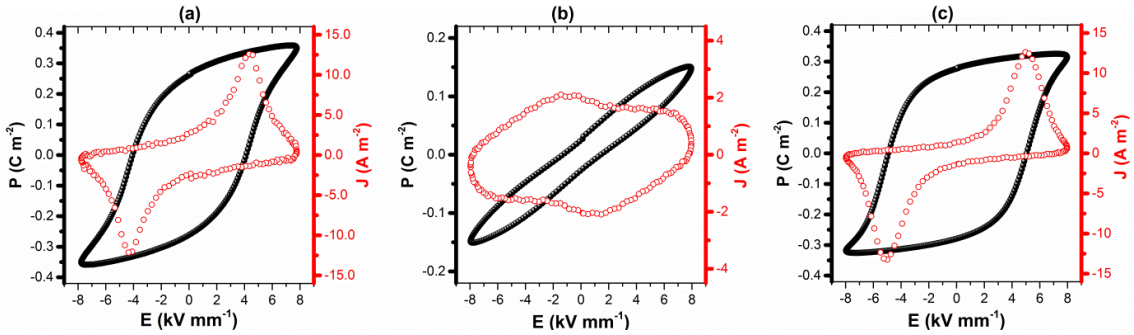

Figure 5 Ferroelectric (P-E) hysteresis loops and Leakage current density (J-E) curves of **a)** LaBi, **b)** LaBa and **c)** quenched-LaBa measured at room temperature.

Constricted P-E hysteresis loops have also been reported recently in rare earth-doped $BiFeO_3$ ceramics and thin films.[82,89–91] It was proposed that this behaviour is associated with the coupling/competition (electric-field induced phase transition) between non-polar/anti-polar *Pnma/Pbam* and polar *R3c* phases under the application of a high electric field. It is reported that incommensurate phases help to bridge the transformations between non-polar and polar phases, for compositions near to the morphotropic phase boundary for certain levels of rare-earth doping, which results in enhanced electromechanical properties. On the other hand, it was found that doping with La^{3+} hinders the nanoscale phase formation, due to the similarity of its ionic radius with that of Bi^{3+}.[90] Similar to the present case, chemically heterogeneous phases were also found as Bi-rich rhombohedral and Sm-rich orthorhombic phases in Sm-doped $BiFeO_3$, but at the nano scale.[91] Core-shell type microstructures have generally gained greater attention recently in Bi-based ferroelectrics, due to their potential for tailoring the ferroelectric and electro-mechanical properties through microstructural engineering.[64,76,92] The critical role of the core-shell interface was emphasised by

Liu, who studied the coupling between the relaxor ferroelectric shell and ordered ferroelectric core regions in $0.75Bi_{1/2}Na_{1/2}TiO_3$-$0.25SrTiO_3$ ceramics.[93]

The use of rapid cooling or thermal quenching procedures has been widely reported as an effective method to enhance the ferroelectric switching behaviour of $BiFeO_3$-based ceramics, although the mechanisms involved are not well-understood.[48,87,94] The influence of such treatment on the ferroelectric domain switching behaviour of the LaBa ceramic is illustrated by the results presented in Figure 5(c). It is apparent that the quenching procedure greatly improved the polarisation switching characteristics of the LaBa composition, increasing the P_r value from 0.02 to 0.28 C m^{-2}. Sharp peaks in the J-E curves near 5 kV/mm also confirm the well-defined switching characteristics. The P_r values of the as-sintered LaBi and the quenched LaBa ceramics were similar, while the P_r/P_s ratio of the quenched-LaBa was somewhat higher than that of the as-sintered LaBi ceramic (0.86 compared with 0.75). This indicates that the ferroelectric domains show a highly irreversible character after the removal of the electric field. On the other hand, the coercive field of the quenched-LaBa was higher than that of LaBi (5 kV mm^{-1} compared with 4.1 kV mm^{-1}).

The occurrence of a constricted P–E loop with high saturation polarisation, P_s, and low remanent polarisation, P_r, for LaBa ceramics led us to investigate its energy storage properties. Figure 6(a) shows the P-E loops measured up to 10 kV mm^{-1} at room temperature. The stored energy density, W_{Stored} and energy loss, W_{Loss}, are shown graphically in Figure 6(b) on the quadrant of the P–E loop associated with the charging and discharging polarisation cycle (i.e increasing and decreasing electric field, E, respectively). In this case, the value of W_{Stored} at a given maximum electric field level was determined by numeric integration of the P-E data according to $W_{Stored} = \int_{Pr}^{Ps} E\, dP$. The energy storage density was found to be approximately 0.61 J cm^{-3} at 10 kV mm^{-1} which is comparable to those reported for other bismuth–barium–titanate[95–97] –niobate[98] and –ferrite[51,99] ceramics, which are generally in the range of 0.5 to 0.9 J cm^{-3} under a maximum field of ≈10 kV mm^{-1}.

One of the key factors to optimise the energy storage density in a dielectric material is to increase dielectric breakdown strength (DBS). It has been found that DBS can be increased by the reduction of grain size[98,100,101] or by the development of core-shell type microstructure[102,103] in ceramic materials. As recently reported[99] by Mishra, the DBS and energy storage density can be significantly increased using spark plasma sintering (SPS) instead of conventional ceramics processing in a $BiFeO_3$-based ceramics (W_{rec} >1 J cm^{-3}). On the other hand, recent modelling carried out by Wu[104] has revealed that the energy storage density can be

improved in core-shell type microstructures. It was proposed that with the presence of the shell (non-polar or non-hysteric), the hysteresis loops become slanted, resulting in a decrease in energy loss, W_{Loss}. The underlying mechanism is attributed to improved homogeneity of the local electric field distribution due to the presence of the shell and therefore the dielectric nonlinearity is weakened, which favours high energy storage performance.

Based on our results for the slow-cooled LaBa ceramics, it is evident that the observed high energy storage density is likely related to the presence of the core-shell type grain formations with the evidence of pseudocubic phase in the shell, which reduces dielectric nonlinearity and hysteresis. Enhanced energy storage density in core-shell type microstructures has been also experimentally reported in $BaTiO_3$-$BiScO_3$ and $BaTiO_3$-$SrTiO_3$.[102,105] It was also suggested that the key aspect for optimising energy storage density is to control the volume of the shell phase[104]. Future investigations for these types of ceramics could assess the influence of modified processing procedures to optimise the performance of the shell and/or reduce the grain size to the sub-micron range.

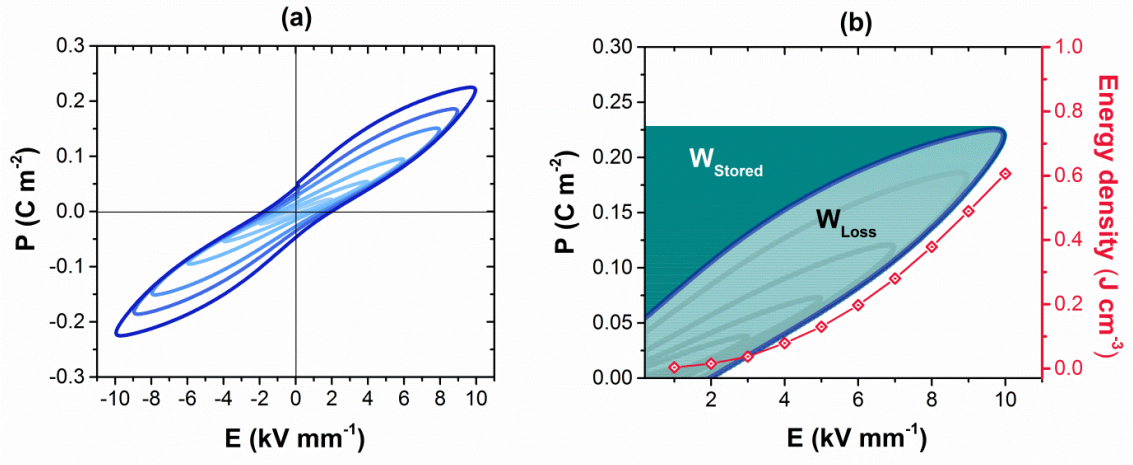

Figure 6 a) Ferroelectric (P-E) hysteresis loops for LaBa ceramics with various maximum electric field levels and **b)** quadrant of the P–E loop with the illustration of stored energy density, W_{Stored} and energy loss, W_{Loss}.

The results presented in sections 3.1 to 3.4 above can be evaluated to elucidate the mechanisms responsible for the observed enhancement in ferroelectric switching behaviour for the LaBa ceramics by air-quenching. Firstly, the observation of micro-scale ferroelectric domains throughout the grains in the quenched-LaBa ceramics (Figure 1(c)), in contrast to the more clearly-defined core and shell regions in the slow-cooled specimen (Figure 1(b), indicates the development of improved ferroelectric ordering within the shell after quenching. The presence of coexisting rhombohedral and cubic, or perhaps more correctly pseudo-cubic, phases was identified using the SXPD patterns presented in Figure

3. In these results, it is apparent that the effect of quenching was to increase the proportion of the ferroelectric rhombohedral phase, which can be correlated generally with the changes in microstructure. However, we should also recognise that the pseudo-cubic phase, which is ascribed to the shell regions, has a relaxor ferroelectric character and may contain polar nanoregions (PNRs) with local non-cubic symmetry.

Evidence from the dielectric and ferroelectric properties of the quenched LaBa ceramics indicates that the shell regions are actually well-ordered and make strong contributions both to the lower-temperature dielectric peak at T_1 and the highly irreversible ferroelectric switching behaviour. Based on the latter results, it seems likely that the quenching procedure could have the effect of reducing the compositional fluctuations in the shell regions and thereby induces a transformation from an *ergodic* to *non-ergodic* relaxor ferroelectric state at room temperature. Further investigations were conducted using *in-situ* x-ray diffraction in order to test this hypothesis, as described in the next section.

3.5 In-situ X-ray Diffraction Studies

The influence of an applied electric field on the XRD patterns of the La-modified 75BFBT ceramics is illustrated by the pseudo-cubic $\{111\}_p$, $\{200\}_p$ and $\{220\}_p$ peak profiles presented in Figure 7. In comparison with the previous results described in section 3.2 above, these patterns were obtained from the bulk sintered ceramics (not crushed powders) and measured using high energy x-rays. This method provides a true indication of the average 'bulk' structure in the solid and enables the influence of the grain orientation relative to the electric field direction to be assessed. By this means, the development of preferred orientation and the associated lattice strain due to ferroelectric domain switching can be readily assessed. For the results presented in Figure 7, the patterns correspond to the 'families' of grains oriented with their scattering vectors parallel to the applied electric field direction i.e. for ψ=0°.

The diffraction peaks obtained by high energy XRD are generally broader than those obtained using high resolution SXPD, which hinders the identification of separate contributions from the rhombohedral core and pseudo-cubic shell regions. Nevertheless, by considering the changes in the peak profiles as a result of the applied electric field and grain orientation it is possible to deduce the main features of the underlying domain switching mechanisms. The influence of the applied electric field can be seen most readily in the $\{111\}_p$ peak profile for the quenched-LaBa ceramic (Figure 7(c)), where a pronounced shift of the peak

occurs toward lower angles, accompanied by the development of a shoulder on the high-angle side. Qualitatively, this observation indicates the development of a large tensile strain in the pseudo-cubic (shell) region on application of the electric field. Ferroelectric domain switching within the core could also be occurring, but the associated changes in the relative intensities of the $(111)_{CO}$ and $(\bar{1}11)_{CO}$ diffraction peaks of the rhombohedral phase are largely masked by overlap with the $(111)_{SH}$ and $(\bar{1}11)_{SH}$ peak of the shell.

The patterns recorded during and after application of the field for quenched-LaBa are similar, indicating that the field-induced strain is largely irreversible and therefore could be due to a form of ferroelectric domain switching rather than pure lattice strain. Compositional gradients and small structural distortions could contribute to broadening of the $(111)_C$ diffraction peak, which may mask the true nature of this '*lattice strain*'. Nevertheless, the active nature of the shell regions in the quenched LaBa ceramics is clearly evident. Further observations of the $\{111\}_p$ peak shifts, presented in the lower part of Figure 7 as surfaces and contour plots, illustrate the responses to the cyclic electric field and highlight the much higher field-induced strain levels achieved for quenched-LaBa in comparison with the as-sintered LaBi and LaBa ceramics.

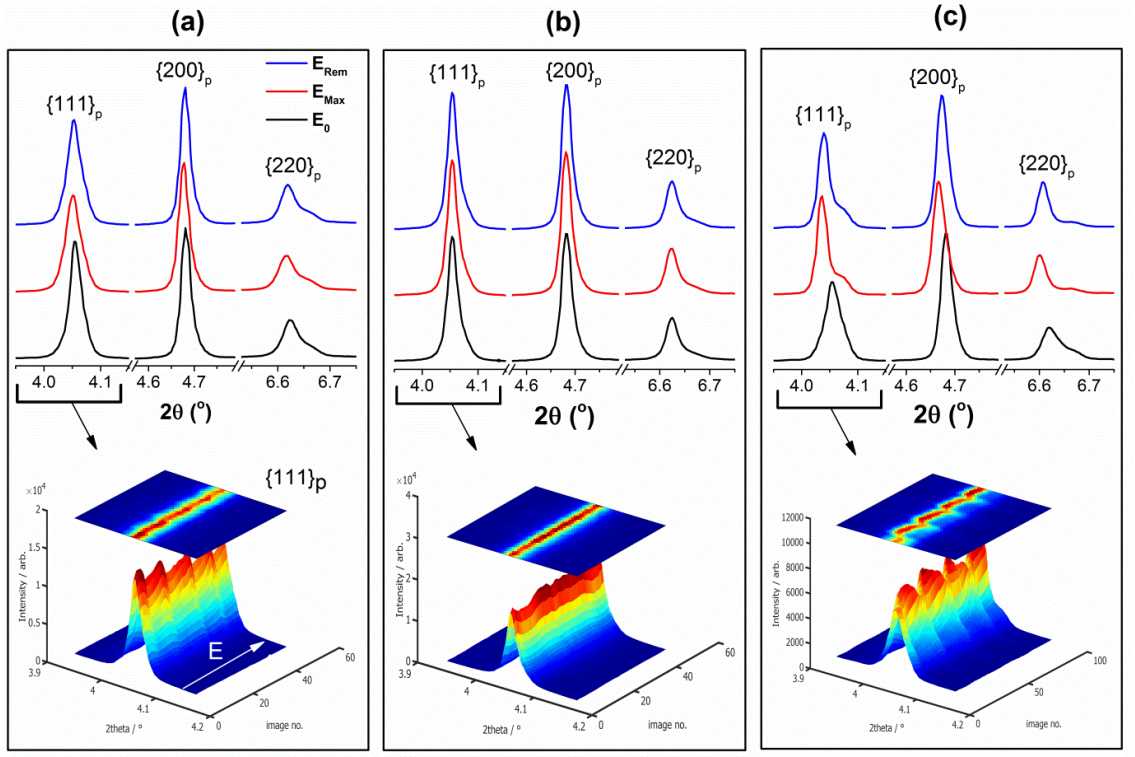

Figure 7 Variations in diffraction peak profiles for {111}, {200} and {220} along the field direction (ψ=0°) for **a)** LaBi, **b)** LaBa, and **c)** quenched-LaBa ceramics prior to application of the electric field (E_0), under a maximum electric field of 5 kV/mm (E_{Max}) and in the remanent state after removal of the electric field (E_{Rem}). The lower figures illustrate the responses of the $\{111\}_p$ peak profiles to the 2 bipolar electric field cycles.

The underlying mechanisms responsible for the electric field-induced strain in the quenched-LaBa ceramics can be clarified by inspection of the $\{111\}_p$ peak profiles, as illustrated in Figure 8(a). While the initial peak at zero electric field is broad, suggesting the presence of several overlapped peaks corresponding to the core and shell phases, the application of the electric field resulted in the suppression of the main peak at 4.065° and the growth of a new dominant peak at 4.04°. It was initially felt that the apparent shift in this peak was associated with the intrinsic lattice strain of a pseudo-cubic shell phase. However, it seems more likely that the abrupt shift in position for an electric field above 3 kV mm^{-1} is actually associated with domain switching in a long range-ordered ferroelectric phase.

The irreversible nature of the peak shift, together with the high remanent polarization reported above for quenched-LaBa (Figure 5(c)), suggest that the evolution of the $\{111\}_p$ peak profile under an electric field is dominated by variations in the relative intensities of the $(111)_{SH}$ and $(\bar{1}11)_{SH}$ peaks (using pseudo-cubic indices), which indicates the occurrence of ferroelectric domain

switching in the shell regions. The implication of these observations is that the shell regions in the quenched-LaBa ceramics are in a *non-ergodic* relaxor ferroelectric state and are transformed into ordered ferroelectric domains having rhombohedral symmetry under the influence of the electric field. The $(111)_{CO}$ and $(\bar{1}11)_{CO}$ peaks associated with the core regions are more widely separated due to the higher rhombohedral distortion of the $BiFeO_3$-rich phase and do not exhibit such clear indications of domain switching, although this is masked by overlap with the more dominant $(111)_{SH}$ and $(\bar{1}11)_{SH}$ peaks.

In the remanent state (Figure 8(b)), the changes in the relative intensities of the $(111)_{SH}$ and $(\bar{1}11)_{SH}$ peaks as a function of the azimuthal angle, ψ, are a direct indication of the preferred orientation of ferroelectric domains after poling under an electric field of 5 kV mm^{-1}. The invariance in the positions of the $(111)_{SH}$ and $(\bar{1}11)_{SH}$ peaks provides further evidence that the apparent shift in peak position is caused by variations in the relative intensities of these peaks due to domain switching rather than lattice strain in a single pseudo-cubic peak. Similar observations were made previously in the analysis of lattice strain and ferroelectric domain orientation distributions in poled rhombohedral PZT ceramics.[106]

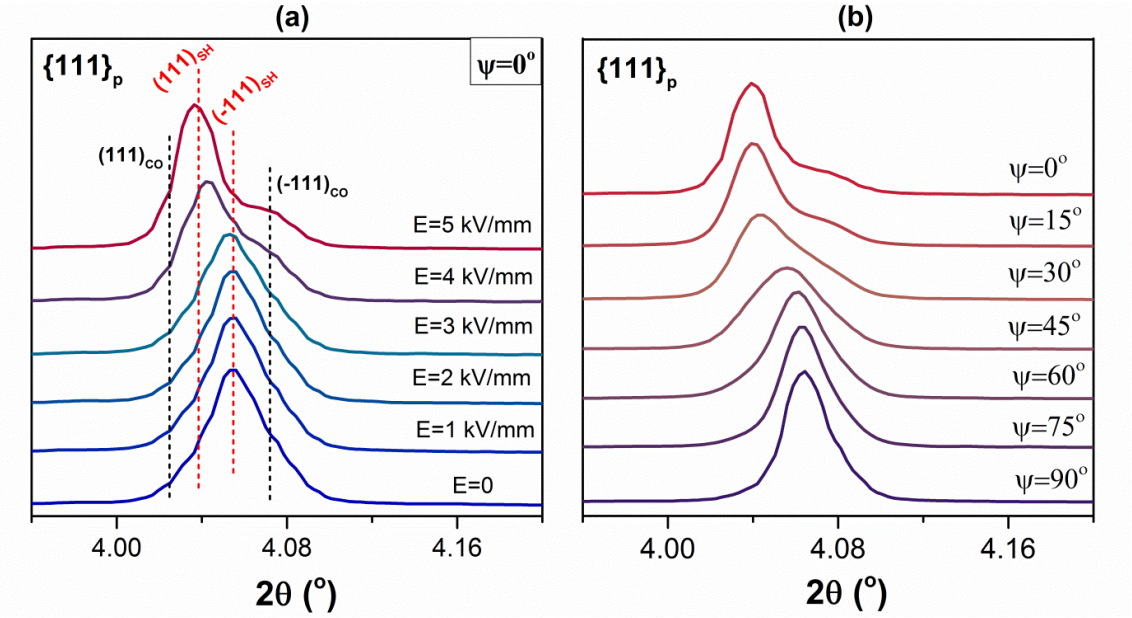

Figure 8 Changes in $\{111\}_p$ peak profiles for quenched-LaBa ceramic due to **(a)** increasing electric field and **(b)** grain orientation after poling. Dashed lines in (a) indicate the variations in the intensity of (111) and $(\bar{1}11)$ peaks due to ferroelectric domain switching in core and shell regions.

The anisotropy in electric field-induced strain, taking into account both the *intrinsic* lattice strain and the *extrinsic* transformation strain due to domain

switching, was quantified by determining the weighted-average peak positions, which were then converted into effective average lattice spacings, d_{hkl}, for several different crystallographic orientations. To accomplish this, peak profile fitting was carried out using a Pseudo-Voigt function within Matlab. The effective field-induced lattice strain associated with each reflection, ε_{hkl}, was then calculated from the initial d-spacing, d_{hkl} (0), as follows:

$$\varepsilon_{hkl}(E) = \frac{d_{hkl}(E) - d_{hkl}(0)}{d_{hkl}(0)}$$

The influence of the applied electric field on the weighted-average lattice strains for the $\{111\}_p$, $\{200\}_p$ and $\{220\}_p$ orientations in quenched-LaBa is illustrated by the results presented in Figure 9(a). The variations in strain can be correlated with the applied electric field, which underwent 2 complete bipolar cycles with an amplitude of 5 kV mm^{-1}. For each orientation, the lattice strain increased sharply on exceeding the coercive electric field around 3 kV mm^{-1} and then underwent a sequence of hysteretic variations in response to the ferroelectric domain switching events. The lattice strains parallel to the electric field direction, for ψ = 0°, were generally positive (tensile) while those in the transverse direction, ψ = 90°, were negative (compressive). This behaviour is consistent with the changes in macroscopic strain that result from poling polycrystalline ferroelectric ceramics.[106]

Although the effective lattice strains associated with different crystallographic orientations were generally correlated together, their magnitudes were strongly heterogeneous, with the values decreasing in the order $\varepsilon_{\{111\}} > \varepsilon_{\{220\}} > \varepsilon_{\{200\}}$. For example, under an electric field level of 5 kV mm^{-1} the lattice strains were recorded as ε_{111}=0.48%, ε_{220}=0.35% and ε_{200}=0.33%. This result supports the suggestion that the crystal structure of the active shell region is rhombohedral, since the largest transformation strains occur by ferroelectric domain switching along the polar <111> directions.

The macroscopic strain was estimated based on the weighted average of the effective lattice strains associated with different crystallographic orientations, according to equation shown below[54,107]

$$\varepsilon(\Psi) = \frac{\sum_{hkl} T_{hkl}\, m_{hkl}\, \varepsilon_{hkl}(\Psi)}{\sum_{hkl} T_{hkl}\, m_{hkl}}$$

where $\varepsilon(\psi)$ is the component of the macroscopic strain tensor for a given orientation, $\varepsilon_{hkl}(\psi)$ is the local lattice strain along the axis parallel to direction ψ for the *{hkl}* orientation, T_{hkl} is the texture index, and m_{hkl} is the multiplicity of the reflection for *{hkl}* planes. This expression relies on the assumption of isotropic

elasticity at the local scale, so that it is expected to give only indicative values.[54] Treating the material as cubic and with random grain texture, T_{hkl} reduces to 1 for any *hkl*, and m_{hkl} is 8, 6, and 12 for {111}, {200}, and {220} orientations, respectively.

The calculated macroscopic strains both parallel and perpendicular to the electric field direction, corresponding to $\psi=0^{\circ}$ and $\psi=90^{\circ}$ respectively, are presented in Figure 9(b). It can be seen that high field-induced strains, $\varepsilon(0^{\circ})\approx0.4\%$ and $\varepsilon(90^{\circ})\approx0.18\%$ at 5 kV mm^{-1}, were obtained for quenched-LaBa. Well-defined butterfly-type strain-field hysteresis loops were obtained, which are similar to those reported for other ferroelectric ceramic materials. In contrast, only a weak electrostrictive response was recorded for the as-sintered LaBa due to the lack of well-ordered ferroelectric domains in the shell regions. Isovalent substitution of La^{3+} in Bi^{3+} in the LaBi ceramics, without thermal quenching also yielded butterfly-type strain-field curves, but with a substantial reduction in magnitude relative to those of the quenched-LaBa. These results indicate that the application of a quenching procedure is vital to optimise the electromechanical properties of La-modified BF-BT ceramics. It seems likely that some nanoscale chemical heterogeneity could also be present in the as-sintered LaBi ceramic, in view of the relatively low electromechanical response in comparison with the quenched LaBa material.

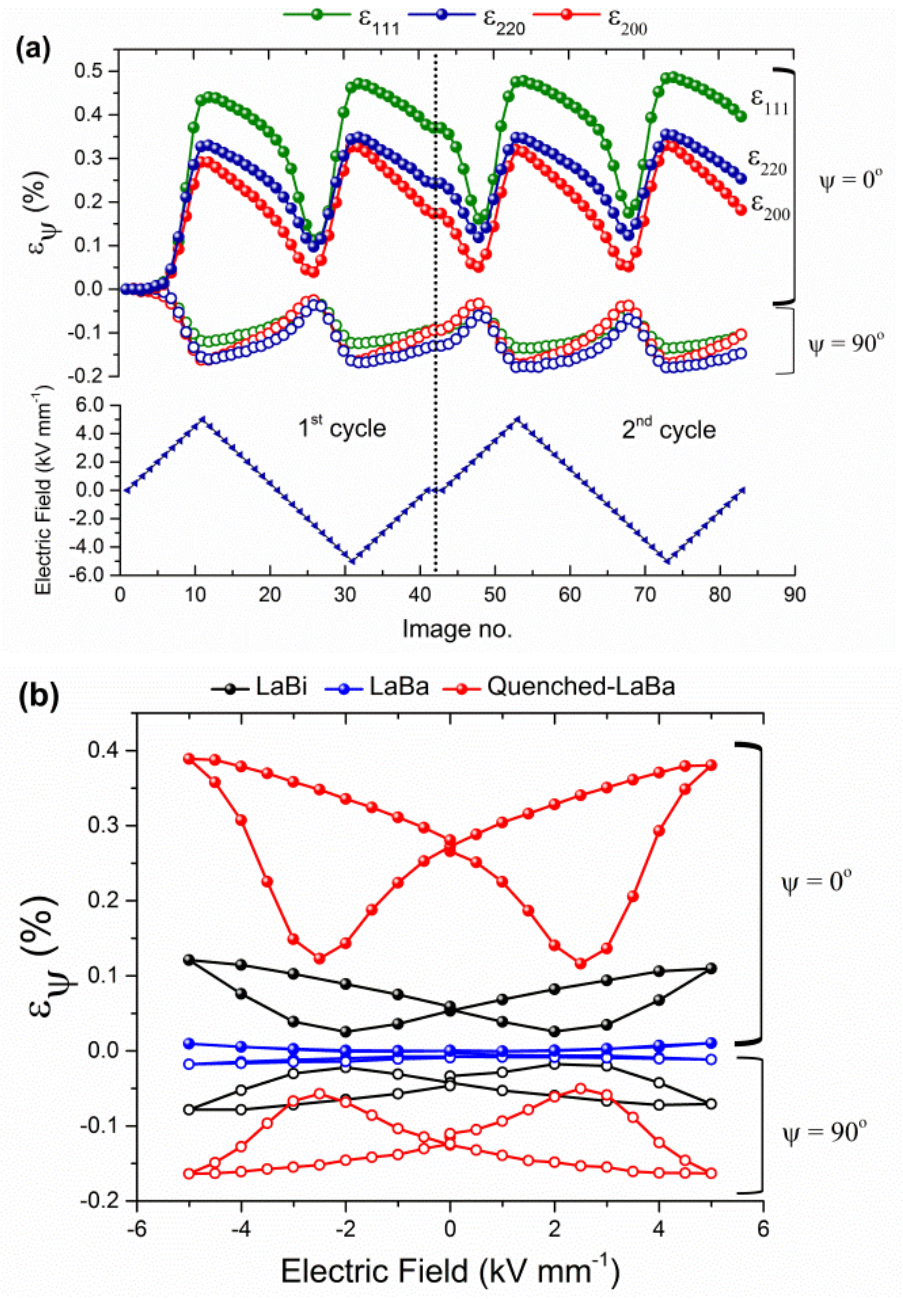

Figure 9 a) Microscopic lattice strain contrubitons of {111}, {200} and {220} for quenched-LaBa at Ψ=0˚ and Ψ=90˚. **b)** Macroscopic strain curves of all compositions at ψ=0˚ and ψ=90˚. Note that error bars are smaller than the marker size.

After 2 bipolar cycles shown above, the ceramics were subjected to a unipolar cycle to determine their effective piezoelectric coefficients, d_{33}^{ef} and d_{31}^{ef} (see Figure S4, Appendix II). It was found that the d_{33}^{ef} and d_{31}^{ef} values were 87 and -81 pm V^{-1} for LaBi, 207 and -100 pm V^{-1} for quenched-LaBa, respectively. These results are comparable with those derived from macroscopic strain-field measurements on other BF–BT ceramics in the as-sintered[27,32] or water-

quenched[9,108] state. It is anticipated that the piezoelectric activity would be improved for BF–BT compositions closer to the MPB at around 67% BF.

3.6 Magnetic Properties

The magnetic (M-H) hysteresis loops of the investigated compositions measured at room temperature, including the undoped 75BFBT, are illustrated in Figure 10. The hysteresis loop of undoped 75BFBT shows a very low but non-zero remanent magnetisation (0.0075 emu/g), indicating the canted antiferromagnetic behaviour (i.e. slightly canted antiparallel alignment of Fe^{3+} spins) which is likely due to occupancies of Ba^{2+} and Ti^{4+} in the $BiFeO_3$ matrix.[33,77] It is well-known that $BiFeO_3$ is G-type antiferromagnetic implying that the alignment of neighbouring Fe magnetic moments is antiparallel.[4] Therefore, the key to enhance the ferromagnetism in $BiFeO_3$ is to disrupt the intrinsic spiral spin structure through foreign ion substitution, as reported previously.[13,109–111]

In the present case, a small amount of La substitution at the A-site effectively increased the ferromagnetic moment, even though the substituent ion is known to be diamagnetic.[13] It can be noticed that the loops are not fully saturated under an applied magnetic field of 20 kOe. However, weak ferromagnetic moments with remanent magnetisation, M_r, values of 0.17, 0.12 and 0.042 emu/g were obtained for LaBi, LaBa, and quenched-LaBa, respectively. It is evident that M_r was increased by isovalent substitution of La^{3+} for Bi^{3+}, whilst it was decreased by donor substitution of La^{3+} for Ba^{2+}. Since the chemical heterogeneity and structural distortion in LaBi was not as pronounced as that in LaBa, the increase of M_r (relative to the unmodified 75BFBT) could be due to disruption of the spatially modulated spin cycloidal structure of the $BiFeO_3$ matrix. However, the micro-segregation of $BiFeO_3$-rich and -depleted regions in the form of core-shell type grain structures makes the interpretation of the loops more complicated for the LaBa ceramics.

It has been shown that the ferromagnetic properties of $BiFeO_3$-based multiferroics are dramatically influenced by structural defects[109,112]. Indeed, even small deviations from the ideal cation–anion stoichiometry can induce the formation of lattice defects, which interfere with the antiferromagnetic ordering and lead to weak ferromagnetic behaviour.[24,109,112] The observation of weak ferromagnetism with a substantial reduction in the magnetic coercive field, H_C, for the as-sintered LaBa in comparison with LaBi could be associated with higher defect populations in the donor-type LaBa. The occurrence of core-shell grain microstructures with poor ferroelectric switching behaviour and relaxor

ferroelectric character in the shell regions for the as-sintered LaBa ceramics provides qualitative evidence for nanoscale phase segregation within the shell or at the interface.

For the case of quenched-LaBa, it can be observed that M_r was significantly reduced after thermal quenching. The cause of this reduction could be associated with changes in the oxygen vacancy concentrations, since it is anticipated that thermal quenching might 'freeze-in' a higher concentration of oxygen vacancies than that of the as-sintered material.[113] On the other hand, the influence of quenching on chemical heterogeneity in the shell regions, which has already been linked to dramatic improvements in the ferroelectric switching behaviour, could provide a more likely explanation for the reduction in M_r. Improvements in ferroelectric properties accompanied by weak ferromagnetic behaviour were also reported by Zhang, who studied the effects of quenching on $BiFeO_3$.[68] Further investigations involving high resolution TEM and Magnetic Force Microscopy are required to confirm the nature of such nanoscale defects and their influence on magnetic properties.

An additional factor that should always be taken into account when considering the origin of weak ferromagnetism in $BiFeO_3$-based ceramics is the presence of parasitic ferromagnetic phases such as Fe_2O_3 or Fe-enriched secondary phases forming during sintering. Close inspection of the high resolution SXPD data does not reveal any prominent secondary phases, although a high background in the patterns could hinder their observation. Nevertheless, small amounts of Fe-rich phases were detected in the LaBi ceramics (see the Figure S3, Appendix II). However the chemical composition of these phases could not be determined accurately by point analysis in SEM-EDS due to their small sizes and high Bi irradiation interfering with the signal collection. Based on previous reports on $BiFeO_3$-based ceramics[6,12,36,110], $Bi_2Fe_4O_9$ is a common Fe-rich secondary phase however it is paramagnetic. A small amount of unreacted Fe_2O_3 could also potentially be present, but its magnetic coercive field ($H_C \approx 100$ Oe) is very low compared to that found for LaBi ($H_C \approx 2700$ Oe).

A recent report by Khomchenko[109] provided similar observations of a Fe-rich phase in $Bi_{0.9}Ba_{0.1}Fe_{0.9}Ti_{0.1}O_3$, with the chemical composition being reported as Ti-doped $BaFe_{12}O_{19}$. It was suggested that there was a close correlation between the H_C of the detected secondary phase and the studied composition ($H_C \approx 3000$ Oe), similarly to the present case. Thus, the contribution of a ferromagnetic parasitic phase cannot completely be ruled out and the ferromagnetic properties of LaBi ceramics should be interpreted with due consideration for this possibility. On the other hand, further systematic studies on increasing La substitution for both Bi

and Ba in 75BFBT showed a gradual increase in magnetisation, which was found to be moderately independent of grain size variation and chemical heterogeneity (see the Figure S5, Appendix II). Additional powder neutron diffraction studies[111] to investigate magnetic Bragg reflections would be useful to provide deeper understanding of the (anti)ferromagnetic nature of the studied compositions.

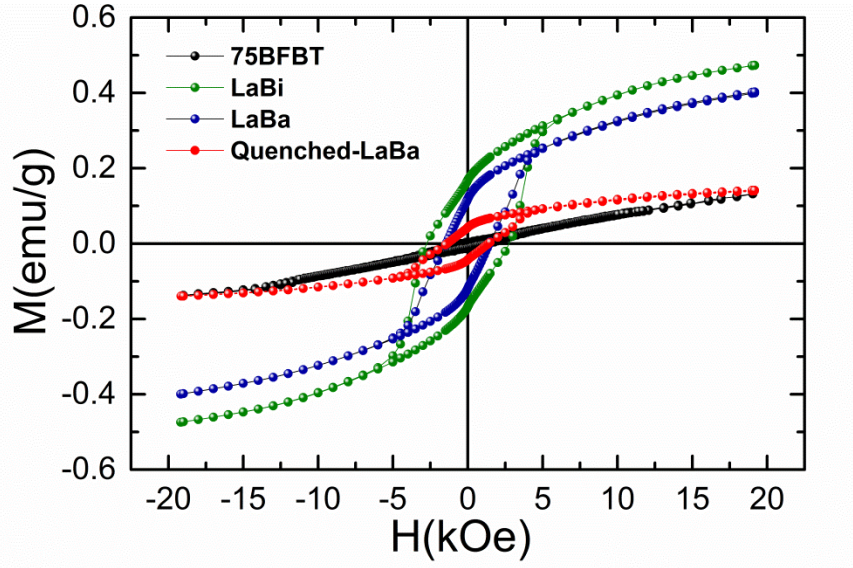

Figure 10 Ferromagnetic (M-H) hysteresis loops of undoped 75BFBT, LaBi, LaBa and quenched-LaBa measured at room temperature.

The changes in magnetoelectric (ME) coefficient α_{ME} as a function of the dc bias magnetic field H, measured at room temperature, for LaBi, LaBa and quenched-LaBa ceramics are presented in Figure 11(a). As the poling field increased from 0.15 to 3.5 kV mm^{-1}, α_{ME} for quenched-LaBa increased from 1.68 to 6.20 mV/cm Oe at 1 Tesla and from 1.98 to 7.40 mV/cm Oe at 7 Tesla. The influence of chemical composition and processing procedures shows a good general correlation with the ferroelectric behaviour and domain switching characteristics described in sections 3.4 and 3.5 respectively. The observation of a monotonic increase in α_{ME} with increasing magnetic field at low and high poling fields for all compositions indicates the coupling between polarisation and magnetisation. As the applied magnetic field increases, then deformation occurs due to the effect of magnetostriction, which couples to the polar phase through piezoelectricity. It has been suggested in many reports[114,115] that the ME properties could effectively be enhanced by constructing a composite comprising a ferromagnetic core coupled elastically to a piezo/ferroelectric shell. Thus, the higher ME coupling for the quenched-LaBa could be a consequence of its enhanced electro-mechanical strain and composite-like microstructure.

In the case of LaBa and quenched-LaBa, it was found that the core consists of a $BiFeO_3$-rich multiferroic phase while the shell is a $BaTiO_3$-rich relaxor or normal long-range ordered ferroelectric, depending on the cooling conditions (as-sintered or quenched state). As discussed in sections 3.4 and 3.5, ferroelectric switching in LaBa is restricted due to the relaxor ferroelectric nature of the shell, which results in a low ME interaction. However, it is apparent that that transformation of the shell component from PNRs to long-range ordered ferroelectric domains by thermal quenching could potentially have a profound effect on the bulk magnetoelectric coupling at room temperature, as shown in Figure 11(a), despite the lower saturation and remanent magnetisation values (Figure 10). Thus, the ME effect in such structures could be dependent on the coexistence of ferroelectric and multiferroic phases, as well as the elastic coupling between them.

The temperature dependencies of the ME coefficients, presented in Figure 11(b), show a maximum in α_{ME} around ≈320˚C for LaBi and ≈363˚C for both LaBa and quenched-LaBa. These maxima in the α_{ME}-T curves can be attributed to strong magnetoelectric ordering near the (anti)ferromagnetic phase transition at the Neel Temperature, T_N. It is interesting to note that the reported T_N value for single phase $BiFeO_3$ is ≈370˚C,[4] which is close to the observed transition points for LaBa and quenched-LaBa. It was shown previously that chemical heterogeneity, in the form of core-shell type microstructures, was persistent in both ceramics, regardless of the structural changes induced by quenching. Therefore, the magnetoelectric response is likely to arise mostly from the $BiFeO_3$–rich phase in the core regions. However, in the case of LaBi the lack of a clear core-shell structure leads to a more transformation with a reduced transition temperature, indicating that the distribution of the ferroelectric and (anti)ferromagnetic phases is more homogeneous. The reduction in T_N is consistent with previous reports on BF-BT ceramics.[77] Such transitions are sometimes correlated with anomalies in the dielectric properties of multiferroics such as $YMnO_3$,[116] $BiMnO_3$,[117] and $BiFeO_3$[4,118] and interpreted as evidence for magnetoelectric coupling. Thus, the remarkable increase in α_{ME} near T_N can be interpreted as a strong coupling between magnetic field and the polarisation, which could contribute to the increased dielectric response in the vicinity of T_1 in the quenched-LaBa composition.

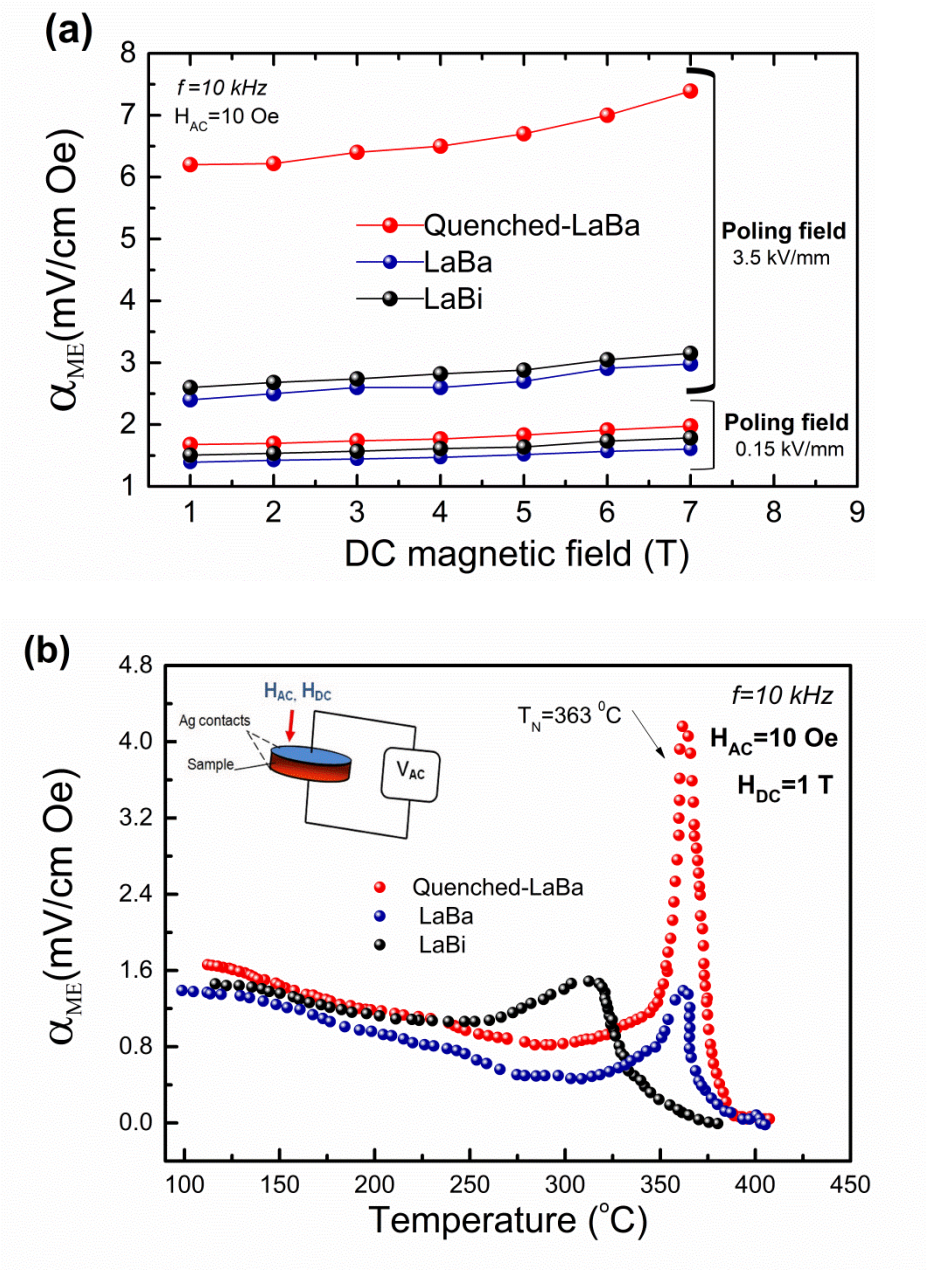

Figure 11 a) Variations in magnetoelectric voltage coefficient, α_{ME}, at poling fields of 0.15 and 3.5 kV mm^{-1} as a function of DC magnetic field at room temperature, **b)** α_{ME} as a function of temperature with a fixed magnetic field (poling field=0.15 kV mm^{-1}).

4. CONCLUSIONS

It has been shown that the microstructure development in 1 mol% La-doped $0.75BiFeO_3$-$0.25BaTiO_3$ (75BFBT) ceramics is strongly dependent on the dopant incorporation strategy, with isovalent substitution yielding relatively homogeneous large-grained structures and donor substitution leading to the formation of fine-grained core-shell type morphology. The ferroelectric switching behaviour in the donor-substituted ceramics was relatively constrained due to its relaxor ferroelectric character, yielding a dielectric energy storage density of 0.61 J cm^{-3} at an electric field of 10 kV mm^{-1}. Enhancement of the ferroelectric characteristics due to air-quenching was attributed to transformation of the pseudo-cubic ergodic relaxor shell phase into a rhombohedral non-ergodic state as a result of improved chemical homogeneity on the nanoscale. This supposition is supported by modifications in the dielectric permittivity-temperature relationships and investigations of the electromechanical actuation mechanisms using in-situ x-ray diffraction, which showed that the electric field-induced strain is dominated by ferroelectric domain switching in the shell regions. Magnetic measurements confirm the weak ferromagnetism in La-modified 75BFBT ceramics, which show significant variations in magnetisation and magnetoelectric properties depending on the processing methods.

Although the as-sintered donor-doped ceramics exhibit constrained ferroelectric switching characteristics, research into their composition-structure-property relationships may bring new insight into the multifunctional properties of $BiFeO_3$-based ceramics and nanocomposites. Additional studies exploring higher dopant levels, different BF/BT ratios, modified heat treatment procedures and nanoscale imaging would help to clarify the influence of the core-shell microstructures on magnetoelectric properties.

Acknowledgements

We thank Diamond Light Source for access to beamlines I11 (proposal number EE17673) and I15 (proposal number EE16390-1) that contributed to the results presented here. The assistance of Dr Stephen Thompson, Dr Claire Murray and Prof Chiu Tang is gratefully acknowledged. The authors are grateful to Dr Kamal G. Abdulvakhidov (Smart Materials Research Center Southern Federal University, Rostov-on-Done, Russia) for helping in magnetic measurements. Magnetic property investigations partially were supported by project “Phase transitions, magnetotransport, magnetocaloric, magnetoelectric phenomena in strongly correlated electron systems” (№ 0203-2016-0009). The authors thank

Prof Ian M. Reaney (Department of Materials Science and Engineering, University of Sheffield, Sheffield, UK) and Dr Alexander Khort (A.V Luikov Heat and Mass Transfer Institute of National Academy of Sciences of Belarus, Minsk, Belarus) for helpful discussion. I. Calisir also thanks the National Education of Turkish Republic for financial support throughout his PhD programme.

5. REFERENCES

1. Rödel, J. *et al.* Transferring lead-free piezoelectric ceramics into application. *J. Eur. Ceram. Soc.* **35,** 1659–1681 (2015).

2. Hong, C.-H. *et al.* Lead-free piezoceramics – Where to move on? *J. Mater.* **2,** 1–24 (2016).

3. Rödel, J. *et al.* Perspective on the development of lead-free piezoceramics. *J. Am. Ceram. Soc.* **92,** 1153–1177 (2009).

4. Catalan, G. & Scott, J. F. Physics and applications of bismuth ferrite. *Adv. Mater.* **21,** 2463–2485 (2009).

5. Ortega, N., Kumar, A., Scott, J. F. & Katiyar, R. S. Multifunctional magnetoelectric materials for device applications. *J. Phys. Condens. Matter* **27,** 504002 (2015).

6. Rojac, T. *et al.* $BiFeO_3$ Ceramics: Processing, electrical, and electromechanical properties. *J. Am. Ceram. Soc.* **97,** 1993–2011 (2014).

7. Ibn-Mohammed, T. *et al.* Integrated hybrid life cycle assessment and supply chain environmental profile evaluations of lead-based (lead zirconate titanate) versus lead-free (potassium sodium niobate) piezoelectric ceramics. *Energy Environ. Sci.* **9,** 3495–3520 (2016).

8. Leontsev, S. O. & Eitel, R. E. Progress in engineering high strain lead-free piezoelectric ceramics. *Sci. Technol. Adv. Mater.* **11,** 044302 (2010).

9. Lee, M. H. *et al.* High-performance lead-free piezoceramics with high curie temperatures. *Adv. Mater.* **27,** 6976–6982 (2015).

10. Beuerlein, M. A. *et al.* Current understanding of structure-processing-property relationships in $BaTiO_3$-$Bi(M)O_3$ dielectrics. *J. Am. Ceram. Soc.* **99,** 2849–2870 (2016).

11. Wang, L., Yang, C.-H. & Wen, J. Physical principles and current status of emerging non-volatile solid state memories. *Electron. Mater. Lett.* **11,** 505–543 (2015).

12. Selbach, S. M., Einarsrud, M. & Grande, T. On the thermodynamic stability of $BiFeO_3$. *Chem. Mater.* **21,** 169–173 (2009).

13. Perejón, A. *et al.* Single phase, electrically insulating, multiferroic La-substituted $BiFeO_3$ prepared by mechanosynthesis. *J. Mater. Chem. C* **2,** 8398–8411 (2014).

14. Kumar, M. & Yadav, K. L. Rapid liquid phase sintered Mn doped $BiFeO_3$ ceramics with enhanced polarization and weak magnetization. *Appl. Phys. Lett.* **91,** 242901 (2007).

15. Suresh, P. & Srinath, S. Effect of synthesis route on the multiferroic properties of $BiFeO_3$: A comparative study between solid state and sol-gel methods. *J. Alloys Compd.* **649,** 843–850 (2015).

16. Reddy, V. R. *et al.* Reduced leakage current of multiferroic $BiFeO_3$ ceramics with microwave synthesis. *Ceram. Int.* **40,** 4247–4250 (2014).

17. Yang, C., Kan, D., Takeuchi, I., Nagarajan, V. & Seidel, J. Doping $BiFeO_3$: approaches and enhanced functionality. *Phys. Chem. Chem. Phys.* **14,** 15953–15962 (2012).

18. Walker, J. *et al.* Temperature dependent piezoelectric response and strain–electric-field hysteresis of rare-earth modified bismuth ferrite ceramics. *J. Mater. Chem. C* **4,** 7859–7868 (2016).

19. Zhang, L. & Yu, J. Residual tensile stress in robust insulating rhombohedral $Bi_{1-x}La_xFe_{1-y}Ti_yO_3$ multiferroic ceramics and its ability to pin ferroelectric polarization switching. *Appl. Phys. Lett.* **106,** 112907 (2015).

20. Uniyal, P. & Yadav, K. L. Pr doped bismuth ferrite ceramics with enhanced multiferroic properties. *J. Phys.Condens. Matter* **21,** 405901 (2009).

21. Trivedi, P. *et al.* Modifications in the electronic structure of rare-earth doped $BiFeO_3$ multiferroic. *Solid State Commun.* **222,** 5–8 (2015).

22. Arnold, D. C. Composition-driven structural phase transitions in rare-earth-doped $BiFeO_3$ ceramics : A review. *IEEE Trans. Ultrason. Ferroelectr. Freq. Control* **62,** 62–82 (2015).

23. Karimi, S., Reaney, I. M., Han, Y., Pokorny, J. & Sterianou, I. Crystal chemistry and domain structure of rare-earth doped $BiFeO_3$ ceramics. *J. Mater. Sci.* **44,** 5102–5112 (2009).

24. Bernardo, M. S. *et al.* Intrinsic compositional inhomogeneities in bulk Ti-doped $BiFeO_3$: Microstructure development and multiferroic properties. *Chem. Mater.* **25,** 1533–1541 (2013).

25. Azough, F. *et al.* Microstructure and properties of Co- , Ni- , Zn- , Nb- and W-modified multiferroic $BiFeO_3$ ceramics. *J. Eur. Ceram. Soc.* **30,** 727–736 (2010).

26. Freitas, V. F. *et al.* Structural phase relations in perovskite-structured $BiFeO_3$-based multiferroic compounds. *J. Adv. Ceram.* **2,** 103–111 (2013).

27. Leontsev, S. O. & Eitel, R. E. Dielectric and piezoelectric properties in Mn-modified (1-x)$BiFeO_3$–x$BaTiO_3$ ceramics. *J. Am. Ceram. Soc.* **92,** 2957–2961 (2009).

28. Lennox, R. C. *et al.* PZT-like structural phase transitions in the $BiFeO_3$–$KNbO_3$ solid solution. *Dalt. Trans.* **44,** 10608–10613 (2015).

29. Lin, D. *et al.* Microstructure, ferroelectric and piezoelectric properties of $Bi_{0.5}K_{0.5}TiO_3$-modified $BiFeO_3$–$BaTiO_3$ lead-free ceramics with high Curie temperature. *J. Eur. Ceram. Soc.* **33,** 3023–3036 (2013).

30. Yabuta, H. *et al.* Microstructure of $BaTiO_3$–$Bi(Mg_{1/2}Ti_{1/2})O_3$–$BiFeO_3$ piezoelectric ceramics. *Jpn. J. Appl. Phys.* **51,** 09LD04 (2012).

31. Sebastian, T. *et al.* High temperature piezoelectric ceramics in the $Bi(Mg_{1/2}Ti_{1/2})O_3$-$BiFeO_3$-$BiScO_3$-$PbTiO_3$ system. *J. Electroceramics* **25,** 130–134 (2010).

32. Wei, J., Fu, D., Cheng, J. & Chen, J. Temperature dependence of the dielectric and piezoelectric properties of x$BiFeO_3$–(1-x)$BaTiO_3$ ceramics near the morphotropic phase boundary. *J. Mater. Sci.* **52,** 10726–10737 (2017).

33. Kumar, M. M., Srinivas, A. & Suryanarayana, S. V. Structure property relations in $BiFeO_3$/$BaTiO_3$ solid solutions. *J. Appl. Phys.* **87,** 855–862 (2000).

34. Leontsev, S. O. & Eitel, R. E. Origin and magnitude of the large piezoelectric response in the lead-free (1– x)$BiFeO_3$– x$BaTiO_3$ solid solution. *J. Mater. Res.* **26,** 9–17 (2011).

35. Amorín, H. *et al.* Very high remnant polarization and phase-change electromechanical response of $BiFeO_3$ -$PbTiO_3$ at the multiferroic morphotropic phase boundary. *Appl. Phys. Lett.* **101,** 172908 (2012).

36. Valant, M., Axelsson, A. & Alford, N. Peculiarities of a solid-state synthesis of multiferroic polycrystalline $BiFeO_3$. *Chem. Mater.* **19,** 5431–5436 (2007).

37. Guo, Y. *et al.* Critical roles of Mn-ions in enhancing the insulation, piezoelectricity and multiferroicity of $BiFeO_3$-based lead-free high temperature ceramics. *J. Mater. Chem. C* **3,** 5811–5824 (2015).

38. Joo, H. W., Kim, D. S., Kim, J. S. & Cheon, C. I. Piezoelectric properties of Mn-doped $0.75BiFeO_3{-}0.25BaTiO_3$ ceramics. *Ceram. Int.* **42,** 10399–10404 (2016).

39. Calisir, I. & Hall, D. A. Chemical heterogeneity and approaches to its control in $BiFeO_3$–$BaTiO_3$ lead-free ferroelectrics. *J. Mater. Chem. C* **6,** 134–146 (2018).

40. Wang, D. *et al.* Temperature dependent, large electromechanical strain in Nd-doped $BiFeO_3$-$BaTiO_3$ lead-free ceramics. *J. Eur. Ceram. Soc.* **37,** 1857–1860 (2017).

41. Zhou, C. *et al.* Dielectric, ferroelectric and piezoelectric properties of La-substituted $BiFeO_3$–$BaTiO_3$ ceramics. *Ceram. Int.* **39,** 4307–4311 (2013).

42. Yu, B. *et al.* Effects of ion doping at different sites on electrical properties of multiferroic $BiFeO_3$ ceramics. *J. Phys. D. Appl. Phys.* **41,** 065003 (2008).

43. Culver, S. P., Stepanov, V., Mecklenburg, M., Takahashi, S. & Brutchey, R. L. Low temperature synthesis and characterization of lanthanide-doped $BaTiO_3$ nanocrystals. *Chem. Commun.* **50,** 3480 (2014).

44. Makovec, D., Samardzija, Z., Delalut, U. & Kolar, D. Defect structure and phase relations of highly lanthanum-doped barium titanate. *J. Am. Ceram. Soc.* **78,** 2193–2197 (1995).

45. West, A. R., Adams, T. B., Morrison, F. D. & Sinclair, D. C. Novel high capacitance materials: $BaTiO_3$:La and $CaCu_3Ti_4O_{12}$. *J. Eur. Ceram. Soc.* **24,** 1439–1448 (2004).

46. Castro, M. S., Salgueiro, W. & Somoza, A. Electron paramagnetic resonance and positron annihilation study of the compensation mechanisms in donor-doped $BaTiO_3$ ceramics. *J. Phys. Chem. Solids* **68,** 1315–1323 (2007).

47. Liu, N. *et al.* Large remanent polarization and enhanced magnetic properties in non-quenched $Bi(Fe,Ga)O_3$-$(Ba,Ca)(Zr,Ti)O_3$ multiferroic ceramics. *Appl. Phys. Lett.* **110,** 112902 (2017).

48. Kim, D. S., Cheon, C. Il, Lee, S. S. & Kim, J. S. Effect of cooling rate on phase transitions and ferroelectric properties in $0.75BiFeO_3$-$0.25BaTiO_3$ ceramics. *Appl. Phys. Lett.* **109,** 202902 (2016).

49. Kim, S. *et al.* Revealing the role of heat treatment in enhancement of electrical properties of lead-free piezoelectric ceramics. *J. Appl. Phys.* **122,** 014103 (2017).

50. Li, Q., Wei, J., Tu, T., Cheng, J. & Chen, J. Remarkable piezoelectricity and stable high-temperature dielectric properties of quenched $BiFeO_3$-$BaTiO_3$ ceramics. *J. Am. Ceram. Soc.* **100,** 5573–5583 (2017).

51. Wang, T. *et al.* Microstructure and ferroelectric properties of Nb_2O_5-modified $BiFeO_3$-$BaTiO_3$ lead-free ceramics for energy storage. *Mater. Lett.* **137,** 79–81 (2014).

52. Fan, Q. *et al.* Normal-to-relaxor ferroelectric phase transition and electrical properties in Nb-modified $0.72BiFeO_3$-$0.28BaTiO_3$ ceramics. *J. Electroceramics* **36,** 1–7 (2016).

53. Filik, J. *et al.* Processing two-dimensional X-ray diffraction and small-angle scattering data in DAWN 2. *J. Appl. Crystallogr.* **50,** 959–966 (2017).

54. Daniel, L. *et al.* Revisiting the blocking force test on ferroelectric ceramics using high energy x-ray diffraction. *J. Appl. Phys.* **117,** 174104 (2015).

55. Stewart, M., Cain, M. G. & Hall, D. Ferroelectric hysteresis measurement & analysis. *NPL Rep. C. 152* 1–57 (1999).

56. Amirov, A. A. *et al.* Magnetoelectric interactions in $BiFeO_3$, $Bi_{0.95}Nd_{0.05}FeO_3$, and $Bi_{0.95}La_{0.05}FeO_3$ multiferroics. *Tech. Phys. Lett.* **34,** 760–762 (2008).

57. Park, Y. & Kim, Y. H. The Dielectric Temperature Characteristic of Additives Modified Barium-Titanate Having Core-Shell Structured Ceramics. *J. Mater. Res.* **10,** 2770–2776 (1995).

58. Park, Y. & Kim, H. Dielectric temperature characteristics of cerium-modified barium titanate based ceramics with core-shell grain structure. *J. Am. Ceram. Soc.* **80,** 106–112 (1997).

59. Hennings, D. & Rosenstein, G. Temperature-stable dielectrics based on chemically inhomogeneous $BaTiO_3$. *J. Am. Ceram. Soc.* **67,** 249–254 (1984).

60. Armstrong, T. R. & Buchanan, R. C. Influence of core-shell grains on the internal stress state and permittivity response of zirconia-modified barium titanate. *J. Am. Ceram. Soc.* **73,** 1268–1273 (1990).

61. Liu, X., Cheng, S. & Randall, C. The core-shell structure in ultrafine X7R dielectric ceramics. *J. Korean Phys. Soc.* **32,** S312 – S315 (1998).

62. Dean, J. S., Foeller, P. Y., Reaney, I. M. & Sinclair, D. C. A resource efficient design strategy to optimise the temperature coefficient of capacitance of $BaTiO_3$ -based ceramics using finite element modelling. *J. Mater. Chem. A* **4,** 6896–6901 (2016).

63. Yang, H. *et al.* Piezoelectric properties and temperature stabilities of Mn- and Cu-modified $BiFeO_3$-$BaTiO_3$ high temperature ceramics. *J. Eur. Ceram. Soc.* **33,** 1177–1183 (2013).

64. Koruza, J. *et al.* Formation of the core-shell microstructure in lead-free $Bi_{1/2}Na_{1/2}TiO_3$-$SrTiO_3$ piezoceramics and its influence on the electromechanical properties. *J. Eur. Ceram. Soc.* **36,** 1009–1016 (2016).

65. Shannon, R. D. Revised effective ionic radii and systematic studies of interatomic distances in halides and chaleogenides. *Acta Cryst.* **A 32,** 751–767 (1976).

66. Selbach, S. M., Tybell, T., Einarsrud, M. & Grande, T. Size-dependent properties of multiferroic $BiFeO_3$ nanoparticles. *Chem. Mater.* **19,** 6478–6484 (2007).

67. Singh, K., Acharya, S. A. & Bhoga, S. S. Nanosized ceria-based ceramics: A comparative study. *Ionics.* **12,** 295–301 (2006).

68. Zhang, S. T., Lu, M. H., Wu, D., Chen, Y. F. & Ming, N. B. Larger polarization and weak ferromagnetism in quenched $BiFeO_3$ ceramics with a distorted rhombohedral crystal structure. *Appl. Phys. Lett.* **87,** 262907 (2005).

69. Soda, M., Matsuura, M., Wakabayashi, Y. & Hirota, K. Superparamagnetism induced by polar nanoregions in relaxor ferroelectric (1-x)$BiFeO_3$–x$BaTiO_3$. *J. Phys. Soc. Japan* **80,** 043705 (2011).

70. Yoneda, Y., Yoshii, K., Kohara, S., Kitagawa, S. & Mori, S. Local structure of $BiFeO_3$–$BaTiO_3$ mixture. *Jpn. J. Appl. Phys.* **47,** 7590–7594 (2008).

71. Llobet, A., Frontera, C., García-Muñoz, J. L., Ritter, C. & Aranda, M. A. G. Chemical heterogeneity in a single phase: $Bi_{0.15}Ca_{0.85}MnO_3$, a case example of macroscopic phase segregation. *Chem. Mater.* **12,** 3648–3657 (2000).

72. Stephens, P. W. Phenomenological model of anisotropic peak broadening in powder diffraction. *J. Appl. Cryst.* **32,** 281–289 (1999).

73. Dolgos, M. *et al.* Chemical control of octahedral tilting and off-axis A cation displacement allows ferroelectric switching in a bismuth-based perovskite. *Chem. Sci.* **3,** 1426–1435 (2012).

74. Singh, A., Moriyoshi, C., Kuroiwa, Y. & Pandey, D. Evidence for local monoclinic structure, polarization rotation, and morphotropic phase transitions in (1-x)$BiFeO_3$-x$BaTiO_3$ solid solutions: A high-energy synchrotron x-ray powder diffraction study. *Phys. Rev. B* **88,** 024113 (2013).

75. Morozov, M. I., Einarsrud, M.-A. & Grande, T. Atmosphere controlled conductivity and Maxwell-Wagner relaxation in $Bi_{0.5}K_{0.5}TiO_3$-$BiFeO_3$ ceramics. *J. Appl. Phys.* **115,** 044104 (2014).

76. Ogihara, H., Randall, C. A. & Trolier-McKinstry, S. Weakly coupled relaxor behavior of $BaTiO_3$-$BiScO_3$ ceramics. *J. Am. Ceram. Soc.* **92,** 110–118 (2009).

77. Kiyanagi, R. *et al.* Structural and magnetic phase determination of (1-x)$BiFeO_3$-x$BaTiO_3$ solid solution. *J. Phys. Soc. Japan* **81,** 024603 (2012).

78. Wei, Y. *et al.* Polar order evolutions near the rhombohedral to pseudocubic and tetragonal to pseudocubic phase boundaries of the $BiFeO_3$-$BaTiO_3$ system. *Materials.* **8,** 8355–8365 (2015).

79. Yao, Z. *et al.* Greatly reduced leakage current and defect mechanism in atmosphere sintered $BiFeO_3$-$BaTiO_3$ high temperature piezoceramics. *J. Mater. Sci. Mater. Electron.* **25,** 4975–4982 (2014).

80. Cen, Z. *et al.* Structural, ferroelectric and piezoelectric properties of Mn-modified $BiFeO_3$-$BaTiO_3$ high-temperature ceramics. *J. Mater. Sci. Mater. Electron.* **24,** 3952–3957 (2013).

81. Liu, X., Xu, Z., Qu, S., Wei, X. & Chen, J. Ferroelectric and ferromagnetic properties of Mn-doped 0.7$BiFeO_3$-0.3$BaTiO_3$ solid solution. *Ceram. Int.* **34,** 797–801 (2008).

82. Kan, D. *et al.* Universal behavior and electric-field-induced structural transition in rare-earth-substituted $BiFeO_3$. *Adv. Funct. Mater.* **20,** 1108–1115 (2010).

83. Tan, X., Ma, C., Frederick, J., Beckman, S. & Webber, K. G. The antiferroelectric ↔ ferroelectric phase transition in lead-containing and lead-free perovskite ceramics. *J. Am. Ceram. Soc.* **94,** 4091–4107 (2011).

84. Yuan, G. L., Yang, Y. & Or, S. W. Aging-induced double ferroelectric hysteresis loops in $BiFeO_3$ multiferroic ceramic. *Appl. Phys. Lett.* **91,** 122907 (2007).

85. Lo, V., Chung, W. W., Cao, H. & Dai, X. Investigating the effect of oxygen vacancy on the dielectric and electromechanical properties in ferroelectric ceramics. *J. Appl. Phys.* **104,** 064105 (2008).

86. Jo, W. *et al.* Giant electric-field-induced strains in lead-free ceramics for actuator applications - Status and perspective. *J. Electroceramics* **29,** 71–93 (2012).

87. Rojac, T., Kosec, M., Budic, B., Setter, N. & Damjanovic, D. Strong ferroelectric domain-wall pinning in $BiFeO_3$ ceramics. *J. Appl. Phys.* **108,** 074107 (2010).

88. Ke, S. *et al.* Tuning of dielectric and ferroelectric properties in single phase $BiFeO_3$ ceramics with controlled Fe^{2+}/ Fe^{3+} ratio. *Ceram. Int.* **40,** 5263–5268 (2014).

89. Walker, J. *et al.* Synthesis-phase-composition relationship and high electric-field-induced electromechanical behavior of samarium-modified $BiFeO_3$ ceramics. *Acta Mater.* **83,** 149–159 (2015).

90. Cheng, C.-J., Kan, D., Anbusathaiah, V., Takeuchi, I. & Nagarajan, V. Microstructure-electromechanical property correlations in rare-earth-substituted $BiFeO_3$ epitaxial thin films at morphotropic phase boundaries. *Appl. Phys. Lett.* **97,** 212905 (2010).

91. Cheng, C.-J. *et al.* Structural transitions and complex domain structures across a ferroelectric-to-antiferroelectric phase boundary in epitaxial Sm-doped $BiFeO_3$ thin films. *Phys. Rev. B* **80,** 014109 (2009).

92. Acosta, M. *et al.* Core-shell lead-free piezoelectric ceramics: Current status and advanced characterization of the $Bi_{1/2}Na_{1/2}TiO_3$-$SrTiO_3$ system. *J. Am. Ceram. Soc.* **98,** 3405–3422 (2015).

93. Liu, N. *et al.* Revealing the core-shell interactions of a giant strain relaxor ferroelectric $0.75Bi_{1/2}Na_{1/2}TiO_3$-$0.25SrTiO_3$. *Sci. Rep.* **6,** 36910 (2016).

94. Lv, J., Lou, X. & Wu, J. Defect dipole-induced poling characteristics and ferroelectricity of quenched bismuth ferrite-based ceramics. *J. Mater. Chem. C* **4,** 6140–6151 (2016).

95. Yang, H., Yan, F., Lin, Y., Wang, T. & Wang, F. High energy storage density over a broad temperature range in sodium bismuth titanate-based lead-free ceramics. *Sci. Rep.* **7,** 8726 (2017).

96. Yang, H. *et al.* A lead free relaxation and high energy storage efficiency ceramics for energy storage applications. *J. Alloys Compd.* **710,** 436–445 (2017).

97. Shen, Z., Wang, X., Luo, B. & Li, L. $BaTiO_3$–$BiYbO_3$ perovskite materials for energy storage applications. *J. Mater. Chem. A* **3,** 18146–18153 (2015).

98. Yang, Z. *et al.* Significantly enhanced recoverable energy storage density in potassium–sodium niobate-based lead free ceramics. *J. Mater. Chem. A* **4,** 13778–13785 (2016).

99. Mishra, A., Majumdar, B. & Ranjan, R. A complex lead-free (Na, Bi, Ba)(Ti, Fe)O_3 single phase perovskite ceramic with a high energy-density and high discharge-efficiency for solid state capacitor applications. *J. Eur. Ceram. Soc.* **37,** 2379–2384 (2017).

100. Tunkasiri, T. & Rujijanagul, G. Dielectric strength of fine grained barium titanate ceramics. *J. Mater. Sci. Lett.* **15,** 1767–1769 (1996).

101. Liu, B., Wang, X., Zhang, R. & Li, L. Grain size effect and microstructure influence on the energy storage properties of fine-grained $BaTiO_3$-based ceramics. *J. Am. Ceram. Soc.* **100,** 3599–3607 (2017).

102. Wu, L. *et al.* Core-satellite $BaTiO_3$@$SrTiO_3$ assemblies for a local compositionally graded relaxor ferroelectric capacitor with enhanced energy storage density and high energy efficiency. *J. Mater. Chem. C* **3,** 750–758 (2015).

103. Wu, L., Wang, X. & Li, L. Core-shell $BaTiO_3$@$BiScO_3$particles for local graded dielectric ceramics with enhanced temperature stability and energy storage capability. *J. Alloys Compd.* **688,** 113–121 (2016).

104. Wu, L., Wang, X. & Li, L. Enhanced Energy Density in Core-Shell Ferroelectric Ceramics: Modeling and Practical Conclusions. *J. Am. Ceram. Soc.* **99,** 930–937 (2016).

105. He, D., Wang, Y., Chen, X. & Deng, Y. Core-shell structured $BaTiO_3$@Al_2O_3 nanoparticles in polymer composites for dielectric loss suppression and breakdown strength enhancement. *Compos. Part A Appl. Sci. Manuf.* **93,** 137–143 (2017).

106. Hall, D. A., Steuwer, A., Cherdhirunkorn, B., Mori, T. & Withers, P. J. A high energy synchrotron x-ray study of crystallographic texture and lattice strain in soft lead zirconate titanate ceramics. *J. Appl. Phys.* **96,** 4245–4252 (2004).

107. Daniels, J. E., Finlayson, T. R., Studer, A. J., Hoffman, M. & Jones, J. L. Time-resolved diffraction measurements of electric-field-induced strain in tetragonal lead zirconate titanate. *J. Appl. Phys.* **101,** 094104 (2007).

108. Kim, S. *et al.* Structural and electrical characteristics of potential candidate lead-free $BiFeO_3$-$BaTiO_3$ piezoelectric ceramics. *J. Appl. Phys.* **122,** 164105 (2017).

109. Khomchenko, V. A., Karpinsky, D. V. & Paixão, J. A. Magnetostructural correlations in $BiFeO_3$-based multiferroics. *J. Mater. Chem. C* **5,** 3623–3629 (2017).

110. Lv, J., Zhao, H., Wu, M., Lou, X. & Wu, J. Modulating the electric and magnetic properties of $BiFeO_3$ ceramics. *Mater. Des.* **125,** 213–221 (2017).

111. Lennox, R. C. *et al.* Strain driven structural phase transformations in dysprosium doped $BiFeO_3$ ceramics. *J. Mater. Chem. C* **2,** 3345–3360 (2014).

112. Paudel, T. R., Jaswal, S. S. & Tsymbal, E. Y. Intrinsic defects in multiferroic $BiFeO_3$ and their effect on magnetism. *Phys. Rev. B* **85,** 104409 (2012).

113. Tamilselvan, A. *et al.* Role of oxygen vacancy and Fe–O–Fe bond angle in compositional, magnetic, and dielectric relaxation on Eu-substituted $BiFeO_3$ nanoparticles. *Dalt. Trans.* **43,** 5731–5738 (2014).

114. Nan, C.-W., Bichurin, M. I., Dong, S., Viehland, D. & Srinivasan, G. Multiferroic magnetoelectric composites: Historical perspective, status, and future directions. *J. Appl. Phys.* **103,** 031101 (2008).

115. Kumar, A. S. *et al.* Multiferroic and magnetoelectric properties of $Ba_{0.85}Ca_{0.15}Zr_{0.1}Ti_{0.9}O_3$-$CoFe_2O_4$ core-shell nanocomposite. *J. Magn. Magn. Mater.* **418,** 294–299 (2015).

116. Huang, Z. J., Cao, Y., Sun, Y. Y., Xue, Y. Y. & Chu, C. W. Coupling between the ferroelectric and antiferromagnetic orders in $YMnO_3$. *Phys. Rev. B* **56,** 2623–2626 (1997).

117. Kimura, T. *et al.* Magnetocapacitance effect in multiferroic in $BiMnO_3$. *Phys. Rev. B* **67,** 180401 (2003).

118. Kumari, S. *et al.* Dielectric anomalies due to grain boundary conduction in chemically substituted $BiFeO_3$. *J. Appl. Phys.* **117,** 114102 (2015).

Quenching-assisted actuation mechanisms in core-shell structured $BiFeO_3$–$BaTiO_3$ lead-free piezoceramics

Ilkan Calisir,[1] Annette K. Kleppe,[2] Antonio Feteira[3] and David A. Hall[1]

[1]School of Materials, University of Manchester, M13 9PL, Manchester, UK

[2]Diamond Light Source Ltd., Harwell Science and Innovation Campus, OX11 0DE, Didcot, UK

[3]Faculty of Science, Sheffield Hallam University, Technology and Arts (STA) City Campus, S1 1WB, Sheffield, UK

ABSTRACT

Large electromechanical actuation in piezoceramics is usually achieved by creating chemically homogeneous materials with structurally heterogeneous morphotropic phase boundaries, leading to abrupt changes in ion displacement directions within the perovskite unit cell. In the present study, an alternative mechanism to enhance electromechanical coupling has been found in both chemically and structurally heterogeneous $BiFeO_3$–$BaTiO_3$ (BF–BT) lead-free piezoceramics. Such a mechanism is observed in compositions exhibiting core-shell type microstructure, associated with donor-type substitution of Ti^{4+} for Fe^{3+}, and is primarily activated by a thermal quenching treatment. Here, we describe the use of *in-situ* high energy synchrotron X-ray powder diffraction to directly monitor the ferroelectric and elastic interactions between these composite-like components, denoted as *core* and *shell* regions within polycrystalline ceramics, upon the application of a high electric field. Analysis of the strain contributions from each phase are calculated, leading to the conclusion that the total macroscopic strain arises predominantly from the transformed shell after quenching.

Short- or long-range ordering in the shell is strongly correlated with the BF content in the BF–BT solid solutions, implying that the BF-rich materials undergo significant structural alterations, from pseudocubic *Pm-3m* relaxor-ferroelectric in conventional slow-cooled ceramics to untilted rhombohedral *R3c* or *R3m* with long-range ferroelectric order in the quenched state. Such observations are

complemented by investigations of microstructure and electrical properties, including ferroelectric behaviour and temperature-dependent dielectric properties. This study proposes a new type of actuation mechanism associated with various functional properties *via* engineering chemical/structural heterogeneity in a wide range of $BiFeO_3$-based solid solutions.

1. INTRODUCTION

Piezoceramics exhibit electromechanical coupling and thus generate relatively large displacements in the unit cell, yielding observable mechanical strain in response to an applied electric field and vice versa. This coupling means that piezoceramics are extensively used as electroactive materials in a number of applications requiring mechanical actuation (actuators), acoustic and resonance (transducers and ultrasonics) and sensing (sensors).[1,2] To achieve high electromechanical sensitivity and piezoelectric coefficients in piezoceramics, there has been a tremendous effort to understand the origin of the high piezoelectric response in both lead-based and lead-free ceramics. Most investigations on the search for lead-free replacements (arising due to the worldwide legislation to reduce the use of hazardous substances such as lead-based oxides including all sectors),[3] aim to achieve at least an equivalent performance to that of lead-based compounds. The search has been mainly focused on identifying the region or boundary, known as the morphotropic phase boundary (MPB), where associated piezoelectric activities are optimised in a solid solution, including piezoelectric coefficient d_{33}, electrostrain ε_{33}, relative permittivity ε_r and electromechanical coupling coefficient k_p, for example. Exhaustive compositional studies on the promising lead-free ceramics including sodium-bismuth-titanate (NBT)–, potassium-sodium-niobate (KNN), barium-calcium-zirconate-titanate (BCZT)– and bismuth-ferrite (BF)–based solid solutions have revealed the occurrence of such regions in those solid solutions, though the reported properties are often insufficient for use as a replacement for lead-based compounds.

Nevertheless, new mechanisms and approaches are still being reported and intriguing properties demonstrated. Such investigations exploit the high flexibility of the perovskite structure, doping strategies, abundance of oxides and their combinations, and composition- or temperature-dependent phase transformations. Novel phenomena have been reported, including the presence of incommensurate phases within multiphase coexistence region/boundary/points, ergodicity in relaxor ferroelectrics and microstructure design.

$BiFeO_3$ (BF) is regarded as a special multiferroic compound and has attracted great attention as a room temperature multiferroic.[4] Its solid solutions with other ABO_3-type perovskite end-members have recently been of great interest amongst ferro-piezoelectric polar dielectric materials, particularly after the issues associated with inherent high leakage current[4] and phase decomposition[5] were addressed successfully *via* doping[6–8] and synthesis strategies.[9] Particular attention can be drawn to $BiFeO_3$–$BaTiO_3$ (BF–BT) solid solutions, which have been intensively studied as promising candidates for high temperature piezoceramic applications,[8,10,11] surpassing the temperature capability of typical lead-based ferroelectrics. To date, the highest d_{33} in *x*BF–BT ceramics was reported as 402 pC/N, with a small amount of $BiGaO_3$ being incorporated in the composition with x=0.67; these ceramics were prepared by water-quenching and were assumed to have an MPB composition, with coexistence of rhombohedral and tetragonal phases.[10] However, this report still remains as the only one showing such a high d_{33} and claiming the presence of rhombohedral and tetragonal phase boundaries in a BF-BT -based solid solution.

Intriguingly, the influence of quenching treatment regardless of the factors including cooling methods[10,12] (*e.g.* liquid nitrogen, water, air, NaCl solution) and type of dopants[10,13,14] is readily accepted as an effective means to modify the piezo-ferroelectric performance in BF-based ceramics, including pristine $BiFeO_3$.[9] However, the underlying mechanism is yet to be understood fully and is under debate. For conventional acceptor-doped hard PZT and BT-based ferroelectrics, the quenching-induced enhancement in polarisation is mainly attributed to the re-orientation of charged defect associates, which generally become oriented along the local domain polarisation direction during an extended *ageing* period and thereby act to constrain domain wall motion.

The present work aims to shed light on the origin of enhancement in the electromechanical coupling as a result of thermal quenching treatments in BF-BT solid solutions. A wide composition range, from x=0.60 to 0.80, was selected to allow evaluation of its effects on crystal structure, microstructure and functional properties such as relaxor ferroelectric behaviour, electrostriction, energy storage density and T_c. In addition, a fine compositional adjustment involving the incorporation of 1 mol% Ti^{4+} as a donor substitution for Fe^{3+} has been applied to the selected compositions. Donor dopants play a key role in *soft* PZT ceramics, improving insulation resistance, enhancing domain wall mobility and hence increasing the piezoelectric performance.[15] In contrast, for BF-BT ceramics we have recently demonstrated that donor-doping with La^{3+} substituted for Ba^{2+} resulted in a unique core-shell type microstructure as a result of chemical phase segregation on the micro- and nano-scale, leading to significant degradation in

polarisation switching.[6] Moreover, the application of quenching significantly altered the crystal structure in the shell regions, accompanied by a dramatic enhancement in polarisation. Therefore, this study provides an extension of the previous investigation, covering a wider compositional range in the BF-BT solid solution and using Ti^{4+} as a B-site donor dopant.

The effect of quenching on the actuation mechanisms in core-shell structured BF-BT ceramics and its influence on the phase assemblages have been revealed by using in-situ high energy synchrotron diffraction techniques. The in-situ diffraction studies have given an unpresented insight into the understanding of this novel actuation mechanism, thereby providing a route to achieve high electromechanical response in newly designed piezoceramics.

2. EXPERIMENTAL PROCEDURES

2.1 Ceramic Processing and Electrical Measurements

1 mol% Ti-substituted ceramics were synthesised based on the chemical formula of $x\mathrm{Bi}(\mathrm{Fe}_{0.99}\ \mathrm{Ti}_{0.01})\mathrm{O}_3-(1-x)\mathrm{BaTiO}_3$; x = 0.60, 0.67, 0.75 and 0.80 by the solid state reaction method. 2 mol% Bi_2O_3 excess was also added in order to compensate for the loss of this volatile oxide during sintering. Bi_2O_3 (99%, Alfa Aesar), Fe_2O_3 (99%, Sigma Aldrich), $BaCO_3$ (99%, Alfa Aesar), and TiO_2 (99%, Fisher Scientific) were ball-milled in propan-2-ol for 24 h. The milled powders were dried overnight and calcined at 850 °C for 2 h. Additional milling was performed again on the calcined powders for 24 h. Polyethylene glycol (PEG1500 with an average molar mass of 1500 g mol^{-1}) solution as a lubricant was added into the calcined powders at a concentration of 2 *wt%* in order to improve compaction behaviour. The organic additive was burned-out at a temperature of 600°C for 1 h, followed by sintering at various temperatures of 1000, 1025 and 1050°C for 2 h in air, depending on the composition. The sintered pellets were annealed at 800°C for 20 min and then divided into two groups based on the cooling procedure: i) a slow cooling rate of 300°C/h, and ii) air-quenched to room temperature. The ceramics are hereafter denoted *slow-cooled* and *quenched*. The relative densities of the sintered ceramics were calculated in terms of the ratio of bulk to theoretical density, which were all found to be >90% during the present study.

Microstructures of chemically etched and non-etched surfaces were examined using a Philips XL30 FEGSEM equipped with EDS. More details on the SEM sample preparation can be found in Refs.[6,7]. Polarisation-electric field hysteresis measurements were carried out using a function generator (HP 33120A) connected to a Chevin Research HV amplifier to generate the desired high voltage. The samples were subjected to 4 cycles of a sinusoidal electric field with

a frequency of 2 Hz. The measured current waveform was integrated numerically over time to yield charge and hence the polarisation was calculated as the surface charge density.[16] Strain-electric field measurements were conducted at room temperature using AixACCT TF 2000 Ferroelectric analyser with a frequency of 0.1 Hz. Low-field dielectric measurements were carried out at fixed frequencies from 1 to 100 kHz over the temperature range from 25 to 670˚C using a HP 4284A Impedance Analyser, Carbolite CWF 12/5 furnace and a desktop computer which was operated by LabVIEW-based program. The measurements were conducted in air upon heating with a rate of 2˚C/min.

2.2 High Energy X-ray Diffraction Characterisation

The ceramic pellets for in-situ high energy x-ray diffraction experiments were prepared by cutting them into dimensions of approximately 0.5 mm (thickness) x 1 mm (width) x 4 mm (length). The experiment was performed on beamline I15 of the Diamond Light Source using high-energy, monochromatic X-rays with photon energy of 76 keV (λ =0.154982 Å). The X-ray beam size was 70 μm in diameter. A custom-designed sample holder was used to support the specimen in the beam and provide electrical contacts, the sample being immersed in silicone oil to avoid arcing during electric field application. The electric field was applied perpendicular to the beam direction using a high voltage amplifier (Matsusada ECA-10). The specimens were subjected to 2 bipolar cycles of an electric field up to 6 kV mm^{-1}, using a step size of 0.5 or 1.0 kV mm^{-1}, depending on the composition. 2D diffraction images were recorded using a Perkin-Elmer XRD 1621 flat-panel detector positioned ≈ 1.1 m from the sample, with a collection time of 10 s. The experimental setup is schematically illustrated in Figure 1. Grain orientations corresponding to the azimuthal angle, Ψ, either parallel or perpendicular to the electric field direction, are denoted as Ψ=0˚ and Ψ=90˚ respectively. In addition, a specific scattering vector of 54.7° was examined, under the assumption that the ferroelectric domain orientations are in a random state (texture-free) and there is zero lattice strain along this direction. The recorded 2D images were integrated into 24 sectors with a 15° interval using *DAWN* software,[17] yielding orientation-dependent 1D XRD patterns. The converted 1D data was later analysed using TOPAS *v*5 and Matlab for structural refinement and line profile fitting analysis respectively.

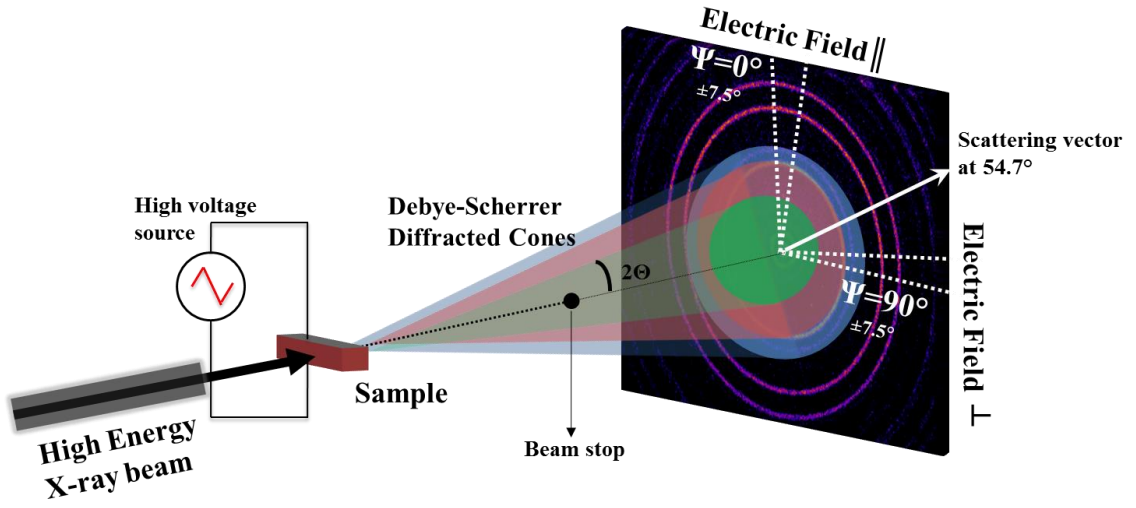

Figure 1 Experimental setup for in-situ high energy X-ray diffraction during application of electric field.

3. RESULTS AND DISCUSSION

3.1 Case study on 1 mol% Ti substituted-0.75$BiFeO_3$-0.25$BaTiO_3$

3.1.1 Phase content and Microstructure

Micrographs and X-ray diffraction patterns of 1 mol% Ti substituted-0.75$BiFeO_3$-0.25$BaTiO_3$ ceramics, for both slow-cooled and quenched ceramics are presented in Figure 2. Microstructural examination of the chemically- etched polished surfaces of the sintered ceramics is also shown in Figure 2(a) and (b) respectively. The appearance of ferroelectric-type domain structures can be clearly observed for both slow-cooled and quenched states, however the domain features are mainly concentrated in the central regions of the grains after slow cooling, while quenching led to additional domain features between the grain boundaries and the centres of the grains. Such features led us to investigate the polished surfaces without the application of etching; the occurrence of chemical heterogeneity was qualitatively confirmed using SEM in back-scattered electron mode (BSE) at high energy, as shown Figure 2(c). It is apparent that the grain boundaries and most grain centres consist of heavier elements giving lighter contrast under BSE mode, indicating that those regions are bismuth-rich, while the darker regions are lacking in bismuth, which is the heaviest element relative to Fe, Ba and Ti.

Since the solid solution is primarily composed of two perovskite phases, with end members $BiFeO_3$ and $BaTiO_3$, the observed regional contrast could be due to phase separation of these two components as a result of both thermodynamic and kinetic factors. This issue has been discussed in detail in our previous investigations of $BiFeO_3$–$BaTiO_3$ ceramics.[7] It is also noted that a minor amount of impurities were also detected, which appeared as the brightest contrast and

could indicate the presence of expelled or excess bismuth oxide. The segregated phases, determined as $BiFeO_3$–rich and –depleted regions, will hereinafter be referred to as *core* and *shell* regions, respectively. These results provide microstructural evidence of chemical heterogeneity at the micro-scale and will be used as the basis of discussions in the following sections.

The aforementioned chemical and domain heterogeneity within grains was also qualitatively confirmed using high energy X-ray diffraction, as illustrated in the detailed peak profiles of particular crystallographic orientations for {111}, {200}, {220} and {222} (Figure 2 (d)). The slow-cooled samples show a pseudocubic structure which is discernible by the absence of preferred orientation, namely lack of splitting of the {111} and {200} peaks. However weak additional peaks were evident along with the main pseudocubic reflections at higher scattering angles, corresponding to {220}, {221} and {222} reflections, thereby suggesting a coexistence of multiple phases. Furthermore, the application of quenching caused pronounced peak splitting of {111} and significant broadening of {200} peaks. This observation strongly suggests that crystal structure, which is multiphase due to the formation of the core-shell microstructure, undergoes significant transformations upon quenching.

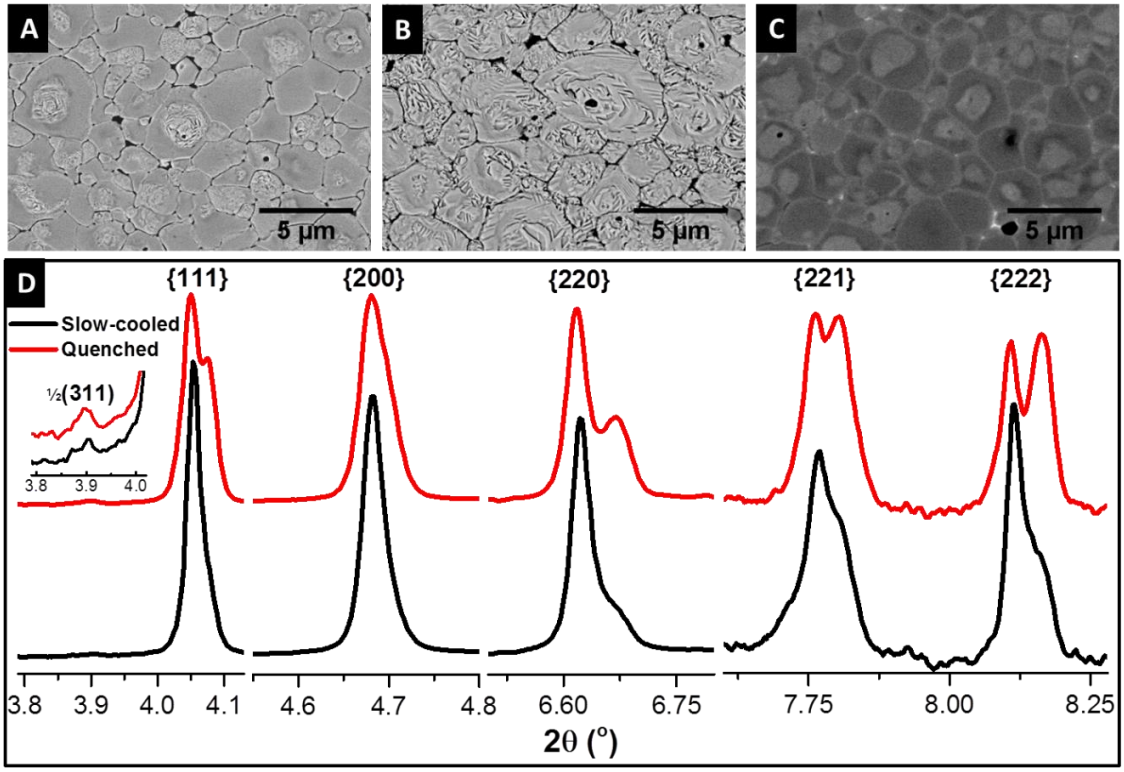

Figure 2 SEM micrographs and high energy XRD patterns of the BF-BT ceramics. Chemically-etched surfaces of **(a)** slow-cooled and **(b)** quenched ceramics, and **(c)** non-etched polished surface of the quenched ceramic. **(d)** High energy XRD profiles of slow-cooled and quenched ceramics for given crystallographic

orientations; inset shows the super-lattice reflections of ½(311) for slow-cooled and quenched ceramics.

Of particular note is a weak peak at $2\Theta \approx 3.9°$ in Figure 2(d), which represents the super-lattice peak, which is ½(311) indexed with respect to the pseudocubic unit cell. It is visible in the diffraction patterns obtained from both ceramics. This superlattice reflection corresponds to the $a^-a^-a^-$ tilt system in the space group *R3c* in Glazer's notation.[18] It is due to oxygen planes caused by antiferrodistortive rotation of oxygen octahedra with an antiphase tilt in relation to the neighbouring octahedra[5], and thus it has a low intensity due to the weak interactions between X-rays and light ions such as oxygen. As the microstructural evidence suggests that the core is present in both cases without prominent changes as compared to the transformed shell, it is concluded that the observed superlattice peak in both patterns corresponds to the common phase of the $BiFeO_3$-rich core.

3.1.2 Structural Analysis

In the light of these observations, Rietveld refinement was performed to identify the crystal structures of the phases present. The high energy x-ray diffraction patterns for the in-situ study were recorded on the panel detector, yielding 2D Debye-Scherer diffraction rings that provide an insight into the full range of grain orientations as a function of crystallographic orientation (Figure 1). However, among these rings there is one specific orientation angle, satisfying the relation $cos^2\psi = 1/3$, $\psi = acos(1/\sqrt{3}) = 54.7°$, which can be used for full-pattern structural refinement even after poling under a high electric field.[19] At this orientation, the domains are randomly oriented and therefore crystallographic texture is almost negligible. Furthermore, the elastic lattice strains associated with the development of inter-granular stresses are close to zero at this orientation, which facilitates the refinement of crystal structure and calculation of phase fractions without the need to incorporate models for the domain and strain orientation distribution functions (DOD and SOD respectively).

The structural model was constructed first based on rhombohedral symmetry with *R3c* space group, which is the well-known crystal structure of $BiFeO_3$.[4,5,9] However, it was found that the single phase model could not resolve the structure properly and therefore another crystal symmetry, pseudocubic *Pm-3m*, which is commonly assigned for *x*BF-BT ceramics (x <75%),[20–23] was added into the model. The refinement was significantly improved. However, the *R3c*+*Pm-3m* model is merely reasonable for the slow-cooled state since the *R3c* phase corresponds to the ferroelectric core, while the featureless shell could comprise the non-polar *Pm-3m* phase. Nonetheless, it is questionable for the quenched

state since the appearance of ferroelectric domains in the shell appears to indicate the transformation from non-polar or relaxor *Pm-3m* to a polar ferroelectric *R3c* configuration. To simplify the model for both states, a new binary model is designated as comprising $R3c^{Core}$ and $R3c^{Shell}$ phases, which serves to represent the core and shell regions in both the slow-cooled and quenched states, as illustrated in Figure 3(a) and (b). According to this simplified approach, the pseudo-cubic phase is represented by a rhombohedral structure with near-zero rhombohedral distortion.

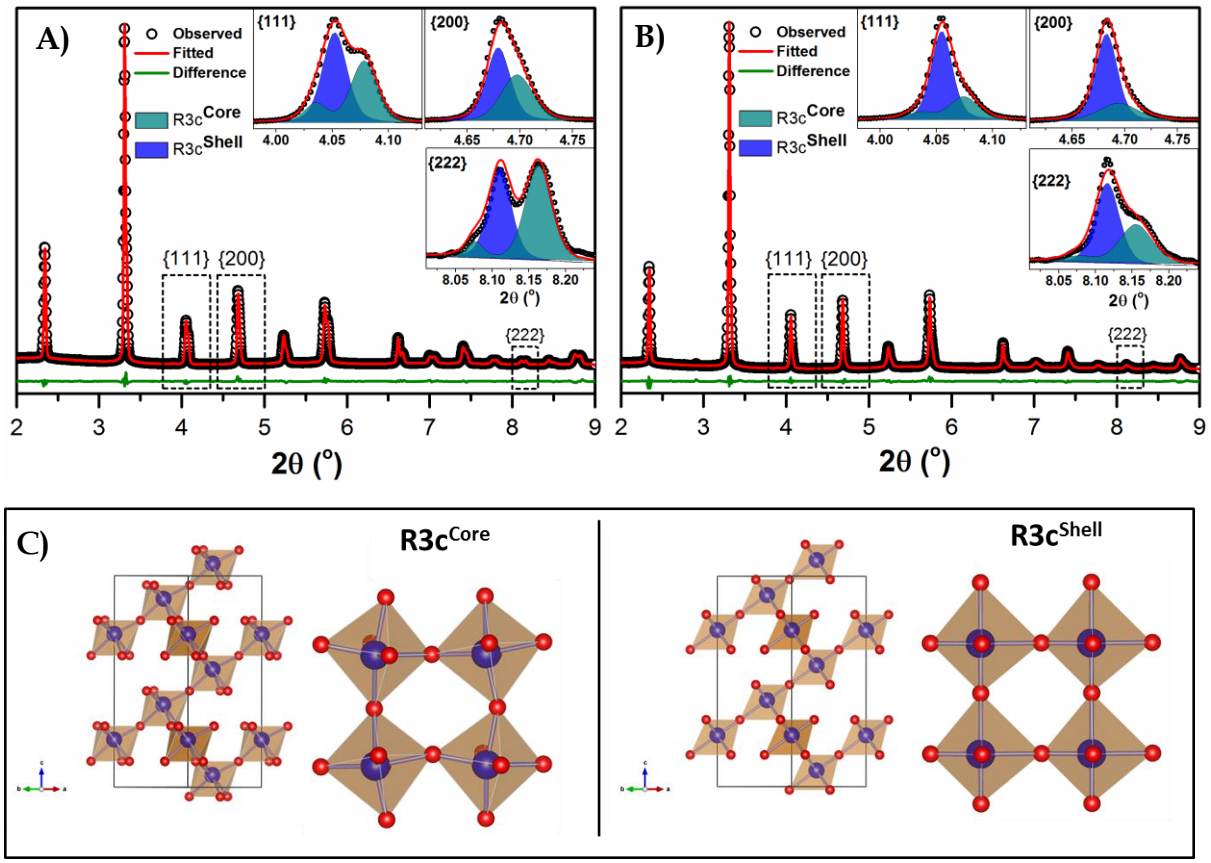

Figure 3 Full-pattern Rietveld refinement of **(a)** quenched and **(b)** slow-cooled ceramics. **(c)** (Fe/Ti)O_6 octahedral illustrations of core and shell structures in the quenched state**.**

Table 1 Crystallographic parameters obtained from Rietveld analysis for slow-cooled and quenched ceramics.

Parameters	**Slow-cooled**		**Quenched**	
Phases	*R3c*^{Core}	*R3c*^{Shell}	*R3c*^{Core}	*R3c*^{Shell}
Fraction (%)	24.6(9)	75.4(9)	39.4(3)	60.5(3)
Unit cell parameters (Å)				
a_h	5.3325(7)	5.3625(6)	5.3263(4)	5.3651(5)
c_h	13.2020(20)	13.1460(20)	13.2034(12)	13.1649(16)
a_{pc}	3.7841	3.7929	3.7813	3.7959
Lattice distortion, (%) η_{rh}	1.07	0.08	1.2	0.18
Distortion angles (°)				
α_{rh}	59.53	59.96	59.47	59.92
α_{pc}	89.59	89.97	89.54	89.93
B-O-B (°)	152.3	178.8	157.4	178.9
U_{iso} (Å^2)				
Bi/Ba	4.85(13)	5.12(12)	5.20(17)	4.24(11)
Fe/Ti	1.25(9)	0.95(8)	0.56(10)	0.18(12)
O	2.1(12)	1.45(8)	0.84(7)	1.27(8)
Reliability-factors				
R_{wp} (%)	3.78		2.76	
R_{exp}(%)	1.74		2.19	
GoF*	1.74		1.26	

The structural parameters obtained from the refinement are summarised in Table 1. It is evident that the *R3c* phase fractions within the core and shell varied significantly after the quenching process, although deviations in the unit cell parameters were minimal. Although *R3c* crystal symmetry is used in the hexagonal setting for the refinement, it is more convenient to convert the hexagonal lattice parameters (a_h and c_h) into the pseudocubic setting, calculated as below:

$$a_{pc} = \sqrt[3]{\frac{\sqrt{3}\, a_h^2\, c_h}{12}} \qquad \textbf{Eq.1}$$

For the refinement procedure, the bismuth ions were situated on the A-site together with barium, and the substituent titanium ions were situated on the B-site together with iron. In order to obtain consistent refinement results, similar sets of parameters were used for all refinements. Although the grains are compositionally graded as $BiFeO_3$-rich and $BaTiO_3$-rich regions, the occupancies of A- and B-site ions were fixed based on the stoichiometry of $0.75Bi(Fe_{0.99}Ti_{0.01})O_3$-$0.25BaTiO_3$, since it may bring more complexity, and hence instability, into the refinement procedure if the occupancies were to be refined. As the isotropic thermal parameters, U_{iso}, were refined, a problem emerged in that there was a drastic increase in the U_{iso} value of the A-site compared with that of the B-site for both *R3c*^{Core} and *R3c*^{Shell} symmetries. This clearly indicates that the distributions of A- and B-site ions are not homogeneous within the assigned crystal structure. In fact, this is confirmed by the microstructural investigation discussed above. By combining results of structural refinement and microstructural observations it can be recognised that large deviations in the isotropic thermal parameters could be a useful indicator of chemical heterogeneity.

Another important parameter in structural analysis is the lattice distortion and associated inter-axial angles. The rhombohedral lattice distortion, η_{rh} can be calculated by Eq.2 [24] while the relation between the lattice inter-axial angles for rhombohedral, α_{rh}, and pseudocubic, α_{pc}, is given in Eq.3 [25]

$$\eta_{rh} = \left[\frac{\sqrt{2}\, c_h}{3\sqrt{2}\, a_h}\right] - 1 \qquad \textbf{Eq.2}$$

$$90 - \alpha_{pc} = (\sqrt{3}/2)\,(60 - \alpha_{rh}) \qquad \textbf{Eq.3}$$

The values of α_{rh}, were found to be 59.53° and 59.47° for the core regions of the slow-cooled and quenched ceramics, while the corresponding angles for *R3c*^{Shell}, 59.96° and 59.92°, exhibited minimal deviation with respect to primitive rhombohedral symmetry ($\alpha_{rh} \cong 60°$), yielding α_{pc}=89.97° and 89.93° in the pseudocubic setting. The inter-axial angle in pristine $BiFeO_3$ [26] is reported as α_{rh}=59.35°. This value is comparable to the observed distortion in the *R3c*^{Core} for both states, suggesting that the assigned crystal structure for the core is close to that of $BiFeO_3$.

To illustrate the differences between the core and shell structures sharing *R3c* symmetry in the quenched state, a crystallographic information file (CIF) was generated from the refinement and plotted in Figure 3(c). It is evident that the

distortions of the (Fe/Ti)O_6 octahedra are clearly distinguished between the *core* and *shell* structures. The Fe−O−Fe angle for $BiFeO_3$ itself is reported as 154.1°.[26] Therefore, it can be deduced that the regions with high $BiFeO_3$ phase content are responsible for the observed large distortions in the octahedra, yielding a B−O−B angle of 157.4° with respect to the occurrence of a-a-a- tilt. On the other hand, suppression of octahedral tilting and a slight deviation in the B–O–B angle of the shell could be an indication of untilted *R3c*, namely *R3m*. The origin of such contrasting character could be due to large ionic radii differences of the A-site ions ($r_{Ba} = 1.35$ Å and $r_{Bi} = 1.03$ Å) since the shell phase is $BiFeO_3$-depleted. This confirms the correlation between tilting and cation size of A-site ions as reported by Megaw,[25] suggesting that reduction in the radii of the A-cations in relation to octahedron edge length, l ($(r_A + r_{Oxygen})/l$) causes the suppression of octahedral tilting.

3.1.3 Dielectric and Ferroelectric Properties

The results presented in Figure 4 illustrate the ε_r-T and P-E relationships for the slow-cooled and quenched ceramics. In the former case, a lower-temperature dielectric anomaly is evident in the vicinity of $T_m^1 \approx 400$°C; whilst with further heating another dielectric maximum is apparent at a higher temperature $T_m^2 \approx 625$°C for both slow-cooled and quenched states. However, a dramatic increase in the magnitude of ε_r near T_m^1 was observed in the quenched ceramic, but the magnitude was relatively suppressed and diffuse with a marked frequency-dependence for the slow-cooled ceramic. Such changes in the magnitude of ε_r can be understood on the basis of the increase in intrinsic polarizability near the phase transition temperatures.

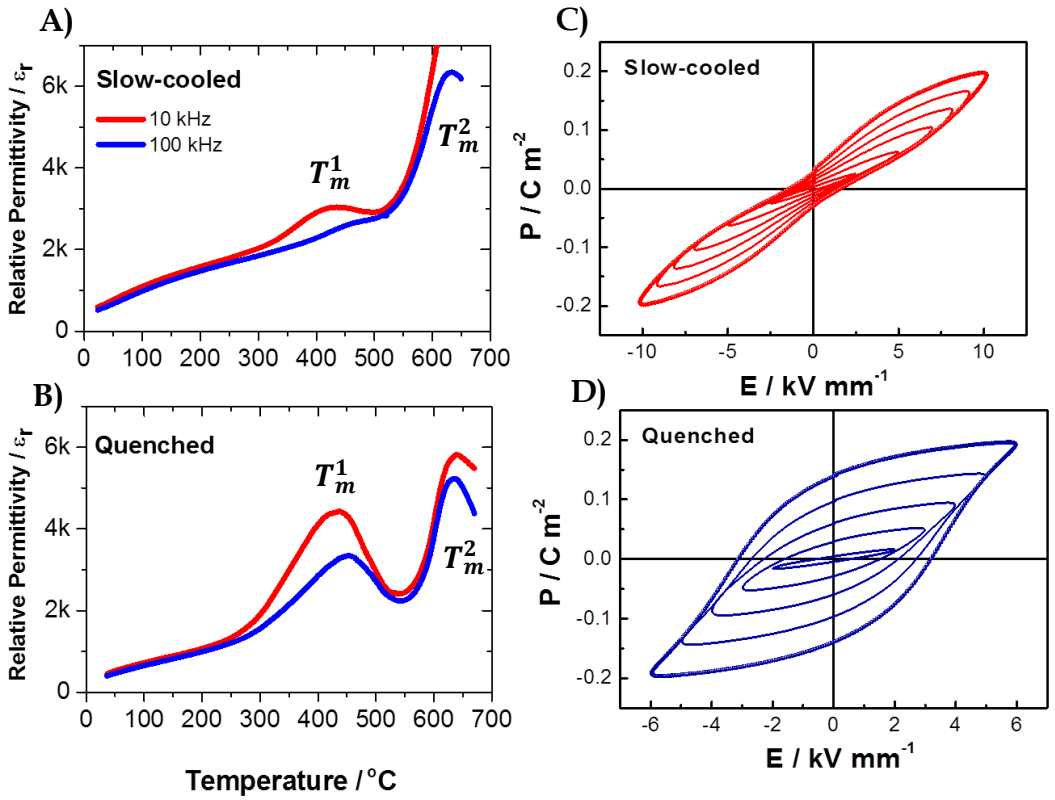

Figure 4 Temperature dependence of the relative permittivity at 10 kHz and 100 kHz frequencies in **(a)** slow-cooled and **(b)** quenched ceramics. P-E relationships in **(c)** slow-cooled and **(d)** quenched ceramics. Inner loops are measured upon increasing the electric field to show the progression of the polarisation switching mechanism.

Ferroelectric P−E hysteresis loops for the slow-cooled and quenched ceramics are shown in parts (c) and (d) of Figure 4, respectively. For the slow-cooled state, constricted P−E loops were obtained under AC electric fields with magnitude up to 10 kV/mm. This constrained switching behaviour is attributed to the presence of polar nanodomains, commonly found in relaxor ferroelectric phases, indicating that the oriented ferroelectric domains developed under high electric fields are unstable and cannot be retained after the removal of the field. It is evident that at a moderate electric field (E=5 kV/mm), an almost linear response was recorded. According to the common interpretation given in the literature for such cases, it is linked to the transformation of randomly oriented polar nano regions (PNRs) to ordered ferroelectric domains, leading to the observed increase in polarization, while upon removal of the electric field the developed domains are dispersed into discrete PNRs, thus leading to almost zero net polarization at zero field.[27] Nevertheless, upon further increasing the field to 10 kV/mm, the loop transformed into a more open shape around the tip, however, the polarisation was not retained on removal of the field. Similar behaviour has been observed previously in acceptor-doped normal ferroelectrics, although in that

case it is generally attributed to domain wall pinning effects rather than the presence of PNRs.[28] On the other hand, for the quenched case, a nonlinear and strongly hysteretic P-E response was developed even at a field of 3 kV/mm, and a well-saturated loop was obtained at 6 kV/mm.

It is known that the nucleation and growth of ferroelectric domains, together with their subsequent mobility, greatly impacts upon the macroscopic polarisation switching behaviour. Grain boundaries are speculated to act as pinning centres for the ferroelectric domains, thereby generally restricting the domain wall motion, which in turn reduces the magnitude of bulk polarization changes during external stimuli.[29] Based on this view, discontinuity in the micro-sized ferroelectric domain structures, observed in the slow-cooled ceramic, could be used as a strong argument that the featureless shell can be treated as an intra-grain boundary that acts to restrain domain switching in the ferroelectric core. On the other hand, the observation of micro-sized ferroelectric domains in the shell of the quenched ceramic indicates that the restrictive intra-granular elastic constraint was diminished and an environment for effective domain wall mobility was created. Therefore, it can be concluded that the observed heterogeneous microstructure gives rise to heterogeneous polarisation switching mechanisms under the electric field, within the grains and surroundings accordingly. In such a case, there is no need to invoke any defect-related pinning mechanisms to explain the constrained polarisation switching behaviour of the slow-cooled ceramic.

3.1.4 In-situ investigation of microscopic actuation mechanisms

A polycrystalline ferroelectric ceramic subject to an applied electric field will give rise to a unique diffraction pattern on the detector for each grain orientation, ψ, relative to the applied field direction[30]. For example, the relative intensities of the *hhh*-type diffraction peaks in rhombohedral symmetry change due to the electric field-induced structural changes such as crystallographic texture (i.e. preferred orientation of the non-180° ferroelectric domain structure), whereas peak shifts occur in *h00*-type peaks due to variations in the lattice spacing .[19] To monitor and quantify the contribution of such changes relative to the total electrostrain, it is necessary to determine the extrinsic and intrinsic contributions associated with domain switching and lattice strain, respectively.[19,30,31] Thus, certain crystallographic orientations such as {111}, {200} and {220} will be examined in order to make an initial assessment of the microscopic actuation mechanisms.

Diffraction patterns corresponding to ψ=0° (i.e. representing grain families oriented with their scattering vectors parallel to the electric field) for the slow-

cooled and quenched ceramics are shown in Figure 5(a) and (b). These patterns correspond to the points where the electric field varies from 0 to ±6 kV/mm ($\pm E_{MAX}$), yielding 2 bipolar cycles in the triangular waveform, as illustrated in Figure 5(c). It is evident that on increasing the electric field, the structural variations in the slow-cooled state were minimal and only a slight peak broadening was observed at $\pm E_{MAX}$. In constrast, the influence of the applied electric field on the peak profiles of {111}, {200} and {220} for the quenched ceramic was substantial, particularly at $\pm E_{MAX}$. After the removal of the field, peak splitting for {111} and {220} was more pronounced and a noticeable peak broadening was also observed for {200}. Qualitatively, these observations indicate that the electromechanical response in the slow-cooled state is minimal and cannot be assessed due to the presence of asymmetric peak broadening and lack of features to inspect. However, the pronounced variations in the {111}, {200} and {220} peak profiles for the quenched state show clear evidence of the ferroelectric domain switching phenomena and electric field-induced strain.

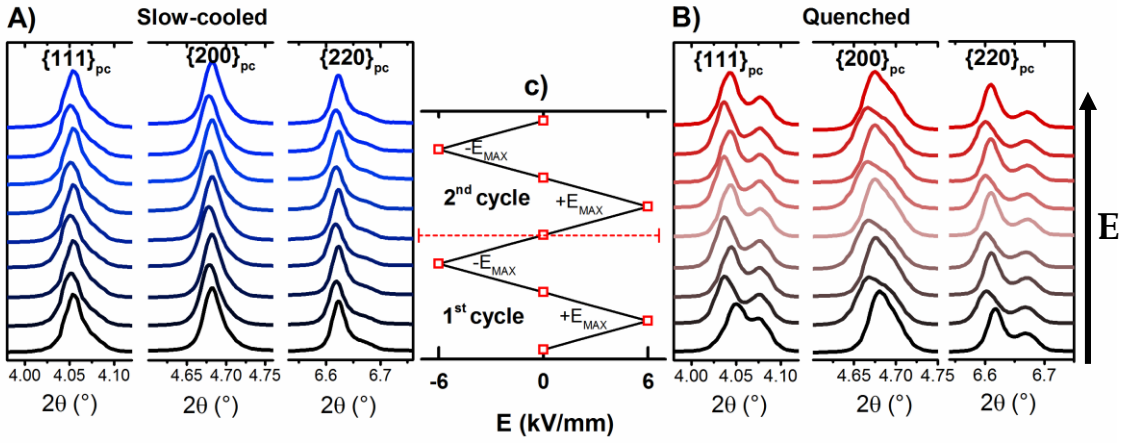

Figure 5 Variations in diffraction profiles for {111}, {200} and {220} along the field direction (ψ=0°): slow-cooled **(a)** and quenched **(b).** 2 bipolar cycles of the applied electric field corresponding to each diffraction profile are also included in **(c)**.

To quantify the microscopic strain for the slow-cooled and quenched ceramics, the {111} peak profile, which is the characteristic polar direction for rhombohedral symmetry, was de-convoluted by two peaks using a pseudo-Voigt function within Matlab. The effective average lattice strain associated with this grain orientation, ε_{ψ}^{111} , was estimated on the basis of a simple weighted average of the diffraction peak positions. This operation was performed on particular grain orientations, with ψ= 0°, 30°, 60° and 90° (Figure 6(a)). It was found that the variations in the strain, ε_{ψ}^{111} as a function of grain orientation are consistent with the response of a typical rhombohedral ferroelectric.[19] The largest positive strain was observed at ψ= 0°, indicating development of tensile strain along the field direction; this was reduced in magnitude at 30° and diminished almost to

zero at 60°, which is expected to be near the texture-free orientation of 54.7°. Subsequently, negative strains were observed at 90° due to development of compressive strain along the transverse direction. It is also evident that the application of the 2nd bipolar cycle to the quenched ceramic enhanced the symmetric shape of the loop for grain orientations at ψ= 0° and 30°. This observation indicates that re-orientation of domains under an electric field for these grain orientations was stabilised with subsequent cycling, which in turn led to a symmetric loop as a result of improved poling. On the other hand, by inspection of the surface contour plots for {111} given in Figure 6(b), it appears that the characteristic preferred orientation in the (111) and (-111) doublet, which is normally expected for domain switching in a typical rhombohedral ferroelectric, is absent.[19,30] Instead, there was a combination of large peak shift starting from 2Θ≈4.06° and slight intensity fluctuations in the peak at 2Θ ≈4.09°.

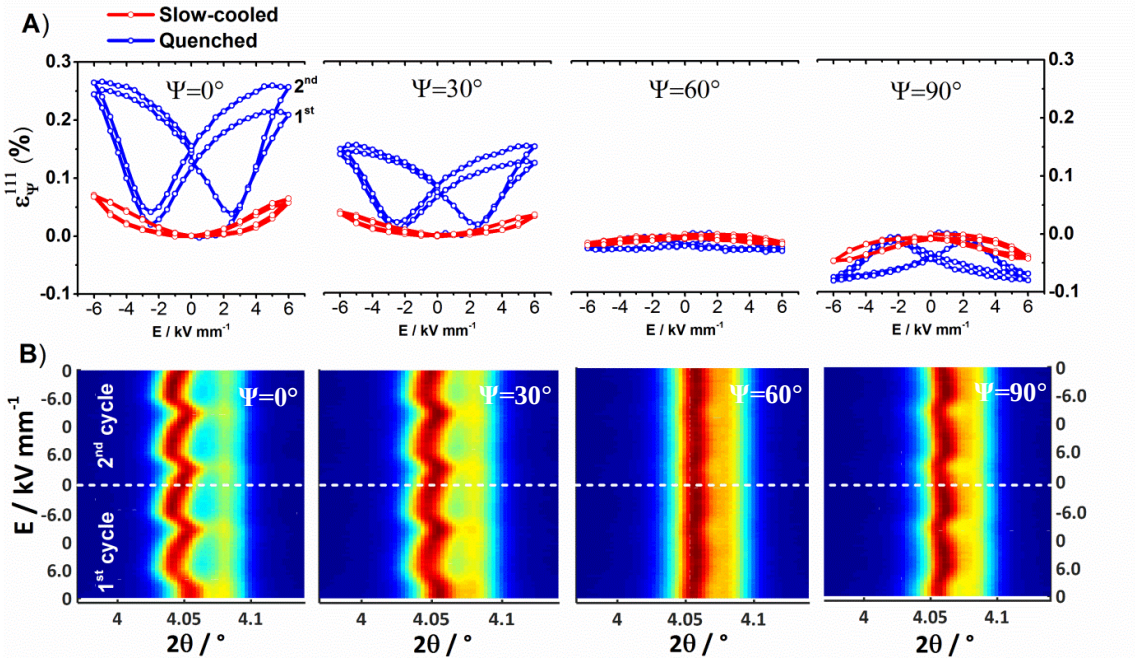

Figure 6 (a) Calculated microscopic lattice strain contribution of {111}, ε_{111} in slow-cooled and quenched ceramics, in relation to the grain orientations, ψ of 0°, 30°, 60° and 90°. **(b)** Surface contour plots of {111} for quenched ceramic as a function of applied electric field for the same grain orientations.

To seek a further indication of domain switching, the response of the {222} reflection with respect to various grain orientations was also inspected, as shown in Figure 7. Similar to the behaviour of the {111} diffraction peak under the electric field, crystallographic variations in {222} are predominantly composed of peak shifts and intensity fluctuations with various grain orientation angles, ψ. However, as the diffraction profile of {222} in the remnant state (after the 1st cycle) is plotted as a function of grain orientations (Figure 7(b)), it can be seen that

preferred domain orientation can be identified with the assistance of the previous structural refinement presented in Figure 3(a).

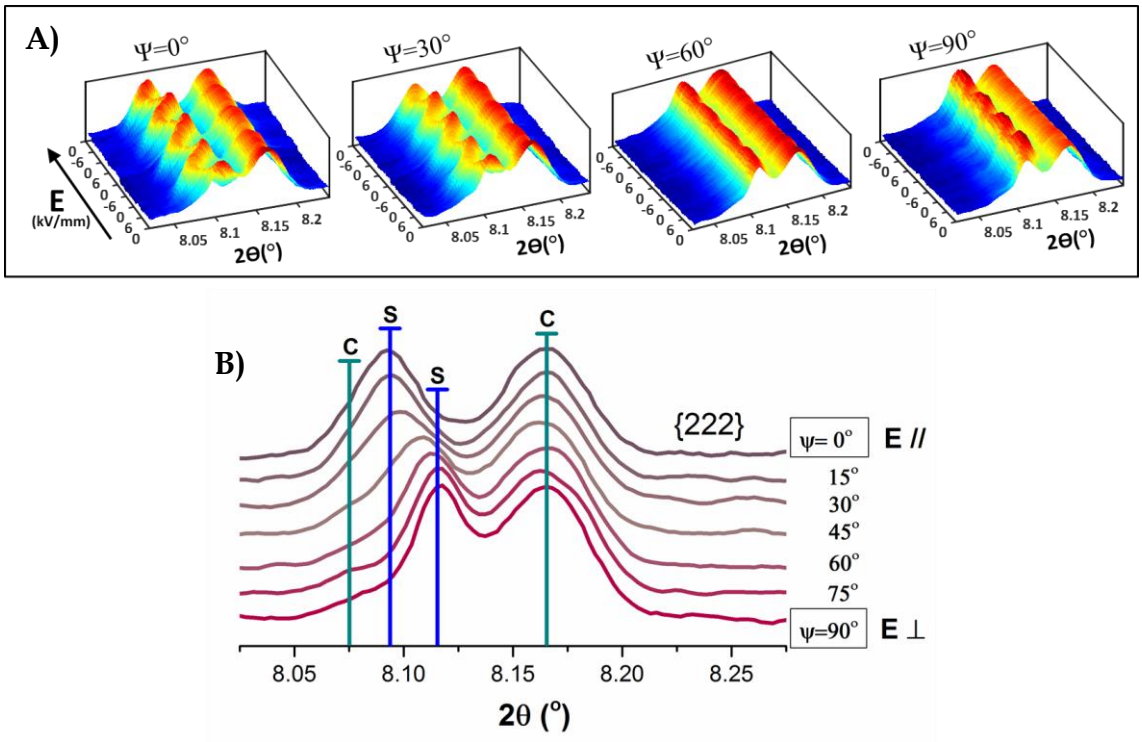

Figure 7 (a) Contour plots of {222} diffration pattern of quenched as a function of applied electric field for the grain orientations, ψ of 0°, 30°, 60° and 90°. **(b)** Corresponding core(C) and shell(S) peaks in {222} as a function of various grain orientations after the removal of electric field (Remanent state).

As we take the scattering angles corresponding to $R3c^{Core}$ and $R3c^{Shell}$ of {222} from the full-pattern refinement and position them on the plot, denoted as C and S respectively (Figure 7(b)), there is a close match with the observed large peak shift, indicating that it could be indeed a consequence of domain switching within the shell component. Since the rhombohedral distortion in the shell is not as large as that in the core, the individual peaks are not resolved and we observe significant peak shifts instead of the typical texturing in rhombohedral *R3c* symmetry.[19,30] This introduces a complication in that the intrinsic and extrinsic contributions of the shell phase cannot be readily distinguished and therefore, for the strain analysis, it is treated as an effective average lattice strain, which is a sum of the intrinsic and extrinsic contributions. The strain contributions from the core and shell regions are quantified in the following section.

3.1.4.1 Determination of strain contributions for core and shell phases

The overall variations in the {111}, {200} and {220} peak profiles under the electric field with 0.5 kV/mm steps for the quenched ceramic are shown in Figure 8 (a),

(b) and (c), respectively. It can be seen that upon application of the electric field, both intensity changes and peak shifts are present in all the reflections. This clearly indicates interplay of actuation mechanisms between domain switching and lattice strain (i.e. unit cell contraction/expansion). It is also apparent that there is no indication of any phase transformation for both $\pm E_{MAX}$ and the remanent state, and therefore there is no need to account for this in the quantification of strain. Thus, it can be suggested that the origin of electromechanical strain in the quenched state is simply attributed to non-180° domain switching and associated lattice deformation, in both core and shell regions. This can be resolved via individual peak fitting analysis in TOPAS and Matlab. We tested these two peak-fitting methods using various peak shape functions and concluded that individual peak fitting *via* TOPAS with the basis of structural refinement yielded better outcomes since it can readily separate out each of the corresponding core (C) and shell (S) phase peaks, as can be seen in Figure 8. In addition, detailed structural information can also accordingly be obtained.

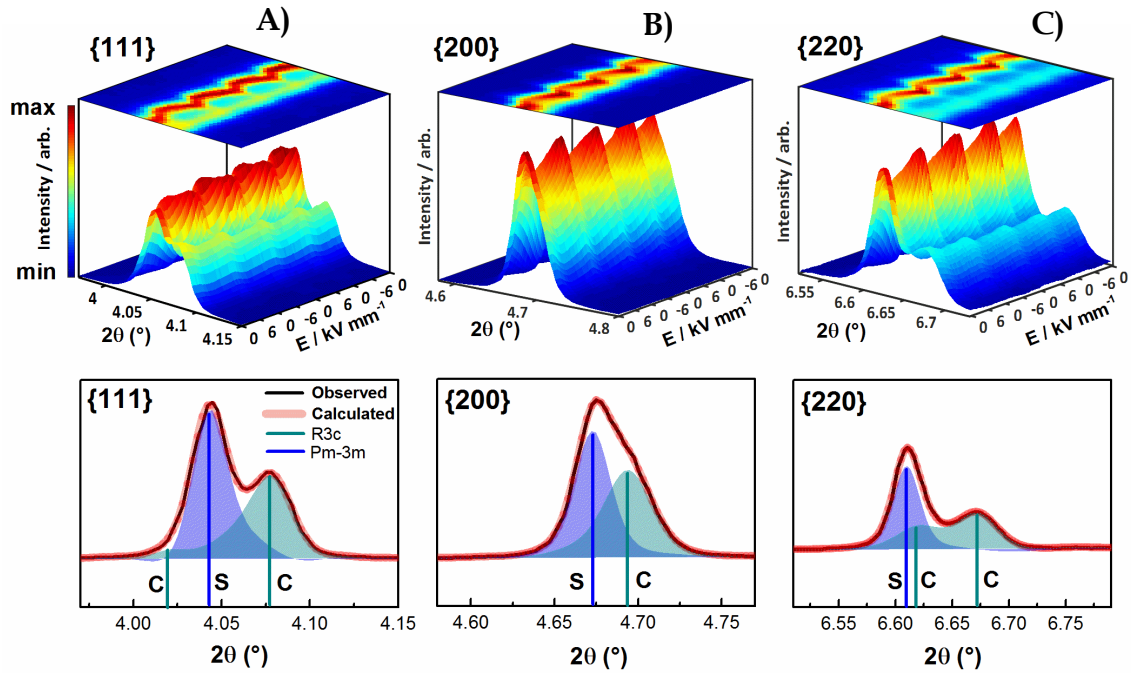

Figure 8 Crystallographic variations for **(a)** {111}, **(b)** {200} and **(c)** {220} under 2 bipolar cycles of electric field in the quenched ceramic. Individual peak fitting is illustrated underneath the corresponding contour plots. The fitted data is taken from the remnant state of 1st cycle. *R3c* and *Pm-3m* phase contributions are abbreviated as C and S, referring to associated core and shell phases, respectively.

The detailed fitting procedure employed the following steps:

(i) The {111}, {200} and {220} crystallographic orientations were evaluated to provide a representative weighted average, enabling an estimation of the total macroscopic strain of the polycrystal.[32] Full pattern fitting of the diffraction patterns obtained under an applied electric field was not considered to be appropriate due to elastic interactions between differently-oriented grains together with anisotropy of elastic and piezoelectric properties, which are not currently accounted for within standard diffraction software.

(ii) An initial attempt was made to fit the individual diffraction peak profiles with *R3c*^{Core} and *R3c*^{Shell} phases, as suggested by the structural refinement in Figure 3(b). However, it was challenging to extract the individual intensities of the (111) and (-111) peaks for the fitted shell phase, due to a combination of peak broadening and the limited resolution of the detector. This problem is exacerbated since the rhombohedral lattice distortion in the shell (η_{rh}=0.18%) was relatively small in comparison with that of the core (η_{rh}=1.2%), as given in Table 1. Therefore, the crystal structure of the shell phase was approximated as pseudocubic *Pm-3m*.

(iii) Asymmetric and broad peaks were fitted by de-convoluting into three peaks for {111} and {220}, and two peaks for {200}. The modified Pseudo-Voigt function (PV-TCHZ) was used to extract the information from which the structural parameters of the associated core and the shell phases (e.g. magnitude of integrated intensity, inter-planar lattice spacing, structure factors).

Based on the fitting procedure described above, the crystal structure is now considered to comprise a combination of *R3c*^{Core} and *Pm-3m*^{Shell} phases. Each phase fraction, f_n can be then determined by

$$f_n = \frac{\left[\frac{I_n^{hkl}}{m_n^{hkl}\left|F_n^{hkl}\right|^2}\right]}{\sum_n\left[\frac{I_n^{hkl}}{m_n^{hkl}\left|F_n^{hkl}\right|^2}\right]} \qquad \textbf{Eq.4}$$

where I_n^{hkl}, m_n^{hkl} and $|F_n^{hkl}|^2$ are the integrated intensity, multiplicity and squared structure factor of associated n^{th} crystallographic planes *hkl* of core (C) and shell (S) phases as highlighted in Figure 6(b). The structure factors for each *hkl* were obtained from the full-pattern Rietveld refinement of the unpoled (randomly-oriented) ceramic. During this peak fitting analysis, the phase fraction of *Pm-3m*^{Shell} was found to be around 60 % and it was invariant under the electric field variation, for ψ=0°. Therefore, the electric field-induced phase transformation was disregarded in the following strain calculations.

Subsequently, the average effective d-spacing at zero electric field, $d_{total}^{hkl^0}$, and under the electric field d_{total}^{hkl} can be expressed in relation to the corresponding phase fractions obtained from Eq.4, $f_n^{hkl^0}$ and f_n^{hkl}, as follows:

$$d_{total}^{hkl} = \sum_n f_n^{hkl}\, d_n^{hkl} \qquad \textbf{Eq.5}$$

$$d_{total}^{hkl^0} = \sum_n f_n^{hkl^0}\, d_n^{hkl^0} \qquad \textbf{Eq.6}$$

The total microscopic strain for each grain orientation, ε_{hkl}, can then be calculated according to the equation given below:

$$\varepsilon_{hkl} = \frac{d_{total}^{hkl} - d_{total}^{hkl^0}}{d_{total}^{hkl^0}} \qquad \textbf{Eq.7}$$

The calculated microscopic strain results for {111}, {200} and {220} grain orientations are shown in Figure 9. Microscopic strain variations for the core and shell regions show clear evidence of strain heterogeneity on the micro scale within the grains. The field-induced strain in the rhombohedral core was generally much lower than that in the shell, for all grain orientations, indicating that the more-active shell regions were actually subject to elastic constrain by the less-active core regions. This strain heterogeneity must cause significant intra-granular stress. Significant differences in strain were also observed between the different grain orientations, due to piezoelectric and elastic anisotropy, which indicates the development of inter-granular stresses.

It should be noted that overlapping of the selected diffraction peaks corresponding to core and shell phases (Figure 8(a) and (c)) may cause relatively large uncertainties and deviations in the strain profiles. Thus, a further modification is required for reliable strain determination, as described in the following section.

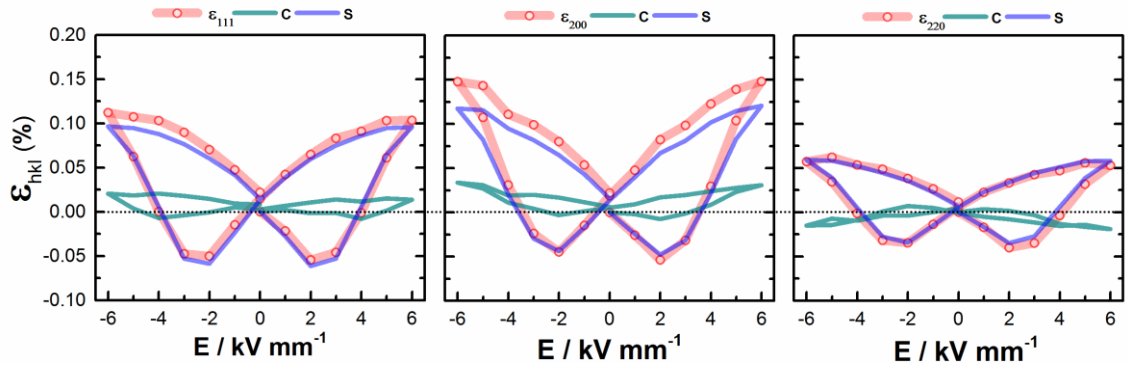

Figure 9 Calculated microscopic strain obtained from {111}, {200} and {220} crystallograpic planes corresponding to core (C) and shell (S) components.

The macroscopic strain was estimated based on the weighted average of the effective lattice strains associated with different crystallographic orientations, according to the equation shown below[30,33]

$$\varepsilon_{33}(\Psi) = \frac{\sum_{hkl} T_{hkl}\, m_{hkl}\, \varepsilon_{hkl}(\Psi)}{\sum_{hkl} T_{hkl}\, m_{hkl}} \qquad \textbf{Eq.8}$$

where ε(ψ) is the component of the macroscopic strain tensor for a given orientation, $\varepsilon_{hkl}(\psi)$ is the local lattice strain along the axis parallel to direction ψ for the *{hkl}* orientation, T_{hkl} is the texture index, and m_{hkl} is the multiplicity of the reflection for *{hkl}* planes. Treating the material as cubic and with random grain texture, T_{hkl} reduces to 1 for any *hkl*, and m_{hkl} is 8, 6, and 12 for {111}, {200}, and {220} orientations, respectively.

The total longitudinal strain, ε_{33}, was calculated in terms of a volume weighted average of the different effective lattice strains, ε_{hkl}, measured parallel to the applied electric field direction, ψ=0°. The calculated results are illustrated in Figure 10(a), comparing each contribution of core and shell phases as well as the net macroscopic strain. It is evident that the macroscopic strain obtained from the shell is predominant, while the core contribution is almost negligible, indicating that the observed large electromechanical actuation is a result of mainly one component. The reliability of the calculated strain is evaluated in Figure 10(b) by comparison with the experimental strain-electric field data. It is apparent that the calculated S-E loop is highly symmetric with a good match on the negative side of electric field, but showing a discrepancy with the asymmetric macroscopic strain measurement for positive fields. This discrepancy is attributed primarily to differences in the experimental procedures employed for the 2 methods, with a much shorter measurement time being employed for the macroscopic measurement in comparison with the in-situ diffraction study (10 s compared with 500 s for a single cycle).

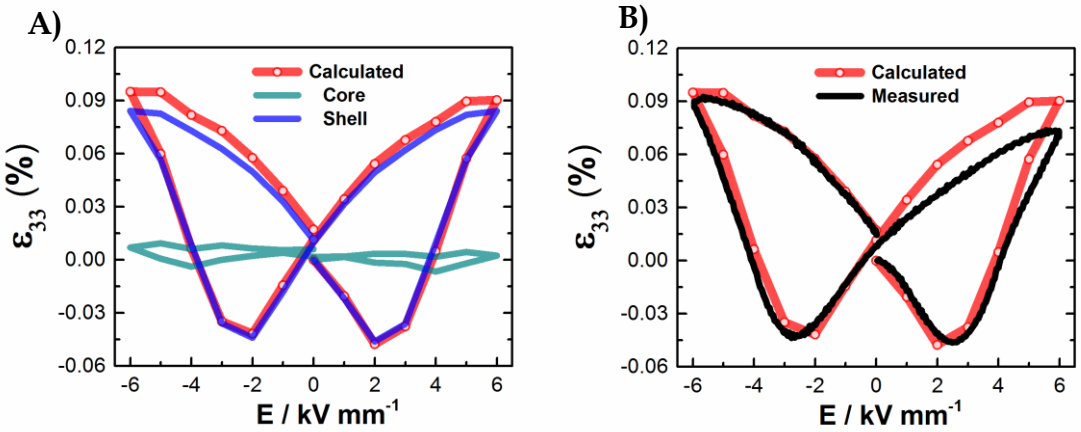

Figure 10 Comparison of measured and calculated strain-electric field responses including calculated core and shell contributions for the in-situ study.

3.2 Tuning functional properties via the core-shell approach — in search of new phase boundaries in heterogeneous BF–BT solid solution

For the purpose of testing the tuneable functionality through the core-shell approach in donor-doped BF–BT ceramics, various compositions were also prepared. The compositions, $x\mathrm{Bi}(\mathrm{Fe}_{0.99}\mathrm{Ti}_{0.01})\mathrm{O}_3 - (1\text{-}x)\mathrm{BaTiO}_3$; x=0.60, 0.67, 0.75 and 0.80, will hereinafter be denoted as 60BF, 67BF, 75BF and 80BF, respectively. Although complete assessment of 75BF was discussed above, it is also included in order to thoroughly assess the compositional dependency. Similar to section 3.1, the compositions are further subdivided into two groups as *slow-cooled* and *quenched*. From the results of this work, it becomes evident that it is possible to consistently attain core-shell type microstructure in a wide range of BF–BT solid solutions and hence tune the electromechanical properties through slow and fast cooling with the assistance of a 1 mol% Ti^{4+} substitution to the Fe^{3+} site in BF–BT solid solutions.

3.2.1 Phase and Microstructure

Chemically etched surfaces for both slow-cooled and quenched ceramics of all compositions are shown in Figure 11. The microstructures in all slow-cooled compositions clearly confirm the presence of chemical heterogeneity in the form of core-shell type grain formations without noticeable abrupt variations, such as abnormal grain growth or severe reduction in grain sizes. On the other hand, it is evident that that decreasing BF content led to a slight decrease in average grain size (from 4.2 to 2.7 μm) and non-uniform grain shapes. It is remarkable that visible ferroic domains in the core are present in all compositions regardless of BF/BT ratio, while the shell is distinguished by a lack of domain features. Regarding the relative volume fractions of the core and shell regions, there is no obvious dependence on BF/BT ratio from the observed microstructures. Interestingly, for the quenched case, the additional ferroelectric domain structures only appeared in the 75BF and 80BF ceramics, while the microstructures of 60BF and 67BF remained similar to those of the slow-cooled state without any noticeable change.

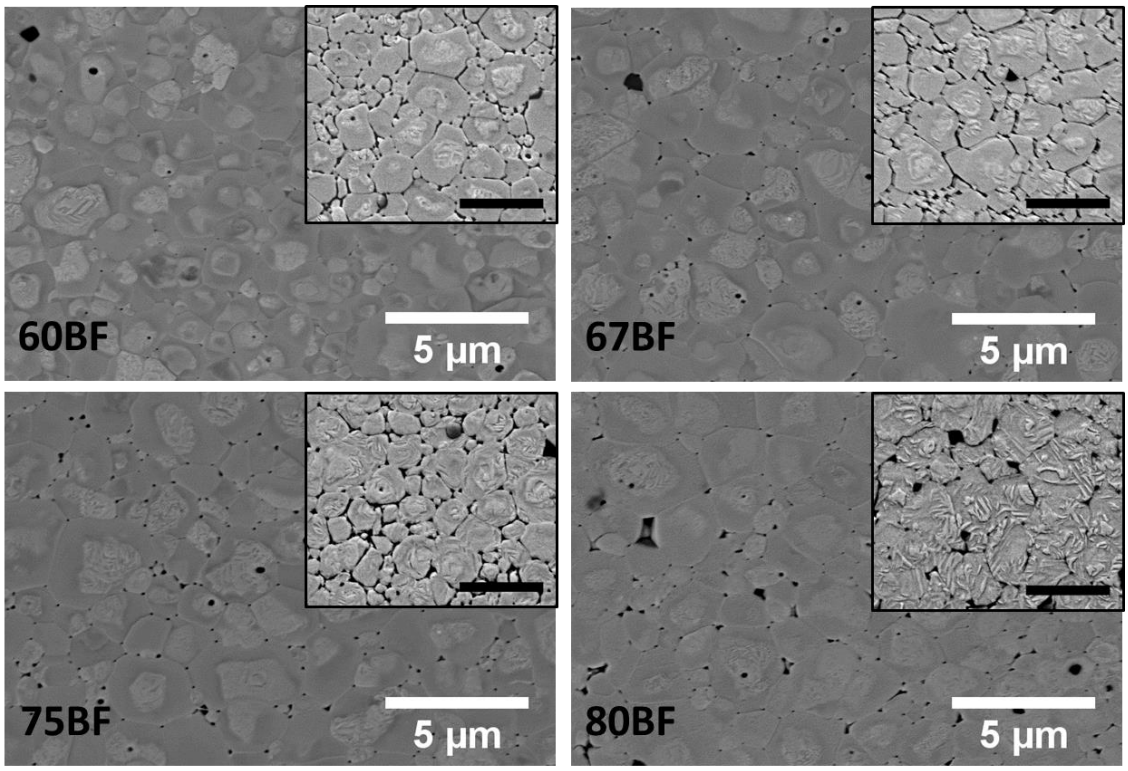

Figure 11 SEM images of chemically etched surfaces of slow cooled 60BF, 67BF, 75BF and 80BF compositions. Insets show the etched surfaces after application of quenching for the associated compositions. The scale bar in the insets is 5µm.

Microstructural observations are complemented by the high energy X-ray diffraction data for all compositions, as shown in Figure 12. It is apparent that the single peaks for the given crystallographic reflections are the dominant feature for the slow-cooled compositions, which indicates the major coexistence of pseudocubic phase, particularly in 60BF and 67BF. With increasing the BF content (75BF and 80BF), the single peaks evolved into broad, asymmetric and even clearly split peaks for high scattering angles comprising {221} and {222} planes, which could be an indication of a phase transformation or multiple phase coexistence. Since the SEM images confirmed the core-shell type grain structures for all compositions, it is anticipated that two heterogeneous phases should be apparent in the XRD patterns, as discussed in-depth in section 3.1. However, it can be seen that the compositions having lower BF contents (60BF and 67BF) greatly mask the expected rhombohedral reflections from the core. On the other hand, the influence of the rhombohedral core in 75BF and 80BF can be readily identified in terms of noticeable peak splitting for {221} and {222}.

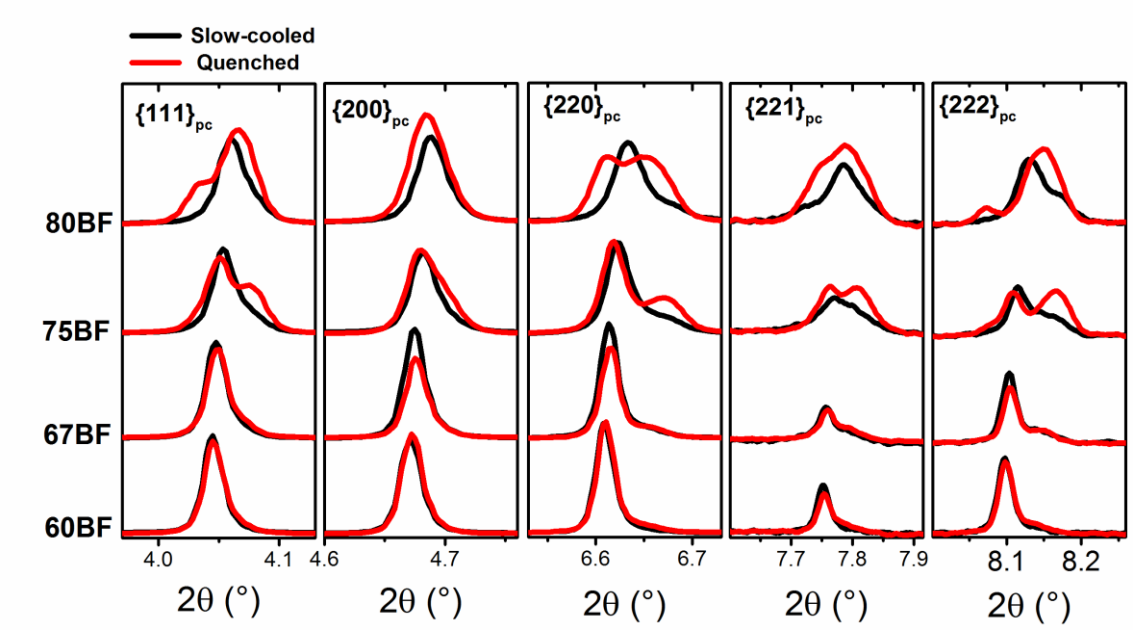

Figure 12 Comparison of normalised high energy X-ray diffraction profiles of slow-cooled and quenched solid solutions.

In order to evaluate the influence of quenching, significant structural changes are only evident in the peak profiles for 75BF and 80BF, similar to the microstructural observations. Particularly, 80BF undergoes a considerable peak splitting, except for the {200} reflection. This could be attributed to presence of major rhombohedral phase, as widely reported for the compositions $x \geq 75$ mol% in xBF-BT ceramics in the literature,[23,34] although strongly asymmetric and broad peaks are still present as a result of structural and chemical heterogeneity.

3.2.2 Dielectric and Ferroelectric Properties

Ferroelectric P-E hysteresis loops for the slow-cooled and quenched states, measured at room temperature, are presented in Figure 13. The derived parameters including saturated polarisation, P_{Sa}, remanent polarisation P_r, coercive field, Ec and Pr/P_{Sa} ratio are compared in Table 2. P-E loops for slow-cooled compositions show suppressed polarisation character, particularly in high BF compositions (75BF and 80BF). Relatively higher P_{Sa} and P_r values were obtained for the 60BF and 67BF compositions; however the shapes of the hysteresis loops are slightly slanted and not fully saturated at an electric field amplitude of 6 kV mm^{-1}.

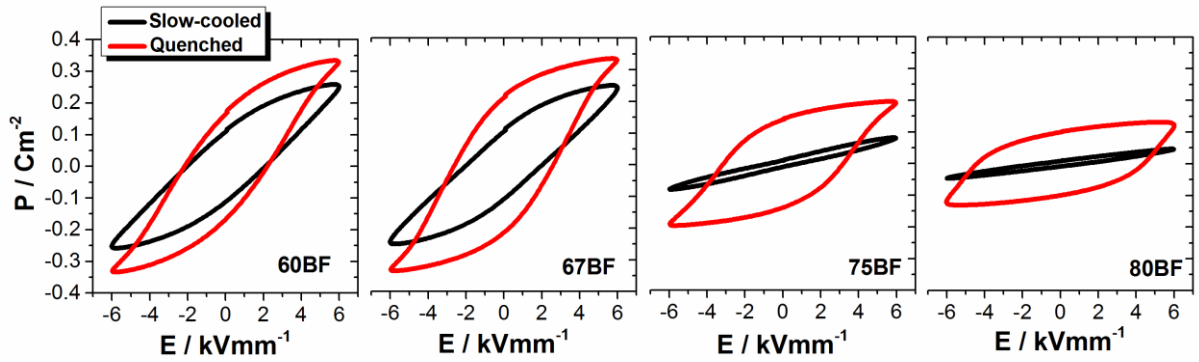

Figure 13 Ferroelectric P-E hysteresis loops of slow-cooled and quenched solid solutions.

On the other hand, quenching greatly restores the character of the hysteresis loops from the constrained well-saturated in 75BF and 80BF, leading to P_r/P_{Sa} ratios above 70% indicating significant enhancement in domain switching. Although this effect was less dramatic at lower BF contents (60BF and 67BF), the P_r/P_{Sa} ratio was still improved from 0.42 to 0.52 for 60BF and from 0.44 to 0.65 in 67BF. It is also evident that the coercive field for the quenched compositions exhibits an incremental trend from 2.2 to 4.4 kV/mm which is in good agreement with the fact that the high field is required for polarisation switching in $BiFeO_3$-based solid solutions.[9,34] The results suggest that ferroelectric properties are modified to a great extent depending on the $BiFeO_3$-content and quenching operation.

Table 2 Summary of derived ferroelectric P-E loop parameters for the studied compositions.

State	Composition	P_{Sa} (C/m^2)	P_r (C/m^2)	E_C (kV/mm)	P_r/P_{Sa}
Slow-cooled	60BF	0.26	0.11	2.1	0.42
	67BF	0.25	0.11	2.0	0.44
	75BF	0.08	0.02	0.9	0.25
	80BF	0.05	0.01	1.2	0.20
Quenched	60BF	0.33	0.17	2.2	0.52
	67BF	0.34	0.22	2.6	0.65
	75BF	0.20	0.14	3.2	0.70
	80BF	0.13	0.10	4.4	0.77

The temperature-dependence of the relative permittivity, ε_r, and dielectric loss, tanδ, for the slow-cooled and quenched ceramics is shown in Figure 14(a) and (b). As shown in the SEM images presented in Figure 11, it is expected that the confirmed chemical heterogeneity for all compositions would have a severe effect on the temperature-dependent dielectric properties. The results here verify that the dielectric properties are affected significantly both by quenching and by the BF content in relation to their chemically heterogeneous nature. Some distinctive features are listed below:

i) Multiple dielectric transition anomalies were detected in all compositions. The highest temperature peak, around 625°C, varied in magnitude varied depending on the BF content. With decreasing BF content this sharp peak developed a more diffuse and broad appearance and it almost disappeared for 60BF. In relation to this, a high temperature dielectric loss peak in the range of 500-550°C was evident for 75BF and 80BF; there was no distinctive loss peak in this range for 60BF and 67BF, which might be linked to the more diffuse higher temperature dielectric peak for these compositions. A broad lower-temperature anomaly was observed for all compositions over the temperature range from 300 to 550°C.

ii) Quenching had a dramatic effect on the dielectric transitions, leading to a sharp increase in the magnitude of relative permittivity for 67BF, 75BF and 80BF within the range 300-550°C. In contrast, the peak in permittivity was more diffuse for 60BF, occurring over the temperature range from ≈200 and ≈550°C and transforming the relatively invariant dielectric response of the slow-cooled state into two closely coupled dielectric peaks.

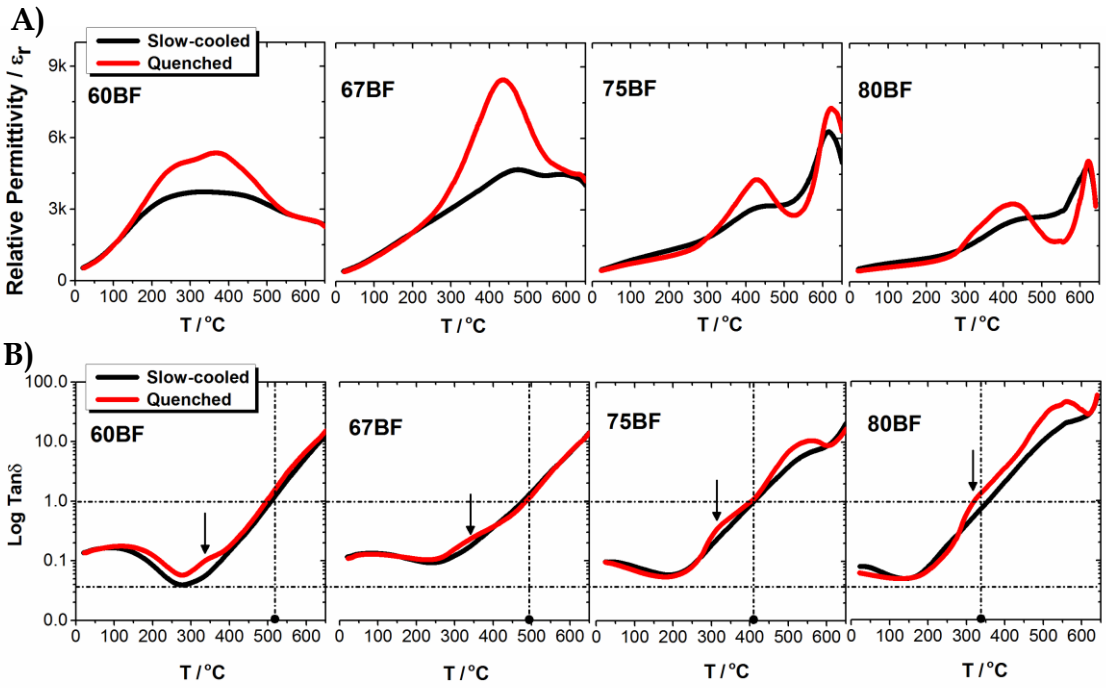

Figure 14 Comparison of temperature dependence of the relative permittivity **(a)** and tanδ **(b)** at 100 kHz in slow-cooled and quenched ceramics

On the basis of the structural and microstructural observations presented in section 3.2.1 above, it is likely that the results presented here can be interpreted broadly in terms of 2 distinct contributions to the ε_r-T relationships, originating the from core and shell regions and giving rise to the low and high temperature dielectric anomalies respectively. Further in-depth investigations, involving impedance spectroscopy measurements and equivalent circuit modelling, are required in order to verify and quantify this assertion.

3.2.3 In-situ investigation of microscopic actuation mechanisms

Contour plots of the {111} diffraction peak profiles corresponding to ψ=0° under the application of 2 bipolar cycles of 5 kV/mm, for both slow-cooled and quenched ceramics, are illustrated in Figure 15(a) and (b). It is evident that the recorded structural responses for the slow-cooled ceramics were minimal compared to those of the quenched ones, with 67BF being the most active amongst the slow-cooled materials. With increasing BF-content (75BF and 80BF), the intensities and positions of the {111} peaks were almost invariant under the applied electric field. Conversely, the influence of the applied field on the {111} peak profiles was substantial for the quenched compositions, particularly for 75BF and 80BF. Single and broad peak shapes for the slow-cooled 75BF and 80BF evolved into split peaks with pronounced peak shifts and intensity variations after quenching. The quenching procedure also further promoted peak shifting of {111} in 60BF and 67BF without introducing any distinct peak splitting.

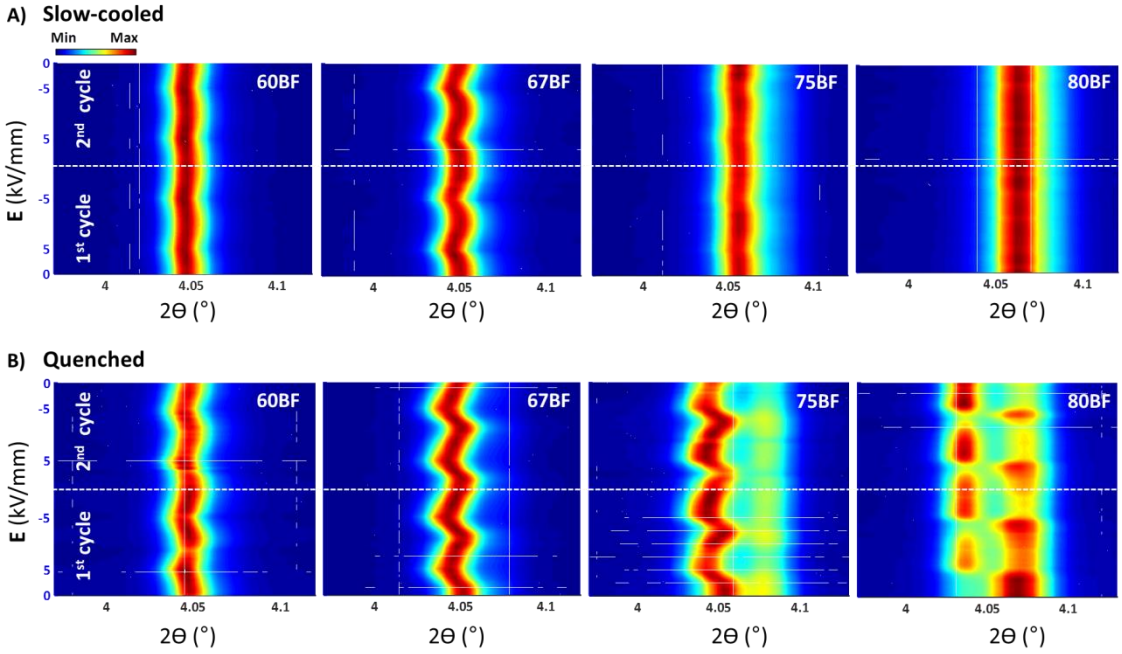

Figure 15 Changes in {111} peak profiles during 2 cycles of a bipolar electric field corresponding to ψ=0° in slow-cooled **(a)** and quenched **(b)** states of studied compositions. Dashed lines indicate the boundary between the 1st and 2nd cycles of the bipolar electric field.

To quantify the effects of such strain-electric field responses on the lattice spacing of {111}, the microscopic strain was calculated using the Matlab peak fitting routine (i.e. single-peak fitting for 60BF and 67BF and double-peak fitting for 75BF and 80BF compositions in both states). The microscopic strain, ε_{111}, values for ψ = 0°, for all the studied compositions were calculated, yielding the results presented in Figure 16. The strains in the slow-cooled 60BF, 67BF and 75BF ceramics exhibit symmetric profiles with relatively low maximum strain, ε_{111}=0.06 , ε_{111} =0.14 and ε_{111} =0.04, whilst the strain in 80BF is almost negligible.

The calculated strain results for all the compositions in both states are summarised in Table 3. It can conclude that the high electromechanical activity in the heterogeneous-type BF–BT ceramics could potentially be found in the vicinity of 67BF composition, and thus it is fascinating that this coincides with MPB claims for this composition which is assumedly with homogeneous-type microstructure.

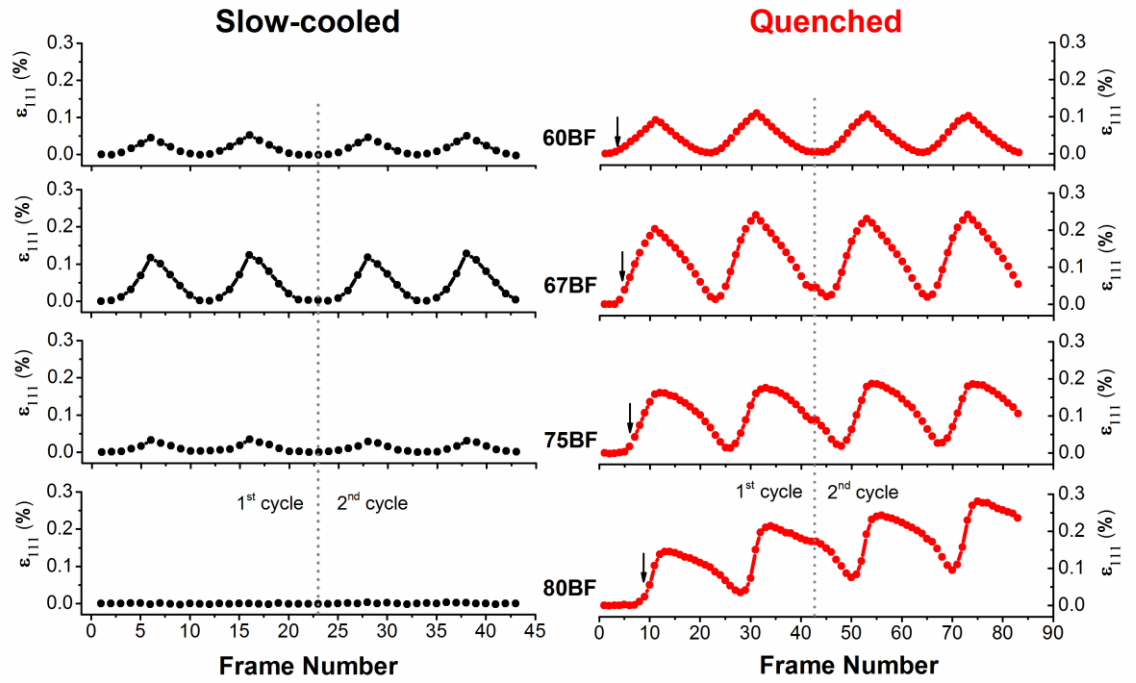

Figure 16 Variations in the calculated microscopic strain for the {111} grain family during the application of the electric field in slow-cooled and quenched ceramics (ψ = 0°). Each frame number corresponds to a step size of 1 kV/mm in the slow-cooled and 0.5 kV/mm in the quenched state. Arrows show the points where domain swiching initiates, corresponding to the coercive field, E_C.

After quenching, the resulting strain responses show significantly improved variations. A symmetric strain profile was observed for quenched 60BF, which evolved into asymmetric profiles after the 2nd cycle of electric field for higher $BiFeO_3$ contents. Increases in remnant strain and upward trends in the strain profiles may signal that the character of the domain switching mechanism is altered. More specifically, a possible crossover from relaxor ferroelectric into a conventional ferroelectric type occurs between 60BF and 80BF for the quenched ceramics. The initiation of domain switching in the quenched compositions is highlighted in Figure 16, verifying the incremental trend in E_C with the addition of $BiFeO_3$. The progressively positive strain profile for 80BF also implies that the domain switching mechanism is still active and progressive improving during the application of 2 bipolar cycles of 5 kV/mm. Thus it can be concluded that higher electric field or additional field cycling is required to effectively complete the domain switching for this composition.

Table 3 Summarised strain results obtained from the peak fitting of {111} diffraction profiles. Usable strain is obtained from $\varepsilon_{111}^{Max} - \varepsilon_{111}^{Remanent}$.

State	Composition	ε_{111}^{Max} (%)	$\varepsilon_{111}^{Remanent}$ (%)	Usable strain
Slow-cooled	60BF	0.06	0.00	0.06
	67BF	0.14	0.02	0.12
	75BF	0.04	0.02	0.02
	80BF	0.00	0.00	0.00
Quenched	60BF	0.10	0.00	0.10
	67BF	0.25	0.05	0.20
	75BF	0.20	0.10	0.10
	80BF	0.30	0.25	0.05

4. CONCLUSIONS

Thorough and comparative investigations were carried out to evaluate the influence of BF/BT ratio on the structure and functional properties of 1 mol% Ti-substituted BF−BT piezoceramics with an emphasis on the electromechanical actuation mechanisms. Structural and microstructural investigations in the selected Ti-modified compositions show a clear evidence for chemical segregation. The segregated regions were then assigned as core and shell phases. Their effects on the functional properties were accordingly analysed based on their ferroelectric nature with respect to cooling state as a function of BF content. The influence of thermal quenching in core-shell structured ceramics on the ferroelectric, electrostrain and dielectric properties was found to be greater for compositions with high BF content.

In the 75BF composition, the crystal structure of the shell region is shown to comprise pseudocubic (*Pm-3m*) in the slow-cooled state and untilted rhombohedral phase (*R3m*) in the quenched state, whilst the core region is defined as a highly distorted rhombohedral phase with *R3c* space group in both cases. The mechanisms that contribute to the electric field-induced strain are evaluated by considering both the intrinsic and extrinsic contributions from each phase through the use of *in-situ* synchrotron X-ray diffraction, illustrating a good agreement with macroscopic strain measurements. The total peak-to-peak strain is found to be $\varepsilon_{33} \approx 0.14\%$; the transformed shell is actively involved in the electric

field-induced actuation mechanism (ε_{33}≈0.13%), while the rhombohedral core is almost inactive upon poling, which yield negligible strain response (ε_{33}≈0.01%). In-situ investigations on the microscopic strain analysis for the {111} crystallographic orientation for the present compositions suggest that the highest usable strain (0.20%) can be obtained for the region around 67BF after quenching.

5. REFERENCES

1. Uchino, K. Piezoelectric Energy Harvesting Systems—Essentials to Successful Developments. *Energy Technol.* **6,** 829–848 (2018).
2. Uchino, K. Glory of piezoelectric perovskites. *Sci. Technol. Adv. Mater.* **16,** (2015).
3. Rödel, J. *et al.* Perspective on the Development of Lead-free Piezoceramics. *J. Am. Ceram. Soc.* **92,** 1153–1177 (2009).
4. Catalan, G. & Scott, J. F. Physics and applications of bismuth ferrite. *Adv. Mater.* **21,** 2463–2485 (2009).
5. Selbach, S. M., Tybell, T., Einarsrud, M. A. & Grande, T. The ferroic phase transitions of $BiFeO_3$. *Adv. Mater.* **20,** 3692–3696 (2008).
6. Calisir, I., Amirov, A. A., Kleppe, A. K. & Hall, D. A. Optimisation of functional properties in lead-free $BiFeO_3$-$BaTiO_3$ceramics through La^{3+}substitution strategy. *J. Mater. Chem. A* **6,** (2018).
7. Calisir, I. & Hall, D. A. Chemical heterogeneity and approaches to its control in $BiFeO_3$–$BaTiO_3$ lead-free ferroelectrics. *J. Mater. Chem. C* **6,** 134–146 (2018).
8. Leontsev, S. O. & Eitel, R. E. Dielectric and Piezoelectric Properties in Mn-Modified (1-x)$BiFeO_3$ - x$BaTiO_3$ Ceramics. *J. Am. Ceram. Soc.* **92,** 2957–2961 (2009).
9. Rojac, T. *et al.* $BiFeO_3$ Ceramics: Processing, Electrical, and Electromechanical Properties. *J. Am. Ceram. Soc.* **97,** 1993–2011 (2014).
10. Lee, M. H. *et al.* High-performance lead-free piezoceramics with high curie temperatures. *Adv. Mater.* **27,** 6976–6982 (2015).
11. Wei, J., Fu, D., Cheng, J. & Chen, J. Temperature dependence of the dielectric and piezoelectric properties of x$BiFeO_3$–(1-x)$BaTiO_3$ ceramics near the morphotropic phase boundary. *J. Mater. Sci.* **52,** 10726–10737 (2017).
12. Shen, S. *et al.* The effect of cooling rate on structural and electrical properties of multiferroic BLF-PT ceramics. *J. Am. Ceram. Soc.* 1–6 (2018).

13. Kim, D. S., Cheon, C. Il, Lee, S. S. & Kim, J. S. Effect of cooling rate on phase transitions and ferroelectric properties in $0.75BiFeO_3$-$0.25BaTiO_3$ ceramics. *Appl. Phys. Lett.* **109,** 202902 (2016).

14. Zheng, T., Zhao, C., Wu, J., Wang, K. & Li, J. F. Large strain of lead-free bismuth ferrite ternary ceramics at elevated temperature. *Scr. Mater.* **155,** 11–15 (2018).

15. Damjanovic, D. in *The Science of Hysteresis* **3,** 337–465 (2005).

16. Stewart, M., Cain, M. G. & Hall, D. Ferroelectric hysteresis measurement & analysis. *NPL Rep. C. 152* 1–57 (1999).

17. Filik, J. *et al.* Processing two-dimensional X-ray diffraction and small-angle scattering data in DAWN 2. *J. Appl. Crystallogr.* **50,** 959–966 (2017).

18. Glazer, a. M. The classification of tilted octahedra in perovskites. *Acta Crystallogr. Sect. B Struct. Crystallogr. Cryst. Chem.* **28,** 3384–3392 (1972).

19. Hall, D. A. *et al.* Domain switching in rhombohedral PZT ceramics under electrical and mechanical loading. *Mater. Sci. Technol.* **24,** 927–933 (2008).

20. Yoneda, Y., Yoshii, K., Kohara, S., Kitagawa, S. & Mori, S. Local structure of $BiFeO_3$–$BaTiO_3$ mixture. *Jpn. J. Appl. Phys.* **47,** 7590–7594 (2008).

21. Kumar, M. M., Srinivas, A. & Suryanarayana, S. V. Structure property relations in $BiFeO_3$/$BaTiO_3$ solid solutions. *J. Appl. Phys.* **87,** 855–862 (2000).

22. Singh, A., Moriyoshi, C., Kuroiwa, Y. & Pandey, D. Evidence for local monoclinic structure, polarization rotation, and morphotropic phase transitions in (1-x)$BiFeO_3$-x$BaTiO_3$ solid solutions: A high-energy synchrotron x-ray powder diffraction study. *Phys. Rev. B* **88,** 024113 (2013).

23. Kiyanagi, R. *et al.* Structural and magnetic phase determination of (1-x)$BiFeO_3$-x$BaTiO_3$ solid solution. *J. Phys. Soc. Japan* **81,** 024603 (2012).

24. Hinterstein, M. *et al.* Cyclic electric field response of morphotropic $Bi_{1/2}Na_{1/2}TiO_3$-$BaTiO_3$ piezoceramics. *Appl. Phys. Lett.* **106,** 222904 (2015).

25. Megaw, D. H. & Darlington, C. N. W. Geometrical and Structural Relations in the Rhombohedral Perovskites. *Acta Cryst.* **A31,** 161–173 (1975).

26. Kubel, F. & Schmid, H. Structure of a ferroelectric and ferroelastic monodomain crystal of the perovskite BiFeO3. *Acta Crystallogr. Sect. B* **46,** 698–702 (1990).

27. Li, F., Zhang, S., Damjanovic, D., Chen, L. Q. & Shrout, T. R. Local Structural Heterogeneity and Electromechanical Responses of Ferroelectrics: Learning from Relaxor Ferroelectrics. *Adv. Funct. Mater.* **1801504,** 1–21 (2018).

28. Jin, L., Li, F. & Zhang, S. Decoding the Fingerprint of Ferroelectric Loops: Comprehension of the Material Properties and Structures. *J. Am. Ceram. Soc.* **97,** 1–27 (2014).

29. Mantri, S., Oddershede, J., Damjanovic, D. & Daniels, J. E. Ferroelectric domain continuity over grain boundaries. *Acta Mater.* **128,** 400–405 (2017).

30. Pramanick, A., Damjanovic, D., Daniels, J. E., Nino, J. C. & Jones, J. L. Origins of Electro-Mechanical Coupling in Polycrystalline Ferroelectrics During Subcoercive Electrical Loading. *J. Am. Ceram. Soc.* **94,** 293–309 (2011).

31. Hall, D. A., Steuwer, A., Cherdhirunkorn, B., Mori, T. & Withers, P. J. A high energy synchrotron x-ray study of crystallographic texture and lattice strain in soft lead zirconate titanate ceramics. *J. Appl. Phys.* **96,** 4245–4252 (2004).

32. Daniel, L. *et al.* Revisiting the blocking force test on ferroelectric ceramics using high energy x-ray diffraction. *J. Appl. Phys.* **117,** 174104 (2015).

33. Daniels, J. E., Finlayson, T. R., Studer, A. J., Hoffman, M. & Jones, J. L. Time-resolved diffraction measurements of electric-field-induced strain in tetragonal lead zirconate titanate. *J. Appl. Phys.* **101,** 094104 (2007).

34. Wei, Y. *et al.* Polar order evolutions near the rhombohedral to pseudocubic and tetragonal to pseudocubic phase boundaries of the $BiFeO_3$-$BaTiO_3$ system. *Materials (Basel).* **8,** 8355–8365 (2015).

Chapter 4

General Conclusions and Future work

In general, the composition-structure-property relationships of $BiFeO_3$–$BaTiO_3$ binary system were investigated in this project. The major aim was to propose optimized processing routes for the studied $BiFeO_3$–$BaTiO_3$ compositions, by employing several approaches including doping strategies and post processing treatments. The impacts of such approaches on the morphology, structure and functional properties were thoroughly investigated.

Some key findings and related issues concerning this work with, together with recommendations for future research, are listed as follows:

Compositional investigations: Since high conductivity was observed in the undoped $BiFeO_3$-$BaTiO_3$ compositions, a particular composition was selected for doping studies, which is rhombohedral perovskite structured $0.75BiFeO_3$-$0.25BaTiO_3$ (75BFBT). The high conductivity was greatly suppressed when Mn, La and Ti are used as dopants. However, it was found that homogeneous microstructures for this composition were only obtained *via* Mn and La doping, when MnO_2 is added to the starting powders and La^{3+} is used as an isovalent substitution for Bi^{3+} in 75BFBT. Therefore it can be suggested that the compositional range can be further extended as well as exploring the effect of different types of sintering additives or modifiers (*e.g.* CuO, Co_2O_3) or isovalent ion substitutions (*e.g.* rare earth ions, transition metal ions with the equal valence of Fe^{3+}) or self-compensated perovskite end-members (*e.g.* $KNbO_3$, $Bi_{0.5}K_{0.5}TiO_3$, $Bi_{0.5}Na_{0.5}TiO_3$). It should be noted that the incorporation of these dopants and their effect on the solubility may vary and this issue should be investigated thoroughly.

Regarding the chemically heterogeneous compositions, it has been proven that using donor doping in 75BFBT (La^{3+} for Ba^{2+} and Ti^{4+} for Fe^{3+}) and addition of MnO_2 into its calcined composition induces chemical heterogeneity in the form of core-shell type microstructure. Although, the methods to obtain such heterogeneity are different, the underlying formation mechanism is assumed to share the same phenomena. We proposed that the formation of the core-shell structure is attributed to kinetic factors and differences in reactivity during sintering, with the $BiFeO_3$-rich core forming initially and the $BaTiO_3$-rich shell forming at a later stage. Thermodynamic immiscibility between the $BiFeO_3$ and $BaTiO_3$ solid solutions is also suggested to play an important role, leading to further nanoscale segregation in the shell region during cooling. This type of heterogeneity was consistently observed in a wide compositional range of Ti-modified BF–BT solid solution system. However, its origin is not fully understood yet and this warrants further investigations on this particular issue.

Thermal Quenching Treatment: This technique is one of the most applied methods to enhance the functional properties of BF-BT ceramics. Its substantial effect on all studied compositions was also confirmed. More importantly, it was found that thermal quenching can have a great impact on the compositions exhibiting core-shell type microstructure. The quenching temperature and holding time were usually fixed in this work (unless stated), however more systematic studies such as changing annealing and quenching temperature/time can be beneficial in order to explore the optimum heat treatment procedures with respect to different applications.

Phase Determination: Coexistence of phases in homogenous and heterogeneous compositions was conducted using both high resolution and high energy x-ray synchrotron radiation. It is found that the presence of pseudocubic phases in the studied compositions is closely correlated with the existence of chemical heterogeneity, particularly corresponding to the observed shell component within the grains. It was also shown that the pseudocubic phases appear as the most pronounced diffraction peaks, even in the high resolution

spectra of La-doped 75BFBT ceramics, which limits the precise structural analysis for the coexistence of phases. In addition, in this study, both bulk samples and crushed powders were used for determination of crystal structure and certain differences were observed between the obtained results, indicating that the reasons causing this and optimizations (experimental set-up, sample preparation, detector type *etc.*) should be investigated further.

Microstructure: Microstructure analysis was a major part of this study due to the challenges associated with revealing clear evidence of chemical heterogeneity in the form of core-shell type microstructures. All the studied compositions were prepared both with and without exposure to chemical etchants on the polished surfaces in order to reveal the domain-like features within chemically heterogeneous grains *via* SEM in BSE mode. The presence of elements corresponding to the core and shell regions was verified by SEM equipped with an EDS detector. For all the heterogeneous compositions, it was verified that the core is composed of $BiFeO_3$-rich phases, while the shell is relatively $BiFeO_3$-deficient. Due to the low levels dopants (1 mol %) involved for the selected compositions, conclusive information about which region (core or shell) they occupy and what is their role in the phase segregation remain for further investigations. Furthermore, the precise nominal chemical composition of the core and shell could likely be determined using high resolution TEM equipped with EDS and/or Electron Energy Loss Spectroscopy (EELS).

According to these findings, it is emphasised that microstructural investigations on BF–BT ceramics must be conducted on polished surfaces, preferably using thermochemical etching methods. Reports of fracture surfaces or natural sintered surfaces in the literature may lead to misinterpretation of the obtained structural and functional properties.

Dielectric Properties: Dielectric anomalies as a function of temperature were predominant feature in the dielectric related sections. It was found that occurrence of the core-shell type microstructure significantly affects the temperature-dielectric dependent properties, yielding noticeable multiple

transition temperatures. As we analyzed the ferroelectric ordering nature of core and shell phases, the shell phase is expected to show diffuse dielectric characteristics as a function of frequency and temperature due to its confirmed relaxor-type behaviour (presence of pseudocubic phase). Conversely, for the case of $BiFeO_3$-rich core, evaluating its temperature-dependent dielectric properties was found challenging due to the observed high dielectric loss above ≈400°C. Although a high temperature dielectric anomaly (≈625°) was noticeable for all heterogeneous type compositions, further electrical characterization is needed in order to verify whether this temperature should be identified as the Curie temperature of the core or an artefact caused by high AC conductivity. One particular electrical characterization method that could be useful is Impedance Spectroscopy, which in principle can separate the capacitive and conductive contributions of the predominant phases as well as revealing the dominant conduction mechanism at high temperatures.

Ferroelectric Properties: Thermal quenching had a significant impact on the P-E loops, transforming the slim (or pinched) loops into well-saturated loops for the studied compositions. On the other hand, it is found that slow-cooling can be beneficial for investigations of dielectric energy storage in BF-based ceramics. This is directly linked to the chemically segregated phases. Therefore, further extending annealing time and/or changing cooling rates could have an impact on the dielectric energy storage performance in core-shell type BF-based ceramics.

Electromechanical Properties: Extensive strain analysis was carried out in this work, using the data obtained from *in-situ* high energy X-ray diffraction studies under high electric field. The aim was to reveal the strain contribution of each associated phase (core and shell) in heterogeneous type compositions. It was found that the observed large strain predominantly arises from the transformed shell phase (from short-range to long-range ordering induced by quenching) while there was almost no observable strain contribution from the core under the applied field range. However, during the strain analysis, one major challenge was that the resolution obtained from the *in-situ* experiments was limited to

precisely resolve the proposed structure for the rhombohedral shell phase with a small rhombohedral distortion. The use of alternative high resolution detector or a longer sample-detector distance could help to resolve this issue.

On the other hand, measuring the piezoelectric coefficient, d_{33}, and electromechanical coupling coefficient, k_p as function of temperature could be useful to provide an insight into the high temperature piezoelectric capability of the presented compositions.

Multiferroic Properties: Although this project is not primarily focused on the aspects of (anti)ferromagnetism in $BiFeO_3$-based ceramics, the observation of core-shell type microstructures motivates further research to explore this property in detail. The composite approach composed of a ferromagnetic core and piezoelectric shell could have potential in magnetoelectric applications in the near future. Therefore, we investigated ferromagnetic and magnetoelectric properties in La-doped 75BF compositions. It is confirmed that a weak ferromagnetism was noticed in the modified compositions as compared to the undoped one. However, the influence of quenching on the ferromagnetic property was opposite to that of enhancement on the ferroelectric property. On the other hand, relatively higher magnetoelectric coupling was confirmed in the core-shell structured quenched composition as compared to the homogeneous (single phase) composition.

The obtained results for multiferroic behaviour were combined with microstructure, structural and functional properties. However, further systematic studies with particular focus on multiferroic properties in core-shell structured BF-BT ceramics should be carried out to reveal their potential in this area. Based on the findings, as poling electric field increases, higher magnetoelectric coupling coefficients are obtained. This could suggest that this relation could be investigated by conducting *in-situ* neutron diffraction experiments to reveal magnetic ordering variations under electric field, using similar methodology to that employed for *in-situ* high energy X-ray diffraction experiments in this study.

APPENDIX I

SUPPORTING INFORMATION

Chemical heterogeneity and approaches to its control in $BiFeO_3$-$BaTiO_3$ lead-free ferroelectrics

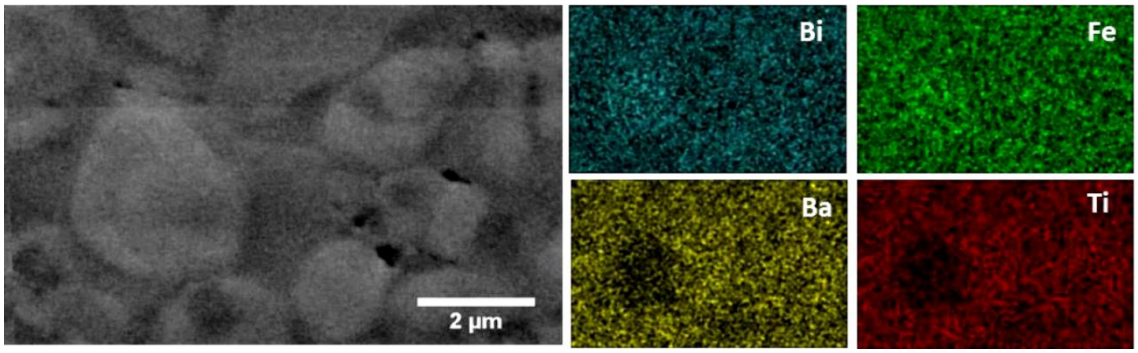

Figure S1.SEM-EDS elemental mapping results of air-quenched (15 min) Mn-AC ceramics. As-sintered Mn-AC was subjected to annealing at 750˚C for 15 min, then directly quenched to room temperature. Brighter regions under SEM-backscattered electron mode are mostly associated with depletion of Ba and Ti elements which are prone to segregate in the shell.

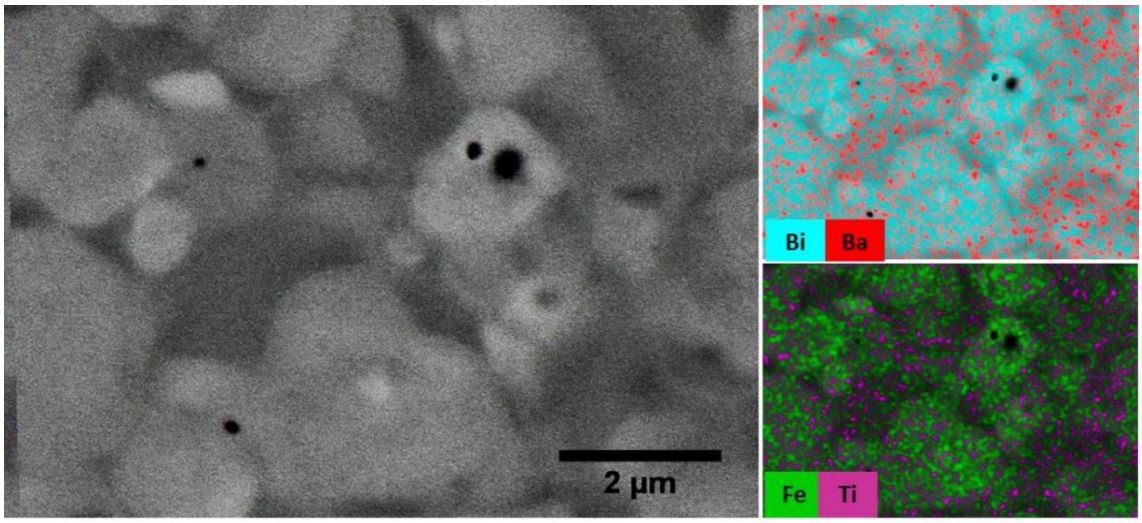

Figure S2. SEM-EDS elemental mapping results of air-quenched (21h) Mn-AC ceramics. As-sintered Mn-AC ceramic was annealed at 750˚C for 21 h, then directly quenched to room temperature. The signals of Bi and Fe elements are prominently collected from the brighter regions under SEM-backscattered mode, which could be the evidence of persistent chemical heterogeneity in the air-quenched even after prolong annealing treatment.

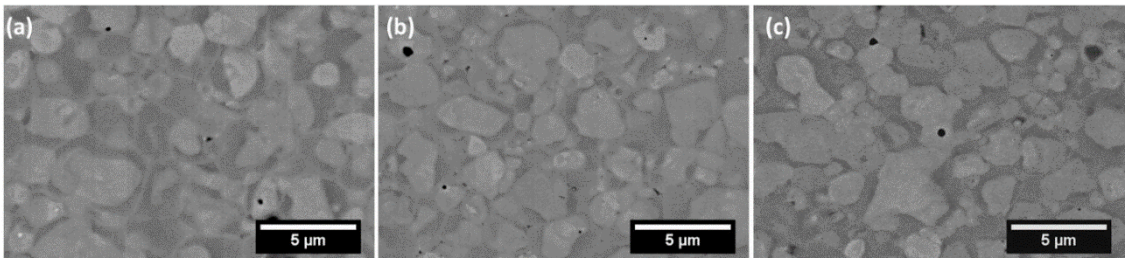

Figure S3. Microstructure of none-etched polished surfaces of **a)** as-sintered Mn-AC, **b)** air-quenched(15min) Mn-AC and **c)** air-quenched (21h) Mn-AC. All images were taken under SEM-backscattered mode.

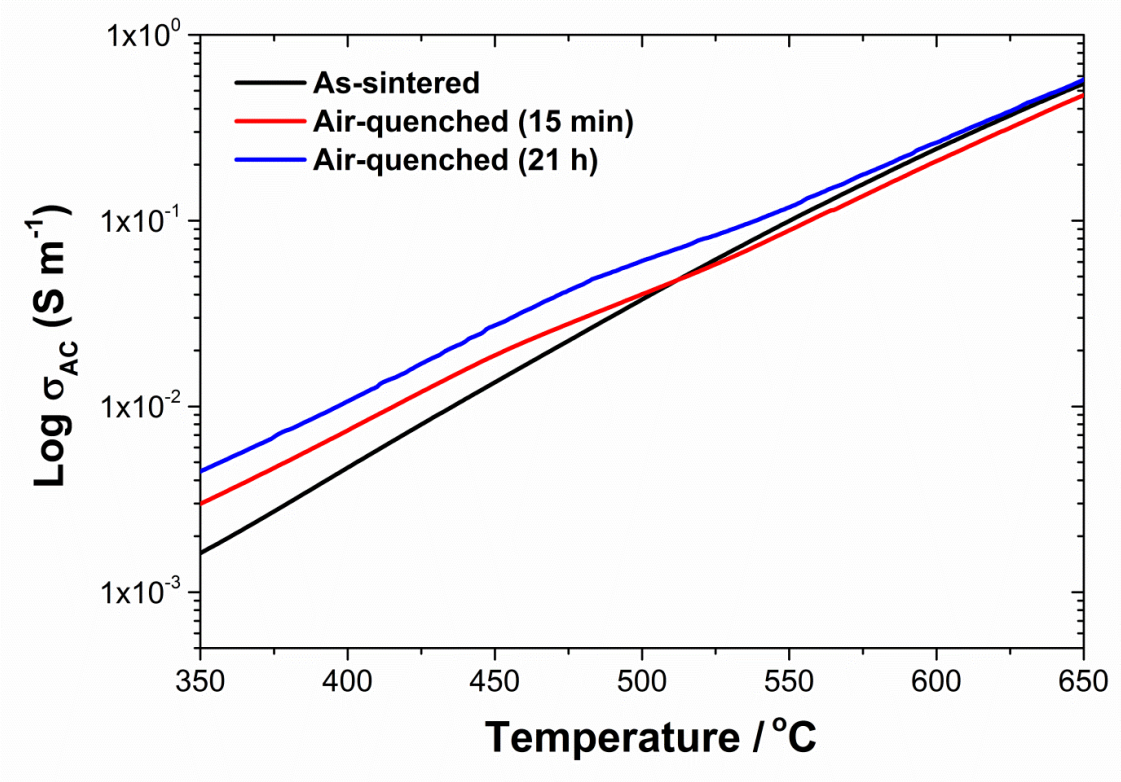

Figure S4. Temperature dependence of AC conductivity, σ_{AC} for as-sintered, air-quenched (annealed at 750°C for 15 min and 21 h) Mn-AC ceramics, measured at 100 kHz.

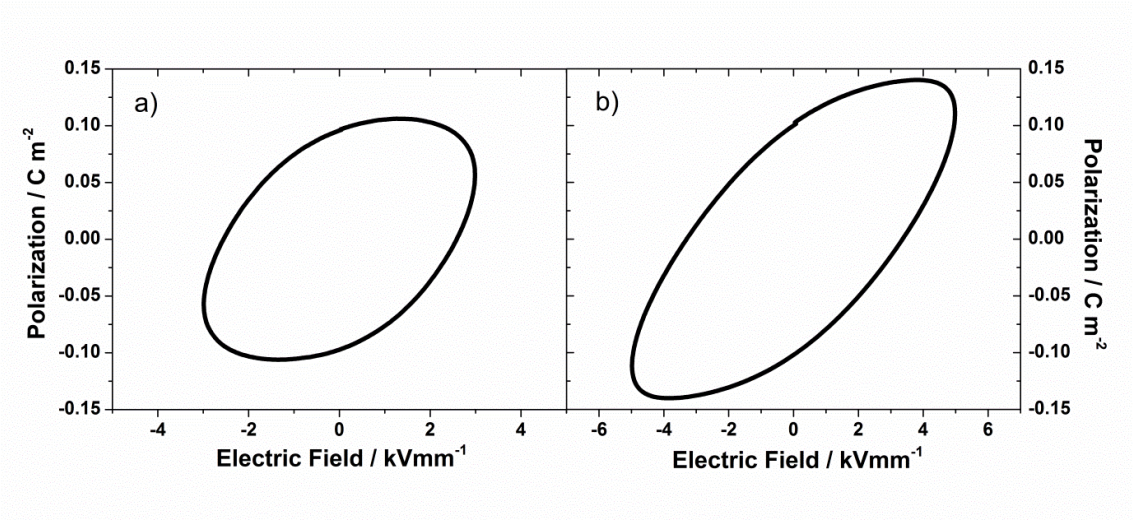

Figure S5. Ferroelectric P-E hysteresis loops of **a)** undoped 75BFBT and **b)** 3 mol% MnO_2 (BC). Observed rounded P-E loops indicate high conductivity without MnO_2 and with excessive MnO_2 addition in 75BFBT ceramics.

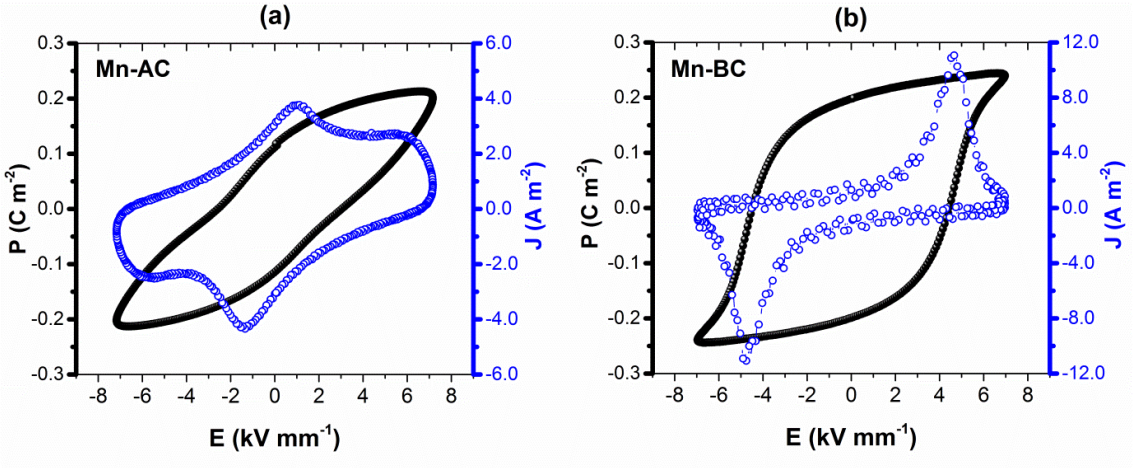

Figure S6. P-E and J-E loops of **a)** Mn-AC, and **b)** Mn-BC ceramics sintered at 1050°C for 2h.

APPENDIX II

SUPPORTING INFORMATION

Optimisation of functional properties in lead-free $BiFeO_3$-$BaTiO_3$ ceramics through La^{3+} substitution strategy

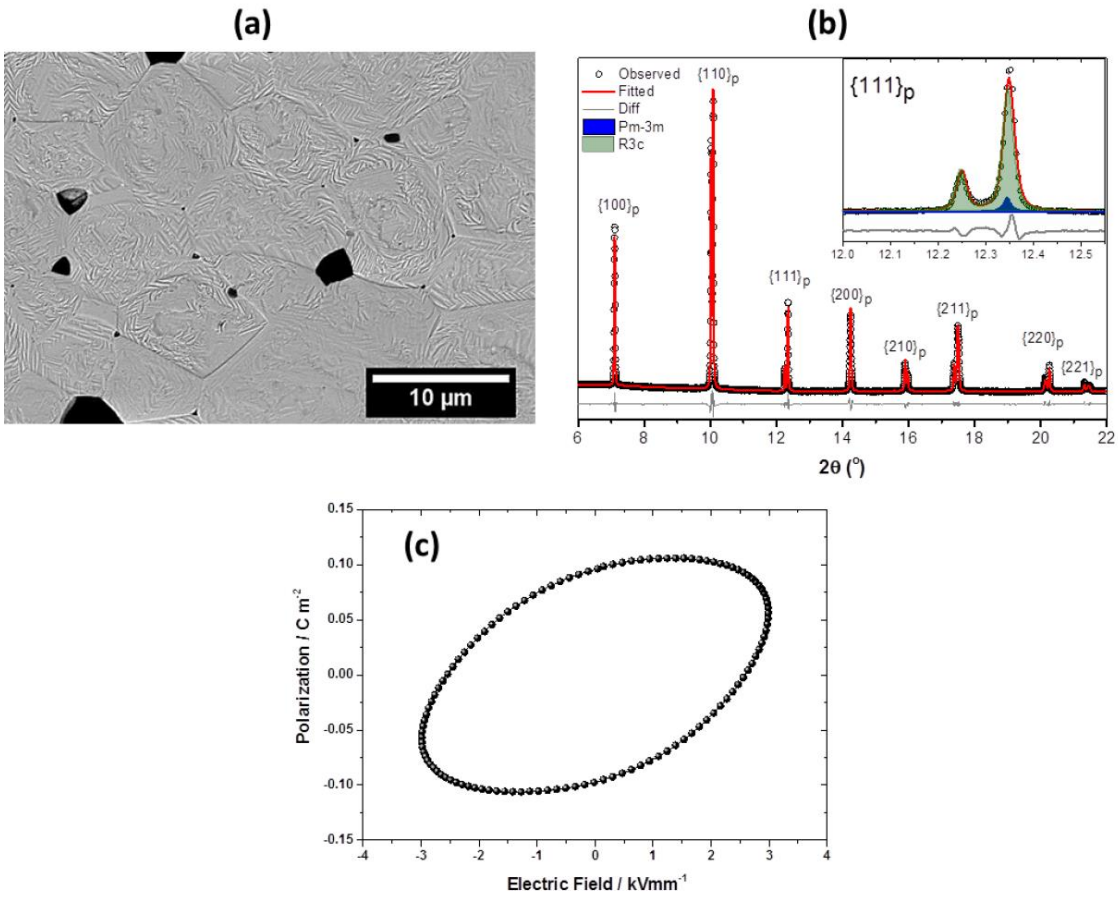

Figure S1. (a) Microstructure, **(b)** refined XRD pattern and **(c)** ferroelectric P-E hysteresis loop of undoped 75BFBT ceramics.

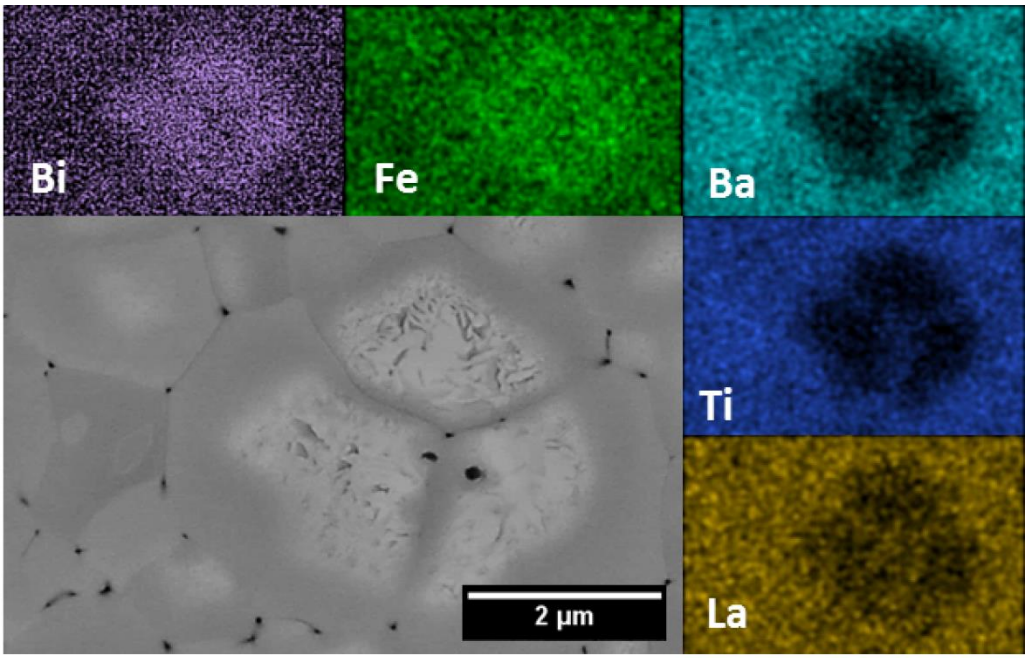

Figure S2. SEM-EDS elemental mapping results for 3 mol% La^{3+} substitution for Ba^{2+} in 75BFBT. The polished surface was chemically etched to reveal its distinct core-shell feature.

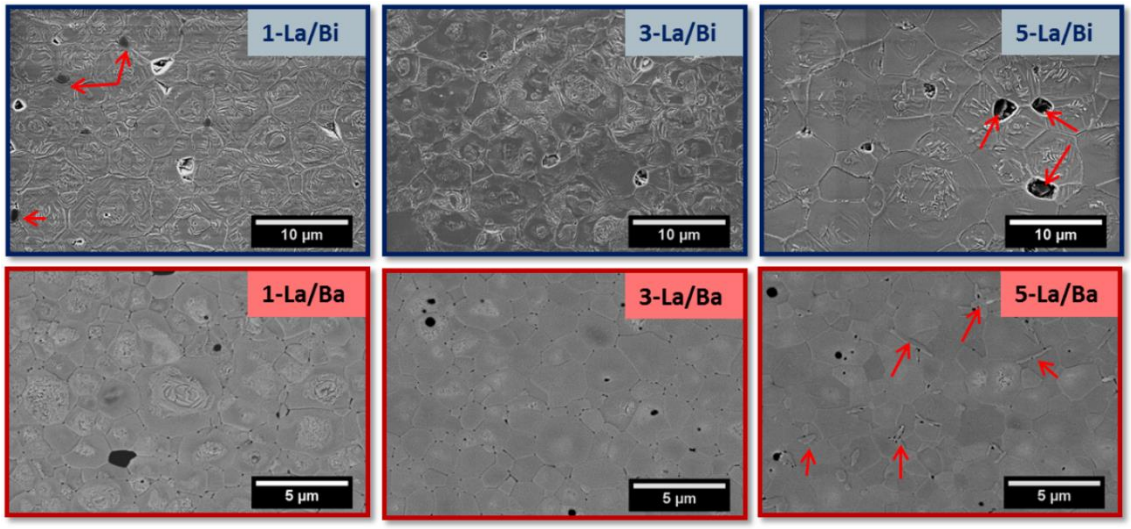

Figure S3. Microstructure of 75BFBT ceramics with 1, 3 and 5 mol% La^{3+} substitution for Bi^{3+} (upper row, denoted as *x*-La/Bi) and for Ba^{2+} (bottom row, denoted as *x*-La/Ba). The polished surfaces were chemically etched. The arrows indicate detected secondary phases.

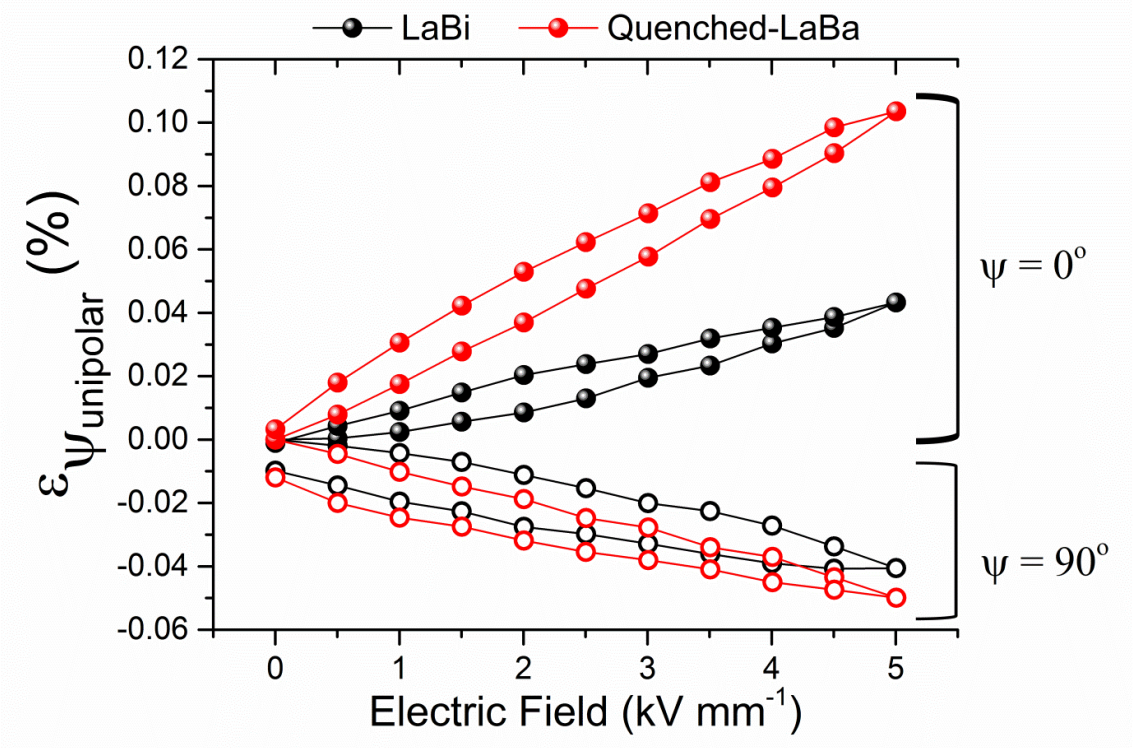

Figure S4. Unipolar macroscopic strain curves of LaBi and quenched-LaBa compositions at Ψ=0˚ and Ψ=90˚

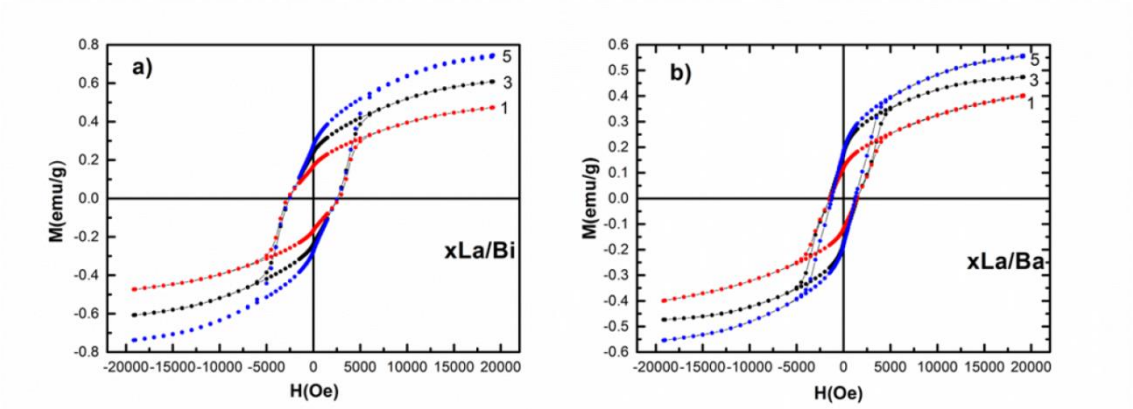

Figure S5. Ferromagnetic (M-H) hysteresis loops of 75BFBT ceramics with **(a)** 1, 3 and 5 mol% La^{3+} substitution for Bi^{3+} (denoted as *x*La/Bi), and **(b)** 1, 3 and 5 mol% La^{3+} substitution for Ba^{2+} (denoted as *x*La/Ba).